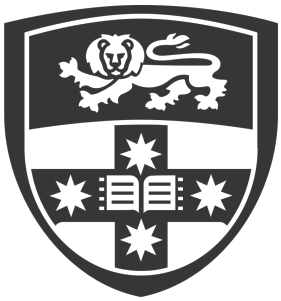

THE UNIVERSITY OF
SYDNEY

The Fluid Dynamics of Cavity Flow Induced Oscillations and the Boundary Layer Effect

A thesis submitted to the University of Sydney, to fulfil requirements for a Doctor of Philosophy in Unsteady Low-Speed Fluid Dynamics from the School of Aerospace, Mechanical & Mechatronic Engineering

Caroline Olivia Louise Hamilton Smith

22nd of September 2025

Statement of Originality

This thesis was completed between 1st Oct. 2021 and 31th May 2025, under supervision of Assoc. Prof. N. Lawson and Dr. G.A Vio in the School of Aerospace, Mechanical and Mechatronic Engineering (AMME), within the Faculty of Engineering and IT, at the University of Sydney.

The following areas of work are carried out in this thesis:

(1) Review of up to 150 years of cavity flow research, as a part of a more extensive review article, published in the European Journal of Mechanics - B/Fluids [1].

(2) Wind-tunnel experiments using Hot-Wire Anemometry (HWA) and Unsteady Surface Pressure (USP) measurement systems, to map the internal and upstream (U/S) fluid structures of a series of open streamwise and narrow spanwise cavity geometries.

(3) Design, development and set-up of hardware and software to conduct experiments.

(4) Error and uncertainty assessment in contribution to post-processing for assessable results.

(5) Development and execution of empirically driven analytical and numerical methods to reconstruct the U/S boundary layer (BL) and cavity flow field from experiment results.

(6) Analysis of post-processed results, highlighting a relationship between the BL and cavity response, driven by the U/S velocity and pressure gradient (dp/dx) profile.

(7) Presentation of an updated Strouhal Number (St) model [2] to predict dimensionless cavity frequency response, accounting U/S BL and dp/dx effects.

(7) Presentation of an updated numerical radiative impedance model [3] to predict cavity peak amplitude response, also accounting U/S BL dp/dx effects.

I certify, the content of this thesis, as summarised above, is my own work, and has not been submitted for any other degree or purpose. I certify, the intellectual content, is the product of my own work, and assistance received and sources used in preparing this thesis are acknowledged.

.....	.....
C.O.L. Hamilton Smith, PhD Student	Date
.....	.....
Assoc. Prof. N. Lawson, Lead Supervisor	Date
.....	.....
Dr. G.A. Vio, Supervisor B	Date

Authorship Attribution

Chapter 2 of this thesis has been published as a review article; "C.O.L. Hamilton Smith, N. Lawson, and G. A. Vio. History, review and summary of the cavity flow phenomena, *European Journal of Mechanics - B/Fluids*, 108:32-72, 2024. doi: 10.1016/j.euromechflu.2024.07.005" cited as [1]. I executed the research, analysed the data and wrote the manuscript drafts. The European Journal of Mechanics requires lead author be corresponding author.

....
C.O.L. Hamilton Smith, PhD Student Date

As supervisor for the candidature upon which this thesis is based, I can confirm that the authorship attribution statements above are correct.

....
Assoc. Prof. N. Lawson, Lead Supervisor Date

....
Dr. G.A. Vio, Supervisor B Date

Acknowledgements

This thesis represents the culmination of an Engineering based Doctor of Philosophy in Fluid Dynamics. I would like to thank my supervisors; Nicholas Lawson and Gareth Vio, for their support and guidance over the years. Dealing with my need for perfection, is not an easy task. A special thank you to my Mother and Father, for their continued love and support, ensuring these years have been as easy as possible. Also to Nishanth Menakath, a fellow PhD candidate, and friend, who assisted in experimental set-up, and provided many a sanity check.

Scholarship Acknowledgement

The research reported in this thesis, was supported by the Australian Government Research Training Program (RTP) Offset Scholarship, and University of Sydney, Faculty of Engineering and IT, Engineering Research Scholarship (ERS).

The Advanced Piezoelectric Materials and Applications (APMA) Program supported by Defence Materials Technology Centre (DMTC) Limited Australia, and funded by the Australian Defence Force (ADF) through the Advanced Strategic Capabilities Accelerator (ASCA) Program is recognised for funding this research, through a top-up scholarship.

Zonta International in provision of the 2022 Amelia Earhart Fellowship, originally established in 1938 in honour of famed pilot Amelia Earhart, awarded to women pursuing PhD degrees in aerospace engineering and space science, is also recognised for funding this research.

AI Acknowledgement

I certify, no content produced by generative AI has been used in the preparation of this thesis, nor was it used during any part of the research detailed in this thesis.

....
C.O.L. Hamilton Smith, PhD Student Date

As supervisor for the candidature upon which this thesis is based, I can confirm acknowledgements above are correct.

....
Assoc. Prof. N. Lawson, Lead Supervisor Date

....
Dr. G.A. Vio, Supervisor B Date

Abstract

This thesis presents experiments, empirical and numerical modelling of incompressible open cavity flow. A literature review identifies gaps in the research for effects of cavity width (W), external geometry, the upstream (U/S) boundary layer (BL), and pressure gradient dp/dx on cavity response. These characteristics are subsequently quantified through experiment in a low-speed wind tunnel (WT), measuring unsteady surface pressure (USP) on cavity surfaces, and velocity with hot-wire anemometry (HWA), to map the U/S BL. To modify the BL, a series of nose cones were fitted U/S of the cavity, and datum-d to a flat-plate BL, whilst cavity geometry was varied for length-to-depth ratio L/D = 1-3, and length-to-width ratio L/W = 1-6.

From result analysis, core findings showed, that the shorter cavities (L/D = 1) sustained high magnitude pressure on all surfaces, whilst the longer cavities (L/D > 1) had distinct low and high pressure regions streamwise, peaking at a primary recirculation point on the floor. For all cavity geometries, which are considered narrow (L/W > 1) at fixed L/D, the narrower cavity (W = 30mm) presented less coherent 3D flow features than the wider cavity (W = 60mm), which had more distinct 3D flow features, presenting as discrete spanwise nodes, flanking the primary recirculation point. Such variation of narrow cavity width was not found in literature.

Varying U/S BL structure, and by correspondence BL thicknesses δ, δ^*, θ, and pressure gradient dp/dx, altered internal cavity response significantly. The thinnest BL, of laminar profile, and largest favourable pressure gradient $dp/dx < 0$, produced by the conic nose U/S, presented a slight shift in cavity frequency response, and very notable increase in magnitude response. In contrast, the thickest BL, of turbulent profile, and $dp/dx = 0$, produced by the flat-plate U/S, had a notably lower magnitude response. Results thus suggest, changing BL structure to reduce δ and increase magnitude $dp/dx < 0$, increases flow periodicity, amplifying internal cavity mechanisms for a more volatile, high magnitude cavity pressure response, essentially to expel flow downstream (D/S) through the shear-layer (SL) mass-exchange cycle.

Based on these results, in the final chapter, the derivation of a viscid model of incompressible open cavity flow is presented. The model empirically estimates dimensionless frequency $\mathrm{St_{HS}}$, derived with respect to the U/S BL, superimposing oscillatory cavity vorticity and feedback modes. The model also numerically estimates dimensionless pressure amplitude $p_p \sim$ SPL, at specified location (x, y, z) and wave number k in the cavity, with respect to TE source $\mathrm{Q}(x', y', z')$ and excitation frequency f. The latter updates a previous radiative impedance model, to include the U/S BL, and superposition of oscillatory cavity vorticity and feedback modes. Based on this model, experimental St and SPL are estimated to within 5% error.

Contents

Copyright i

Statement of Originality ii

Authorship Attribution iii

Acknowledgements iv

Abstract v

List of Figures x

List of Tables xiv

List of Abbreviations xvii

List of Symbols xix

1 Introduction 1

1.1 Application and Relevance . . . 1

1.2 Present Work . . . 2

2 Literature Review 4

2.1 The Cavity Flow Phenomena . . . 4

2.1.1 Streamwise Flow Type . . . 4

2.1.2 Spanwise Flow Type . . . 6

2.1.3 Cavity Modes . . . 7

2.1.4 Cavity Oscillatory Wave Types . . . 8

2.1.5 Cavity Flow Structures . . . 10

2.2 Internal Geometry and Airspeed . . . 12

2.2.1 Summary of Internal Geometry Effects . . . 17

2.2.2 Summary of Airspeed Effects . . . 18

2.3 Cavity Spectral Response . . . 18

2.4 The Boundary-Layer . . . 22

2.4.1 Turbulent Boundary Layer . . . 22

2.4.2 Laminar vs. Turbulent Boundary Layer . . . 23

2.4.3 Summary of Boundary Layer Effects . . . 26

2.5 Review Summary . . . 26

3 Experimental Set-Up **27**
3.1 The Wind Tunnel . . . 27
3.2 The Cavity Model . . . 29
3.2.1 Baseline Flat Cavity . . . 29
3.2.2 Cavity in a Fuselage . . . 30
3.3 Hot-Wire Anemometry Set-Up . . . 32
3.3.1 Mount Structure . . . 32
3.3.2 Data Instrumentation . . . 32
3.3.3 Data Acquisition . . . 33
3.4 Unsteady Surface Pressure Set-Up . . . 35
3.4.1 Pressure Taps . . . 35
3.4.2 Data Acquisition and Instrumentation . . . 37

4 Data Processing & Analysis **39**
4.1 Wind Tunnel Corrections . . . 39
4.1.1 Airspeed . . . 39
4.1.2 Wall Interference . . . 39
4.1.3 Blockage . . . 40
4.2 Hot-Wire Anemometry . . . 41
4.2.1 Data Calibration, Conversion and Statistics . . . 42
4.2.2 Data Error and Uncertainty . . . 44
4.3 Boundary Layer Data . . . 46
4.3.1 Boundary Layer Flow over a Flat-Plate . . . 46
4.3.2 Boundary Layer Flow over a Wedge . . . 47
4.3.3 Boundary Layer Flow over a Curved Surface . . . 50
4.3.4 Boundary Layer Flow with a Cavity Downstream . . . 53
4.4 Unsteady Surface Pressure . . . 53
4.4.1 Data Reduction . . . 53
4.4.2 Tube Distortion Error . . . 54
4.5 Signal Analysis . . . 56
4.5.1 Fast Fourier Transform . . . 56
4.5.2 Dynamic Mode Decomposition . . . 57
4.5.3 Strouhal Number Prediction . . . 60
4.6 Data Processing and Analysis Summary . . . 61

5 Hot-Wire Results & Discussion **62**
5.1 Velocity Profiles . . . 62
5.1.1 Effect of Free-Stream Reynolds Number Re_∞ . . . 62
5.1.2 Effect of Upstream Geometry . . . 63
5.1.3 Effect of Cavity Downstream . . . 64
5.1.4 Integral Time Scale . . . 65
5.2 The Boundary Layer . . . 66
5.3 Velocity Spectra . . . 68

5.3.1 Effect of Free-Stream Reynolds Number Re_∞ . . . 68
5.3.2 Effect of Upstream Geometry . . . 70
5.3.3 Effect of Distance from the Wall $+y$ . . . 70
5.3.4 Effect of the Cavity Downstream . . . 71
5.3.5 Summary of Magnitude Response . . . 72
5.4 Hot-Wire Results Summary . . . 72

6 Pressure Results & Discussion **74**
6.1 Surface Pressure Distributions . . . 75
6.1.1 Effect of Internal Cavity Geometry: Length and Width . . . 75
6.1.2 Effect of Free-Stream Reynolds Number Re_∞ . . . 79
6.1.3 Effect of Upstream Geometry . . . 84
6.2 Pressure Spectra . . . 87
6.2.1 Effect of Internal Geometry . . . 88
6.2.2 Effect of Free-Stream Reynolds Number Re_∞ . . . 89
6.2.3 Effect of Upstream Geometry . . . 90
6.3 Pressure Results Summary . . . 92

7 Physical Cavity Model **93**
7.1 Dimensionless Frequency . . . 93
7.2 Dimensionless Pressure Amplitude . . . 99

8 Conclusions & Recommendations **104**
8.1 Conclusion . . . 104
8.2 Further Recommended Work . . . 106

Appendices **119**

A Wind Tunnel Data **120**
A.1 Ambient Conditions . . . 120
A.2 Empty Wind Tunnel Boundary Layer Data . . . 134

B Boundary Layer Theory **137**
B.1 Boundary Layer Equations of Motion . . . 138
B.1.1 Laminar Flow . . . 138
B.1.2 Turbulent Flow . . . 139
B.1.3 Momentum Integral Equations . . . 139
B.2 Boundary Layer Similar Solutions . . . 139
B.2.1 Boundary Layer Flow over a Flat-Plate . . . 140
B.2.2 Boundary Layer Flow over a Wedge . . . 140
B.2.3 Boundary Layer Flow over a Curved Surface . . . 143

C Signal Analysis **149**
C.1 Fourier Transform . . . 149
C.2 Dynamic Mode Decomposition (DMD) . . . 149

C.2.1 Theory and Architecture . . . 150
C.2.2 Algorithm . . . 150
C.2.3 Reduction and Graphing . . . 151

D Additional Supporting Data **153**
D.1 Surface Pressure Data . . . 153
D.1.1 Effect of Internal Cavity Geometry: Length and Width . . . 153
D.1.2 Effect of Free-Stream Reynolds Number Re_∞/m . . . 155
D.2 Surface Pressure Spectral Data . . . 160
D.3 Hot-Wire Spectral Data . . . 170

E Viscid Physical Cavity Model **174**
E.1 Dimensionless Frequency . . . 174
E.2 Dimensionless Pressure Amplification . . . 176
E.3 Strouhal Number . . . 179

F Algorithms **181**
F.1 Pressure Data Processing . . . 181
F.1.1 Unsteady Surface Pressure Reduction . . . 181
F.1.2 Tube Distortion Code . . . 182
F.1.3 Atmospheric Conditions . . . 183
F.2 Hot-Wire Data Processing . . . 183
F.2.1 Hot-Wire Acquisition . . . 183
F.2.2 Hot-Wire Reduction . . . 184
F.2.3 Flat-Plate Boundary Layer Characteristics . . . 185
F.2.4 Falkner-Skan Similar Solution . . . 186
F.2.4.1 Numerical Runge Kutta Solution . . . 186
F.2.4.2 Wedge Boundary Layer Characteristics . . . 187
F.2.5 Murphy's Curved Surface Similar Solution . . . 188
F.2.5.1 Curve Boundary Layer Characteristics . . . 188
F.2.5.2 Curvature Function . . . 188
F.2.5.3 Taylor-Series Numerical Solution . . . 189
F.2.6 Shear Stress . . . 189
F.3 Modal Analysis . . . 190
F.3.1 Unsteady Surface Pressure Fast-Fourier Transform . . . 190
F.3.2 Hot-Wire Anemometry Fast-Fourier Transform . . . 190
F.3.3 Dynamic Mode Decomposition . . . 191
F.4 Amplitude Prediction . . . 192
F.4.1 Radiation Impedance Model . . . 192
F.4.2 Characteristic Radiation Coefficients . . . 193
F.4.3 Boundary Function g_m . . . 194

List of Figures

1 Introduction **1**

1.1 Basic Cavity Schematic 1

2 Literature Review **4**

2.1 Kelvin-Helmholtz Instability 5
2.2 Streamwise Cavity Flow Types 6
2.3 Spanwise Cavity Flow Types 7
2.4 Fluid-Dynamic, Resonant, & Elastic Type Oscillations[4] 9
2.5 Deep Open Cavity Flow Mechanism: Normal Mode 11
2.6 Open Cavity Flow Mechanism: Shear Layer Mode 11
2.7 Closed Cavity Flow Mechanism: Wake Mode 12

3 Experimental Set-Up **27**

3.1 University of Sydney Low-Speed Wind Tunnel Diagram 27
3.2 WT TS Schematic with Baseline Cavity Model: cross-section 28
3.3 WT TS Schematic with Baseline Cavity Model: observing direction of flow 28
3.4 Internal Cavity Geometry: dimensions in mm 29
3.5 Flat Cavity Model Schematic: Isometric View: dimensions in mm 29
3.6 Flat Cavity Model Schematic: Top, Bottom, Front, Back View: dimensions in mm . 30
3.7 Flat Cavity Model Schematic: Length & Width Variations: dimensions in mm . . . 30
3.8 Fuselage Cavity Model Schematic: Side and Front Part Drawing: dimensions in mm 31
3.9 Fuselage Cavity Model Schematic: Isometric View with Noses: dimensions in mm . . 31
3.10 Fuselage Cavity Model: 3D Printed Parts 31
3.11 Fuselage Cavity Model Schematic: Length & Width Variations: dimensions in mm . 32
3.12 HWA: WT TS Set-up 33
3.13 HWA: System Diagram 34
3.14 HWA: System Components: dimensions in mm 34
3.15 USP: System Diagram: Tube Tap connection to Pressure Sensor 36
3.16 USP: Pressure Tap Components 37
3.17 USP: Surface Pressure Tap Distribution, all dimensions in mm 37
3.18 USP: Scanivalve 4264/64Px MPS[5] 38
3.19 USP: Scanivalve 4264/64Px MPS Sensor Assembly with Tube Volume[5] 38

4 Data Processing & Analysis **39**

4.1 Wind Tunnel Corrections 41

4.2 HWA: Skewness & Kurtosis of C5: L/D = L/W = 3, Conic U/S, ΔU_∞ 42
4.3 HWA: Skewness & Kurtosis of C11: L/D = L/W = 3, Ogive U/S, ΔU_∞ 43
4.4 HWA: Skewness & Kurtosis of C17: L/D = L/W = 3, Parabola U/S, ΔU_∞ 43
4.5 HWA: Skewness & Kurtosis of C23: L/D = L/W = 3, Flat U/S, ΔU_∞ 43
4.6 HWA: Auto-Correlation of C5: L/D = L/W = 3, Conic U/S, y = 2mm, U_∞ = 50m/s 44
4.7 HWA: Uncertainty based on Table 4.1 45
4.8 HWA: Boundary Layer Schematic 46
4.9 HWA: Flat-Plate Boundary Layer Thicknesses 47
4.10 HWA: Wedge Boundary Layer Flow 48
4.11 HWA: Falkner-Skan Function in terms of η 49
4.12 HWA: Conic Nose Boundary Layer Thicknesses 49
4.13 HWA: Axisymmetric Boundary Layer Flow 50
4.14 HWA: Curved Similar Solution & Potential Velocity Profile Intersection for δ 51
4.15 HWA: Ogive Nose Boundary Layer Thicknesses 52
4.16 HWA: Parabola Nose Boundary Layer Thicknesses 53
4.17 USP: Series Connection of Tubes and Transducers 54
4.18 USP: Tube Distortion on $C_{p,rms}$ of C5: L/D = L/W = 3, Conic U/S, U_∞ = 50m/s . 55
4.19 USP: Tube Distortion on Cavity Spectra of C6: L/D = 3, L/W = 6, Conic U/S, U_∞ = 50m/s from a Pressure Tap on the floor at x/L = 0.5, z/W = 0.3 56
4.20 USP: Conjugate Combination of C5 TE: L/D = L/W = 3, Conic U/S, U_∞ = 50m/s 58
4.21 USP: Modes of C5 Floor: L/D = L/W = 3, Conic U/S, U_∞ = 50m/s 59
4.22 USP: Modes of C5: L/D = L/W = 3, Conic U/S, U_∞ = 50m/s 59

5 Hot-Wire Results & Discussion 62

5.1 HWA: Velocity Profile ΔRe_∞/m Effect: $x = -5$mm from cavity LE, $y = 0 - 270$mm 63
5.2 HWA: Velocity Profile Geometry Effect: $x = -5$mm from cavity LE, $y = 0 - 270$mm 64
5.3 HWA: Velocity Profile Cavity Effect: $x = -5$mm from cavity LE, $y = 0 - 270$mm . . 65
5.4 HWA: Integral Time Scale τ_i at Δ Re_∞/m: $x = -5$mm from cavity LE, $y = 0-270$mm 66
5.5 HWA: BL Disturbance Thickness δ at $x = -5$mm from cavity LE 67
5.6 HWA: BL Displacement Thickness δ^* at $x = -5$mm from cavity LE 67
5.7 HWA: BL Momentum Thickness θ at $x = -5$mm from cavity LE 67
5.8 HWA: Wall Shear Stress τ_w (Pa) at $x = -5$mm from cavity LE 68
5.9 HWA: Favourable Pressure Gradient dp/dx (Pa/m) at $x = -5$mm from cavity LE . 68
5.10 HWA: ΔRe FFT: y = 1.2mm, $x = -5$mm from cavity LE 69
5.11 HWA: ΔRe FFT: y = 32.3mm, $x = -5$mm from cavity LE 69
5.12 HWA: ΔU/S Geometry FFT: $x = -5$mm from cavity LE, Re_∞/m = 2.5×10^6 70
5.13 HWA: $+y$ FFT: $x = -5$mm from cavity LE, Re_∞/m = 2.5×10^6 71
5.14 HWA: Cavity Effect FFT: $x = -5$mm from cavity LE, Re_∞/m = 2.5×10^6 72
5.15 HWA: SPL (dB) for ΔRe_∞/m, Δy, and different U/S geometry 73

6 Pressure Results & Discussion 74

6.1 USP: ΔL for C1, C3, C5: Conic Nose U/S, W = 60mm, Re_∞/m = 3.1×10^6 76
6.2 USP: ΔL for C2, C4, C6: Conic Nose U/S, W = 30mm, Re_∞/m = 3.1×10^6 76

6.3 USP: ΔL and ΔW: Conic Nose U/S at Re_∞/m = 3.1×10^6 . . . 77
6.4 USP: ΔL for C7, C9, C11: Ogive Nose U/S, W = 60mm, Re_∞/m = 3.1×10^6 . . . 77
6.5 USP: ΔL for C8, C10, C12: Ogive Nose U/S, W = 30mm, Re_∞/m = 3.1×10^6 . . . 78
6.6 USP: ΔL and ΔW: Ogive Nose U/S at Re_∞/m = 3.1×10^6 . . . 78
6.7 USP: ΔRe_∞/m for C1: L/D = 1, L/W = 1, Conic Nose U/S . . . 79
6.8 USP: ΔRe_∞/m for C3: L/D = 2, L/W = 2, Conic Nose U/S . . . 80
6.9 USP: ΔRe_∞/m for C4: L/D = 2, L/W = 4, Conic Nose U/S . . . 80
6.10 USP: ΔRe_∞/m for C5: L/D = 3, L/W = 3, Conic Nose U/S . . . 81
6.11 USP: ΔRe_∞/m for C7: L/D = 1, L/W = 1, Ogive Nose U/S . . . 81
6.12 USP: ΔRe_∞/m for C9: L/D = 2, L/W = 2, Ogive Nose U/S . . . 82
6.13 USP: ΔRe_∞/m for C11: L/D = 3, L/W = 3, Ogive Nose U/S . . . 82
6.14 USP: ΔRe_∞/m for C19: L/D = 1, L/W = 1, Flat-plate U/S . . . 83
6.15 USP: ΔRe_∞/m for C22: L/D = 2, L/W = 4, Flat-plate U/S . . . 83
6.16 USP: ΔRe_∞/ for C23: L/D = 3, L/W = 3, Flat-plate U/S . . . 83
6.17 USP: ΔBL for L/D = 1, L/W = 1, Re_∞/m = 3.1×10^6 . . . 84
6.18 USP: ΔBL for L/D = 1, L/W = 2, Re_∞/m = 3.1×10^6 . . . 85
6.19 USP: ΔBL for L/D = 2, L/W = 2, Re_∞/m = 3.1×10^6 . . . 85
6.20 USP: ΔBL for L/D = 2, L/W = 4, Re_∞/m = 3.1×10^6 . . . 86
6.21 USP: ΔBL for L/D = 3, L/W = 3, Re_∞/m = 3.1×10^6 . . . 86
6.22 USP: ΔBL for L/D = 3, L/W = 6, Re_∞/m = 3.1×10^6 . . . 87
6.23 USP: ΔL FFT: W = 60mm, Re_∞/m = 0.6×10^6, x/L = 0.6, z/W = 0.3 . . . 88
6.24 USP: ΔW FFT: L = 120mm, Re_∞/m = 0.6×10^6, x/L = 0.6, z/W = 0.3 . . . 89
6.25 USP: ΔRe FFT: L/D = 1, L/W = 1, x/L = 0.6, z/W = 0.3 . . . 90
6.26 USP: ΔBL FFT: W = 60mm, Re_∞/m = 0.6×10^6, x/L = 0.6, y/D = 1, z/W = 0.3 . 91

7 Physical Cavity Model 93

7.1 Viscid Incompressible Open Cavity Flow Model . . . 95
7.2 Strouhal Number St_{HS} vs Boundary Layer Thickness δ . . . 96
7.3 Strouhal Number: Flat-Baseline U/S . . . 97
7.4 Strouhal Number: Conic Nose U/S . . . 98
7.5 Strouhal Number: Comparison to Rossiter's[2] Experimental Data . . . 98
7.6 Strouhal Number: Comparison to Block's[6] Experimental Data . . . 99
7.7 Strouhal Number: Comparison to Various Subsonic Experimental Data . . . 99
7.8 Amplitude Experimental vs. Numerical: Flat-plate U/S C19: L/D = L/W = 1 . . . 102
7.9 Amplitude Experimental vs. Numerical: Flat-plate U/S C21: L/D = L/W = 2 . . . 103
7.10 Amplitude Experimental vs. Numerical: Flat-plate U/S C23: L/D = L/W = 3 . . . 103

A Wind Tunnel Data 120

A.1 HWA: Empty WT Flat-Plate Boundary Layer Thicknesses . . . 135
A.2 HWA: BL U_M for ΔX at each Airspeed (airflow moves left to right) . . . 136
A.3 HWA: BL TI for ΔX at each Airspeed (airflow moves left to right) . . . 136
A.4 HWA: BL U_M for ΔU_∞ at each Stream-wise Location (airflow moves left to right) . 136
A.5 HWA: BL TI for ΔU_∞ at each Stream-wise Location (airflow moves left to right) . . 136

B Boundary Layer Theory **137**

B.1 Boundary Layer Schematic 137
B.2 Boundary Layer Thicknesses: Disturbance δ, Displacement δ^*, Momentum θ 138
B.3 Wedge Boundary Layer Flow 141
B.4 Curved Boundary Layer Flow 143
B.5 Curvature Constant C_2 based on Proportionality Constant A_p [7] 148

C Signal Analysis **149**

C.1 USP: Modes of C5: L/D = L/W = 1, Conic U/S, U_∞ = 50m/s 152

D Additional Supporting Data **153**

D.1 USP: ΔL for C13, C15, C17: Parabola U/S, W = 60mm, Re_∞/m = 3.1×10^6 153
D.2 USP: ΔL for C14, C16, C18: Parabola U/S, W = 30mm, Re_∞/m = 3.1×10^6 154
D.3 USP: ΔL and ΔW: Parabola U/S at Re_∞/m = 3.1×10^6 154
D.4 USP: ΔL for C19, C21, C23: Flat-Plate U/S, W = 60mm, Re_∞/m = 3.1×10^6 154
D.5 USP: ΔL for C20, C22, C24: Flat-Plate U/S, W = 30mm, Re_∞/m = 3.1×10^6 155
D.6 USP: ΔL and ΔW: Flat-Plate U/S at Re_∞/m = 3.1×10^6 155
D.7 USP: ΔRe_∞/m for C2: L/D = 1, L/W = 2, Conic U/S 155
D.8 USP: ΔRe_∞/m for C6: L/D = 3, L/W = 6, Conic U/S 156
D.9 USP: ΔRe_∞/m for C8: L/D = 1, L/W = 2, Ogive U/S 156
D.10 USP: ΔRe_∞/m for C10: L/D = 2, L/W = 4, Ogive U/S 156
D.11 USP: ΔRe_∞/m for C12: L/D = 3, L/W = 6, Ogive U/S 157
D.12 USP: ΔRe_∞/m for C13: L/D = 1, L/W = 1, Parabola U/S 157
D.13 USP: ΔRe_∞/m for C14: L/D = 1, L/W = 2, Parabola U/S 157
D.14 USP: ΔRe_∞/m for C15: L/D = 2, L/W = 2, Parabola U/S 158
D.15 USP: ΔRe_∞/m for C16: L/D = 2, L/W = 4, Parabola U/S 158
D.16 USP: ΔRe_∞/m for C17: L/D = L/W = 3, Parabola U/S 158
D.17 USP: ΔRe_∞/m for C18: L/D = 3, L/W = 6, Parabola U/S 159
D.18 USP: ΔRe_∞/m for C20: L/D = 1, L/W = 2, Flat U/S 159
D.19 USP: ΔRe_∞/m for C24: L/D = 3, L/W = 6, Flat U/S 159

E.1 Strouhal Number: Ogive Nose U/S 179
E.2 Strouhal Number: Parabola Nose U/S 180

List of Tables

3 Experimental Set-Up **27**

3.1 USP: Pressure Tap Numbers 36

4 Data Processing & Analysis **39**

4.1 HWA: Maximum Uncertainty Values ($\times 10^{-4}$ m/s) 45
4.2 HWA: Flat-Plate Boundary Layer Data 47
4.3 HWA: Conic Nose Boundary Layer Data 49
4.4 HWA: Curve Nose Boundary Layer Data 52
4.5 USP: Tube Volume for each Port in Scanivalve MPS 4264 55
4.6 USP: Transducer Volume for each Port in Scanivalve MPS 4264 56

5 Hot-Wire Results & Discussion **62**

5.1 HWA: SPL (dB) for $\Delta \mathrm{Re}_\infty$/m, ΔGeometry and Δy 73

6 Pressure Results & Discussion **74**

6.1 USP: Cavity Case Reference Table 74

A Wind Tunnel Data **120**

A.1 USP: Ambient Conditions of C1: L/D = 1, L/W = 1, Conic U/S 120
A.2 USP: Ambient Conditions of C2: L/D = 1, L/W = 2, Conic U/S 121
A.3 USP: Ambient Conditions of C3: L/D = 2, L/W = 2, Conic U/S 121
A.4 USP: Ambient Conditions of C4: L/D = 2, L/W = 4, Conic U/S 122
A.5 USP: Ambient Conditions of C5: L/D = 3, L/W = 3, Conic U/S 122
A.6 USP: Ambient Conditions of C6: L/D = 3, L/W = 6, Conic U/S 122
A.7 USP: Ambient Conditions of C7: L/D = 1, L/W = 1, Ogive U/S 123
A.8 USP: Ambient Conditions of C8: L/D = 1, L/W = 2, Ogive U/S 123
A.9 USP: Ambient Conditions of C9: L/D = 2, L/W = 2, Ogive U/S 124
A.10 USP: Ambient Conditions of C10: L/D = 2, L/W = 4, Ogive U/S 124
A.11 USP: Ambient Conditions of C11: L/D = 3, L/W = 3, Ogive U/S 124
A.12 USP: Ambient Conditions of C12: L/D = 3, L/W = 6, Ogive U/S 125
A.13 USP: Ambient Conditions of C13: L/D = 1, L/W = 1, Parabola U/S 125
A.14 USP: Ambient Conditions of C14: L/D = 1, L/W = 2, Parabola U/S 126
A.15 USP: Ambient Conditions of C15: L/D = 2, L/W = 2, Parabola U/S 126
A.16 USP: Ambient Conditions of C16: L/D = 2, L/W = 4, Parabola U/S 126
A.17 USP: Ambient Conditions of C17: L/D = 3, L/W = 3, Parabola U/S 127
A.18 USP: Ambient Conditions of C18: L/D = 3, L/W = 6, Parabola U/S 127

A.19 USP: Ambient Conditions of C19: L/D = 1, L/W = 1, Flat U/S 128
A.20 USP: Ambient Conditions of C20: L/D = 1, L/W = 2, Flat U/S 128
A.21 USP: Ambient Conditions of C21: L/D = 2, L/W = 2, Flat U/S 128
A.22 USP: Ambient Conditions of C22: L/D = 2, L/W = 4, Flat U/S 129
A.23 USP: Ambient Conditions of C23: L/D = 3, L/W = 3, Flat U/S 129
A.24 USP: Ambient Conditions of C24: L/D = 3, L/W = 6, Flat U/S 130
A.25 HWA: Ambient Conditions of C5, C11, C17, C23: Cavity Open 130
A.26 HWA: Ambient Conditions of C25-28: Cavity Closed 131
A.27 HWA: Ambient Conditions of Empty WT Streamwise Traverse 132
A.28 HWA: Boundary Layer Disturbance Thickness δ (mm) 134
A.29 HWA: Boundary Layer Displacement Thickness δ^* (mm) 134
A.30 HWA: Boundary Layer Momentum Thickness θ (mm) 135
A.31 HWA: Free-Stream Turbulence Intensity (%) 135

B Boundary Layer Theory **137**

B.1 HWA: Falkner-Skan Similarity Solution Functions 142
B.2 HWA: Curved Surface Similarity Function 147
B.3 HWA: Proportionality Constant A_p $[10^{-3}]$ 148

D Additional Supporting Data **153**

D.1 USP: Modes of C1: L/D = 1, L/W = 1, Conic U/S 160
D.2 USP: Modes of C2: L/D = 1, L/W = 2, Conic U/S 160
D.3 USP: Modes of C3: L/D = 2, L/W = 2, Conic U/S 161
D.4 USP: Modes of C4: L/D = 2, L/W = 4, Conic U/S 161
D.5 USP: Modes of C5: L/D = 3, L/W = 3, Conic U/S 161
D.6 USP: Modes of C6: L/D = 3, L/W = 6, Conic U/S 162
D.7 USP: Modes of C7: L/D = 1, L/W = 1, Ogive U/S 162
D.8 USP: Modes of C8: L/D = 1, L/W = 2, Ogive U/S 163
D.9 USP: Modes of C9: L/D = 2, L/W = 2, Ogive U/S 163
D.10 USP: Modes of C10: L/D = 2, L/W = 4, Ogive U/S 163
D.11 USP: Modes of C11: L/D = 3, L/W = 3, Ogive U/S 164
D.12 USP: Modes of C12: L/D = 3, L/W = 6, Ogive U/S 164
D.13 USP: Modes of C13: L/D = 1, L/W = 1, Parabola U/S 165
D.14 USP: Modes of C14: L/D = 1, L/W = 2, Parabola U/S 165
D.15 USP: Modes of C15: L/D = 2, L/W = 2, Parabola U/S 165
D.16 USP: Modes of C16: L/D = 2, L/W = 4, Parabola U/S 166
D.17 USP: Modes of C17: L/D = 3, L/W = 3, Parabola U/S 166
D.18 USP: Modes of C18: L/D = 3, L/W = 6, Parabola U/S 167
D.19 USP: Modes of C19: L/D = 1, L/W = 1, Flat U/S 167
D.20 USP: Modes of C20: L/D = 1, L/W = 2, Flat U/S 167
D.21 USP: Modes of C21: L/D = 2, L/W = 2, Flat U/S 168
D.22 USP: Modes of C22: L/D = 2, L/W = 4, Flat U/S 168
D.23 USP: Modes of C23: L/D = 3, L/W = 3, Flat U/S 169

D.24 USP: Modes of C24: L/D = 3, L/W = 6, Flat U/S 169
D.25 HWA: Modes of C5: Cavity Open, Conic U/S 170
D.26 HWA: Modes of C11: Cavity Open, Ogive U/S 170
D.27 HWA: Modes of C17: Cavity Open, Parabola U/S 171
D.28 HWA: Modes of C23: Cavity Open, Flat U/S 171
D.29 HWA: Modes of C25: Cavity Closed, Conic U/S 171
D.30 HWA: Modes of C26: Cavity Closed, Ogive U/S 172
D.31 HWA: Modes of C27: Cavity Closed, Parabola U/S 172
D.32 HWA: Modes of C28: Cavity Closed, Flat U/S 173

E Viscid Physical Cavity Model **174**

E.1 Experiment vs. Numerical Amplitude: Conic Nose U/S C1: L/D = L/W = 1 176
E.2 Experiment vs. Numerical Amplitude: Conic Nose U/S C5: L/D = L/W = 3 177
E.3 Experiment vs. Numerical Amplitude: Ogive Nose U/S C11: L/D = L/W = 3 . . . 177
E.4 Experiment vs. Numerical Amplitude: Parabola Nose U/S C17: L/D = L/W = 3 . 177
E.5 Experiment vs. Numerical Amplitude: Flat-plate U/S C19: L/D = L/W = 1 178
E.6 Experiment vs. Numerical Amplitude: Flat-plate U/S C21: L/D = L/W = 2 178
E.7 Experiment vs. Numerical Amplitude: Flat-plate U/S C23: L/D = L/W = 3 178

List of Abbreviations

Abbreviation	Description	Units
A/C	Analog-to-Digital	-
A	Area	m^2
BC	Boundary Condition	-
BL	Boundary Layer	-
BVP	Boundary Value Problem	-
CL	Centre Line	-
CFD	Computational Fluid Dynamics	-
CTA	Constant Temperature Anemometer	-
D	Cavity Depth	mm
DAQ	Data Acquisition	-
DMD	Dynamic Mode Decomposition	-
D/S	Downstream	-
EOM	Equations of Motion	-
Exp.	Experimental	-
FS	Free-Stream	-
FFT	Fast-Fourier Transform	-
FT	Fourier Transform	-
HWA	Hot-Wire Anemometry	-
IC	Initial Condition	-
ITS	Integral Time Scale	s
L	Cavity Length	mm
LE	Leading Edge	-
LES	Large Eddy Simulation	-
L/D	Length-to-Depth Ratio	-
$(L/D)_{cr}$	Critical Length-to-Depth Ratio	-
L/W	Length-to-Width Ratio	-
MPS	Miniature Pressure Scanner	-
ML	Mixing Layer	-
NI	National Instrumentation	-
NS	Navier-Stokes	-
Num.	Numerical	-
ODE	Ordinary Differential Equations	-

List of Abbreviations (Cont.)

Abbreviation	Description	Units
OASPL	Overall Sound Pressure Level	dB
PDE	Partial Differential Equations	-
PIV	Particle Image Velocimetry	-
PLA	Polylactic acid	-
P/N	Part Number	-
POD	Proper Orthogonal Decomposition	-
Pr	Prandtl Number	-
QTY	Quantity	-
RANS	Reynolds Averaged Navier Stokes	-
Re	Reynolds Number	-
RMS	Root-Mean Square	-
RPM	Revolutions per Minute	-
SSO	Self-Sustained Oscillation	-
SL	Shear Layer	-
SPL	Sound Pressure Level	dB
sR	Sample Rate	Hz
St	Strouhal Number	-
SVD	Single Value Decomposition	-
TE	Trailing Edge	-
TI	Turbulence Intensity	%
TR	Time-Resolved	-
TS	Test-Section	-
URANS	Unsteady RANS	-
USP	Unsteady Surface Pressure	-
U/S	Upstream	-
V	Volume	m^3
W	Cavity Width	mm
WM	Wake Mode	-
WT	Wind Tunnel	-

List of Symbols

Symbol	Description	Units
a	Speed of Sound	m/s
A_p	Curvature Proportionality Constant	-
A_e	East's[8] Constant A = 0.65	-
B_e	East's[8] Constant B = 0.75	-
C	Integration Constant	-
C_d	Drag Coefficient	-
C_i	Polynomial Calibration Coefficients	-
C_p	Pressure Coefficient	-
$C_{p,rms}$	Root-Mean Square Pressure Coefficient	-
C_2	Curvature Constant	-
E	Voltage	Volts (V)
F_m	Morse Forcing Function	N
F_0,G_1	Taylor Series Functions	-
f	Frequency	Hz
g_m	Morse Boundary Function $g_m = \xi + i\eta$	
K	Surface Curvature	$1/m^2$
K	Kurtosis	-
k	Wave Number ($k = f/\lambda$)	rad/m
$\bar{k}$	Dimensionless Wave Number	-
l	Falkner-Skan Wedge Length	mm
M	Mach Number	-
m	Mode Number	-
m_f	Feedback Wave Mode Number	-
m_v	Vorticity Wave Mode Number	-
m_β	Falkner-Skan Power Law Parameter	-
N	Number of Samples	-
$O(.)$	Order of Magnitude	-
p	Pressure	Pa
dp/dx	Pressure Gradient	Pa/m
$\bar{p}_x$	Dimensionless Pressure Gradient	-
Q_m	Source Strength	/s
q	Dynamic Pressure	Pa

List of Symbols (Cont.)

Symbol	Description	Units
R	Gas Constant of Air	J/kg.K
R	Resistance	Ohms (Ω)
$\mathrm{R_z}$	Radiation Resistance	Ohms (Ω)
S	Skewness	-
T	Temperature	K
t	Time	s
U	Velocity	m/s
$\mathrm{U_e}$	Boundary Layer Edge Velocity	m/s
$\mathrm{U_p}$	Potential Velocity	m/s
$\mathrm{U_{pw}}$	Potential Velocity at the Wall	m/s
u	x-axis Velocity Component	m/s
v	y-axis Velocity Component	m/s
V_m	Mode Wave Velocity	m/s
$\mathrm{X_z}$	Radiation Reactance	Ohms (Ω)
Z	Radiation Impedance $\mathrm{Z = R_z + iX_z}$	Ohms (Ω)
$\varnothing$	Diameter	mm
$\propto$	Proportional to	-
∞	Subscript denoting a Free-Stream value	-
β	Falkner-Skan Similar Pressure Gradient	-
β	$\sqrt{1 - \mathrm{M}_\infty^2}$	-
γ	Specific Heat Ratio	-
γ_v	Feedback Phase Difference Empirical Constant	-
Δ	Change in the respective variable	-
δ	Boundary Layer Thickness	mm
δ_ω	Vorticity Thickness	mm
δ/L	Effective Cavity Length	-
δ^*	Boundary Layer Displacement Thickness	mm
δ^*/D	Effective Cavity Depth	-
ϵ	Error	%
ζ	Cavity Width to Length Ratio (W/L)	-
η	Similarity Parameter for y	-
η_m	Morse Boundary Function Real Root	-

List of Symbols (Cont.)

Symbol	Description	Units
θ	Boundary Layer Momentum Thickness	mm
θ_{SL}	Shear Layer Momentum Thickness	mm
$d\theta/dx$	Momentum Growth Rate	-
$\mathrm{\theta}$	Radiation Cylindrical Coordinate	$\circ$
κ	Empirical SL to FS Velocity Ratio	-
λ	Wavelength	m
λ_a	Acoustic Wavelength	m
λ_f	Feedback Wavelength	m
λ_v	Vorticity Wavelength	m
μ	Dynamic Viscosity	N.s/m^2
ν	Kinematic Viscosity	m^2/s
ξ	Similarity Parameter for x	-
ξ_m	Morse Boundary Function Imaginary Roots	-
ρ	Density	kg/m^3
$d\rho/dx$	Density Gradient	kg/m^4
$\rho_x(\tau_i)$	Auto-Correlation Function	-
σ	Time Variance	s
τ_i	Integral Time Scale	s
τ_w	Wall Shear Stress	Pa
ϕ	Potential Function	-
$\mathrm{\phi}_m$	Morse Characteristic Response Function	-
ψ	Stream Function	-
ω	Continuous-Time Frequency	Hz
ω_n	Natural Frequency	Hz

Chapter 1

Introduction

The interaction between free-stream (FS, ∞) flow, and a cavity (see Fig. 1.1), with varying geometry, is a recurring research topic, with significant history. Cavity flow produces notable performance deficit in ships, cars, aircraft and submarines, due to effects such as; unsteady oscillation, drag, acoustics, vibration and ultimately structural fatigue. Cavity flow has thus become a building block of modern fluid dynamics, in contribution to progression of empirical, numerical, experimental and flow control methods. Moreover, expanding our central understanding of how fluids interact in separation, shearing, mixing, oscillation, momentum and energy transfer, dependant on upstream (U/S) conditions, external and internal cavity geometry.

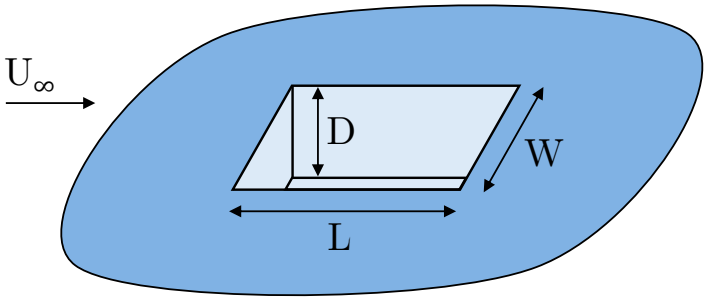

Figure 1.1: Basic Cavity Schematic

This thesis presents wind tunnel (WT) experiments, measuring unsteady surface pressure (USP), internally and externally to the cavity, and hot-wire anemometry (HWA) of the U/S velocity profile. Analysis focuses on the boundary layer (BL) influence and feedback on cavity response, with respect to internal and external cavity geometry.

1.1 Application and Relevance

Cavity flow is often associated with the large aircraft applications of; landing gear and bomb bays. However, small cavities in motor vehicle and in hydrodynamic applications are critical to improve dynamic, and propulsive efficiency. Research has been conducted on the former applications, to address the impact of acoustics, increased drag/fuel burn, reduced fatigue life due to fluid-elastic modes, and interference between acoustics and instrumentation. In extreme cases, the risk of activating aircraft elastic modes can lead to structural failure [2,9].

With aircraft, when landing gear are deployed, acoustics can be perceived overhead from the ground, and by onboard passengers. Also increased drag in these configurations, increases fuel burn and pollutant emissions. The growth of flights and noise results in authorities tightening allowable noise and emission levels. As a result, manufacturer's are optimising designs, to increase fuel efficiency for reduced emission and carrier cost, whilst also reducing noise pollution.

Most early cavity research focused on stealth efforts for high-speed defence applications, to reduce drag and noise in bomb or instrumentation bays [2,9–14]. However, with commercial industry progression, toward quiet and more efficient aircraft, attention has shifted to the airframe, landing gear and instrumentation bays, in subsonic conditions [6,8,15–17]. This work has established cavity governing parameters and dependencies on flow conditions, such as Mach number M_∞.

From a climate change perspective, aircraft emissions are associated with greenhouse gas and other pollutants. Aerodynamics is capable of reducing these impacts via flow optimisation. This allows designers to reduce drag, fuel burn and resultant emissions. From the cavities unsteady flow, there is also potential for energy harvesting via structural vibration or flow pumping. This could reduce fuel burn, and increase propulsive efficiency by reducing engine load at take-off and landing. Therefore, cavity flow optimisation offers the potential to improve performance by reducing structural fatigue, noise, and drag, the latter to reduce fuel burn [1,4,18–20].

Over the past century, cavity flow research has provided; empirical, numerical, experimental and flight test data on cavity flow, for a variety of geometry and flow conditions. This data has been used, to define solutions, which attempt to predict the cavity flow response. Further analysis of these methods, has been executed, over a variety of geometry and conditions, dependent on application. Nonetheless, understanding of the nonlinear, unsteady flow, lacks accuracy, especially regarding the impact of viscosity, to predict magnitude response.

There are a large number of factors to determine how a cavity responds to incoming flow. Research has primarily observed the effect of cavity length (L) and depth (D) via length-to-depth ratio (L/D), as a function of airspeed U_∞, M_∞. Limited work has observed the effects of cavity width (W), length-to-width ratio (L/W), external geometry, and U/S conditions i.e., BL thickness δ, displacement δ^*, momentum θ, and energy transport through feedback. Chapter 2 provides a detailed review of prior research, highlighting such, as the foundation of this thesis.

1.2 Present Work

This thesis provides detailed review, and analysis, in contribution to empirical and numerical prediction of cavity response to U/S and internal flow phenomena, based on detailed low-speed WT measurements. With potential to apply cavity flow to energy harvesting, in line with the APMA program*. To achieve such, this thesis focuses on the following objectives:

(1) To complete a detailed literature review on the physics of cavity flow, and establish knowledge gaps, specifically focusing on governing flow-field characteristics.

(2) To design and execute an experiment to study cavity flow, observing open streamwise and

*Task 5 of the APMA Program supported by DMTC, in partnership with DSTG, to harvest energy using piezo-electric materials in the aerospace environment of cavity flow.

narrow spanwise type flow geometry with variable length L = 60, 120, 180mm, at width W = 30 and 60mm, and constant depth D = 60mm, subject to incompressible flow of U_∞ = 10-65m/s (Re_∞ = 0.6-4.1 $\times 10^6$/m and M_∞ = 0.03-0.2), comparing effects of a baseline thick flat-plate turbulent BL, to a set of progressively thinner laminar BLs formed by increasing favourable pressure gradient $dp/dx < 0$ U/S, through variation of U/S geometry.

(3) To experimentally capture and analyse the internal cavity and BL flow-field, using unsteady pressure (USP), and hot wire anemometry (HWA) respectively, in a low-speed WT.

(4) To reconstruct the internal flow-field and U/S BL environment using numerical methods, adjusted for empirical knowledge from experimental observation.

(5) Investigate the U/S BL effect on internal cavity pressure, and feedback on the U/S BL, and velocity profile. Specifically with respect to cavity internal geometry, when L/W ratio is varied, and where spanwise flow is apparent, in terms of length and U_∞.

(6) To identify contribution of the U/S BL to cavity modal response, and corresponding frequency prediction models, using Strouhal number (St), and sound pressure level (SPL).

This thesis has a series of chapters, as follows:

(1) Introduction: application, relevance of the topic with respect to present research.

(2) Literature Review: a comprehensive review of the cavity flow phenomena, outlining key studies contributing to research presented by this thesis.

(3) Experimental Set-up: design of experiments to assess the cavity flow-field, from model design, and construction, to means of attaining USP, and velocity data with HWA, to empirically re-construct the flow environment.

(4) Data Processing & Analysis: flow corrections to map the WT environment onto a model of true flow. Reduction of experimental pressure data to account for tube distortion error as a consequence of the technique. Conversion of voltage based HWA data into calibrated velocity values, to reconstruct the BL profile U/S of the cavity, using empirically adjusted numerical methods; Blasius [21], Falkner-Skan [22], Goldstein [23] and Murphy [7]. Signal processing from each measurement for spectral reduction of dominant system modes, using Fourier transform (FT), and dynamic mode decomposition (DMD).

(5) Hot-Wire Results & Discussion: presentation of velocity and BL data U/S of the cavity, highlighting the effect of viscous variables, to deduce objectives of the thesis.

(6) Pressure Results & Discussion: presentation of USP data, highlighting the effect of external and internal cavity geometry on cavity response, to deduce objectives of the thesis.

(7) Physical Cavity Model: amalgamate result findings, into a set of core fundamental fluid principles, and parameters, to form a viscous physical incompressible cavity flow model. To predict dimensionless frequency and amplitude as the final outcome of this research.

(8) Conclusion: summary of core findings, and suggestion for future research to solidify developed concepts, and progress the cavity flow research field.

Chapter 2

Literature Review

This chapter is the reduced version of a review article on cavity flow in fluid mechanics, which was published in the European Journal of Mechanics/B-Fluids [1] by the author of this thesis, drawing focus to content of the research. The published article [1] summarises major and minor governing parameters, with influences of technology, numerical models, experimental methods, analysis, industry application, and control. The paper assesses all flow regimes, and a large variety of geometries, mostly rectangular, and that of industry application. Where available, boundary layer (BL) assessment was included, to support the focus of this thesis.

2.1 The Cavity Flow Phenomena

Cavity flow is a complex fluid mechanism, with an unsteady flow-field, dependant on internal geometry and upstream (U/S) flow, driving dominant oscillatory response characteristics in many forms. Research into flow at the cavity mouth, has provided robust evidence the flow response is governed by; development, growth, and convection of instabilities within a shear-layer (SL). From flow initiation along a surface, developing a BL, which then separates at impingement of the cavity leading edge (LE), to produce the SL. The SL sheds from the LE, as discrete vortices, which interact with internal cavity fluid as it convects downstream (D/S) toward the trailing edge (TE), where flow is either recirculated back U/S, or propagates out. SL instabilities can take the form of Kelvin-Helmholtz waves in open flow per Fig. 2.1, or bow waves in closed per Fig. 2.2, with transition in between dependant on geometry and momentum.

Once initial SL state is developed, and flow continues to enter the cavity, vortices periodically shed from the LE, further disturbing the SL. This behaviour increases momentum growth within flow instabilities as they convect D/S, interacting with cavity geometry, to form secondary disturbances, in response to built-up energy. These features become predominant as the cavity responds, typically as a characteristic method of momentum and energy transfer, to maintain flow equilibrium, at an effective steady state, which defines modes.

2.1.1 Streamwise Flow Type

Common cavity flows, are of the streamwise flow type; **open** or **closed**. They are defined with respect to SL placement over the cavity, and through internal and external fluid interactions.

This terminology was characterised by Charwat et al[24], who aligned streamwise flow type with the cavity length-to-depth (L/D) ratio, with regard to SL recompression characteristics, and axis of formation. **Transitional** flow was also coined, for the region between open and closed cavity flows. Research uses these terms, as a basis for comparative study.

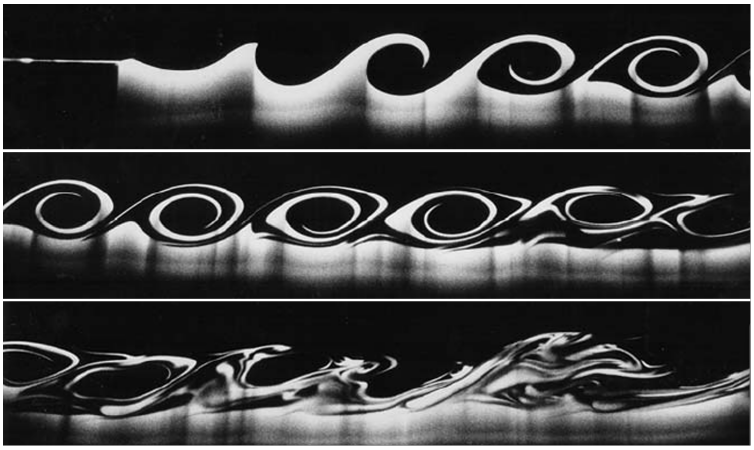

Figure 2.1: Kelvin-Helmholtz Instability

Stallings & Willcox and Plentovich et al[25–27] expand the transitional flow region into; open-transitional, transitional and transitional-closed, where behaviour is not precise to open, or closed though has characteristics leaning in either direction, due to; width, M_∞ and the BL effect. Effectively highlighting, that change in streamwise flow type, is not exclusive to L/D, with the boundary between open, and closed also dependant on various factors. A guide is provided below, with a diagram in Fig. 2.2. It is recognised, there has been deliberation of exact boundaries based on L/D, as changes in M_∞, BL and width do alter boundaries.

Open $L/D < 5$: the SL bridges the cavity, reattaching at the TE corner, nearby on the TE wall, or just after the cavity, enabling mass exchange between external and internal fluid as the SL oscillates at the TE. Typically self-sustained oscillations (SSOs) form, creating large SL instabilities, due to excited internal recirculation, which produce a feedback effect emanating pressure waves U/S. Under ideal conditions, the feedback generates acoustic tones of specific frequencies, aligned to either cavity normal (deep) or Rossiter's SL mode (shallow). If the SL attaches further D/S after the TE, the mechanism associated with gap flow is more appropriate.

Open-Transitional $5 < L/D < 7$: flow is predominantly open, however, the SL is pulled slightly further into the cavity, and instead reattaches on the lower TE wall exhibiting open modes with features of transition to closed. A bridge term, used to describe transitional flow as M_∞, BL and/or width changes to trigger open or transitional flow.

Transitional $7 < L/D < 9$: the SL is pulled further into the cavity, reattaching near the bottom of the TE wall close to the floor, or close to the TE wall on the floor. External flow still impacts the dominant modal structures. But major features have been diminished. The flow is not strongly open or closed, but instead has elements of both.

Transitional-Closed $9 < L/D < 12$: predominantly closed, however, the SL reattaches on the floor D/S, not quite separating completely before the TE where secondary reattachment may occur. Thus, closed modal structures are dominant but external flow weakens prominence.

Closed L/D > 12: the SL sweeps inside reattaches on the floor and separates before the TE, like flow over a back-step. A large pressure difference exists between low LE regional pressure, and high regional TE pressure, inducing high drag conditions. Closed flow typically responds in wake mode (WM) [28], if BL mass and momentum permit. WM is detrimental to store separation, due to the formation of a wake D/S in the cavity, which produces an internal adverse pitching moment on the payload. No discrete acoustic tones are typically produced, however high-speed broadband noise in response to wake separation in the oscillatory cycle, can be excessive.

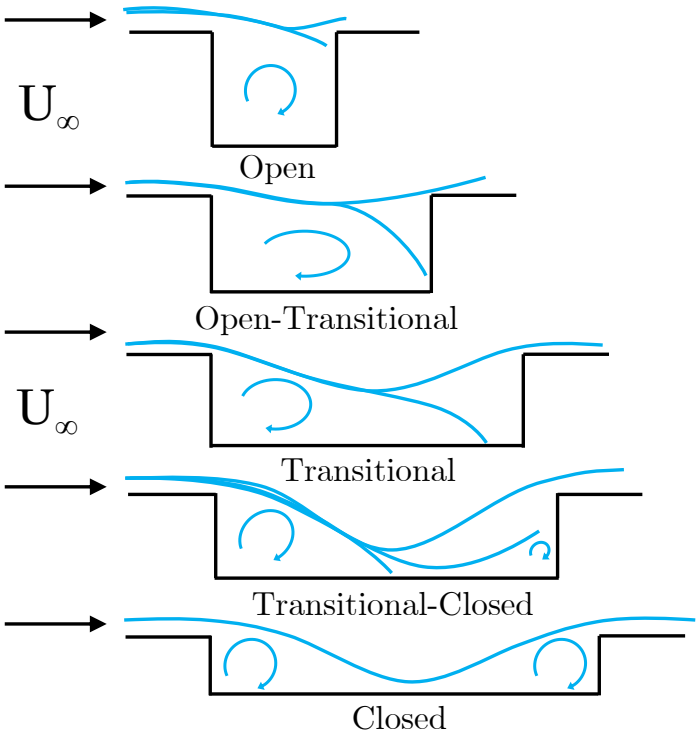

Figure 2.2: Streamwise Cavity Flow Types

2.1.2 Spanwise Flow Type

Spanwise flow type terminology is less ubiquitous, and often ignored by assuming 2D flow, which is adequate for very wide cavities (L/W << 1). However, if narrow for L/W $\geq$ 1, or close to unity, ignoring spanwise effects is insufficient, thence requirement for spanwise flow type definition. Section 2.2.1 details the impact of changing span from prior research, regarding induced 3D effects, defined by spanwise categories below, based on L/W, and Fig. 2.3.

Wide 2D L/W << 1: streamwise features are dominant, as spanwise flow features are dispersed into the far-field. The flow is 2D, with no sign of three-dimensionality.

Transitional L/W $\approx$ 1 (within vicinity of): spanwise correlation may impede streamwise flow by altering flow-field structures. 3D effects may be present, however are not strong enough to shift dominant streamwise modes completely, however an emerging effect to reduce amplitude or shift streamwise flow structures is apparent.

Narrow 3D L/W >> 1: width effects streamwise flow, the presence of sidewalls recirculates spanwise flow, which alters dominant 2D streamwise flow, muting their impact or causing dominant mode switching dependent on U/S flow M_∞ and BL conditions.

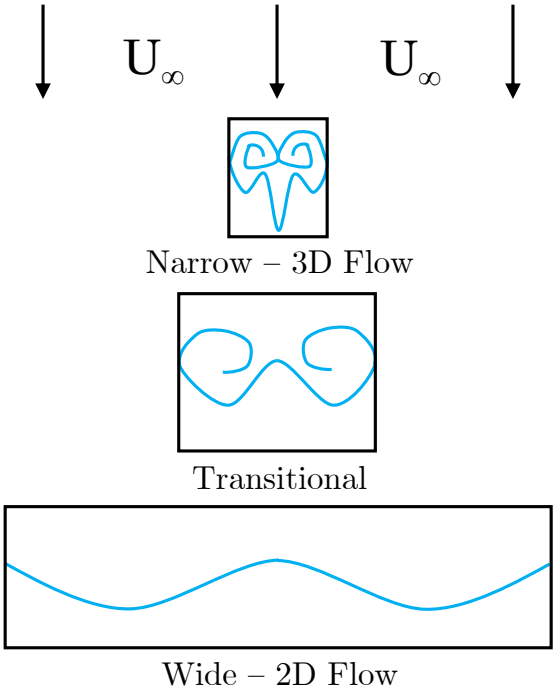

Figure 2.3: Spanwise Cavity Flow Types

2.1.3 Cavity Modes

Cavity flow has three primary response modes; normal, SL and WM. Other less abundant modes exist in-between, as facets of predominant transition between these modes, typically existing as harmonics in the presence of dominant modes. I.e., Bassioni et al's [29,30] **back-step mode**, exhibited in shallow open cavities subject to very low M_∞, existing as typically open flow tends closed, due to low momentum U/S, with a thick BL, and/or spanwise 3D flow present. It is similar to WM, in terms of the back-step profile due to low momentum, however is not fully developed, as L/D is too small, instead exhibiting SL resonance of a typically longer cavity.

Cavity Normal/Deep Mode usually Mode 1, dominates deep open cavities (L/D < 1) alike a classic resonator[6, 8]. As length increases above L/D $= 1$, dominance fades, as the SL begins to oscillate lengthwise, and transition to SL mode [2]. Plumblee [3] observed the mode, but did not correlate features of a classic resonator. Heller et al [13] prescribed the mode to high Q-factor, meaning response is under-damped relative to characteristic resonance bandwidth, and natural frequency ω_n. Effectively, the fluid structure can resonate at ω_n, with no negative feedback or dampening. Due to depth dominance of this mode, the SL driven by streamwise geometry length, has not yet established capacity to suppress associated transverse standing waves, which are responsible for depth resonance. As length increases, relative depth is reduced, and Q-factor reduces proportionally, resulting in a dampening effect on transverse standing waves, until they are subdued. SL dominance thus its mode grows.

SL Mode is the SL resonant frequency response, a defining factor of cavity flow. The mode was investigated using Schlieren imagery by Rossiter [2], who observed discrete vortices to shed from the cavity LE. As a result, Rossiter developed a semi-empirical adaption of Strouhal number [31], to estimate frequency response of the cavity, a dimensionless number, representing oscillating flow mechanisms formed by vorticity. Vortices shed from the cavity LE, propagate D/S, and

interact with internal fluid to form the SL. Rossiter's[2] model assumes, acoustics are excited by SL instabilities, causing them to couple, amplify, modify, prompt feedback, and continue the cycle. Individual and coupled energetic flow then propagates D/S disrupting internal flow, and impinging the TE. The result is pressure oscillations on the cavity boundary, causing flow reattachment, and if conditions align, acoustics in a feedback loop with the SL.

The mode is length dominant per Eqn. 2.2, which provides reasonable alignment with experimental data when flow is subsonic and geometry aligns to Rossiter's experiment. However, for higher speed flow, Heller et al[13] included compressibility effects in contribution to SL oscillation, especially acoustics per Eqn. 2.6. Similarly, East derived a solution for incompressible open cavity flow, where depth has a larger impact, including L/D as more prescriptive in Eqn. 2.3 and 2.4. Block[6,32] further adapted the subsonic SL Mode, including L/D. These equations relative to L/D and SL development are 2D. Its proposed, inclusion of width and/or BL characteristics will improve accuracy, especially in the transitionary region, to cover all cavity type flow. Discussed in subsequent sections.

Wake Mode (WM) only occurs in transitional-closed or closed cavities, subject to laminar or a thin turbulent BL relative to cavity depth; δ/D. WM takes the form of; propagated SL disturbances attaching to the floor, and completely separating before the TE, effectively splitting the cavity into two sections: (1) TE region of high pressure, and (2) LE region of low pressure by $\sim 40\%$ compared to SL mode. This behaviour triggers high drag, due to Δp. Gharib & Roshko[28] defined WM, when observing a wake structure in the TE region, corresponding to sharp drag increase, and spectra change. Unique conditions are required, as very long closed flow has not transitioned to WM unless U/S conditions permit. The BL must be laminar or thin with respect to cavity depth, where a particularly large δ of the same order of depth, instead turns the cavity into a low pass filter, inhibiting transition from SL mode.

WM has commonly been observed in defence applications, due to the geometry and operative airspeed of bomb-bays, with a thin BL at flight-scale relative to the cavity depth. In these cases, WM has induced an adverse pitching moment on cavity stores, due to difference in pressure between fore and aft regions. It is therefore ideal to prevent WM, which comes at a higher detriment to the internal structure than the SL mode. Nonetheless, in design, both acoustic SPL and drag, can be suppressed with a thick BL relative to cavity depth. Without impeding on D/S structures and flow quality to optimise flight, and prevent activation of elastic modes.

2.1.4 Cavity Oscillatory Wave Types

Wave-structures or oscillations are the physical make-up of cavity modal response, extant alone, or as multiple subdued, and or amplified waves. While modes provide a system response summary, wave-structure defines response execution as a function of energy, and input. There are three main cavity oscillatory waves; fluid-dynamic, resonant, and elastic. Each detailed by Rockwell & Naudascher[4], refer Fig. 2.4[4], as summarised below with ubiquitous updates since.

Fluid-Dynamic oscillations describe positive dynamic amplification of SL disturbances along the cavity mouth, enhanced by a feedback loop. They occur when the ratio of length to acoustic wave-length (λ_a) is very small ($L/\lambda_a << 1$). The structure and frequencies, are a response to

instability amplification from LE flow impingement, dependant on U/S BL and cavity geometry. These instabilities travel D/S, and are enhanced by TE interaction, which creates a feedback mechanism of flow recirculating U/S toward the LE, located below the SL, and within the cavity, consistent of both streamwise and normal velocity components. This movement, develops of a feedback loop, which produces positive attenuation along the cavity mouth. Even though motion during LE BL separation is turbulent, and propagates instability. Resulting steady state is coherently organised at the TE, once in oscillatory form.

The spectra typically has two dominant peaks; SL mode 2 and 3, which are periodic due to recirculation, switching dominance as U/S conditions change, promoting streamwise type transition, alike L/D increase. Concurrently, predominant St jumps; 1^{st} to 2^{nd} then 3^{rd} as depth reduces compared to δ. Spectrum coherence occurs as a result of shear characteristics. Primarily, selective disturbance amplification of discrete frequencies, matched by positive feedback. Factors driving mode descriptors, are dependent on flow structure and internal geometry. L/D typically sets frequency, as the SLs ability to propagate streamwise, while oscillatory clarity and selective amplification is limited by the U/S BL, and L/W, which impact dynamic strength.

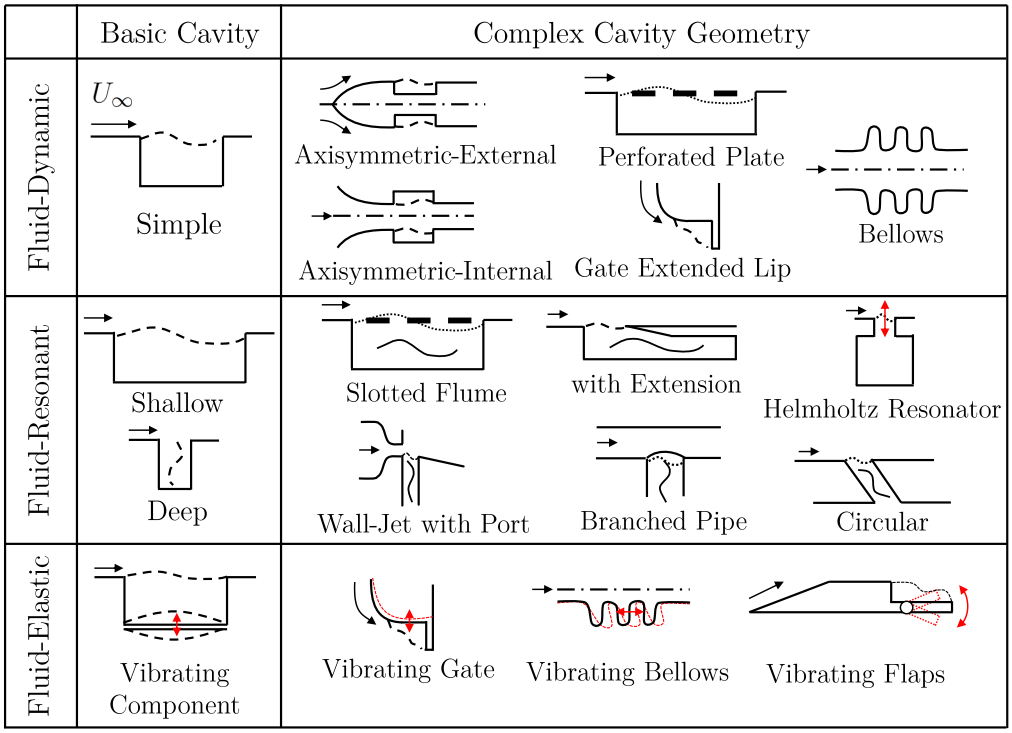

Figure 2.4: Fluid-Dynamic, Resonant, & Elastic Type Oscillations [4]

Fluid-Resonant oscillations are coupled resonant and dynamic wave phenomena governed by; compressibility, free-surface and/or standing wave structures. To form resonance, frequencies must be high enough, for λ_a to be of the same order or less than cavity length; $L/\lambda_a \geq 1$. The exact boundary and λ_a, are influenced by U/S momentum; M_∞, δ, and width with respect to acoustic wave transmission. Therefore, all elements must be considered, to diagnose acoustics with respect to geometric resonator qualities. Resonance is capable of forming irrespective of L/D and L/W, if dynamic movement and wave type align with coherant acoustic structures in the U/S BL. I.e., tone attenuation is linked to a very thick U/S BL relative to cavity depth,

like a low pass filter[10,33–37]. On the other hand, a laminar or thin BL promotes clarification and coherence in dynamic and acoustic flow, amplifying discrete relative tones.

The exact characteristics of resonant oscillations differ, between open and closed flow. Open flow has intense resonant conditions due to transverse standing waves, impeding LE and TE walls at high magnitude, further complicated by BL δ, TE mass exchange and other effects, causing deviation from ideal resonator behaviour. Such conditions are predominant, with increase of L/D, resulting in deviation from ideal resonance. Closed flow forms longitudinal waves, impeding the cavity floor, typically weaker in radiative quality, instead experiencing localised compressibility or wake effects. Exact formation of resonant conditions, is thus dependant on M_∞, U/S BL δ, and cavity geometry. It is possible, for acoustics to be generated in closed flow, when conditions U/S are ideal. Effectively, geometrically closed flow will tend open, as M_∞ is increased, meaning effects of open flow at low speed, may be the same as closed at high speed.

Fluid-Elastic oscillations are the displacement of a physical boundary, producing consistent feedback, further disturbing the SL. Such displacement requires volatile conditions to impede material elasticity, inertial and dampening properties. The response degrades structural integrity, increasing fatigue, toward potential structural failure. In extreme cases, dynamic and resonant phenomena amplify, fuelling the positive feedback loop. This changes cavity modality, as elastic motion propagates U/S and or D/S, through oscillatory motion, impeding external or connected structure. In catastrophic conditions, elastic displacement can become so large, flutter initiates, activating main aircraft modes, and potentially structural failure. References for fluid-elastic research are; Harrington & Dunham[38], and Dunham[39], also Charwat et al[40] who inferred elasticity, via temperature changes, alike Goldman et al[41] for re-entry vehicles.

2.1.5 Cavity Flow Structures

Several cavity flow structure result as an amalgamation of streamwise and spanwise flow, modes and wave types discussed above. One or more of five primary below are usually evident, dependant on cavity internal geometry, external geometry, airspeed and the BL;

The Classic Resonator occurs in deep open cavities $L/D < 1$, implicating cavity normal mode. The flow is modelled with a classic acoustic resonator model[8], where U/S flow disturbance produces traversing depth standing waves, oscillating within the boundaries of cavity length, creating strong acoustic tones as a function of cavity depth per Fig. 2.5. Open flow features are present, with SL modes 2-3 in the spectra, dominated by normal mode 1.

Fluid Mass Exchange: SL oscillates up and down periodically, in and out of the cavity, in a mass exchange cycle. On the up SL cycle, the SL bridges the cavity, pushing internal fluid out at the TE, and oncoming external fluid over the cavity, both directed D/S into the far-field. On the down SL cycle, external fluid is drawn in, and recirculated U/S. This is a predominant feature of the SL mode, in open flow, refer Fig. 2.6.

Fluid Feedback: occurs as the fluid moving D/S recirculates back U/S during the SL mass exchange down cycle near the TE. An acoustic source can form, prompting acoustic propagation U/S, with the feedback mechanism. Either or both dynamic and acoustic U/S wave propagation

disrupts the SL, as it develops from the BL at LE separation, producing a secondary periodic element at the LE. Another feature of the SL mode in open flow per Fig. 2.6.

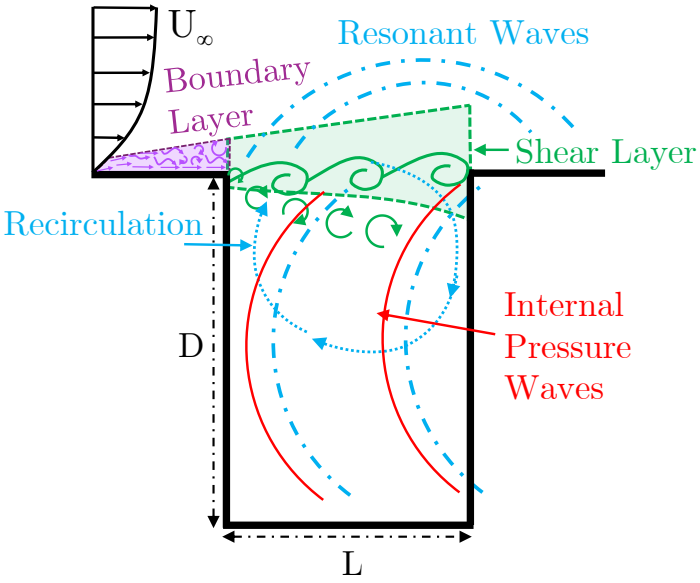

Figure 2.5: Deep Open Cavity Flow Mechanism: Normal Mode

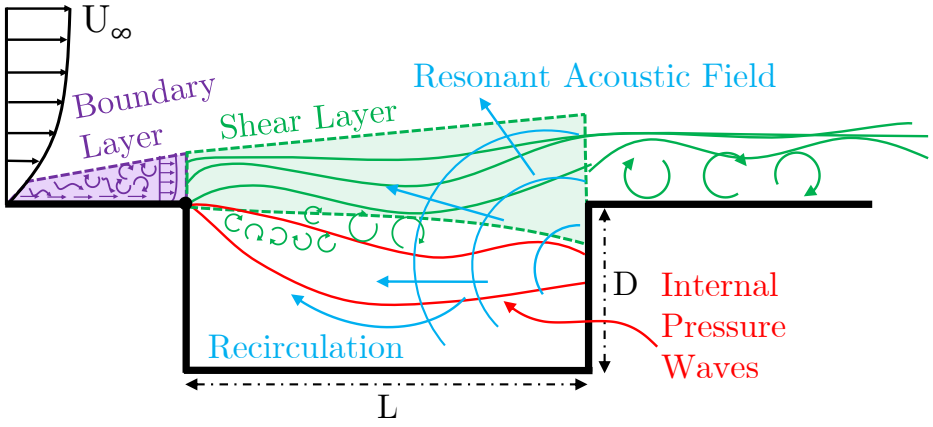

Figure 2.6: Open Cavity Flow Mechanism: Shear Layer Mode

Wake occurs in closed geometry subject to a thin BL. The SL instead bows into the cavity, attaching to the floor before the TE, and recirculating U/S discretely in the LE region, producing a wake in the TE region. The disparity in regions, creates high TE pressure and low LE pressure, resulting in drag, and a pitching moment on internal stores if present. This behaviour is more reflective of in-flight geometry and conditions, where cavities are typically longer, and subject to thin BLs relative to depth $\delta/D << 1$ at flight-scale, thus at a higher risk of drag, which is under-researched compared to the SL mode, per Fig. 2.7.

Span-wise Interference occurs as vortices shed from the LE and spiral spanwise toward the sidewalls, intercepting and reducing intensity of streamwise oscillations along their path. In narrow flow $L/W > 1$, outward motion reflects off side walls and moves back to the centre, introducing additional interference and TI as a sort of spanwise feedback. In wide flow $L/W < 1$, spanwise motion disperses before the sidewall, thus is somewhat negligible. Spanwise interference is responsible for 3D flow effects, an under-researched area, with no distinct modes discretised, even though presently abundant with respect to typically narrow in-flight geometry.

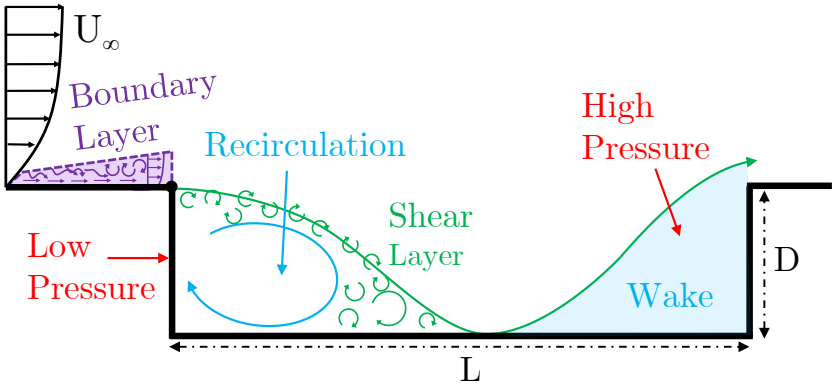

Figure 2.7: Closed Cavity Flow Mechanism: Wake Mode

Magnitude and frequency of these motions define; fluid-dynamic, acoustic and or elastic properties, if present. The oscillatory archetype of each, defined by interaction of the SL and location of recirculating flow within structural boundaries. All can exist together in catastrophic cases, modifying and exciting each other, though most commonly, only dynamic and acoustic. As a result, elastic oscillations are heavily under-researched, with no notable advances in the modern era. Cavity spectra harmonics and broadband noise, likely representing tertiary interactions of mass exchange, feedback, and spanwise flow, which are also under-researched.

2.2 Internal Geometry and Airspeed

Key studies below, provide insight to the effect of internal cavity geometry and subsonic airspeed on cavity response. They were consulted, to select the open flow geometry, and confirm experimental observation within the incompressible subsonic regime. Krishnamurty [15,42] and Roshko [43] presented the first research with respect to aircraft applications, observing a variety of rectangular cut-outs in aerodynamic surfaces. To understand bomb bay buffet, in similarity to bluff-body flow. As they discerned flow disturbances in both phenomena, with a similar energy balance of the driving force, and pressure in the wake.

Krishnamurty [15,42] studied the energy balance, and force distribution, between internal and external cavity flow. Length was varied at constant depth, and width, for L/D = 0-20 and L/W = 0-0.5, subject to sub, trans and supersonic M_∞ = 0.25-1.5, and varying δ. Acoustic tones were dependant on M_∞ and geometry, with an observable change in energy for subsonic flow, otherwise independent. Propagated resonance was weaker for a turbulent BL, with more random buffet, compared to a laminar BL, which produced well defined periodic pressure waves. For constant depth, a critical length $(L/D)_{cr}$ for resonance was observed. Its value growing with M_∞. As no resonance was observed at low M_∞ and large L/D, because wave propagation $\propto (L/D)_{cr}$ at fixed depth, dependant on M_∞. Therefore, at constant M_∞, a turbulent BL required a longer cavity than a laminar BL, to produce acoustics. As the turbulent BL produced random harmonic tones, opposed to dominant modes of the laminar BL, of the same cavity L/D.

Krishnamurty [15,42] found a dominant fundamental frequency, with harmonics for a laminar BL, and two dominant frequencies for a turbulent BL, one almost twice the magnitude, for certain M_∞ and L/D. However, laminar and turbulent BL frequencies were not of the same order. For some M_∞ and geometry; weak acoustics grew in dominance with L/D or temperature, sug-

gesting speed of sound dependence. Thus concluding, subsonic cavities emit acoustic resonance dependant on U_∞, geometry and U/S BL, becoming less apparent in supersonic flow, as acoustic waves travelling at the speed of sound are unable to penetrate D/S moving shock waves, as proven by [44]. There is also a relationship between frequency at fixed depth, inversely proportional to length for laminar and turbulent BLs, where smaller L/D produced high-frequencies contributing to the requirement for further work on M_∞ and SL instabilities.

Roshko[43] analysed cavities with L/D = 1-62.5 and L/W = 0.125, subject to incompressible flow M_∞ = 0.07-0.19. To understand formation of vortices, and how their magnitude is governed by depth, U_∞ and BL δ. Roshko worked from Wieghardt & Tillman's[45] observation of surface irregularities, concluding systematic change in L/D resulted in periodic drag variation, due to cavity unsteady surface pressure (USP), and change in external friction. Roshko[43] proposed a steady state model, aligning vortex presence to resonance of [15, 42] concluding as follows:

(1) A single vortex forms in a cavity of L/D = 1, independent of BL profile, however its pressure and force distribution, is driven by the BL.

(2) Drag increase due to wall pressure, is not due to external surface friction per [45]. Instead, it is a momentum transfer between internal and external flow, to balance drag, as determined by modelling vortices without friction.

(3) While friction is negligible in vortex equilibrium, it is necessary to define vortex stability, as formation is relative to the TE, and part of the separated SL deflects internally, producing high wall pressure, accounting for drag increase.

(4) Depth directly correlates to TE pressure, as an open cavity has more intense vorticity.

(5) High TE stagnation pressure correlates to sound production, as vortex fluctuations result in oscillating stagnation streamlines, and TE pressure variation.

(6) Periodic behaviour correlates to large drag oscillation, as flow varies between stable states

(7) Pressure increase with depth, due to more intense vorticity internally and stronger acoustics.

Charwat et al[24] investigated cavities with; L/D = 0-30 and L/W = 0-2.5, varying length at fixed depth, and width, subject to sub to supersonic flow at M_∞ = 0.6-4. They studied the separated flow regions within cavity flow, and their relationship to internal geometry, M_∞ and the U/S BL, regarding flow development and propagation. Analysing the critical ratio of separated SL length, to depression depth; $(L/D)_{cr}$. Their research defined steam-wise type flow; open, and closed, representing separation and re-attachment behaviour of the SL, detailed in Section 2.1.1. Critical length $(L/D)_{cr}$ was also observed to alter dependent on U/S BL δ, laminar or turbulent, and if laminar, when it transitioned in the SL, with respect to M_∞.

Maull & East[46] observed incompressible subsonic flow M_∞ = 0.2 over open wide cavities; L/D = 0.3-4 and L/W = 0.11 - 0.4, of fixed length, with variable depth and width. They found clear evidence of 3D flow features as width reduced. Firstly, a wave appeared at L/D = 2.2, then as L/D decreased, its amplitude grew without changing wavelength, until an integral number of cells in the total span altered dynamics. Secondly, increasing width transformed the flow from 3D to predominantly 2D, the exact L/W dependant on L/D, proving cavity width an important facet. This was largely ignored in research following, which drew focus on 2D flow $L/W << 1$.

However, in-flight geometry and dynamics, typically have L/W > 1, so understanding associated geometry and 3D cavity flow phenomena is vital.

Block & Heller[47] measured pressure and acoustic spectra of subsonic flow M_∞ = 0.125-0.25 over open narrow cavities; L/D = 1-4 and L/W = 2.5-5. They observed periodic modes when L/D $\sim$ 1, the lower depth frequencies radiating more efficiently, increasing noise in the far-field. Effectively proving use of a classic resonator model, to predict peaks where depth-based acoustic waves have more powerful radiation. They also studied the U/S BL impact on noise, and observed the effectiveness of increasing BL δ U/S to reduce acoustics. However, effectiveness decreased as M_∞ or length increased, due to deviation from classic resonator behaviour.

Stallings & Wilcox[25] investigated the pressure distributions of open to closed and wide to narrow cavities; L/D = L/W = 0.2-24 subject to supersonic M_∞ = 1.5-2.86 and a laminar U/S BL δ = 5mm to define; $(L/D)_{cr}$. Hysteresis was found with $(L/D)_{cr}$ when decreasing length, less than increasing length in contrast to increasing M_∞. For all M_∞ when D = 12.7mm, and when D = 25.4mm for M_∞ = 1.5-2.15, floor pressure in the impingement region of transitional flow D/S of the LE, increased with L/D. Pressure also reduced on the LE and TE walls overall for L/D $\lessapprox$ 3, where the flow re-configures from two to one vortex. They also observed the effect of reducing width, and found $(L/D)_{cr}$ proportionally reduced. However the magnitude effect on pressure distribution within the cavity, was greater in closed or transitional flow compared to open flow. For closed flow, large lateral pressure gradients on the TE wall were indicative of 3D flow in narrower cavities, and open-transitional at L/D = 3-6.

Zhang & Edwards[44] studied open to closed, wide to narrow cavities of L/D = 1-9 and L/W = 0.13-1.18, subject to supersonic flow M_∞ = 1.5 and 2.5. They observed open flow to oscillate transversely, and closed longitudinally, with transition between. Transverse is movement of a single vortex, whereas longitudinal is interaction between a large unstable TE vortex, and several LE vortices. For open flow, longitudinal motion is present but weak, as transverse dominates. When L/D increases, oscillation magnitude longitudinally increases alike M_∞ effects. However, once oscillation is established, increasing L/D reduces dominance, due to SL diffusion with length, when M_∞, depth and width are constant. For open-transitional flow at L/D $\geq$ 5, length governs dominant frequencies, due to correlation with TE vorticity. As length increases, TE vorticity diffuses at a fixed M_∞, where U/S flow has a consistent rate of fluid to feed. But the region to be fed is increasing, causing magnitude to subside. Overall, open flow is characterised by a large TE vortex, and increasing length toward closed flow causes SL diffusion, leading to reduced fluctuation and pressure drop U/S as less fluid recirculates. The downward SL deflection at the TE results in recompression, causing an intense pressure rise in the TE region.

Tracy et al[48] measured the pressure and acoustics of open to closed narrow cavities; L/D = 4.4-20 and L/W = 4.5, subject to subsonic flow; M_∞ = 0.2-0.9, and found Reynolds number (Re) negligible. Closed flow (L/D = 20) did not produce discrete tones, neither did open (L/D = 4.4, 6.7), until M_∞ = 0.6-0.9, which caused amplitude changes as bandwidth broadened. Therefore, modal amplitude and bandwidth were proven M_∞ dependant in open flow. Transitional-closed (L/D = 12.67) tones appeared at M_∞ = 0.6, and disappeared at $M_\infty \approx$ 0.8, 0.9, indicating flow change. However; L/D = 12.67 $\approx (L/D)_{cr}$, thus susceptible to transition.

Plentovich et al[26,27] measured static and USP from cavities of open to closed and wide to narrow geometry; L/D = 1-17 and L/W = 0.125-17.5, subject to subsonic flow M_∞ = 0.2-0.95, and δ = 12.7mm. They discretised streamwise flow into; open, open-transitional, transitional, transitional-closed and closed. Open-transitional at L/D $\sim$ 6-8, and transitional-closed at L/D $\sim$ 9-15, also dependant on M_∞, and L/W, with -transitional denoting stages between, where features of the foreword are dominant. They observe decreasing width, or increasing depth, to push flow toward closed type, where for a given geometry; increasing M_∞ increases transition range. Overall flow type changes with M_∞, width and BL δ.

Tracy & Plentovich[49] studied resonant 3D flow characteristics, using USP measurements of open to closed, and wide to narrow cavities; L/D = 1-17 and L/W = 0.25-7, subject to subsonic flow M_∞ = 0.2-0.95, and δ = 12.7mm. Increasing L/D, was found to reduce dominant spectra and resonant tones, as flow transitioned open to closed. Increasing width, increased resonant SPL, inducing resonance on non-resonant L/D. This indicated that a narrower cavity attenuates resonance toward closed flow. Increasing width, also increased frequency of peak resonance at lower L/D, which decreased with increasing L/D. Peak SPL remained with increasing L/D, however background levels decreased, suggesting peak SPL increased over the noise.

Disimile et al[50] studied wide flow; L/W = 0.12-0.68, for a deep open cavity; L/D = 1, subject to low subsonic flow of M_∞ = 0.035, and a thick BL; δ = 210mm, δ/D = 2. Oscillatory pressure, and frequency, were all width dependant. As increasing L/W, induced a large pressure change, whilst oscillatory dominance transitioned into acoustic from dynamic, as two modes became three. Between certain L/W, two stronger modes were constant, only switching dominance. Therefore, whilst peak source isn't necessarily related to width, its amplitude is, as narrower L/W are dominated by acoustics and wider instead dynamic.

East[8] identified width as negligible compared to streamwise SL edge tone amplification, and Block[6] identified a sustained peak frequency regardless of width. East[8] and Block's[6] cavities were wide (L/W << 1) with no 3D effects. Block[6] did not provide BL data, so no exact comparison can be made, though based on the facility from published research, δ as δ/D is thin alike East. Ahuja & Mendoza[51] also found peak frequency unaffected by width, their BL was also very thin, with very small δ/D. Overall Block[6], East[8] and Ahuja & Mendoza's[51] experiments had thin BLs, much lower δ/D, and much wider width compared to Disimile et al[50]. Therefore, width effects correspond with BL, above a certain threshold of L/W.

Chung[52] examined open wide to narrow cavities; L/D = 2.43-4 and L/W = 0.5-2, subject to supersonic flow M_∞ = 1.28. Increasing L/D, increased peak pressure. Increasing L/W induced 3D flow, and stronger TE vorticity, with a proportional increase in TE pressure gradient, and peak fluctuation. Therefore, 3D flow effected TE vorticity, impacting oscillation, and peak pressure ahead of the TE pressure gradient. Lastly, L/W was found necessary to define $(L/D)_{cr}$ in transition, due to notable impacts U/S, and D/S of LE and TE faces respectively.

Faure et al[53] visualised incompressible subsonic laminar flow; U_∞ = 0.69-1.6m/s, over open wide cavities; L/D = 0.5-2 and L/W = 0.08-0.3 with PIV. Transverse flow was examined with parallel plane images, to emphasise 3D flow, and dynamic structures spatially. SL instabilities remained 2D, with no secondary effects, as L/W << 1, such that flow remained 2D, due to

lack of spanwise flow. They also renounced Re, as a significant variable, compared to L/D. At L/D = 2 and 1.5, SL and TE wall interaction drove 2D internal flow and mass injection. Two vortical structures were present; a strong primary unsteady vortex D/S, and a counter-rotating secondary vortex near the bottom LE wall. Induced flow from vortical motion evolved spanwise, with a secondary vortex causing further unsteadiness, by structurally opposing Görtler [54] instability propagation. For L/D = 1, the primary vortex was dominated by length, with a time-evolving boundary, and the secondary vortex reduced to a corner. The primary vortex core, exhibited counter-flow nearby side walls, with Görtler [54] vortices moving out spanwise, due to spanwise flow acting in the periphery of the primary vortex, from centre out. For L/D = 0.5, two vortices superimposed at a low velocity, and became laminar internally.

Zhang & Naguib [55] used USP and HWA to study SSOs, and the effect of width, on open narrow to wide cavity geometry; L/D = 2.6, 3.4, and 7.1 at L/W = 1.7-0.4, subject to low subsonic flow M_∞, and a turbulent U/S BL. USP and velocity measurements aligned oscillatory motion to large lateral SL displacement, with a recirculating hydrodynamic feedback mechanism in the TE region, critical to establish SSOs, in narrower cavities. This movement reduced intensity as width increased, eventually ceasing, as feedback attenuated and 3D flow reduced. Overall, width significantly altered the flow, proving a critical parameter for SSOs, of greater impact in narrower flow due to sidewalls, which reduce dissipative capability.

Crook et al [56–58] used PIV and USP to study an open narrow cavity; L/D = 6 and L/W = 3, subject to incompressible laminar flow; U_∞ = 0.108m/s, δ = 11.1mm. First [56], they investigated the following system: BL to SL transition traversing D/S, TE wall impingement to TE vortex entertainment, recirculating flow U/S into main recirculation, and LE vortex entertainment moving flow spanwise to sidewalls. Main recirculation agreed with past work, however spanwise features are less ubiquitous. On the TE wall, a "*centrally located saddle point flanked by a pair of nodes*" [56] was observed, with two down-wash regions underneath. The saddle point next to the TE vortex, aligned with measured maximum and minimum pressure. Second [57], they studied SL growth rate from LE formation, traversing D/S, and impinging the TE. Analysis was performed using vorticity thickness (δ_ω) as a length scale, with a compact-Richardson scheme [59] to calculate vorticity, accounting spanwise SL flow $v(x, y) \neq 0$. Growth rate along $y = 0$ was 12% higher than assumed, and off-centre SL growth was impeded prior to the TE. The latter a result of interaction with spanwise cross flow produced at the sidewalls.

Wagner and Beresh et al [60–64] used PIV to visualise supersonic flow M_∞ = 1.5, over an open cavity L/D = 5. Specifically, analysing 3D effects of width in narrow flow for; L/W = 1, 1.167, 5.08. A turbulent SL streamwise was present in all cases, with large-scale turbulent eddies and internal recirculation. However, their position was dependant on width. Width also lowered turbulence intensity (TI) in the SL, compared to main recirculation, causing change of eddy characteristics, SL undulations and temporal recirculation strength. L/W = 1.67 had the lowest SL TI, compared to wider L/W = 1 and narrower L/W = 5, its mean recirculation weaker, and closer to the floor, highlighting nonlinearity during transition from 2D to 3D flow.

Beresh et al [65] follow-up with cross-plane PIV, to investigate spanwise flow. Images reveal turbulent sidewall flow, with a strip of turbulence streamwise. Correlation proves SL TI a

function of L/W. As reducing width, is observed to increase recirculation strength, due to sidewalls, which re-entrain spanwise flow in the SL, thus increasing SL TI via recirculation. SL TI was suppressed at L/W = 1.67, compared to wider L/W = 1 and narrower L/W = 5. Based on prior work[46,55,66], spanwise motion at L/W = 1.67, is not yet strong enough to alter flow propagation D/S. Therefore, modes are not dominantly streamwise in wide L/W << 1 nor dominantly narrow spanwise L/W >> 1, with L/W = 1.67 a transition state.

Jones & Watmuff[67] measured acoustics in a deep open wide cavity; L/D = 0.5 and L/W = 0.167, subject to subsonic flow U_∞ = 16-30m/s in a WT. They also present flight data of internal acoustic SPL excited by resonance ≈ 170dB, which leads to: excess noise radiation, heat transfer, fatigue and avionics interference. At all U_∞, spectral peaks occurred at a fixed frequency in both U/S and D/S BLs, aligned to East's[8] normal mode, with no SL coupling, suggesting a mismatch of Rossiter's model[2] for low speed deep cavities. They also performed HWA in the SL and U/S BL, both showing broadband velocity spectra, correlating to non-resonant pressure tones, and fundamental acoustic modes from the SL without feedback.

2.2.1 Summary of Internal Geometry Effects

2D flow of length and depth ∼ L/D, has been the focus of cavity research. Width has often been overlooked for characteristic behaviour, and effect on streamwise flow. Primarily because initial studies prioritised wide cavities, where 3D flow is dispersed. Studies then continued to neglect width, and focus on streamwise flow, especially numerical models, which are predominantly 2D. However, associated amplitude prediction models always fall short, and even frequency models have limitations, thought to be a result of neglecting width, and BL δ (See Section 2.4).

Maull & East[46] identified the importance of width to diagnose variable 3D flow, and its spanwise effect on streamwise mode structure. However, many considered the effect negligible, paradoxically remarking on lack of similarity, between results of the same L/D and M_∞, with different L/W. Stalling & Willcox[25] highlighted effects of width on streamwise flow transition open to closed, with $(L/D)_{cr}$ decreasing proportionally. Effectively, a wide cavity sustained open flow longer than a narrow cavity, due to dispersion of spanwise 3D flow. Moreover, at fixed L/D, a closed narrow cavity produced larger lateral pressure gradients on the TE wall than a wide cavity. Plentovich et al[26] also observed transition in pressure distribution open to closed, when decreasing width at constant L/D, due to induced 3D flow.

Chung[52] aligned strong TE vortices resulting in large pressure gradients near the TE, to narrow flow L/W = 1. Effectively, 3D flow alters peak pressure ahead of the TE pressure gradient, causing more extreme fluctuation, thus volatility in streamwise flow limits. Zhang & Naguib[55] discretely proved sufficient 3D flow thus appropriate L/W, to be required for SSO formation. Identifying large lateral SL displacement aligned to increased strength of the TE recirculating feedback mechanism, to establish SSOs. Their theory aligned with Chung[52], who observed stronger TE vortices due to 3D flow as a result of reduced width. Stalling & Willcox's[25] notable increase in lateral pressure gradients, is also explained by volatile SSO SL TE flapping.

Grace et al[68] note an absence of SSOs, even though flow was open, and L/D, M_∞ requirements were met. However, their cavity geometry was very wide L/W << 1 = 0.11. Therefore, based

on the narrow requirement, SSOs were dispersed spanwise regardless of similarity in L/D. Such correlation is extant in most research where SSOs were not observed. Therefore, it is absolutely vital to consider width when comparing data, especially in diagnoses of dominant flow features alike SSOs. SSOs also have an upper limit, when the cavity is too narrow, their impact is reduced, and eventually cease, with an optimal range near $L/W \sim 1$.

Ahuja & Mendoza[51] believed modes were independant of width, from observing very wide cavity flow. However, Tracy & Plentovich[49] and Disimile et all[50] observed proportional increase of resonant amplitude with width, inducing resonance on non-resonant L/D. Effectively, tending wide cavities toward open flow of increasing resonant character, and narrow cavities toward closed. They also observed an increase in reduced frequency of peak resonance at lower L/W with increasing width, meaning width prescribes characteristic dominance.

Hence, it is clear, width is critical in defining spanwise flow, it's contribution to 3D flow, and impact on streamwise flow. Reducing width, increases 3D flow, which disturbs dominant streamwise flow, initiating mode switching. This effect is unexplained by 2D assessment. In some cases amplifying or attenuating the cavity response, based on L/D, or shift the point of transition from open to closed flow. Therefore, research should observe width and spanwise effects instead of isolated L/D, as streamwise flow is largely understood. Width is particularly influential in 3D flow, when the geometry is narrow $L/W > 1$, due to sidewalls.

2.2.2 Summary of Airspeed Effects

Cavity effects notably change between incompressible $M_\infty < 0.3$, sub $0.3 < M_\infty < 0.8$, trans $0.8 < M_\infty < 1.2$, super $1.2 < M_\infty < 5$ and hypersonic flow $M_\infty > 5$. It is well researched, with alteration in flow type observed through variable M_∞ in the same regime, and also when traversing boundaries. However, the latter presents significant change due to induced compressibility, causing emanation of shock-waves, limiting the travel of dynamic and acoustic waves. Especially in formation of dominant oscillatory pressures, and flow feedback.

The primary effect of airspeed $\sim M_\infty$, is on the point of transition between open and closed flow; $(L/D)_{cr}$, as supersonic flow has a higher value of $(L/D)_{cr}$ than subsonic. Similarly for constant typically closed L/D, when increasing M_∞, flow tends open. This reflects a change in push and pull mechanisms, as a higher momentum fluid streamwise, sustains a greater acceleration D/S, compared to the net force pulling flow into the cavity, and causing transition, resulting in open flow[24]. Effectively, a faster driven SL traverses more distance in less time with more momentum, before internal forces can pull in. Alternatively, a faster flow bridges a longer cavity in the same time a slower flow falls short. Overall, M_∞ effect is alike L/D effect, for transition from open to closed flow, which is also altered by the BL, per below.

2.3 Cavity Spectral Response

Cavity flow research dates back to the 19th century, from experimental physicist Strouhal[31], who observed flow over geometric discontinuities. Strouhal studied induced vibration and acoustic resonance in relation to vorticity, to mathematical describe oscillatory phenomena. In contemporary physics, Strouhal Number (St) is one of the most frequently used parameters, pro-

viding a basic set of scaling laws, to diagnose if vorticity is the root cause of an oscillatory response, and when vorticity begins, with respect to frequency. In this case, where vorticity sheds off the cavity LE, propagating into larger vortices, oscillatory pressure, acoustics, and vibrational modes, St number is implicated, per Eqn. 2.1: f is shedding frequency, L is length scale of the phenomena, allowing vortices to shed per application, and U_∞ is FS airspeed.

There is a limit on St number, as M_∞ increases, due to the presence of unsteady turbulence, and compressibility effects. Shock-waves change the governing vortex mechanisms, as they are stiffer than subsonic phenomena, and their dynamics occupy a higher frequency range. This requires a shift in length scale for St number, as vortex convection in time becomes dominant over frequency. However, such limitations are only relevant when shock waves present, outside the realm of this thesis, which observes incompressible cavity flow.

St number for cavity flow, was first derived empirically by Rossiter [2] in Eqn. 2.2. Here, m is mode number, $\gamma_v = 0.25$ is an empirical constant, representing phase difference between arrival of U/S acoustics, resultant shed vorticity, and interaction D/S with the LE, producing acoustics, and $\kappa = 0.57$ is another empirical constant, for the ratio of vortex convection velocity in the SL, to FS velocity. For incompressible flow $M_\infty < 0.3$, East [8] adjusted the length-scale to give Eqn. 2.3 and 2.4: $A_e = 0.65$, with $B_e = 0.75$ as constants. Block [6,32] also presented a low-speed form closer to that of Rossiter in Eqn. 2.5. Heller et al [13] similarly modified for higher $M_\infty > 1$ in Eqn. 2.6, where γ is the specific heat ratio. Each is discussed in further detail following.

$$\mathrm{St} = \frac{f\mathrm{L}}{\mathrm{U}_\infty} \tag{2.1}$$

$$\mathrm{St_R} = \frac{(m - \gamma_v)}{(\kappa^{-1} + \mathrm{M}_\infty)} \tag{2.2}$$

$$\mathrm{St_{E_D}} = \frac{f\mathrm{D}}{\mathrm{a}_\infty} = \frac{\gamma_v}{1 + \mathrm{A_e}(\mathrm{L/D})^{\mathrm{B_e}}} \tag{2.3}$$

$$\mathrm{St_{E_L}} = \frac{f\mathrm{L}}{\mathrm{U}_\infty} = \frac{\gamma_v(\mathrm{L/D})}{\mathrm{M}_\infty(1 + \mathrm{A_e}(\mathrm{L/D})^{\mathrm{B_e}})} \tag{2.4}$$

$$\mathrm{St_B} = m\left[\frac{1}{\kappa} + \mathrm{M}_\infty\left(1 + \frac{0.514}{\mathrm{L/D}}\right)\right]^{-1} \tag{2.5}$$

$$\mathrm{St_H} = (m - \gamma_v)\left[\frac{\mathrm{M}_\infty}{\sqrt{1 + 0.5\mathrm{M}_\infty^2(\gamma - 1)}} + \frac{1}{\kappa}\right]^{-1} \tag{2.6}$$

Rossiter [2] executed WT experiments on open to closed narrow cavity geometry; L/D = 2-10 and L/W = 4, subject to sub, trans and supersonic flow M_∞ = 0.4-1.2, using USP and Schlieren. Schlieren highlighted SL roll-up into discrete vortices, shed at regular intervals from the LE, propagating D/S. Thus implicating St number to predict frequency response in Eqn. 2.2. The model associates behaviour with an external velocity increase as flow enters the cavity, proportionally decreasing pressure. Then on flow reattachment on the floor or TE wall, the inverse occurs, its magnitude dependent on geometry. Implicating a BL effect on oscillatory pressure magnitude, where for the same values of length and depth, increasing BL δ decreases floor $C_{p,rms}$. However, Rossiter [2] did not include the BL in his model.

USP was measured and transformed into acoustic spectra, to determine frequency and magnitude of resonant mode oscillations, to confirm the model. Results highlighted the convergence of separation and reattachment points as L/D decreased. Until flow reversed between high-pressure ahead of the TE, and low-pressure near the LE, producing a large vortex, in a deep

cavity, with large periodic oscillations, that increased with M_∞, in a narrow discrete frequency band. As length increased L/D > 4, random frequencies took over as broadband spectra, and as depth increased periodicity superimposed. The periodic fluctuations starting with a peak in amplitude larger than others, fluctuating as M_∞ increased, similarly for other frequencies, as integral multiple peaks of the dominant frequencies, or harmonic oscillatory distortions.

East [8] studied the resonance of deep open and wide cavities; L/D = 0.1-1 and L/W = 0.05-0.16, subject to incompressible flow U_∞ = 30-60m/s. To improve Rossiter's model for deep cavities, which present discrete acoustic oscillations [3], aligning with the acoustic depth or normal mode of a classic resonator. Additional SL resonance was also perceived, as tones reached obvious maxima at certain U_∞, yielding two St numbers with suggestion of a third. For SL instability, and simultaneous doubly tuned amplification of SL edge tones for cavity resonance, conclusions of depth mode were drawn to Plumblee et al [3]. Both observing flow across a deep cavity, to produce pressure oscillations of the normal mode. East [8] only observed tones when SL oscillations were amplified by acoustic coupling between the SL and cavity modes, proposing inferred SL feedback as the cause of certain frequency amplification, resulting non-dimensionally in certain Strouhal alike [2]. However, while Rossiter aligned well, East [8] believed more detail was required for SL effects and external flow coupling at low M_∞, per; Eqn. 2.3 relative to cavity depth and speed of sound a_∞ [3], and Eqn. 2.4 for U_∞ and length.

Block [6] performed WT tests on deep open and wide to narrow cavities, with fixed depth and variable length and width for; L/D = 0.3-2 and L/W = 0.33-1.85, subject to subsonic flow at M_∞ = 0.1-0.5. To correlate acoustics with oscillatory pressure phenomena. For $M_\infty \geq 0.4$, Rossiter's mode for lengthwise oscillations, changed slowly with M_∞. However, for incompressible flow $M_\infty < 0.4$, below Rossiter's experimental range, St instead increased with L/D at a given M_∞, implying L/D dependence, instead of length alone. An empirical model was thus developed, to predict resonant frequencies, including L/D for incompressible flow. The model accounts interactions observed between length-wise vortical-acoustic modes, and depth-wise standing-wave modes. Providing a means to determine the M_∞, when maximum-amplitude occurs. Therefore, if $M_\infty \leq 0.4$, St number depends on cavity length and depth. With L/D $\leq$ 4 required for resonance, as depth is dominant for normal cavity modes.

Block [32] also studied noise components of subsonic flow $M_\infty = 0.05-4$ over open to transitional, and wide to narrow cavities; L/D = 0.27-8.46 and L/W = 0.28-5.55. The effect of length on St number was observed for decreasing M_∞ in bands of increasing gradient. Specific to $M_\infty \geq$ 0.15, Block's [6] model in Eqn. 2.5 was reasonable, however for $M_\infty \leq 0.2$, East's model in Eqn. 2.3 was more aligned to slope steepening, though incorrect in values. However, there is an intersection of the two curves, as an indication of M_∞ where given L/D, start to oscillate for a specific mode. This was formulated as a predictable change in St number proportional to L/D, noting that for L/D $\geq$ 3, St number becomes relatively insensitive to L/D, as depth is dominant. This is because, L_{min} is required for oscillation to occur, tending to increase with M_∞. Block also observed discontinuity in the data, suspected to be changing BL conditions.

Heller et al [13] studied supersonic flow M_∞ = 1.5, 2, and 3, over open narrow cavities; L/D = 4-7 and L/W = 3, and observed longitudinal distribution of USP in longer cavities, distinguishing

from pure resonator form in short. As depth dominated, energy capacity responded in normal mode, with high Q-factor, and shallow cavities with low Q-factor resonated poorly. Q-factor as a dimensionless parameter for how under-damped an oscillator is, regarding characteristic resonance bandwidth relative to centre frequency. Therefore, a deep cavity is under-damped, resonating at characteristic frequency, but the shallow cavity is damped, and acoustics disappear relative to forcing magnitude. Nonetheless, FS flow drives relatively definite acoustic frequencies in a shallow-open cavity, as an acoustic source at the TE compensates for low Q-factor, hence acoustic response in the shallow cavity at analogous M_∞. Eqn. 2.6 was thus formed correcting for compressibility effects at higher $M_\infty \approx a_\infty$: $\gamma_v = 0.25$ and $\kappa = 0.57$.

Kaufman & Clark[14] investigated the aero-acoustics of bomb bays. Recording USP in transitional narrow cavities; L/D = 5.1-9.9 with L/W = 1.9-3.7 subject to sub-supersonic flow; M_∞ = 0.6-3. All cavities subject to supersonic flow, responded with an increase in pressure on the TE wall, much higher than the FS, indicative of increased drag. Acoustic recordings presented complex 3D results, contributing to proposed improvement of St number to satisfy 3D mode frequencies per Eqn. 2.7: γ_v, κ are Rossiter's constant, re-derived[14] for higher M_∞.

$$St_{KC} = (m - \gamma_v)\left[\frac{M_\infty}{\sqrt{1 + 0.2M_\infty^2}} + \frac{1}{\kappa}\right]^{-1} \tag{2.7}$$

Bassioni et al[29,30] measured USP on the floor of open and transitional narrow cavities; L/D = 5,8 and L/W = 2.1, subject to incompressible flow; M_∞ = 0.086. Wave frequency analysis extracted mode signatures, to establish spatial and temporal resolution of acoustic and dynamic oscillation. When increasing L/D = 5 → 8, a long-cavity resonant type SL mode coined **back-step resonance**[29,30] appeared. The mode was aligned to enhancement of back-step flow structures via acoustic feedback at the TE, with large-scale structures toward the floor reattachment zone. This differed from Rossiter's SL mode, as the separating SL exhibited mean reattachment near the floor per closed flow, but in transitional geometry with weak re-circulation. Effectively, the slow momentum of M_∞ = 0.086, reduced the transition point $(L/D)_{cr}$ from open to closed flow, toward a lower L/D, such that open flow closed, but still presented resonant properties, likely as a function of BL δ, and cavity width.

Seena & Sung[69] applied dynamic mode decomposition (DMD) to 3D CFD results, of incompressible turbulent flow over an open wide cavity; L/D = 2 and L/W = 0.5. Two cases with and without oscillating pressures were observed, aligned to a thin and thick U/S BL. Results of thick BL DMD emulated a viscous BL profile, with coexistence of BL and SL structures along the cavity mouth, coincident in frequency, but differing in wave number space. The thin BL DMD however, presented full coherence amongst modes, with a structurally dominant peak aligned to the dynamic mode of SSOs. Instantaneous velocity distributions were processed to observe the SSOs, which were coincident with SL Mode 3. Therefore, dynamic resonance of SSOs are only viable when the U/S BL, and cavity SL coincide in frequency and wave space, meaning the U/S BL is a driving parameter to determine SSO presence.

Casper & Arunajatesan[70] decomposed USP data using POD and DMD from an open transitional narrow cavity; L/D = 7 and L/W = 2, subject to subsonic flow M_∞ = 0.8. POD extracted coherant modes across the LE span, with higher, particularly turbulent frequency

modes, in the TE region, varying spanwise. POD modes had multiple frequencies in the flow, which DMD further isolated. DMD extracted SL mode coherent structures across the LE span, with more complex structures in the TE region, alike POD. DMD also presented intermediate modes, between dominant SL frequencies, associated with lower-frequency modulation of cavity tones. Overall, modal decomposition provided a solid base for flow analysis, with DMD providing more discrete spectral information, when spatial resolution was adequate.

Singh et al[71] implemented DMD on 2D TR-PIV data of subsonic flow M_∞ = 0.6-0.94 over an open cavity; L/D = 6, L/W = 1. A sequential single block of data for trends in singular values of oscillation, and multi-block non-sequential data, so rank and run could be determined from mode invariance. Multi-block non-sequential identified higher resolution structures, with growth rates peaking in correlation with expected oscillatory pressure, and eigenvectors with coherant structures in modality of their wavelength. By re-constructing flow-field SL modes 1-3, eddy frequencies were observed to shed from the LE, and grow as they convected D/S, dominating the spectra as instabilities toward and aft the TE. Eigenvalue growth rates in the vicinity, also highlighted large scale vortical modes, and smaller structures. Low frequencies varying with M_∞, exhibited DMD peaks consistent to Rossiter. However, higher frequencies, deviated from Rossiter, requiring further study, also identified by [66, 72].

2.4 The Boundary-Layer

The BL is an important facet of cavity flow. It defines parameter boundaries, in which U/S fluid can interact with internal cavity geometry. Mode type and clarity of amplitude have been observed to drastically alter between laminar, turbulent, and very thick BLs. Therefore, knowledge of the U/S BL, is necessary to define cavity response, where dominant oscillatory or resonant phenomena can not be predicted, nor even occur, unless BL characteristics are considered. Following are key studies referencing the BL effects, which fed into choice of model geometry to attain certain BL structures for this thesis.

2.4.1 Turbulent Boundary Layer

Scheiman[73] observed turbulent U/S BLs, and found, increasing BL δ, decreased amplitudes in the test range, alike Sarohia[16] and Karamcheti[15]. Ahuja & Mendoza[51] also thickened a turbulent BL until noise was eliminated, aligned to $\delta/L \approx 0.07$ at fixed length. Also observed when widening a cavity for L/W << 1, as the predominant SL wavelength is dispersed and reduced in amplitude, similarly decreasing amplitude. This comparative response sparks intrigue toward the impact of controlled SL dispersion for removal of cavity noise. Several control studies have successfully implemented LE steady blowing to alter SL structure and attenuate tones, the flow alteration emulating an effect akin to SL dispersion, refer Section 8 of [1].

Plentovich[74] studied open and closed narrow cavities; L/D = 4.4 and 11.7 at L/W = 4.375, subject to sub and transonic flow of M_∞ = 0.3-0.95. Static and USP were recorded to observe effects of Re number, U/S BL δ and L/D. The closed cavity (L/D = 11.7), showed an increase in TE pressure with increasing δ. However, for all conditions, static pressure was steadier than the open cavity L/D = 4, where floor pressure fluctuated significantly. The initial U/S BL was

δ = 50.8mm, then further thickened. However, when constant, Re number had no impact on pressure in the range, suggesting Re negligible comparative to U/S BL δ.

Ahuja & Mendoza[51] studied subsonic turbulent flow over open and wide to narrow cavity flow; L/D = 0.5-6 and L/W = 0.19-3.75. Measurements were taken with USP, HWA and tuft flow visualisation, to study BL δ effect on noise. Results reveal increasing δ for δ/L = 0.07 at fixed length via a backward facing step, eventually eliminated all detrimental acoustic tones.

Ritchie[75] observed the effect of increasing δ = 4.8-18.7mm on streamwise flow. Results indicated a thick BL at larger L/D, produced flow alike a thinner BL at lower L/D. Effectively, increased BL δ altered streamwise flow type. A 3D URANS companion simulation[75] also observed increasing δ to alter flow type, however contradicted experimental results. This was due to poor SL growth in URANS for a thick BL, which produced a low SL spreading rate aft LE separation, compared to experimental results. Difficulty in modelling thick turbulent BL separation is a common subsonic CFD issue[76], especially in transition from a thick BL into a SL, as present turbulence models are unable to handle subsonic flow separation.

Seena & Sung[69] varied δ before an open wide cavity; L/D = 2 and L/W = 0.5, observing USP and velocity distributions via DMD. The thick BL, had no abundant oscillations, with a viscous SL structure, indicating coexistence of BL and SL structures along the cavity mouth, coincident with frequency and differing wave space. The thin BL, produced large-scale structures at LE separation, resulting in formation of a fully coherant, structurally dominant dynamic peak, aligned to the large oscillatory pressures of SSOs, and instantaneous velocity distribution spectral characteristics of SL Mode 3. Therefore, dynamic resonant characteristic of SSOs are only viable if the U/S BL, and SL coincide in frequency and wave space.

Haigermoser et al[77] executed TR-PIV in a water tunnel, to observe an open wide cavity; L/D = 4 and L/W = 0.1, subject to incompressible flow; U_∞ = 0.4m/s, and a thick U/S BL; L/θ = 18. SSOs were identified despite $L/\theta < 81$, the limit of Gharib & Roshko[28]. PIV was wall-normal and parallel, for mean characteristics and TR flow, allowing for examination of SL vorticity, dynamic behaviour and feedback. Irregular SL vortex shedding was detected, and correlated to coherant structures in the BL. Indicating SL instabilities, and vorticity propagation, are BL dependant for SSO formation, agreeing with [28], however, disagreeing on the limit.

2.4.2 Laminar vs. Turbulent Boundary Layer

Karamcheti[15] compared laminar and turbulent BLs, aligning a thick turbulent BL, to weak propagation of cavity resonance, due to random buffet, while a laminar BL, instead had defined periodic pressure waves, and distinct acoustic tones. Effectively, the turbulent BL, required a longer cavity to produce acoustics for fixed width and M_∞, compared to the laminar BL, in order to establish flow periodicity, as the turbulent BL created random harmonic buffet, and the laminar produced dominant periodic flow in the same length. Moreover, the laminar BL produced one dominant fundamental frequency with harmonics, while the turbulent produced two weaker dominant frequencies, one almost doubled in magnitude, and harmony.

Roshko[43] observed internal vorticity, independent of U/S BL for sustained frequency. However, amplitude and modal response structure overall changed, dependant on δ. Also observed by

Charwat et al[24], who found $(L/D)_{cr}$ to vary with δ, especially in supersonic flow when δ/D = 0.3-3, with almost no dependence on M_∞ and Re number. Block & Heller[47] proved the effectivity of increasing δ to reduce cavity noise. However, the impact decreased with increasing M_∞ or length, as flow transitions from open to closed, changing the noise mechanism from a classic resonator toward more periodic, which is less BL δ dependant.

Sarohia[16] studied laminar incompressible flow of $M_\infty \approx$ 0.002-0.025 over open wide cavities; L/D = 0.52-3.8 and L/W = 0.17-1.2. Observing LE BL separation, into SL propagation dependant on δ, Re and cavity geometry. Response was assessed for amplified disturbances in the SL, with and without resonance, aligned to feedback and cavity length. Findings as follows;

(1) Dimensionless length $(L_{min}/\delta)\sqrt{Re_\delta}$ is independent of depth $D/\delta \geq 2$. If $D/\delta > 2$, no oscillations occur when $(L_{min}/\delta)\sqrt{Re_\delta} < 0.29 \times 10^3$. Thus, depth has a limited effect on SL oscillations unless in the order of BL δ, due to a depth stabilising effect on the SL.

(2) For fixed BL edge velocity U_e and kinematic viscosity v; $L_{min} \sim \sqrt{\delta}$. If no pressure gradient, $\delta \sim 1/\sqrt{U_e}$. Then $L_{min} \sim \sqrt{\delta^3}$. Thus, increasing δ delays oscillation onset.

(3) There is a sharp increase in $(L_{min}/\delta)\sqrt{Re_\delta}$ for $D/\delta < 2$, below which no oscillations occur.

(4) Decreasing D/δ stabilises laminar shear layer flow over the cavity.

(5) A longer cavity is required for oscillations if D/δ is small, which is pronounced in very shallow cavities, with a strong lateral constraint on cavity shear-flow, averting growth of 3D disturbances, which contribute to turbulent transition.

(6) Oscillatory frequency f depends on L/θ, δ/D and $Re_\delta = U_e\delta/\nu$ depends on $St = fL/U_e$, which is lower for a given mode when LE BL separation is turbulent vs. laminar.

(7) Oscillation wavelength λ has an integral relation to $L = \lambda(m + 0.5)$ and $St = fL/U_e = (U_c/U_e)(m + 0.5)$. Thus disturbance propagation speed U_c increases with L at fixed Re, meaning St increases for each mode of oscillation.

(8) There are three regions of SL development.

  (i) Separation: the BL separates at the cavity LE, propagating into a SL, this region extends 10-15 times θ D/S from the point of separation.

  (ii) Oscillation: greater part of the cavity, where velocity fluctuations occur at the frequency f(Hz) of cavity oscillations, propagating at a constant phase speed.

  (iii) Periodic Shedding: SL deflects in and out near the TE at f (Hz), lateral motion causes large velocity fluctuation, and vortices shed periodically from the corner at f (Hz). The effect postpones transition to turbulent until L_{max}, correlated to $Re_\delta = 500 - 2000$ and $L_{max}\theta \gtrapprox 100$, where L_{max} is nearly twice the distance of transition.

(9) The stabilising effect is attributed to large SSOs induced in the cavity SL, due to presence of the TE, these oscillations delay roll-up of the laminar SL into vortices.

(10) Presence of cavity oscillations in flow induces large increase in SL growth rate, potentially due to increased Reynolds stress due to large amplitude oscillations in the SL.

Overall, incompressible cavity oscillations are not acoustic resonant, longitudinally. Instead, they are amplified disturbances of large lateral SL motion, close to the TE, producing periodic

shedding of vortices from the TE at f (Hz). Laminar to turbulent transition in the SL, is postponed by the large amplitude of these oscillations, until L_{max}. As the SL does not roll into vortices if $L/\theta > 100$, with transition occurring at $L > L_{max}$. Depth $\delta/D << 1$ also delays transition. Strong oscillations correlate with large SL growth akin to $d\theta/dx \cong 0.022$, such that θ and its derivatives with respect to SL propagation are vital to the oscillatory phenomena.

Gharib & Roshko[28] studied periodic SL SSOs and their relation to drag based on the BL. They identified dependency on a laminar or thin BL for SSOs, and high drag, coined the *Wake Mode* (WM), dependant on SL momentum thickness θ_{SL}. SSOs only occurred when $L/\theta_{SL} \geq 81$, below which, the SL bridges the cavity and oscillations cease. Mode 2 was aligned with SSO occurrence, where increasing L/θ_{SL} decreased mode 2 frequency, then jumping to mode 3 dominance with further L/θ_{SL} increase, and then decreased mode 3 frequency. Eventually SSO presence was intermittent, and disappeared. Overall, they proved a laminar or thin BL is required for SSOs, and mode switching occurs in the region between dominance per L/θ_{SL}.

Colonius et al[78,79] simulated laminar and turbulent BLs, and proposed laminar separation as the cause of WM[28], from observed increase in separation resistance with a thick BL, preventing oscillatory growth and convection to WM. WM is identified by high TE and low LE pressure, forming high drag. Therefore, a thick BL not only reduces resonant amplitudes, but also drag by preventing WM. Experimental studies also perceived a thick turbulent BL to filter WM. Milbank[80] observed change in oscillatory response when altering location of flow attachment, with respect to cavity location in the object of attachment. Effectively, BL δ entering the cavity was altered by structural transition. Results prescribed U/S BL behaviour akin to a low pass filter. As a cavity closer to flow impingement responds more readily to local fluctuations, than those further D/S in a fully developed BL. Moreover, a cavity even further D/S, subject to a very thick turbulent BL, completely filtered transition from SL mode to WM[78,79].

Grace et al[68] compared the laminar and turbulent BL effect on a non-resonating open wide cavity; $L/D = 4$ and $L/W = 0.11$, subject to incompressible flow; $U_\infty = 7.5 - 15$m/s. The laminar BL produced a single vortex, 31% stronger and closer to the TE, with mean flow of negligible vertical velocity near the TE. The turbulent BL was of greater impact U/S, due to mean flow at the TE, moving U/S with positive vertical velocity close to the wall. Flow D/S of the cavity converged on flat-plate turbulence faster in response to the laminar BL. While the turbulent BL produced random buffet, delaying transition. Also observed by Chang et al[81]. For shear stress, v' approached a maxima at the mouth, extending above for the laminar BL, and below for the turbulent BL. Lengthwise however, the laminar BL produced lower values near the LE, then increasing D/S, as the SL transitioned, before stabilising at double the value compared to the turbulent BL, which was fixed lengthwise, only increasing just before the TE.

Chang et al[81] compared turbulent and laminar BL in SL transition. The laminar BL, produced 3D instabilities in the SL, convecting streamwise, and interacting with internal recirculation. The initial interaction, disturbed LE shed spanwise vortices as they approached the TE, where they are clipped into small hair-pin structures, and convect D/S. The turbulent BL however, was of broader spectrum, with recirculated flow U/S, and a strong normal velocity component producing SL buffet D/S, from incoming near-wall coherant structures. This effect influenced

SL eddy formation and convection, as a randomised interaction, instead of the large spanwise structures formed by a laminar BL. Turbulent BL random buffet, also impacted mass exchange characteristics. The laminar BL with no random buffet, was aligned to simultaneous mass exchange injection and ejection, via large scale spanwise vortices D/S aft the cavity. However, turbulent BL random buffet accelerates mass ejection, removing flow uniformity as the SL is perturbed U/S in the external flow, delaying injection to main recirculation.

2.4.3 Summary of Boundary Layer Effects

In summary, formation and propagation of instabilities in the SL and internal cavity flow, are highly dependant on the U/S BL, with respect to internal cavity geometry. Most research has observed turbulent BL effects, with few on laminar BLs, and none on different BL structures i.e., varying pressure gradient effects. Based on cavity flow studies with BL data provided, it has been identified, SSOs are responsible for detrimental cavity phenomena, and require a thin or laminar BL. SSOs also initiate the highly periodic shedding of vorticity from the cavity LE, and contribution to stable fluid mass exchange at the TE, as well as the radiation of resonant acoustic tones. Further research into cavity flow with a laminar BL, will provide insight into SSO phenomena, primarily underpinning adverse cavity flow features.

This thesis proposes, that there is a stronger relationship between the BL and cavity width, than currently recognised, requiring further investigation. Furthermore, it is also proposed the integral relationship of the δ/D ratio in spectral prediction, including frequency, may provide more consistent characterisation. As an extension to current understanding, with frequency based on length alone, as shown by Rossiter [2] and Heller et al's [13] ST model, and based on L/D alone for subsonic open flow by East [8], and Block [6], with no reference to BL characteristics.

2.5 Review Summary

Key areas of cavity flow research have been identified through review of the literature. In general, cavity flow-fields generate unsteady oscillatory phenomena, resulting in dominant spectra. These spectra represent propagation of distinct flow features or modes, dependent on; U/S momentum, viscosity (the BL) and geometry; L/D and L/W.

2D or 3D flow development is dependent on width. Narrow cavities tend to be 3D, with the effects decreasing proportional to increasing width. Dominant streamwise modes, and transitional phases between are skewed by width, and the BL structure. Overall, there is complex vortical motion, acoustics, and potentially elastics, proportional to modal behaviour.

This review has clearly identified the effects of cavity length, depth, and M_∞, on the cavity flow phenomena, and spectral response. Effects of width, and the BL are also covered. However, conclusions are less concrete. Therefore, the present thesis focuses on effects of; width, and the BL, through variation of U/S geometry, with respect to streamwise flow, through variable cavity length and airspeed U_∞. More complex external and internal geometries also need further investigation, such as aircraft; wings, fuselage, stores or nose curvature at Re numbers of flight-scale, which has been discussed in detail in the review paper by this author in [1].

Chapter 3

Experimental Set-Up

This chapter outlines wind-tunnel (WT) measurement acquisition, to experimentally assess cavity flow. Specifics of the facility, equipment, instrumentation, and their set-up are detailed. Along with methods and metrics for data obtainment with regard to; the WT, models, support structure, and measurement hardware and software systems. Data was extracted using unsteady surface pressure (USP) and hot-wire anemometry (HWA), with respect to variables of; internal cavity length (L), depth (D) and width (W), with upstream (U/S) variation of airspeed U_∞, boundary layer (BL) thickness δ and pressure gradient dp/dx, through varied external geometry

3.1 The Wind Tunnel

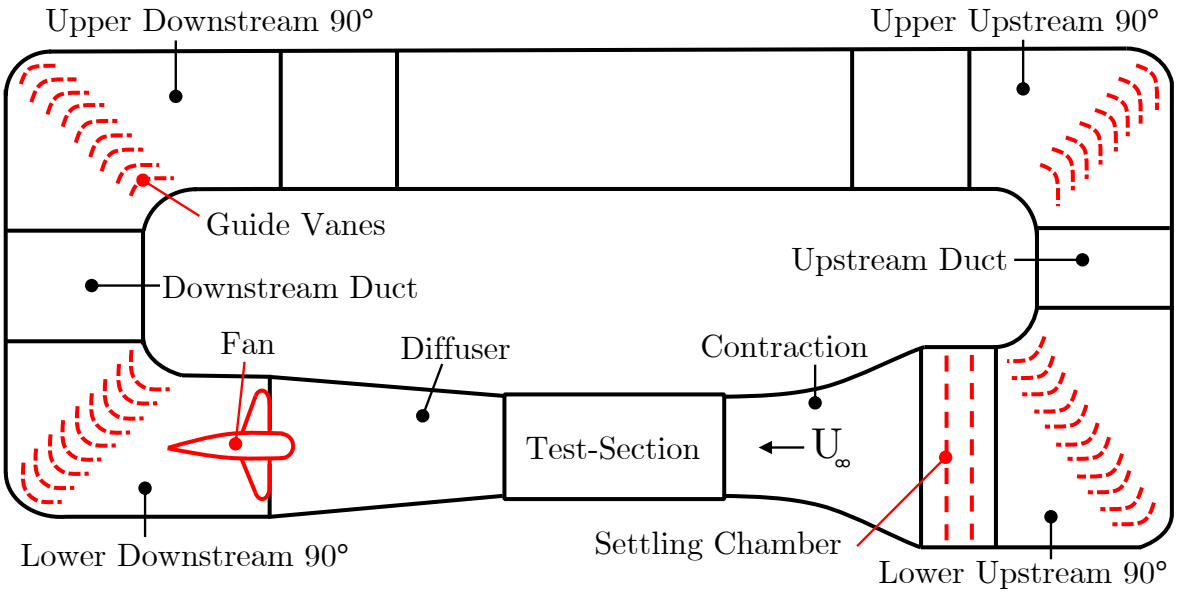

Figure 3.1: University of Sydney Low-Speed Wind Tunnel Diagram

Fig. 3.1 is a schematic of the University of Sydney low-speed WT with a 4 × 3ft test-section (TS). Airspeed is measured and controlled by a PC, calculating U_∞ through correlation of fan RPM, TS geometry, and static pressure measurements at the end of contraction, and beginning of expansion, which is further calibrated with HWA. In initial tests, the WT had a maximum speed $U_\infty = 70$m/s, and recommended minimum of $U_\infty \approx 10$m/s for flow stability.

Fig. 3.2 and 3.3 are cross-section, and direction of flow TS schematics, with the baseline cavity model installed, for axis reference, dimensions and flow direction. The fuselage cavity is similarly located in the TS. However, the fuselage shape protrudes into the TS, and the axis origin shifts with the cavity leading edge (LE) centre line (CL), to keep cavity flow analysis consistent.

Tests were performed at 13 airspeeds, over the range U_∞ = 10-70m/s for USP, and U_∞ = 10-50m/s for HWA, both in 5m/s increments. It was not possible to run the entire airspeed range for HWA, due a motor issue mid-thesis, resulting in latter measurements being restricted to 50m/s. However, a maximum of 50m/s for HWA provided adequate data for analysis.

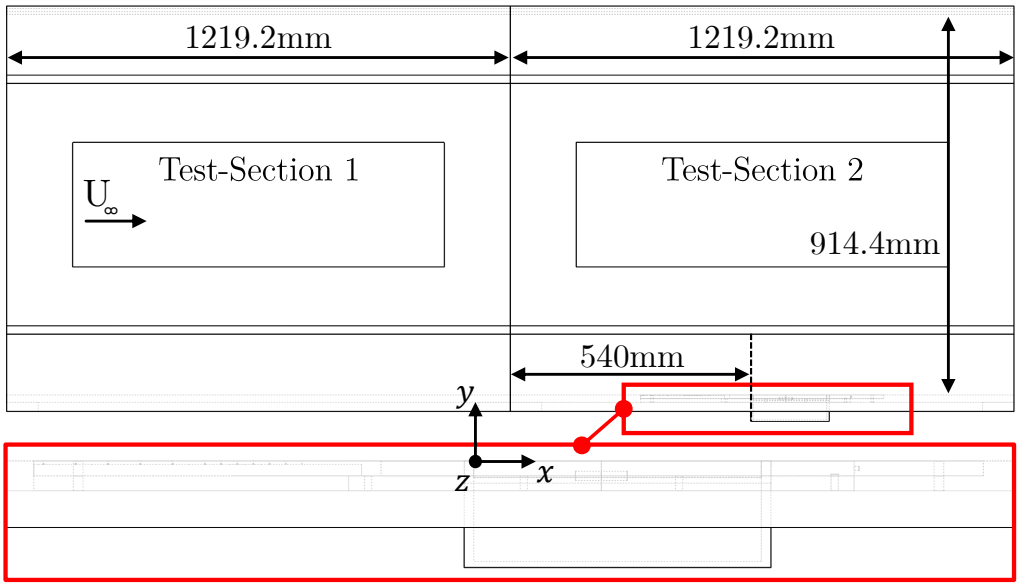

Figure 3.2: WT TS Schematic with Baseline Cavity Model: cross-section

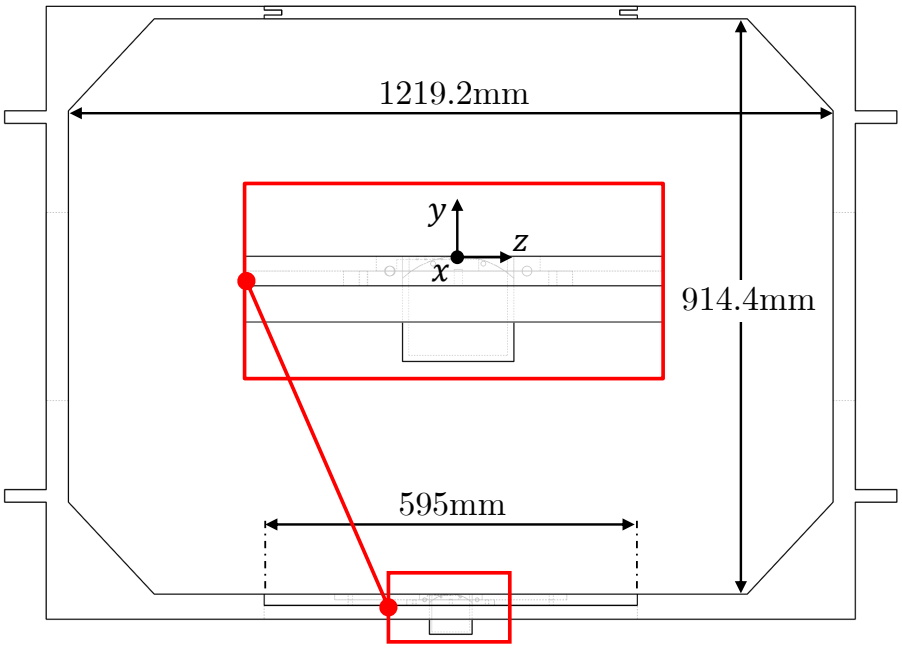

Figure 3.3: WT TS Schematic with Baseline Cavity Model: observing direction of flow

3.2 The Cavity Model

With reference to Fig. 3.4, the cavity has fixed depth D = 60mm, variable length L = 60, 120, and 180mm for L/D = 1, 2, and 3, and variable width of W = 60mm for L/W = 1, 2, and 3 and W = 30mm for L/W = 2, 4, and 6 respectively, corresponding to open streamwise and narrow spanwise type cavity flow. The model is placed TS floor centre, for baseline and fuselage models, with variable distance to the floor. The baseline cavity LE is flush with the TS floor, however the fuselage cavity LE is 85.4mm above the floor, to account fuselage curvature. However, during analysis, the origin is the cavity LE CL, where the BL has been measured.

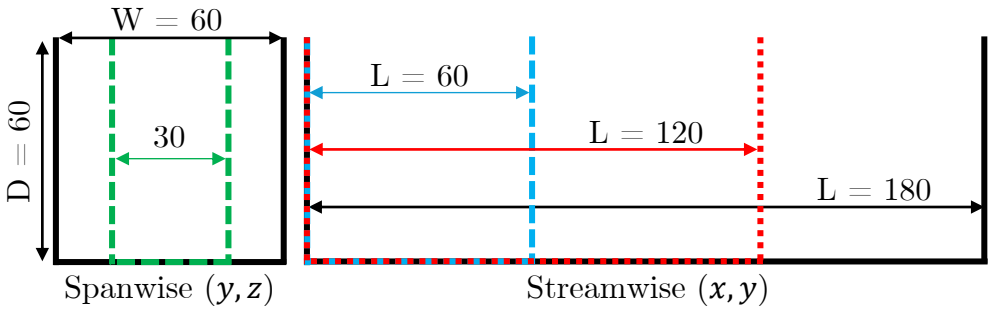

Figure 3.4: Internal Cavity Geometry: dimensions in mm

3.2.1 Baseline Flat Cavity

The flat cavity insert was 3D printed, and locked-in with quantity (QTY) × 9 ⌀5mm zinc cap screws to the perspex floor insert (see Fig. 3.6-3.7). The floor insert is installed with QTY × 4 ⌀6.6mm steel cap screws, to a plywood TS insert, and locked to the TS floor with QTY × 4 ⌀10mm steel cap screws from outside the TS. Variable length and width is achieved with 3D printed blocks locked to place. The base cavity was used in the fuselage, cut to fit fuselage curvature and maintain pressure tap locations. All printed parts are 4mm thick PLA with 0.1mm layer height and 15% infill, treated with acetone and sanded for a smooth finish.

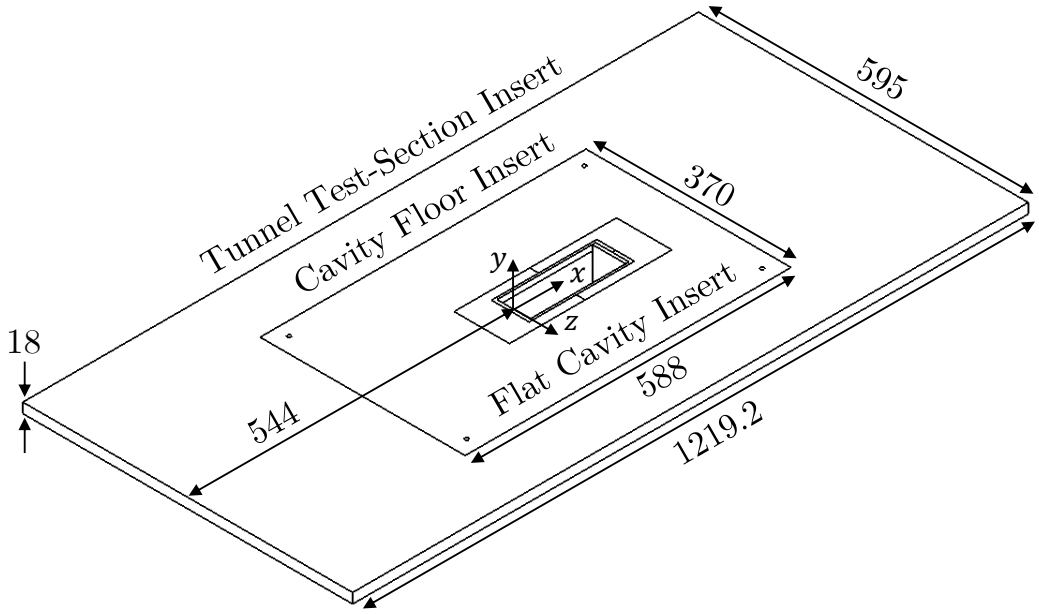

Figure 3.5: Flat Cavity Model Schematic: Isometric View: dimensions in mm

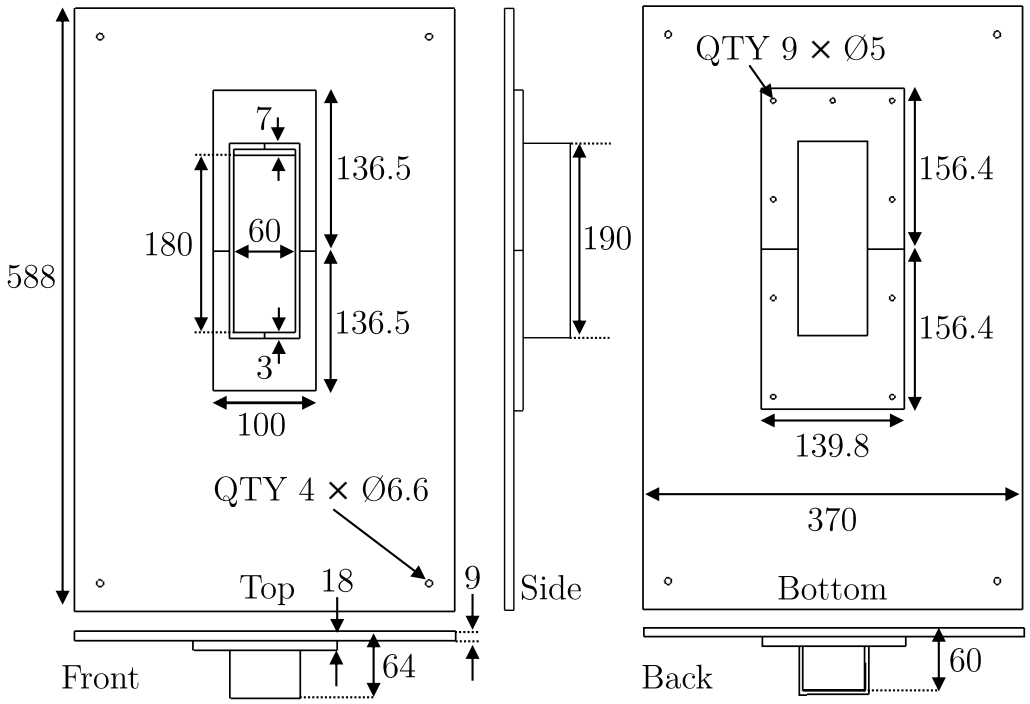

Figure 3.6: Flat Cavity Model Schematic: Top, Bottom, Front, Back View: dimensions in mm

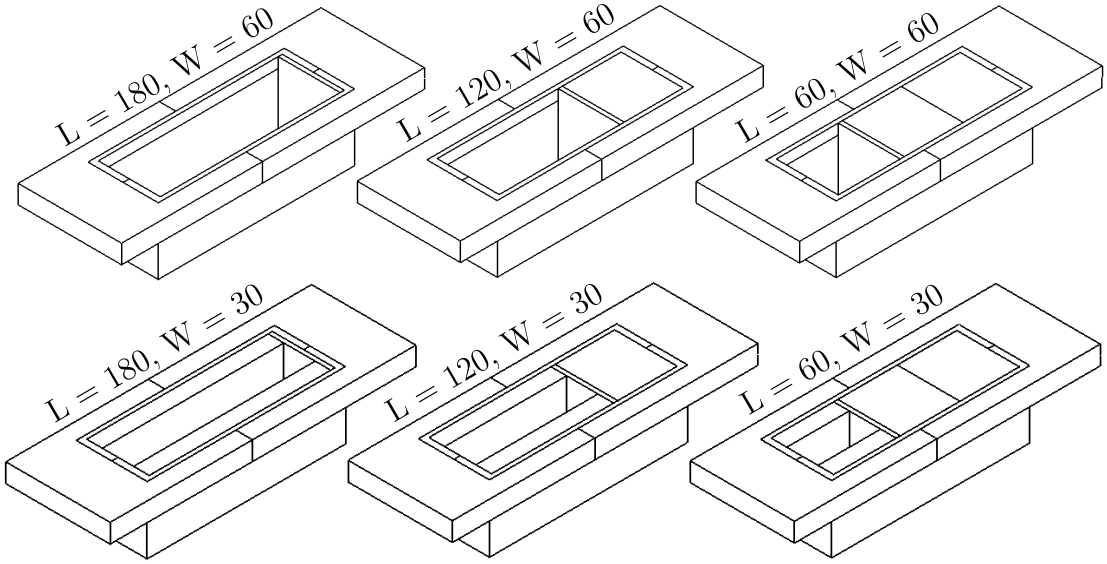

Figure 3.7: Flat Cavity Model Schematic: Length & Width Variations: dimensions in mm

3.2.2 Cavity in a Fuselage

The cavity sits in a ⌀100mm, 505mm long fuselage, mounted to the TS floor with 270° circumference protruding into the TS by 85.4mm, per Fig. 3.8-3.11. The fuselage has three U/S noses; conic, ogive, and parabola, all equal in length and height, to alter the BL. Ogive and parabola profiles are common commercial airliner shapes, while the conic shape is representative of supersonic aircraft. The fuselage is mounted to the cavity floor insert and TS insert per Fig. 3.5. Due to the fuselage curvature, cavity depth varies spanwise with curvature, deviating from the flat cavity model. All parts were 3D printed as Fig. 3.10, with 4mm thick PLA of 0.1mm layer height and 15% infill, treated with acetone and sanded for a smooth finish.

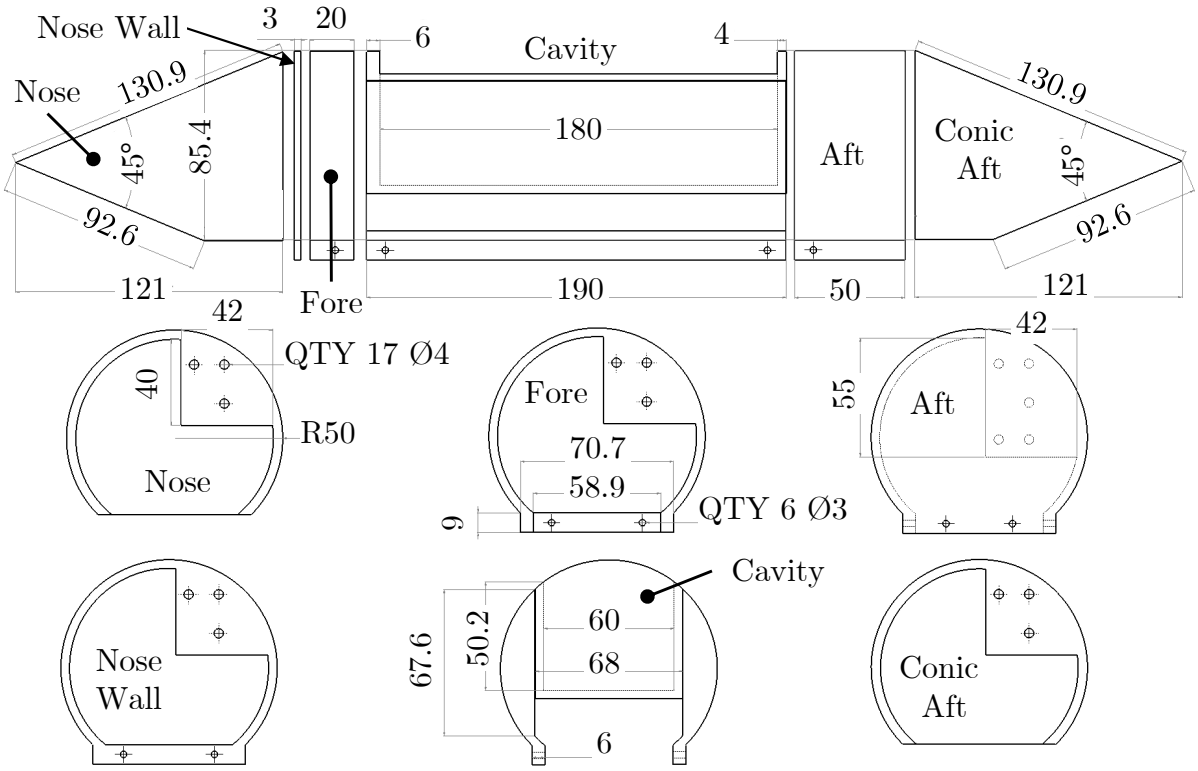

Figure 3.8: Fuselage Cavity Model Schematic: Side and Front Part Drawing: dimensions in mm

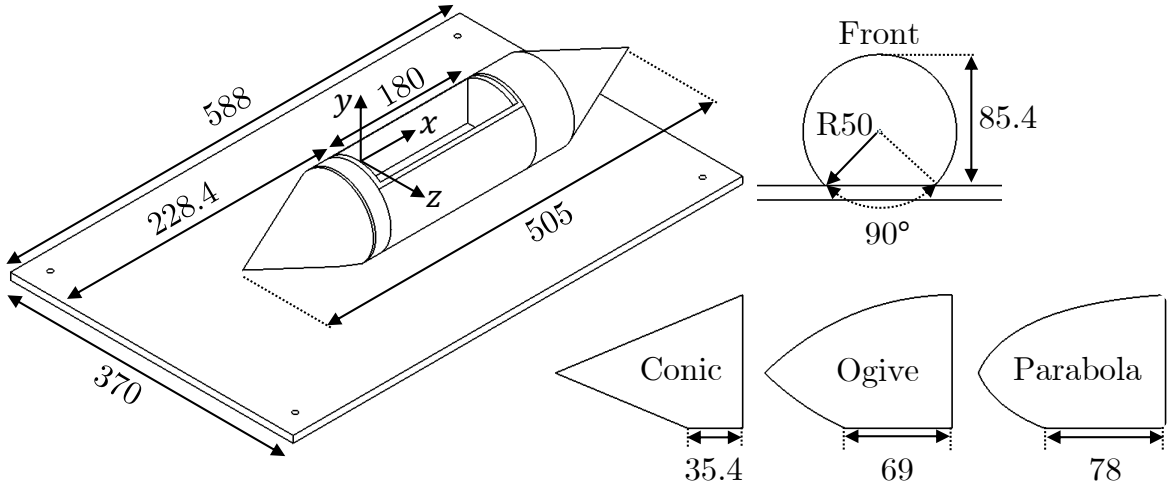

Figure 3.9: Fuselage Cavity Model Schematic: Isometric View with Noses: dimensions in mm

Figure 3.10: Fuselage Cavity Model: 3D Printed Parts

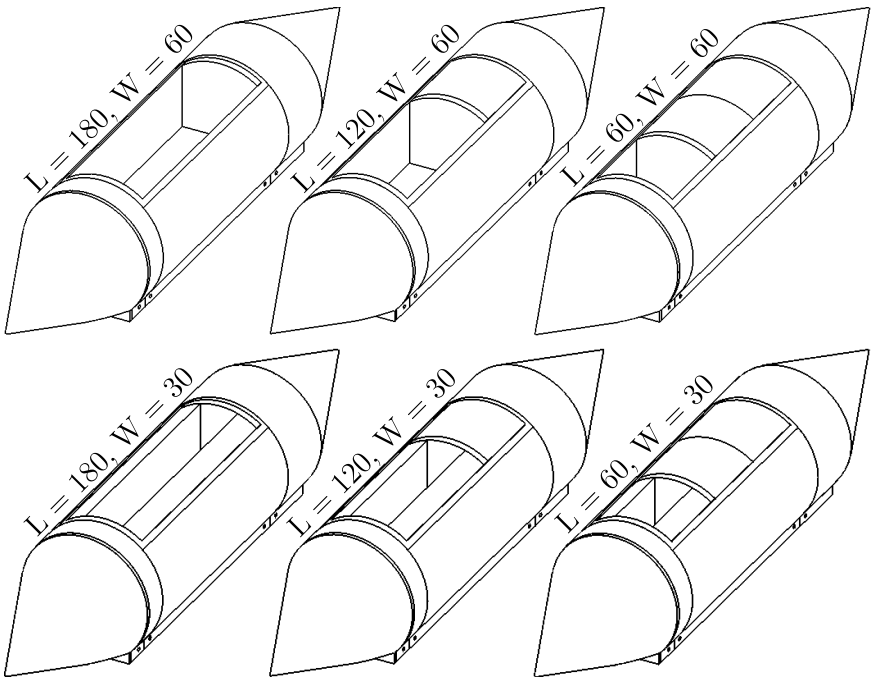

Figure 3.11: Fuselage Cavity Model Schematic: Length & Width Variations: dimensions in mm

3.3 Hot-Wire Anemometry Set-Up

This section outlines the HWA set-up and mount system, used to collate velocity profiles, and generate BL data U/S of the cavity. For further details of the technique, refer [82, 83].

3.3.1 Mount Structure

Per the schematic in Fig. 3.12. The TS roof was supplemented with a cut-out to insert the HWA mount, probe support and probe. The mount is a ⌀12mm steel rod, with an end cut-out, to secure the ⌀4mm probe support with a lock-clip. The probe is attached to the support with a slit in contact-holder, oriented, so the plane faces the probe rear, perpendicular to the support plane, refer Fig. 3.13. The mount is locked to a translation stage outside the TS, with a steel lock-clip, to reduce flow vibration. The translation stage provides range of movement; x = 0-550mm, y = 0-450mm, and $z = \pm$ 100mm, with 0.001mm resolution.

3.3.2 Data Instrumentation

Dantec Dynamics Streamline Pro hardware, constant temperature anemometer (CTA), and StreamWare Pro software were used. The CTA sits in a frame controller, to sustain power and control at bridge ratio 1:1, for long BNC cable interfacing the following components; calibrator, HWA probe via support, and dedicated temperature probe. The controller operates components through USB connection to PC StreamWare Pro software with an Analog-to-Digital (A/D) device. The A/D is operated by an in-house Matlab script, designed to extract BL profiles, by controlling probe position through a 3-axis traverse; ISEL IMC-S8 Step Controller. StreamWare Pro facilitates instantaneous velocity measurement, using the constant temperature method, providing instantaneous CTA voltage E_i output, as a function of current (Amps, A) pulled to maintain constant temperature, by sensor resistance (Ohms, Ω); $E_i = A\Omega$. CTA voltage is

used to calculate velocity using calibration of polynomial derived constants, to determine; mean velocity u_M, turbulent intensity (TI), high order moments and spectra in space.

The Streamline Pro automatic calibrator facilitates in situ velocity alignment, using the probe in a free-jet of known velocity, with a flat low-turbulent profile, connected to the PC via USB for StreamWare Pro control. The probe is a single sensor gold-plated straight wire (P/N: 55P01) with a $\varnothing 5\mu$m, 1.2mm long tungsten wire suspended between two needle prongs, held by a $\varnothing$4mm, 235mm long single sensor right-angle support (P/N: 55H22), connected to the frame with a BNC cable. The A/D is a 4-channel C-series National Instruments (NI) data-acquisition (DAQ) module with; 16-bit resolution, ±10V simultaneous input voltage range, NI Standards & Technology traceable calibration, and 250Vrms channel-earth isolation barrier for safety and noise immunity. Fig. 3.13 and 3.14 provide a schematic and component detail.

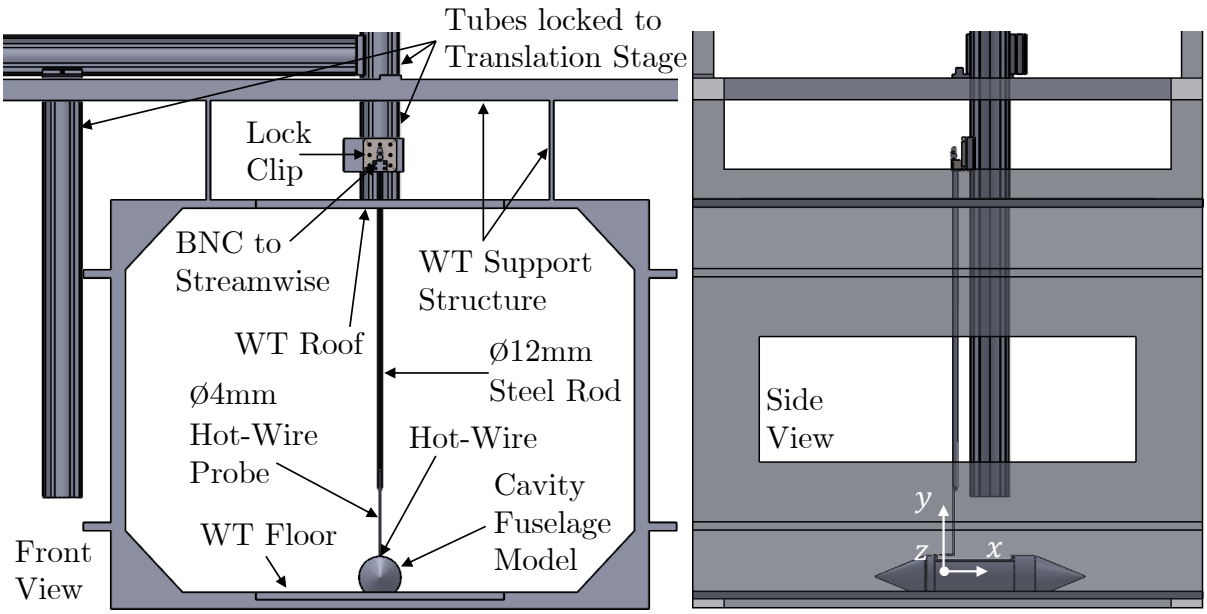

Figure 3.12: HWA: WT TS Set-up

3.3.3 Data Acquisition

The step controller translated the sensor through 30 log distributed points over 270mm in the y-axis (vertical). Log distribution was chosen, to capture the Newtonian BL profile of air developing close to the surface of a structure, which becomes uniform, requiring less spatial coordinates away from the surface. HWA y-axis traverse was performed for the largest cavity geometry; L/D = L/W = 3, in closed and open configuration, at a constant streamwise (x) and spanwise (z) coordinate, centred U/S of the cavity LE CL; x = -5mm, z = 0mm.

Effects of varying U/S geometry, and thus BL profile between the three nose cones and flat baseline case are analysed. Also when the cavity is open versus closed, to quantify feedback effects. Therefore, y-axis traverse of 30 log points was executed for eight cases, thus 240 points, at nine U_∞ = 10-50m/s in 5m/s increments, a total of 2,160 points. This data, is to be mapped against USP from attributed cavity cases at the same airspeeds. An empty WT test was performed to quantify the TS flow quality at an additional nine x, z coordinate test-points along the streamwise CL of the TS, presented in Appendix A.2.

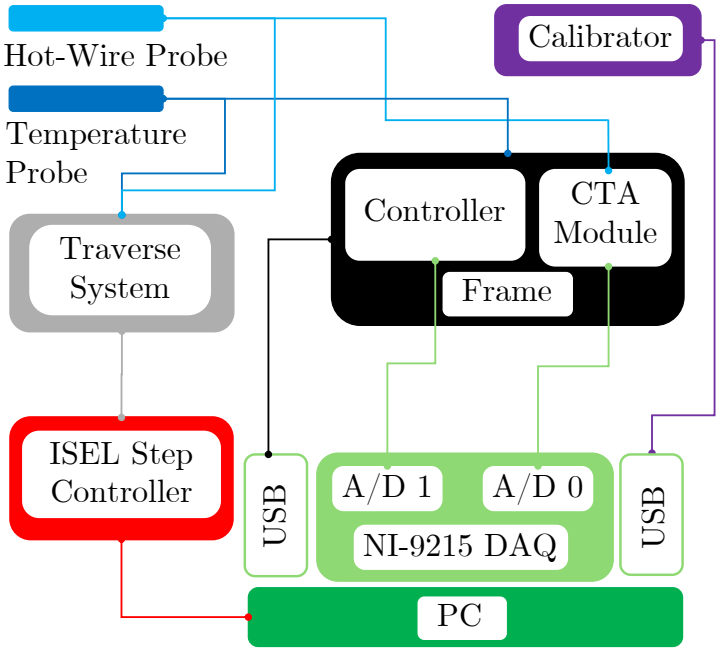

Figure 3.13: HWA: System Diagram

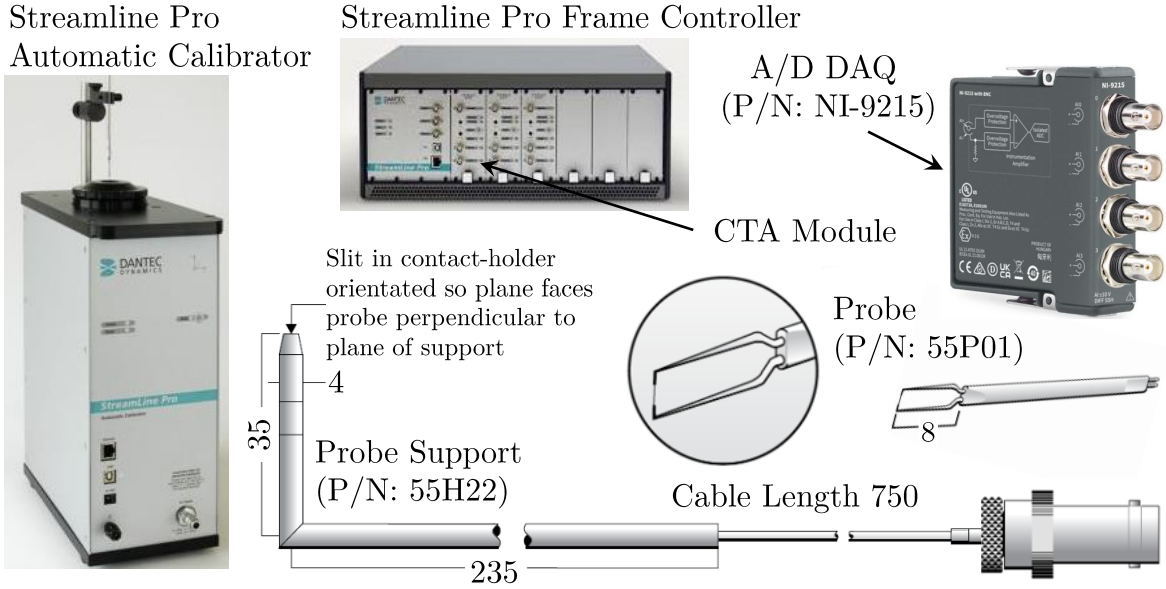

Figure 3.14: HWA: System Components: dimensions in mm

Overheat Adjustment & Signal Conditioning: Dantec Dynamics CTA hardware, which is operated with StreamWare Pro software[84], accounts; signal conditioner offset, and gain for overheat adjustment, with static bridge balancing, and a square wave test for dynamic balancing. The signal conditioner, provides low-pass filtering, and optional gain settings. Overheat adjustment is applied before each vertical traverse, to align sensor working temperature to the constant temperature. The overheat resistor (decade resistor), in the right bridge arm, is also adjusted, to establish the constant sensor operating temperature, when the bridge is operative. Eqn. 3.1 describes the temperature relationship between cold and hot, within the resistors, via overheat ratio a where; R_w is sensor resistance at operating temperature T_w, and R_0 is ambient reference resistance at ambient temperature T_0. Eqn. 3.2 is then used to compute

over-temperature, where α_0 is the sensor temperature coefficient of resistance at T_0. Associated temperatures and coefficients are recorded via the hot-wire and temperature probe for these calculations in StreamWare Pro software[84], with probe lead, support and cable resistances.

Measurement: a script was written to interface the CTA through StreamLine pro, using the NI-DAQ A/D to PC, to record, store data, and control probe movement over a set of spatial coordinates with the traverse. The script establishes a connection, moves the probe to a pre-determined y-axis point, takes a measurement, then moves to the next y-axis point, until all points in the traverse are recorded. Then it increases U_∞, and repeats the traverse.

Each measurement was taken over $t = 60s$, at sample rate $2 \cdot f_{max} = 2^{15}Hz$, based on Nyquist criterion f_{max} of an over sampled time series, for $N = 1.97 \times 10^6$ samples. N was calculated with Eqn. 3.3, where $z_a/2$ is a variable of Gaussian probability function $p(z)$, with standard ISO uncertainty. This gives a typical total systematic and random velocity error of 3.05×10^{-2} m/s. Detail of the error is in Section 4.2.2, and acquisition code is in Appendix F.2.1.

$$a = \frac{\mathrm{R_w} - \mathrm{R_0}}{\mathrm{R_0}} \qquad (3.1) \qquad \mathrm{T_w} - \mathrm{T_0} = \frac{\alpha}{\alpha_0} \qquad (3.2) \qquad N = \left(\frac{z_a \mathrm{TI}}{2u}\right)^2 \qquad (3.3)$$

Sensor Position: a limit was imposed, due to model position and curvature relative to the probe and mount structure, to avoid sensor breakage. The traverse zero position was held constant relative to the WT axis, meaning sensor position relative to the model slightly varied for each geometry. Notably in the flat and parabola U/S case, where the probe sat closer to the surface, enabling more variation, to smaller $y/\delta_{0.99}$, without probe bend or breakage. This variation was not an observable problem. As BL profile variation remained apparent and quantifiable, in response to U/S geometry, and cavity presence.

Moreover, notably in HWA, sensors break, most commonly due to dust particles, or structural interference. Following each instance of breakage, a new-wire was calibrated, installed at the same position with resistance re-aligned, and the traverse redone. Any error due to comparison between sensors, is thus accounted for by re-calibration.

3.4 Unsteady Surface Pressure Set-Up

USP measurements are used to record pressure on internal and external cavity surfaces; cavity walls, the WT floor and fuselage exterior. Pressure taps were installed flush to the model surface at over 500 points. Each connected via plastic tube to a Scanivalve 4264/64Px miniature pressure scanner (MPS)[5], measuring unsteady pressure at 64 points simultaneously, relative to static pressure. Effects of tap presence on the signal are accounted for in Section 4.4.2. A high-density of pressure taps was required, for adequate spatial resolution, to apply dynamic mode decomposition (DMD), that is, decompose the multi-dimensional complex flow into spatio-temporal coherent structures. Root-mean square (RMS) profiles are also assessed for peaks.

3.4.1 Pressure Taps

From Fig. 3.15, each pressure tap is a ⌀1mm hole, accommodating a surface flush 12mm long brass tube of ⌀1mm OD and ⌀0.8mm ID, fixed with epoxy. A 750mm long plastic tube connects

to the brass tube, and runs to an 8mm long Scanivalve port of ⌀1mm OD and ⌀0.8mm ID, fixed with interference fit. Plastic tubes are Saint Gobain Tygon E-3603 (P/N: ACF00001) [85] with ⌀2.4mm OD, and ⌀0.8mm ID, min bend radius 3.2mm and working pressure up to 4.8bar.

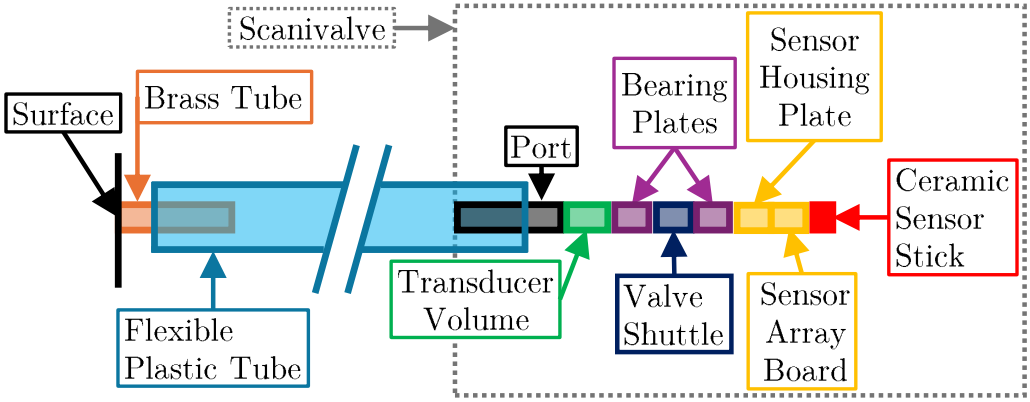

Figure 3.15: USP: System Diagram: Tube Tap connection to Pressure Sensor

Cavity walls were fitted with 258 taps, including LE and TE walls with 75 each, and the floor with 108 taps. Each nose cone had a different number of taps due to geometric installation limits; conic 51 taps, ogive 50 taps, and parabola 46 taps. Between the nose and cavity there is an U/S fuselage section with 12 taps, and between the cavity and TE cone, a D/S section with 30 taps. To vary length to L = 120mm, a 60mm block was installed with 30 taps, and another for L = 60mm with 30 taps. 55 taps are located on a section of WT floor U/S of the model. Taps are 5mm apart spanwise for 6 taps per row from $z = 0 - 30$mm, each row 10mm apart, except on the LE and TE wall with 5mm between rows. Table 3.1 provides a reference for tap identification numbers, Fig. 3.16 shows installation, and Fig. 3.17 surface distribution.

Table 3.1: USP: Pressure Tap Numbers

TE Wall	W60	1-75
	W30	1-3, 5-7, 10-12, 16-18, 22-24, 28-30, 34-36, 40-42, 46-48, 52-54 58-60, 64-66, 70-73
LE Wall	W60	184-258
	W30	184-186, 188-190, 193-195, 199-201, 205-207, 211-213, 217-219, 223-225, 229-231, 235-237, 241-243, 247-249, 253-255
Floor	W60	L180: 76-183, L120: 112-183, L60: 148-183
	W30	L180: 76-78, 82-84, 88-90, 94-96, 100-102, 106-108, 112-114, 118-120, 124-126, 130-132, 136-138, 142-144, 148-150, 154-156, 160-162, 166-168, 172-174, 178-182
		L120: 112-114, 118-120, 124-126, 130-132, 136-138, 142-144, 148-150, 154-156, 160-162, 166-168, 172-174, 178-182
		L60: 148-150, 154-156, 160-162, 166-168, 172-174, 178-182
Length Block		Aft: 506-535, Fore: 536-565
Fuselage		U/S: 259-270, D/S: 271-300
Nose		Ogive: 301-351, Parabola: 352-397, Conic: 403-447
Tunnel Floor		448-505

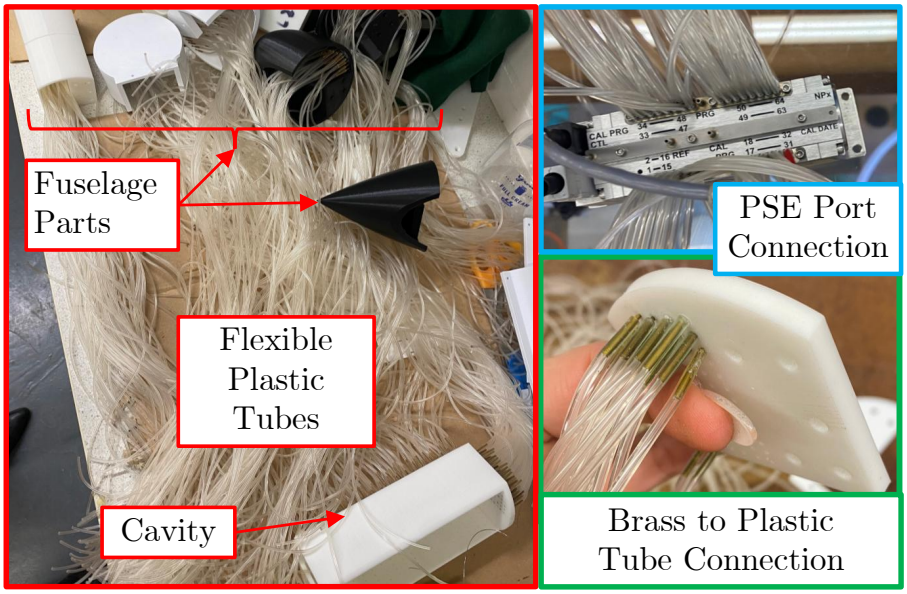

Figure 3.16: USP: Pressure Tap Components

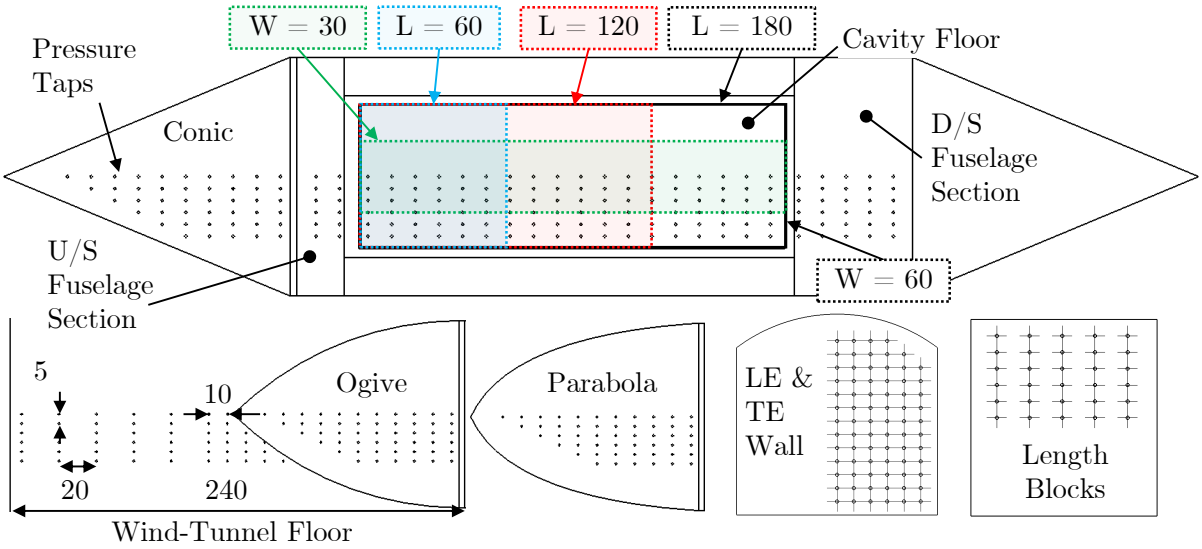

Figure 3.17: USP: Surface Pressure Tap Distribution, all dimensions in mm

3.4.2 Data Acquisition and Instrumentation

The Scanivalve MPS4264/64Px[5] in Fig. 3.18, is a 64 port miniature pressure sensor (MPS) DAQ system, using low current DC power (9-36Vdc), and Ethernet connection to PC, to initiate measurement, record and store data. Fig. 3.19 presents the assembly drawing with tube and transducer volumes. MPS accuracy reduces for scan rates above 500Hz[86]. Therefore, as error negation was a priority, and the phenomena was expected below 250Hz, $f = 500$Hz was sufficient, based on Nyquist theory[87]. Scan time was alternated, to select an adequate sampling rate, and difference in spectra for t = 10-20s at 500Hz was negligible, thus $t = 10s$ was chosen. Data was thus extracted at $f = 500$Hz, over $t = 10s$ for $N = 5000$ samples, giving an output; time vector, temporal pressure array, averaged, max and min with standard deviation. Several MPS were used simultaneously to extract data at all points. Each case scanned three times, and analysed for robustness. Error due to the set-up is detailed and corrected in Section 4.4.2.

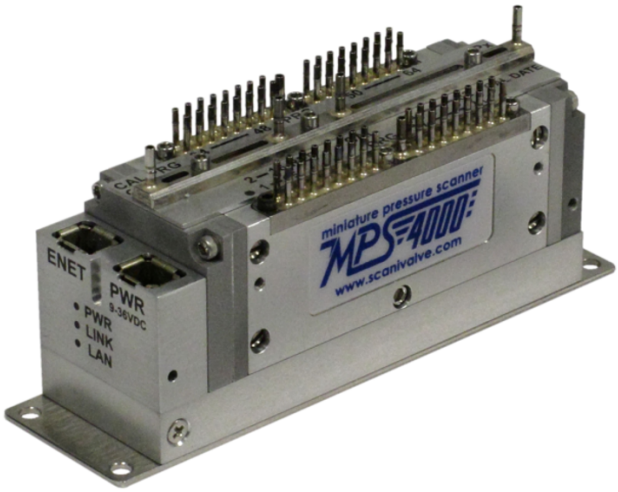

Figure 3.18: USP: Scanivalve 4264/64Px MPS [5]

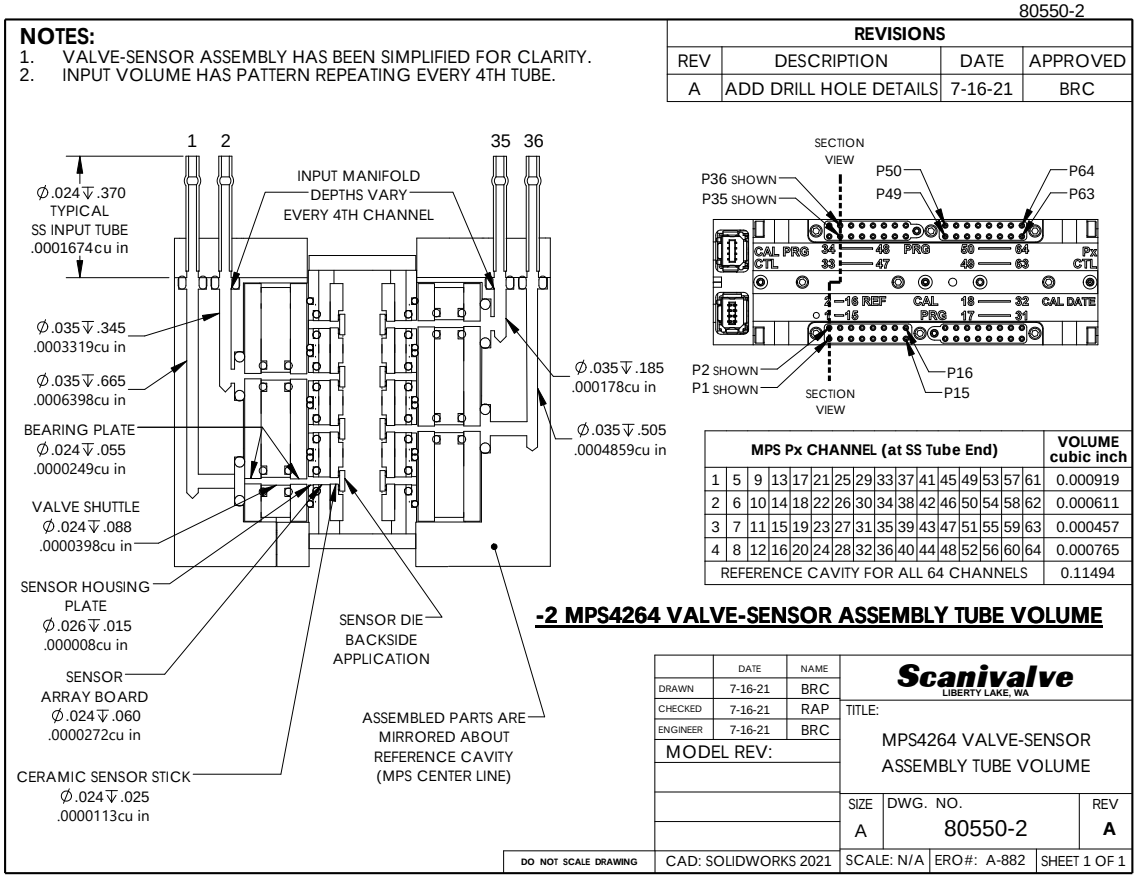

Figure 3.19: USP: Scanivalve 4264/64Px MPS Sensor Assembly with Tube Volume [5]

Chapter 4

Data Processing & Analysis

This chapter details post-processing of raw experimental data, including; calibration, conversion, reduction, uncertainty and error analysis of the model and equipment. Wind-tunnel corrections are presented. Followed by a detailed prescription of boundary layer (BL) theory [23,88], to support BL reconstruction methods from hot-wire anemometry (HWA), which on integration with cavity flow prediction, is a significant part of this thesis. Further, unsteady surface pressure (USP) correction for coefficients, spectra, and dynamic mode decomposition (DMD) is provided.

4.1 Wind Tunnel Corrections

Data correction due to model and equipment design, size, and position in the wind tunnel (WT), are considered, including WT wall interference, blockage and buoyancy. Streamline curvature, down/up-wash, force and moment corrections are not required, due to the type of data recorded and model design. Sting correction for HWA structures is covered by blockage. HWA specific data correction and uncertainty is in Section 4.2.2, and USP in Section 4.4.2.

4.1.1 Airspeed

To confirm airspeed, values recorded by the WT indicator, were compared to pitot-tube, and HWA jet-calibrated recordings in the WT test-section (TS). Pitot and HWA values agreed within negligible error of ± 0.1m/s. However, the WT airspeed indicator had poor resolution and deviated by $\pm 2 - 8$m/s, thus indicator control points were calibrated by a separate pitot, which was used in USP, and HWA recordings, to ensure alignment, with adjusted WT indicator values. Airspeed deviations from set control points were recorded, and accounted through statistical and uncertainty analysis in Section 4.2.1 and 4.2.2 respectively. This occurs as WT air heats up, and structure expands with use during the day. For redundancy, changes in ambient conditions were recorded to non-dimensionalise results for comparative analysis.

4.1.2 Wall Interference

Considering WT boundaries relative to model location and size, wall interference is considered negligible per [89]. Buoyancy effects are accounted with HWA BL data, with and without the model present. Solid and wake blockage per Section 4.1.3 are also considered negligible.

For cavity oscillation, Wagner et al[90] studied mitigation of WT wall interactions in subsonic cavity flow experiments, and quantified the effect. They discovered, that WT amplified cavity perturbations coupled to WT modes, produced feedback and spanwise flow. However, the effect reduced with increasing distance and size of the cavity, with respect to the wall. McGregor & White[91] provided a reduction scale, assigning a limit on cavity length to avoid amplification: "if h/L > 5, h = tunnel height, and L = cavity length, wall interference is negligible". TS height is h = 914.4mm, and max cavity L = 180mm, for h/L = 5.08 > 5. Moreover, the fuselage was located floor centre line (CL), with edge distance to side walls of $\approx 6d$ (d = cylinder diameter), and $\approx 8.8d$ to the ceiling. Therefore, due to model size relative to TS height and distance from walls, wall interference on the cavity flow phenomena is considered negligible.

4.1.3 Blockage

2D Solid Blockage is considered, based on a 2D finite ratio of frontal model frontal to TS area, which is zero during true operation. The ratio assumes no change in distribution of surface stress, which is valid for a blockage ratio of < 10%, and it is customary to have < 5% per [92].

Per Fig. 4.1, accounting TS dimensions (1.22 × 0.914)m, and octagonal protrusions; TS area $A_{TS} = 1.08m^2$. The flat cavity model is in the TS floor, producing no blockage. The fuselage model, protrudes into the TS, with diameter $d = 100$mm and circumference 270°, giving model frontal area $A_{fuselage} = 0.007m^2$. The HWA support is a ⌀12mm mount rod and ⌀4mm probe support, for total area; $A_M + A_{PS} = 0.0086m^2$. Therefore, the set-up blockage ration for USP is 0.007/1.08 = +0.67%, and HWA is 0.016/1.08 = +1.5%, which is considered negligible.

3D Solid Blockage is considered for a streamline body of revolution alike the fuselage model, using Eqn. 4.1, as a function of; fuselage model body volume V_{body}, diameter d, length l, and shape factor K_3, with tunnel shape factor τ_1, TS area A_{TS}, model to WT breadth ratio; B_{body}/B_{WT}, and WT breadth to height ratio; B/H_{WT}.

For USP set-up, per Fig. 10.2 in [93], with fuselage $d/l = 100/505 = 0.198$; $K_3 = 0.946$. Per Fig. 10.3 in [93], with TS octagonal shape; $W_{body}/W_{WT} = 0.100/(1.22 - 2 \times 0.15) = 0.108$ and $B/H_{WT} = (1.22 - 2 \times 0.15)/(0.91 - 2 \times 0.14) = 1.45$; $\tau_1 = 0.87$. Lastly, fuselage $V_{body} = \pi r^2 l = 0.004m^3$ and $A_{TS} = 1.08m^2$. Therefore, $\varepsilon_{sb} = +0.3\% << 5\%$, which is considered negligible.

For HWA set-up, the support strut is also accounted. Per Fig. 10.2 in [93], for $d/l < 0.04$; $K_3 = 0.885$. Per Fig. 10.3 in [93], with TS octagonal shape; $W_{body}/W_{WT} = 0.012/(1.22 - 2 \times 0.15) = 0.013$ and $B/H_{WT} = 1.45$; $\tau_1 = 0.87$. Lastly, with $V_{body} = \pi r^2 l = 0.00008m^3$ and $A_{TS} = 1.08m^2$; $\varepsilon_{sb} = +0.005\% << 5\%$, which is even lower for the real model, as probe and support assumed ⌀12mm. Therefore, $\varepsilon_{sb} = +0.305\%$, which is considered negligible.

Wake Blockage accounts change in the flow-field due to presence of the wake, behind a solid object. The fuselage model was designed with a back facing conic section on the end, to decelerate flow, reduce drag, thus wake, and its blockage effects. To support this, Maskell's check method[94] is applied, referencing Eqn. 4.2[93], where C_{d_u} is uncorrected drag coefficient.

For the USP set-up, with fuselage frontal area $A_{fuselage} = 0.007m^2$ in Fig. 4.1, modelled as a cylinder perpendicular to the flow with $l/d = 505/100 = 5.05$ and a conic nose with $C_{d_u} = 0.47$

(worst case) per Fig.34 in [95] (half-vertex angle 22.45°, Eiffel type). Per Fig. 21 in [95], wake blockage is $\varepsilon_{wb} = +0.076\%$, which does not account further streamline factors to reduce C_d, thus wake blockage is negligible. For the HWA set-up, the support strut is also accounted, as a curved cylindrical face perpendicular to flow for; $C_d = 1.2$, and $\mathrm{Re_D} = 10^3 - 10^4$, per Fig. 1 of [96]. Thence, for HWA support area $\mathrm{A_M} + \mathrm{A_{PS}} = 0.0086$ per Fig. 4.1; $\varepsilon_{wb_{M-PS}} = +0.24\%$, for total wake blockage $\varepsilon_{wb_{HW}} = \varepsilon_{wb} + \varepsilon_{wb_{M-PS}} = +0.3\%$, which is considered negligible.

$$\varepsilon_{sb} = \frac{\mathrm{K_3 \tau_1 V_{body}}}{\mathrm{A_{TS}}^{3/2}} \qquad (4.1)$$

$$\varepsilon_{wb} = \frac{\Delta \mathrm{U}}{\mathrm{U_u}} = \frac{\mathrm{A_{model}} C_d}{4\mathrm{A_{TS}}} \qquad (4.2)$$

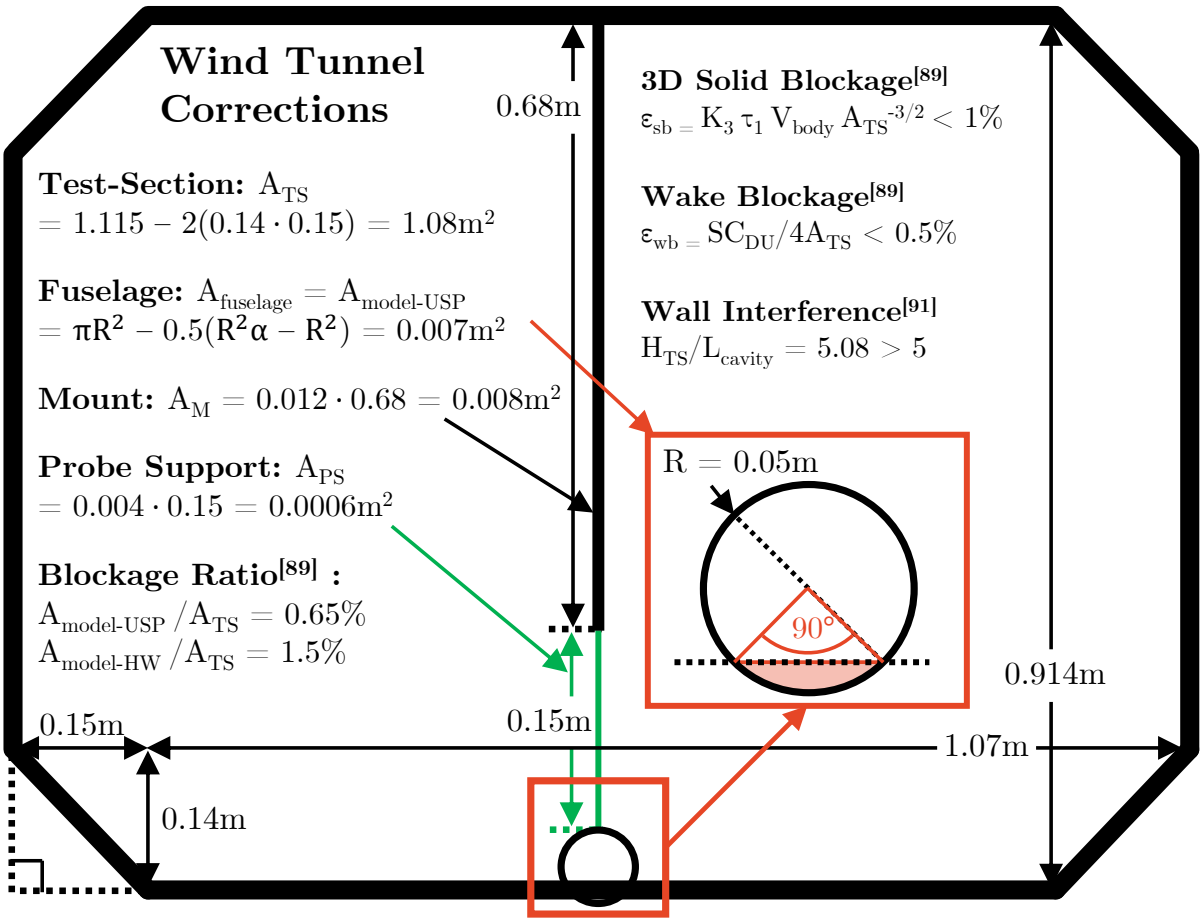

Figure 4.1: Wind Tunnel Corrections

4.2 Hot-Wire Anemometry

This section details methodology used to formulate, and transform HWA results into BL metrics, to build logical velocity profiles upstream (U/S) of the cavity. Qualitative assessment identifies areas for quantitative integration, and assessment, by aligning characteristics of cavity response, from USP, to the U/S BL profile per Prandtl[88] and Goldstein[23].

This approach allows for more accurate cavity response prediction, based on the BL and its pressure gradient dp/dx. Feedback U/S is also assessed, by comparing BL structures on the same model, when the cavity is open versus closed. These methods allow for assessment of shear layer (SL) disturbance nearby[2,97], and mapping of modal behaviour in the BL, thus SL.

4.2.1 Data Calibration, Conversion and Statistics

The Dantec Dynamics [84] automatic calibrator, exposes the HWA sensor to a free-jet of known velocities u_i, while measuring voltage E_i, and tracking temperature, of the constant temperature anemometer (CTA). A 4$^{\text{th}}$ order polynomial transfer function is then established in Eqn. 4.3, to convert measured E_i, into calibrated velocity u_i, where $\mathrm{C}_0 - \mathrm{C}_4$ are calibration coefficients, for linearisation error $< 1\%$. Experimental velocities are $\mathrm{U}_\infty = 10 - 50\mathrm{m/s}$, therefore calibration velocities per $\mathrm{U}_\infty = 0.1\mathrm{U}_{\infty,\min} - 1.5\mathrm{U}_{\infty,\max}$ [82] are $\mathrm{U}_{\text{cal}} = 1 - 75\mathrm{m/s}$ with 100 interval points.

$$u_i = \mathrm{C}_0 + \mathrm{C}_1 E_i + \mathrm{C}_2 E_i^2 + \mathrm{C}_3 E_i^3 + \mathrm{C}_4 E_i^4 \tag{4.3}$$

Pre- and post-calibration was executed, with correction for sensor drift per Talluru et al [98]. Voltage re-scaling was unrequired, as signal conditioner gain, and offset were unrequired under equipment condition. Temperature correction was also unrequired as overheat adjustments were made. The array of N samples of u_i, is thus processed for mean velocity (u_m), standard deviation (u_{sd}) and turbulence intensity (TI) in Eqn. 4.4, 4.5 and 4.6 respectively, with computer time variance (σ) in Eqn. 4.7, which is used to calculate measurement flow statistics following.

$$u_m = \frac{1}{N}\sum_{1}^{N} u_i \tag{4.4}$$

$$u_{sd} = \sqrt{\frac{1}{N-1}\sum_{1}^{N}(u_i - u_m)^2} \tag{4.5}$$

$$\mathrm{TI}\,(\%) = \frac{u_{sd}}{u_m} \tag{4.6}$$

$$\sigma = \sqrt{\sum_{1}^{N}\frac{(u_i - u_m)^2}{N-1}} \tag{4.7}$$

Skewness (S), the lack of flow symmetry in Eqn. 4.8, and kurtosis (K), the amplitude flatness causing distortion in Eqn. 4.9, are given in Fig. 4.2-4.5. For noses, values are large in the near wall accelerated flow region, due a favourable pressure gradient $dp/dx < 0$, then becomes uniform. The flat case is uniform, except at BL to free-stream (FS) transition, due to a change in viscosity, which is small in nose cases compared to dp/dx [23]. Overall, $dp/dx < 0$ and viscosity effects increase statistical uncertainty, as expected per Chapter 8 of [83], and theory per [99].

$$S = \sum_{1}^{N}\frac{(u_i - u_m)^3}{N\sigma^3} \tag{4.8}$$

$$K = \sum_{1}^{N}\frac{(u_i - u_m)^4}{N\sigma^4} \tag{4.9}$$

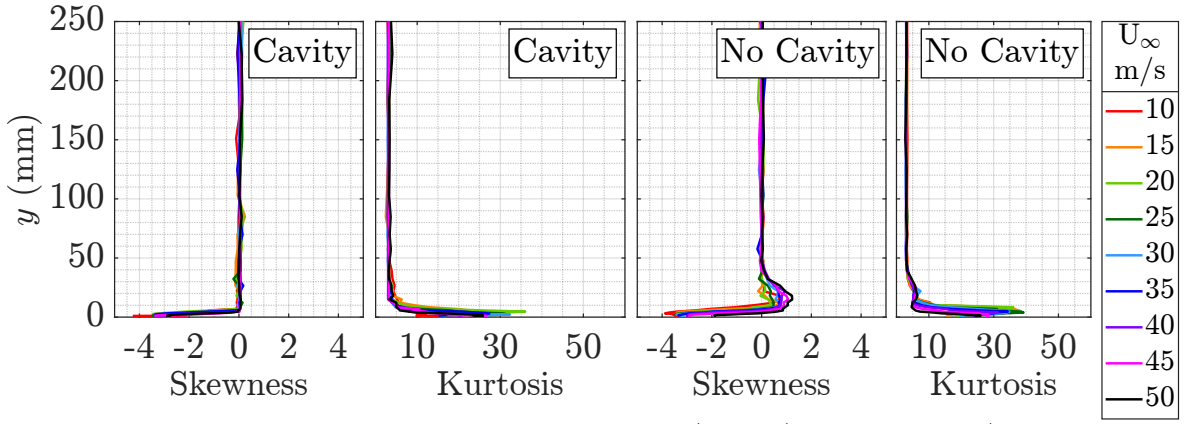

Figure 4.2: HWA: Skewness & Kurtosis of C5: L/D = L/W = 3, Conic U/S, $\Delta\mathrm{U}_\infty$

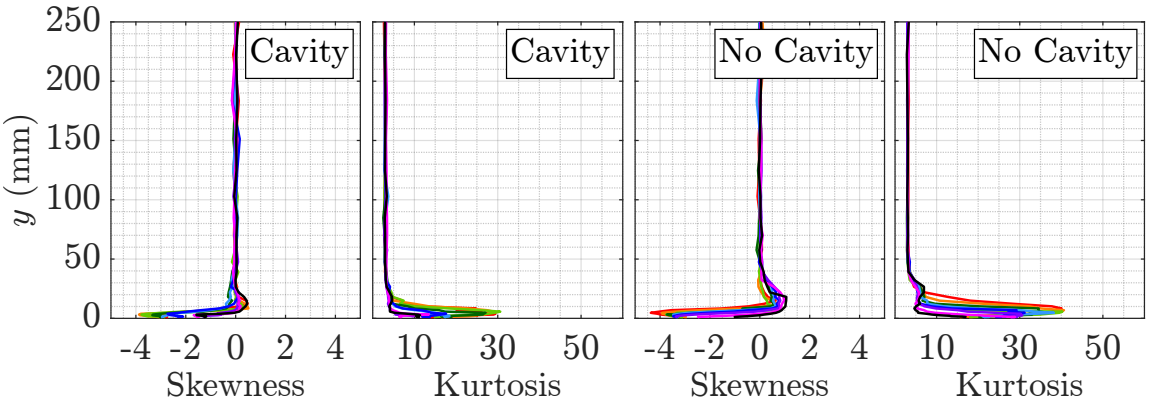

Figure 4.3: HWA: Skewness & Kurtosis of C11: L/D = L/W = 3, Ogive U/S, ΔU_∞

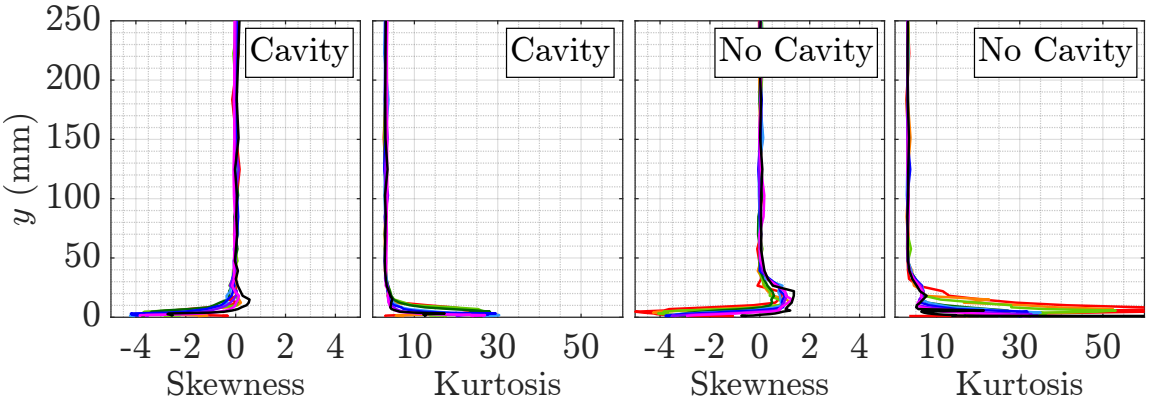

Figure 4.4: HWA: Skewness & Kurtosis of C17: L/D = L/W = 3, Parabola U/S, ΔU_∞

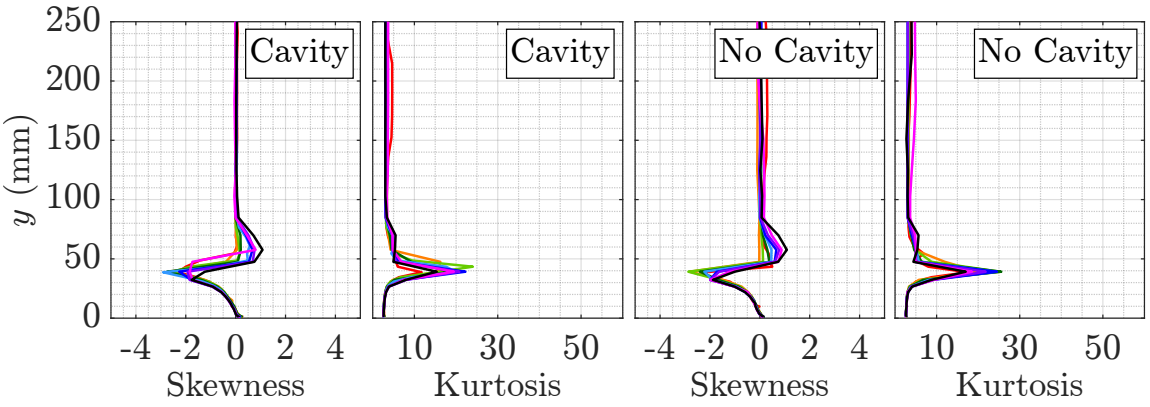

Figure 4.5: HWA: Skewness & Kurtosis of C23: L/D = L/W = 3, Flat U/S, ΔU_∞

Autocorrelation function $\rho_x(\tau_i)$ was defined per Eqn. 4.10 for each measurement. Results trended per Fig. 4.6, with $\rho_x(\tau_i) = 1$ at t = 0s, then converging toward zero. In the near wall region, $\rho_x(\tau_i)$ oscillates toward zero, remaining positively correlated near $\rho_x(\tau_i) \sim 0 - 0.1$. This indicates an increase in time interval, thus proportionate increase in lag. Therefore, data is clustered with narrow confidence, for a higher probability of convergence, which is per expectation of turbulent HWA measurement using Dantec Dynamics CTA hardware [82].

Integral time scale τ_i (ITS) is the integral of autocorrelation function $\rho_x(\tau_i)$, for each fluctuating velocity measurement in time, per Eqn. 4.11. It is the sum of correlation between the signal, at different time lags, that is, time taken for correlation to decay. ITS is thus a time interval between statistically uncorrelated samples, or correlation distance of a process in time [100].

Large ITS indicates persistent large-scale turbulent structures, with slower dynamic decay. The structure correlates with its past position and behaviour, and is the most energetic, and significant contribution to overall turbulent mixing. I.e., very low Reynolds flow, which are fully reversible, and correlate with past particle position, have large τ_i. Small ITS indicated quick decay of $\rho_x(\tau_i)$, thus flow rapidly loses correlation to its past. This is characteristic of highly turbulent flow, where small eddies dominate, rapidly changing direction, and losing memory of their past, typically in high-shear or high-energy flow. Results are in Section 5.1.4.

$$\rho_x(\tau_i) = \frac{R_x(\tau_i)}{R_x(0)} \rightarrow R_x = \lim_{T\to\infty} \frac{1}{T} \int_0^T x(t)x(t+\tau_i)dt \quad (4.10) \qquad \text{ITS} = \int_0^\infty \rho_x(\tau_i)d\tau_i \quad (4.11)$$

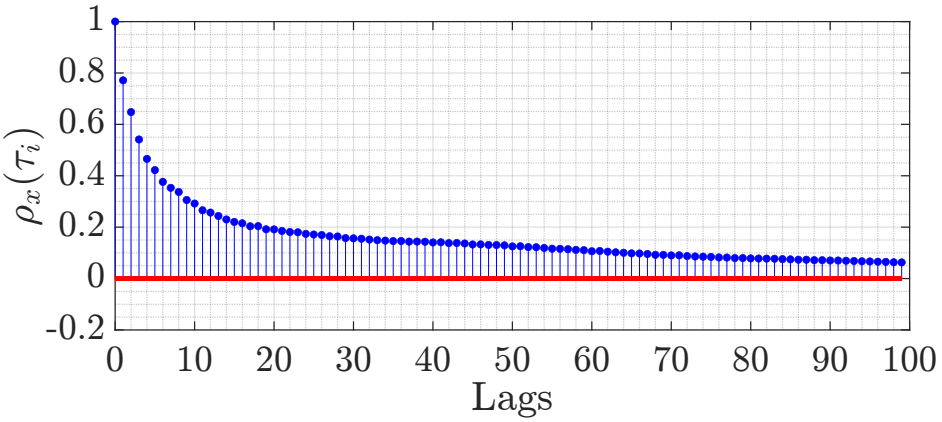

Figure 4.6: HWA: Auto-Correlation of C5: L/D = L/W = 3, Conic U/S, y = 2mm, U_∞ = 50m/s

4.2.2 Data Error and Uncertainty

A standard Gaussian error distribution of 95% confidence level was used, for standard velocity uncertainty contributions $u_i(y_i)$ in Eqn. 4.12 of; velocity sample, acquisition and experimental conditions, calculated below, with coverage factor $k_i = 1.96$, and sensitivity factor $\partial y_i/\partial x_i$, accounted by summation in Eqn. 4.13. Table 4.1 presents the max for each contribution, Fig. 4.7 is an example of the negligible deviation, and the algorithm is in Appendix F.2.2.

$$u_i(y_i) = \frac{\partial y_i}{\partial x_i} \frac{1}{y_i} \frac{\Delta x_i}{k_i} \quad (4.12) \qquad u_{i,tot} = 2\sqrt{\sum u_i(y_i)^2} \quad (4.13)$$

Velocity Sample Uncertainty of the sensor considers; drift, noise, repeatability, and frequency response. The sensor has high repeatability, with negligible drift and noise, compared to other error. Frequency response added no uncertainty, as test frequencies were $\lessapprox$ 50% of cut-off, and the characteristic deviation is flat up to this point, per square wave testing.

Calibration was the primary uncertainty, with an error stochastic in nature of normal distribution, and relative standard deviation per Eqn. 4.14, where; $\text{SD}(u_{i,cal,\%}) = \pm a_{cal} + b_{cal}$, given test velocities are $>$ 5m/s ($b_{cal} = 0$), and a Dantec calibrator was used for; $\text{SD}(u_{i,cal}) = 1\%$, thus $u_{i,cal} = 0.01$. Linearisation or conversion error, using the transfer function in Eqn. 4.3, requires addition of the error in Eqn. 4.15, a stochastic curve fit of normal distribution, where $\Delta u_{i,lin}$ is standard deviation of the curve fit in calibration points.

$$u_{i,cal} = 0.01 \cdot \text{SD}(u_{i,cal}(\%)) \quad (4.14) \qquad u_{i,lin} = 0.01 \cdot \text{SD}(\Delta u_{i,lin}(\%)) \quad (4.15)$$

Acquisition Uncertainty accounts for A/D device resolution, which is stochastic of relative standard square distribution per Eqn. 4.16; $E_{AD} = \pm 10\text{V}$ is A/D input range, $n = 16$ is bit resolution, u is velocity and $\partial u/\partial E = 46.5$ is slope sensitivity of calibration curve $u = f(E)$ [82].

$$u_{i,res} = \frac{E_{AD}}{2^n u\sqrt{3}} \frac{\partial u}{\partial E} \tag{4.16}$$

Experimental Condition Uncertainty accounts probe set-up after calibration, a stochastic square distribution of relative standard uncertainty per Eqn. 4.17, $\theta_i = 1^\circ$ [82]. Also change in temperature ΔT, between calibration, and velocity measurements, altering sensor over-temperature, of relative standard stochastic regular distribution per Eqn. 4.18. An estimate based on the calibration function in Eqn. 4.19, where $\Delta T = T_w - T_0$ is the difference between sensor and ambient temperature, and ρU is mass flux, represented by $u_{i,cal}$.

Fluid density $\Delta\rho_\infty$ adds relative standard uncertainty in Eqn. 4.20. Ambient pressure influences fluid density thence velocity u, contributing stochastically with rectangular distribution per Eqn. 4.21. Fluid humidity, is a stochastic rectangular distribution per Eqn. 4.22, where influence of heat transfer is small: $\partial u/\partial P_{wv} \approx 0.01 \cdot \text{U}$ per 1kPa, and p_{wv} is water vapour pressure.

$$u_{i,pos} = \frac{1 - \cos(\theta_i)}{\sqrt{3}} \tag{4.17}$$

$$u_{i,temp} = \frac{1}{U\Delta T\sqrt{3}} \sqrt{\frac{A}{B\sqrt{U}} + 1} \tag{4.18}$$

$$E^2 = \Delta\text{T}(\text{A} + \text{B}_1\sqrt{\rho\text{U}}) \tag{4.19}$$

$$u_{i,den} = \frac{\Delta\rho_T}{\sqrt{3}} = \frac{\Delta\text{T}}{273\sqrt{3}} \tag{4.20}$$

$$u_{i,pre} = \frac{1}{\sqrt{3}} \left(\frac{p_0}{p_0 + \Delta p} \right) \tag{4.21}$$

$$u_{i,hum} = \frac{\Delta p_{wv}}{\text{U}\sqrt{3}} \frac{\partial \text{U}}{\partial p_{wv}} \tag{4.22}$$

Table 4.1: HWA: Maximum Uncertainty Values ($\times 10^{-4}$ m/s)

$u_{i,cal}$	$u_{i,lin}$	$u_{i,res}$	$u_{i,pos}$	$u_{i,tem}$	$u_{i,den}$	$u_{i,pre}$	$u_{i,hum}$	$u_{i,tot}$
1	1.4	6.9	0.88	43	36.6	57.7	0.58	305

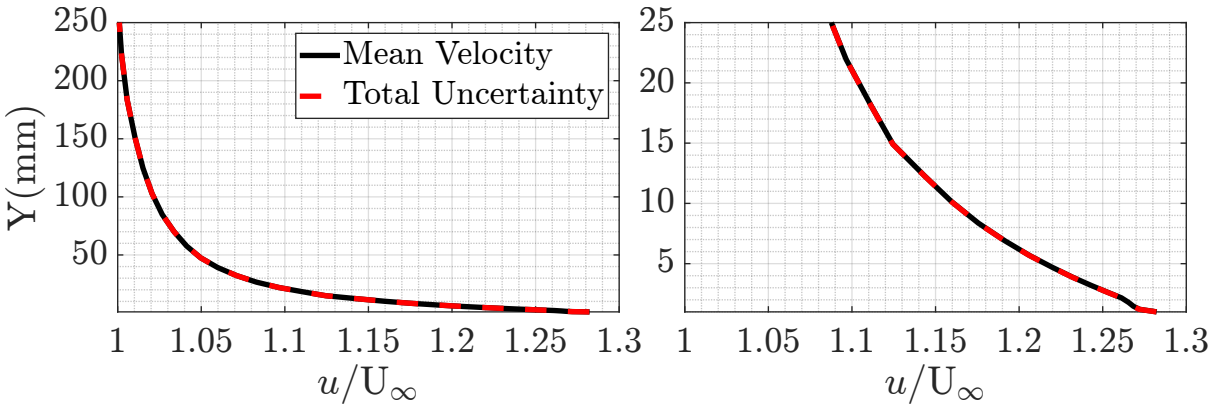

Figure 4.7: HWA: Uncertainty based on Table 4.1

4.3 Boundary Layer Data

This section covers methods used to resolve the BL and its thickness δ, displacement δ^*, and momentum θ, for each U/S geometry from HWA, and BL theory, where HWA cannot entirely resolve the BL, in axisymmetric nose cases. The flat-plate follows the 1/7th power law [101]. The conic nose is modelled with Falkner-Skan's [22] wedge solution. Ogive and parabola noses are modelled with Murphy's [7] extended Falkner-Skan solution, using Goldstein's [23] curved incompressible Navier-Stokes (NS) equations. Further detail is provided in Appendix F.2.4.

4.3.1 Boundary Layer Flow over a Flat-Plate

For a laminar BL over a flat-plate of length x, inertia $\rho u(\partial u/\partial x)$ becomes $\rho \mathrm{U}_\infty^2/x$ as; $\partial u/\partial x \propto \mathrm{U}_\infty/x$, and friction; $\mu \mathrm{U}_\infty/\delta^2$ define δ per Eqn. 4.23. For a turbulent BL, transition at $\mathrm{Re}_{x,\mathrm{crit}} = 5\times10^5$, from a laminar BL is considered [102] in Eqn. 4.24 as; $\partial u/\partial x \not\propto \mathrm{U}_\infty/x$. Transition induces large δ and wall shear stress τ_w increase. Eqn. 4.24 holds true if flow is turbulent at the plate LE, with virtual origin $\mathrm{Re}_x = 1.5 \times 10^5$ to transition at 3×10^5 for $\mathrm{Re}_{x,\mathrm{crit}} \approx 5 \times 10^5$ [99,103]. A schematic of laminar to turbulent flat-plate BL flow, is given below Fig. 4.8.

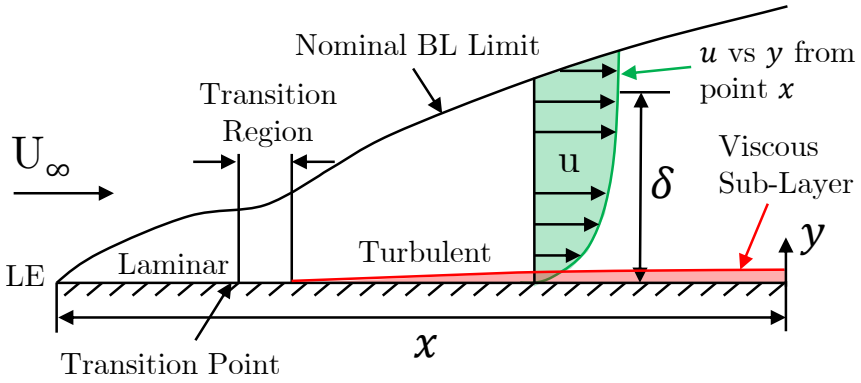

Figure 4.8: HWA: Boundary Layer Schematic

Using HWA data, the BL of interest was measured 5mm U/S of the cavity LE, which is 1.76m from the WT TS LE. The BL thickness δ, is located at $+y$ in the HWA velocity profile at this x point, where $u/\mathrm{U}_\infty = 0.99$. Flat-plate displacement δ^* and momentum θ thickness are then calculated by integrating u/U_∞ per Eqn. 4.25 and 4.26. Trapezoidal integration is used, representing fluid displaced δ^* or mass lost, and fluid momentum θ, or integral mass lost. Wall shear stress is derived; $\tau_w = \mu(du/dy)$ per the algorithm in Appendix F.2.6.

Table 4.2 presents flat-plate BL data, with Re_x from the TS LE. Fig. 4.9 compares δ^* and θ from HWA, to Blasius's [21] laminar flat-plate solution in Eqn. 4.27-4.28 (See Appendix B.2.1), and the $1/7^{\mathrm{th}}$ turbulent power law [99] in Eqn. 4.29-4.30. These results indicate a turbulent BL, as $\mathrm{Re}_x > \mathrm{Re}_{x,\mathrm{crit}} = 5 \times 10^5$, and δ^*, θ align with the $1/7^{\mathrm{th}}$ turbulent power law. Moreover, as U_∞ increases, τ_w increases, and δ reduces, as expected. τ_w also increases, as δ reduces, when the cavity is open downstream (D/S). Appendix B provides further theory, and F.2.3 the algorithm.

$$\rho u\frac{\partial u}{\partial x} = \frac{\partial \tau_w}{\partial y} \quad \rightarrow \quad \rho \mathrm{U}_\infty \frac{\mathrm{U}_\infty}{x} = \mu\frac{\partial^2 u}{\partial y^2} \quad \rightarrow \quad \frac{\rho \mathrm{U}_\infty^2}{x} = \frac{\mu \mathrm{U}_\infty}{\delta^2} \quad \rightarrow \quad \delta \sim \sqrt{\frac{\nu x}{\mathrm{U}_\infty}} \tag{4.23}$$

$$\frac{\delta \mathrm{U}_\infty}{\nu} = 0.14\frac{\mathrm{Re_x}}{\ln \mathrm{Re_x}} G\left(\ln \mathrm{Re_x}\right) \quad \rightarrow \quad \delta \sim 5.29\sqrt{\frac{\nu x}{\mathrm{U}_\infty}} \tag{4.24}$$

$$\delta^* = \int_0^\delta \left(1 - \frac{u}{\mathrm{U}_\infty}\right) dy \qquad (4.25) \qquad \theta = \int_0^\delta \frac{u}{\mathrm{U}_\infty}\left(1 - \frac{u}{\mathrm{U}_\infty}\right) dy \qquad (4.26)$$

$$\delta^*_{Blasius} = 1.7209\sqrt{\frac{\nu x}{\mathrm{U}_\infty}} \qquad (4.27) \qquad \theta_{Blasius} = 0.664\sqrt{\frac{\nu x}{\mathrm{U}_\infty}} \qquad (4.28)$$

$$\delta^*_{1/7^{th}} = \delta/8 \qquad (4.29) \qquad \theta_{1/7^{th}} = 7\delta/72 \qquad (4.30)$$

Table 4.2: HWA: Flat-Plate Boundary Layer Data

U_∞(m/s)	10	15	20	25	30	35	40	45	50
$\mathrm{Re}_x(10^6)$	1.1	1.6	2.2	2.7	3.2	3.7	4.3	4.7	5.2
Flat-Plate Baseline U/S, Cavity Open									
δ (mm)	35.8	34.7	33.9	32.8	32.0	30.3	29.1	28.1	27.9
δ^*(mm)	5.8	5.5	5.3	5.0	4.8	4.6	4.5	4.1	3.8
θ (mm)	3.9	3.7	3.6	3.5	3.3	3.0	2.7	2.6	2.5
τ_w (Pa)	0.038	0.069	0.114	0.155	0.198	0.250	0.300	0.370	0.409
Flat-Plate Baseline U/S, Cavity Closed									
δ (mm)	38.6	37.3	36.2	35.8	34.8	33.9	32.1	31.1	30.1
δ^*(mm)	6.1	5.9	5.5	5.3	5.1	4.9	4.7	4.3	3.9
θ (mm)	4.1	3.9	3.8	3.6	3.5	3.2	3.0	2.7	2.6
τ_w (Pa)	0.030	0.055	0.091	0.113	0.141	0.190	0.252	0.290	0.371

Flat-plate BL theory detailed above, is also applied to the empty WT HWA data, which was recorded to map the BL, and velocity flow quality of the WT. Velocity profiles were measured logarithmically at nine locations on the WT floor, per Appendix A.2. Results aligned with the expectation of [88, 99], where BL δ decreased with increasing U_∞, and δ increased with increasing x. Spanwise flow was also found to be symmetrical within in model vicinity.

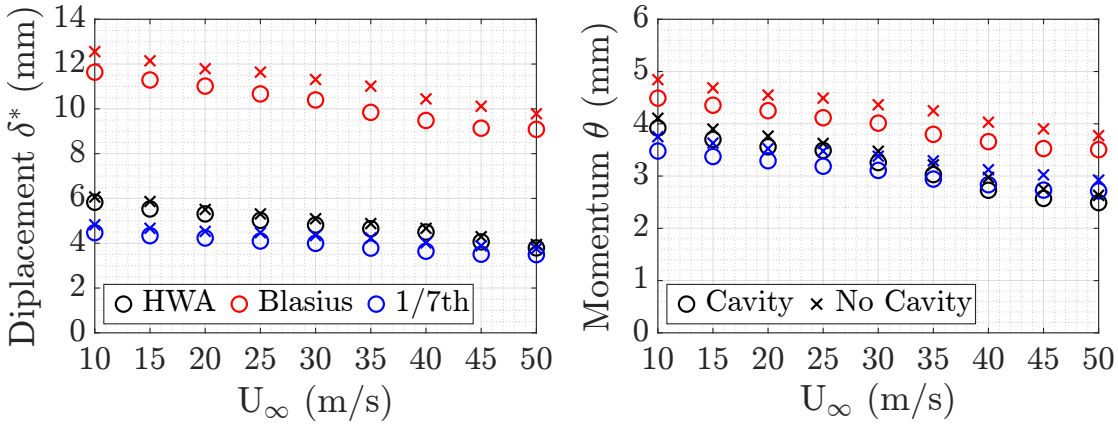

Figure 4.9: HWA: Flat-Plate Boundary Layer Thicknesses

4.3.2 Boundary Layer Flow over a Wedge

For flow over the conic nose in Fig. 4.10, the flat-plate BL solution no-longer holds due to $dp/dx < 0$, and HWA cannot fully resolve a BL over an axisymmetric nose. Therefore, Falkner-Skan's[22] wedge flow similar solution is applied, using HWA results to validate boundary con-

ditions (BCs) and assumptions. To resolve BL flow over the conic nose, modelled as a wedge, in x, y coordinates, with velocity components u, v, and pressure gradient $dp/dx < 0$. Similarity is achieved by adjusting the flat-plate solution, for pressure gradient $dp/dx \sim \beta$, and transforming x, y to similar variables; $\xi = x/l$ and η in Eqn. 4.31. See further detail in Appendix B.2.

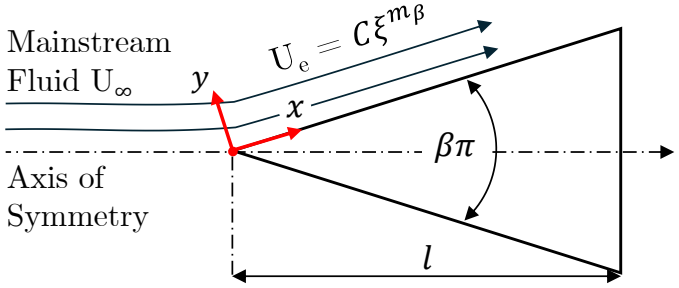

Figure 4.10: HWA: Wedge Boundary Layer Flow

To model inviscid flow outside the BL along a wedge, a tangential power-law velocity profile is assumed per potential flow in Eqn. 4.32, with dp/dx in Eqn. 4.33. $\mathrm{U_e}$ is BL edge velocity, $m_\beta = \beta/(2-\beta)$ is the Falkner-Skan power-law parameter with similar $dp/dx \sim \beta$, C is a constant, x is along the wedge, y is normal to, and l is wedge length. Stream function ψ is given by Eqn. 4.35, to derive u, v in Eqn. 4.36 and 4.37, which substitute into potential momentum Eqn. B.12, for the Falkner-Skan solution in Eqn. 4.34. Similar τ_w is derived by Eqn. 4.38, and $f'(\eta)$ is the similar velocity profile per Eqn. 4.36, where $\delta \propto \eta$ at $f'(\eta) = u/\mathrm{U_e} \approx 1$. Therefore, function $f(\eta) \sim f$ is required, with f', f'', f''' denoting derivatives of $f(\eta)$.

$$\eta = y\sqrt{\frac{\mathrm{U_e}(1+m_\beta)}{2\nu x}} \tag{4.31}$$

$$\mathrm{U_e} = C\xi^{m_\beta} \tag{4.32}$$

$$\frac{\partial p}{\partial x} = -\rho \mathrm{U_e}\frac{d\mathrm{U_e}}{d\xi} = -\rho m_\beta C^2 \xi^{2m_\beta - 1} \tag{4.33}$$

$$f''' + ff'' + \beta(1 - f'^2) = 0 \tag{4.34}$$

$$\psi = f\sqrt{\frac{2\mathrm{U_e}\nu x}{(1+m_\beta)}} \tag{4.35}$$

$$u = \frac{\partial \psi}{\partial y} = \mathrm{U_e} f' \tag{4.36}$$

$$v = -\frac{\partial \psi}{\partial x} = \sqrt{\frac{\mathrm{U_e}\nu(1+m_\beta)}{2x}}\left[\eta f' \frac{m_\beta - 1}{m_\beta + 1} - f\right] \tag{4.37}$$

$$\tau_w = \mu\sqrt{\frac{\mathrm{U_e}^3(m_\beta+1)}{2\nu x}} f''(0) \tag{4.38}$$

Falkner-Skan's solution in Eqn. 4.34, is a numerical 3rd order, non-linear boundary value problem (BVP), with no analytical solution [104], and BCs; $\eta = 0 : f(0) = f'(0) = 0$, and $\eta \to \infty : f'(\infty) = 1$. A numerical method is thus required, to approximate the solution. A shooting technique [105] is applied, using Newton's method [106] to define the target, in a 4th order Runge Kutta scheme for iterative convergence. For Falkner-Skan, a solution to $f''(0)$ is required to satisfy the initial condition (IC), which is found by shooting at values of $f''(0)$, until a solution arises for $f'(\eta)$ and its derivatives. See Appendix B.2.2 for detail, and F.2.4 the algorithm.

To find $y \sim \delta$, $f'(\eta) = u/\mathrm{U_e} \approx 1$ is then converged by iterating η, which is substituted into Eqn. 4.31. The solution requires wedge geometry, and velocity profile location. In this case, conic $\varnothing$0.1m, length $l = 0.121$, and angle $\beta\pi = 45°$; $x = \sqrt{l^2 + 0.05^2} = 0.13$m, $\beta = 0.25$, $m_\beta = 0.14$ and $\xi = 1.08$. Power-law defines $\mathrm{U_e} = C\xi^{m_\beta}$, using constant C as the IC from HWA.

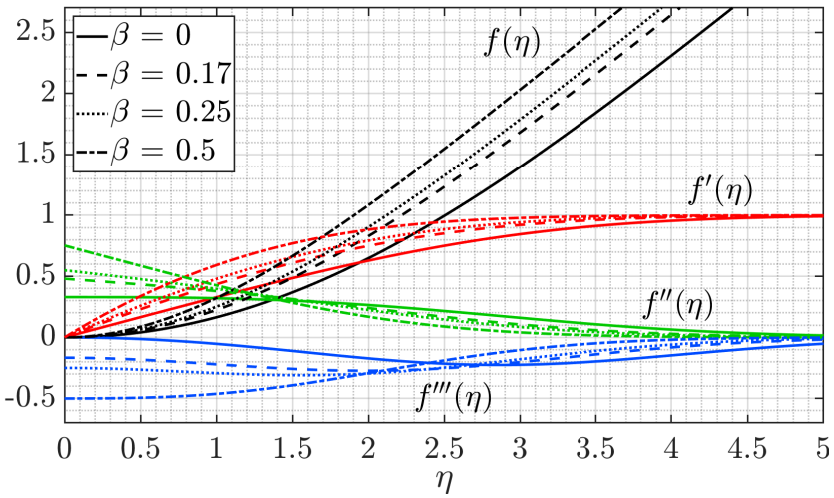

Figure 4.11: HWA: Falkner-Skan Function in terms of η

To find δ^* and θ, $f'(\eta)$ is integrated per Eqn. 4.39 and 4.40. τ_w is found with the algorithm in Appendix F.2.6, which aligned to HWA within 0.1%, to validate the method. Table 4.3 presents conic BL data, with Re_x from the nose LE. Fig. 4.12 compares the result to Blasius's [21] laminar BL and the 1/7th turbulent power law. These results indicate the BL is laminar, as $\mathrm{Re}_x < \mathrm{Re}_{x,\mathrm{crit}}$ and data aligns to Blasius's profile. Moreover, increasing U_∞ increases τ_w, and reduces BL δ, with cavity presence also increasing τ_w and reducing δ, indicating amplified $dp/dx < 0$.

$$\delta^* = \sqrt{\frac{2\nu x}{\mathrm{U_e}}} \int_0^\eta (1 - f')d\eta \qquad (4.39) \qquad \theta = \sqrt{\frac{2\nu x}{\mathrm{U_e}}} \int_0^\eta f'(1 - f')d\eta \qquad (4.40)$$

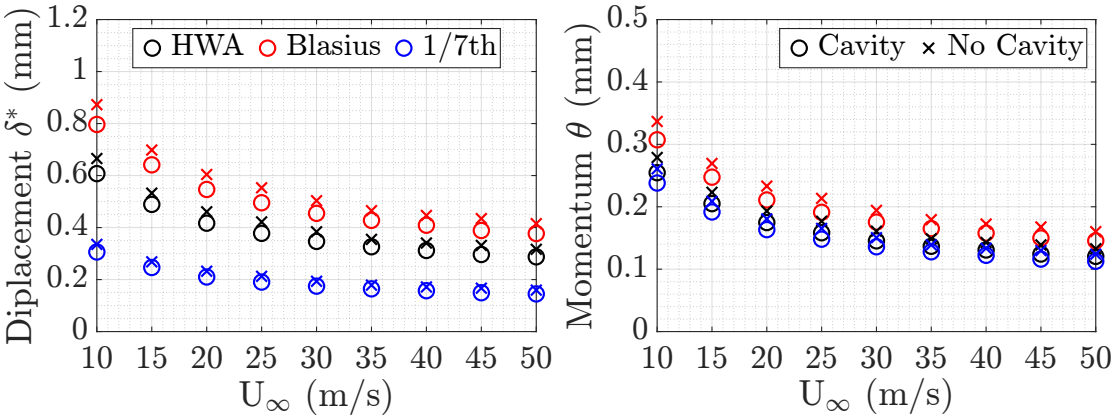

Figure 4.12: HWA: Conic Nose Boundary Layer Thicknesses

Table 4.3: HWA: Conic Nose Boundary Layer Data

U_∞ (m/s)	10	15	20	25	30	35	40	45	50
Re_x (10^5)	0.9	1.3	1.8	2.2	2.7	3.1	3.5	3.9	4.4
Conic Nose U/S, Cavity Open									
δ (mm)	2.45	1.97	1.68	1.52	1.40	1.31	1.26	1.19	1.16
δ^*(mm)	0.61	0.49	0.42	0.38	0.35	0.33	0.31	0.30	0.29
θ (mm)	0.25	0.20	0.17	0.16	0.15	0.14	0.13	0.12	0.12
dp/dx (Pa/m)	-43	-78	-118	-168	-222	-286	-350	-430	-510
τ_w (Pa)	0.014	0.017	0.025	0.035	0.043	0.053	0.061	0.075	0.086

Conic Nose U/S, Cavity Closed									
δ (mm)	2.68	2.15	1.86	1.70	1.55	1.43	1.37	1.34	1.28
δ^*(mm)	0.67	0.53	0.46	0.42	0.38	0.35	0.34	0.33	0.32
θ (mm)	0.28	0.22	0.19	0.18	0.16	0.15	0.14	0.14	0.13
dp/dx (Pa/m)	-24	-59	-103	-151	-204	-275	-338	-417	-498
τ_w (Pa)	0.009	0.015	0.021	0.030	0.038	0.048	0.059	0.067	0.075

4.3.3 Boundary Layer Flow over a Curved Surface

For flow over ogive and parabola noses per Fig. 4.13, with $dp/dx < 0$, as HWA is unable to fully resolve the BL over an axisymmetric nose, and Falkner-Skan does not account curvature. Murphy's[7,107] extended Falkner-Skan for curvature is applied, as derived from Goldstein's[23] curved streamline BL equations in Eqn. 4.41-4.43, with HWA results to validate BCs and assumptions. Both nose curvatures are small, with proportionality constant $\mathrm{A_p} << 1$ per Table B.3 and Eqn. 4.46. x is arc length along the curve in Cartesian coordinates x_c, y_c per Eqn. 4.45, y is normal to, with velocity u, v, and curvature K per Eqn. 4.44. See Appendix B.2.3 for detail.

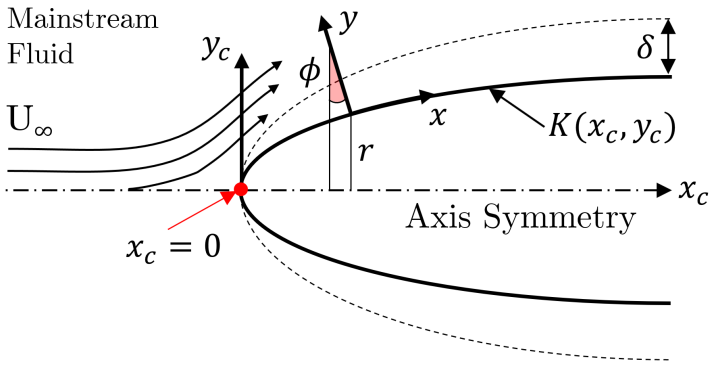

Figure 4.13: HWA: Axisymmetric Boundary Layer Flow

$$u\frac{\partial u}{\partial x} + v\frac{\partial u}{\partial y} = -\frac{1}{\rho}\frac{\partial p}{\partial x} + v\frac{\partial^2 u}{\partial y^2} \qquad (4.41)$$

$$\mathrm{K}u^2 = \frac{1}{\rho}\frac{\partial p}{\partial y} \qquad (4.42)$$

$$\frac{\partial u}{\partial x} + \frac{\partial v}{\partial y} = 0 \qquad (4.43)$$

$$\mathrm{K} = \frac{\left|d^2 y_c/dx_c^2\right|}{\sqrt{\left(1 + dy_c/dx_c\right)^3}} \qquad (4.44)$$

$$x = \int_0^{x_c} \sqrt{1 + \left(\frac{dy_c}{dx_c}\right)^2}\, dx_c \qquad (4.45)$$

$$\mathrm{A_p} = \mathrm{K}\sqrt{\frac{\nu x}{\mathrm{U_{pw}}}} \qquad (4.46)$$

A no-slip condition on the wall; $y = 0 : u = v = 0 \rightarrow \eta = 0 : f(0) = f'(0) = 0$, satisfies continuity in Eqn. 4.43, with stream function ψ in Eqn. 4.47, and similar variable; η in Eqn. 4.48, to transform from x, y. Asymptotic transition from the BL to external flow for small curvature, is satisfied by potential irrotationality; $(1/u)(\partial u/\partial y) = -\mathrm{K}$, requiring $\mathrm{U_p} = \mathrm{U_{pw}}^{-\mathrm{K}y}$. $\mathrm{U_p}$ is potential flow velocity, and $\mathrm{U_{pw}} = \sqrt{2(p_\infty - p_0)/\rho_\infty}$ is wall potential velocity, calculated from USP; $(p_\infty - p_0)$. Velocity u, v and derivatives are then defined in Eqn. 4.49-4.51, and substituted into Eqn. 4.42, for $\partial p/\partial \eta$ and τ_w in Eqn. 4.52 and 4.53, with results in Table 4.4.

$$\psi = f\sqrt{\mathrm{U_{pw}}\nu x} \qquad (4.47)$$

$$\eta = 0.5y\sqrt{\mathrm{U_{pw}}/\nu x} \qquad (4.48)$$

$$u = \frac{\partial \psi}{\partial y} = \frac{\mathrm{U_{pw}} f'}{2} \qquad (4.49) \qquad v = -\frac{1}{1+\mathrm{K}y}\frac{\partial \psi}{\partial x} = \frac{\eta f' - f}{2 + 4\mathrm{A_p}\eta}\sqrt{\frac{\mathrm{U_{pw}}\nu}{x}} \qquad (4.50)$$

$$\frac{\partial u}{\partial x} = -\frac{\mathrm{U_{pw}}\eta f''}{4x} \qquad \frac{\partial u}{\partial y} = \frac{\mathrm{U_{pw}} f''}{4}\sqrt{\frac{\mathrm{U_{pw}}}{\nu x}} \qquad \frac{\partial^2 u}{\partial y^2} = \frac{{\mathrm{U_{pw}}}^2 f'''}{8\nu x} \qquad (4.51)$$

$$\frac{\partial p}{\partial \eta} = \frac{\rho {\mathrm{U_{pw}}}^2 f'^2}{4 + 4\mathrm{A_p}\eta} \qquad (4.52) \qquad \tau_w = \frac{\mu \mathrm{U_{pw}} \mathrm{C_2}}{4}\sqrt{\frac{\mathrm{U_{pw}}}{\nu x}} \qquad (4.53)$$

By substituting Eqn. 4.49-4.52 into Eqn. 4.41. A similar solution for small convex curvature is given by Eqn. 4.54[7], with BCs; $f = f' = 0$ at $\eta = 0$ and $f' \to 2 - 4\mathrm{A_p}\eta$ at $\eta > 0$. Function $f(\eta)$ is thus required. A Taylor-series method[23] is utilised per Eqn. 4.55, see Appendix B.2.3 for detail on the derivation. $\mathrm{C_2}$ is a constant determined from Fig. B.5[7], as a function of curvature; $A_p \sim$K, and $\mathrm{F_0}, \mathrm{G_1}$ are Taylor series functions in Eqn. B.56 and B.57[7] respectively.

$$f''' + ff'' + 2\mathrm{A_p}\eta f'^2 = 0 \qquad (4.54)$$

$$f = \sqrt[3]{\mathrm{C_2}}\mathrm{F_0}\left(\eta\sqrt[3]{\mathrm{C_2}}\right) - \mathrm{A_p}\mathrm{G_1}\left(\eta\sqrt[3]{\mathrm{C_2}}\right) \qquad (4.55)$$

To determine δ, the potential velocity profile representing external flow; $\mathrm{U_p/U_{pw}} = e^{-\mathrm{K}y}$, with $y = 2\eta/\sqrt{\mathrm{U_{pw}}/\nu x}$, is plotted against η, with similar BL velocity profile; $u/\mathrm{U} = f'(\eta)/2$, and curve intersection represents convergence of BL and external flow solutions at the BL edge. Therefore, η in Eqn. 4.48 at intersection, is rearranged for $y \sim \delta$. Fig. 4.14 provides an example of the intersection. The method follows Goldstein's[23] curved BL EOM, with Murphy's[7] Taylor series, Falkner-Skan curvature adjustment, and reference to [107–119]. Appendix B.2.3 provides detail, Table B.2 is $f(\eta)$ solutions, and the algorithm is in Appendix B.2.3.

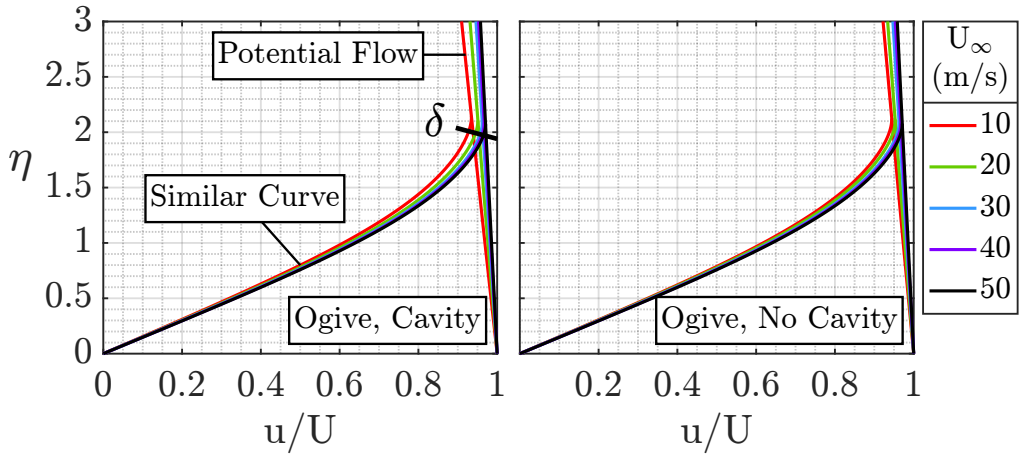

Figure 4.14: HWA: Curved Similar Solution & Potential Velocity Profile Intersection for δ

To determine δ^* and θ, similar profile $u/\mathrm{U} = f'(\eta)/2$ is integrated per Eqn. 4.56 and 4.57. τ_w was calculated per Appendix F.2.6, where similar τ_{wf} and HWA τ_w align within error $\varepsilon = 0.1\%$, to validate the method. Table 4.3 has curved BL data, with Re_x from the nose LE. Fig. 4.15-4.16 are δ^*, θ against Blasius's[21] laminar BL and 1/7th turbulent power law. Indicating, the BL is laminar, as $\mathrm{Re}_x < \mathrm{Re_{x,crit}}$, and δ^*, θ align with Blasius's profile. Moreover, increasing U_∞ increases τ_w, and reduces BL δ. Cavity presence does also, indicating amplied $dp/dx < 0$.

$$\delta^* = \int_0^{\eta_\delta} \left(1 - \frac{f'(\eta)}{2}\right) d\eta \qquad (4.56) \qquad \theta = \int_0^{\eta_\delta} \frac{f'(\eta)}{2} \left(1 - \frac{f'(\eta)}{2}\right) d\eta \qquad (4.57)$$

Table 4.4: HWA: Curve Nose Boundary Layer Data

U_∞ (m/s)	10	15	20	25	30	35	40	45	50
Re_x (10^5)	0.9	1.3	1.8	2.2	2.7	3.1	3.5	3.9	4.4
Ogive Nose U/S, Cavity Open									
δ (mm)	2.76	2.23	1.89	1.72	1.57	1.46	1.40	1.32	1.24
δ^*(mm)	1.07	0.87	0.74	0.66	0.61	0.56	0.54	0.50	0.47
θ (mm)	0.40	0.32	0.27	0.25	0.22	0.21	0.20	0.19	0.18
dp/dx (Pa/m)	-32	-52	-100	-151	-208	-274	-334	-419	-500
τ_w (Pa)	0.009	0.015	0.021	0.030	0.038	0.048	0.059	0.067	0.075
Ogive Nose U/S, Cavity Closed									
δ (mm)	2.96	2.31	1.99	1.76	1.62	1.51	1.41	1.36	1.27
δ^*(mm)	1.17	0.91	0.78	0.69	0.63	0.59	0.56	0.54	0.49
θ (mm)	0.44	0.34	0.29	0.26	0.24	0.22	0.21	0.20	0.19
dp/dx (Pa/m)	-20	-44	-93	-134	-191	-259	-326	-405	-485
τ_w (Pa)	0.006	0.012	0.019	0.025	0.033	0.042	0.051	0.061	0.072
Parabola Nose U/S, Cavity Open									
δ (mm)	2.92	2.37	2.02	1.83	1.65	1.54	1.44	1.37	1.29
δ^*(mm)	1.12	0.92	0.78	0.71	0.64	0.60	0.56	0.54	0.51
θ (mm)	0.45	0.34	0.29	0.26	0.24	0.22	0.20	0.20	0.18
dp/dx (Pa/m)	-25	-48	-93	-142	-200	-263	-322	-410	-493
τ_w (Pa)	0.007	0.011	0.018	0.024	0.035	0.044	0.053	0.070	0.078
Parabola Nose U/S, Cavity Closed									
δ (mm)	3.13	2.56	2.16	1.88	1.66	1.56	1.45	1.38	1.31
δ^*(mm)	1.29	1.15	0.95	0.86	0.77	0.70	0.63	0.58	0.55
θ (mm)	0.47	0.38	0.34	0.29	0.25	0.23	0.22	0.22	0.19
dp/dx (Pa/m)	-17	-41	-80	-123	-182	-242	-318	-392	-477
τ_w (Pa)	0.005	0.010	0.015	0.020	0.031	0.041	0.050	0.059	0.071

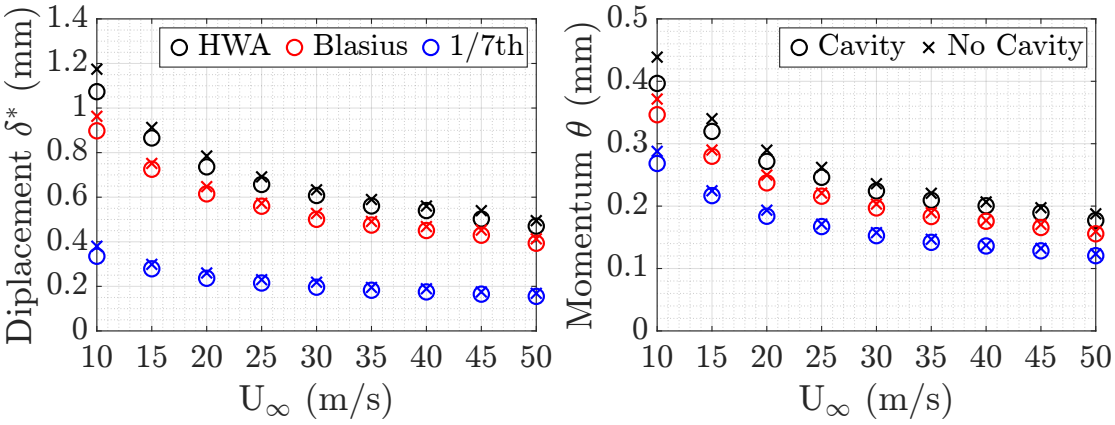

Figure 4.15: HWA: Ogive Nose Boundary Layer Thicknesses

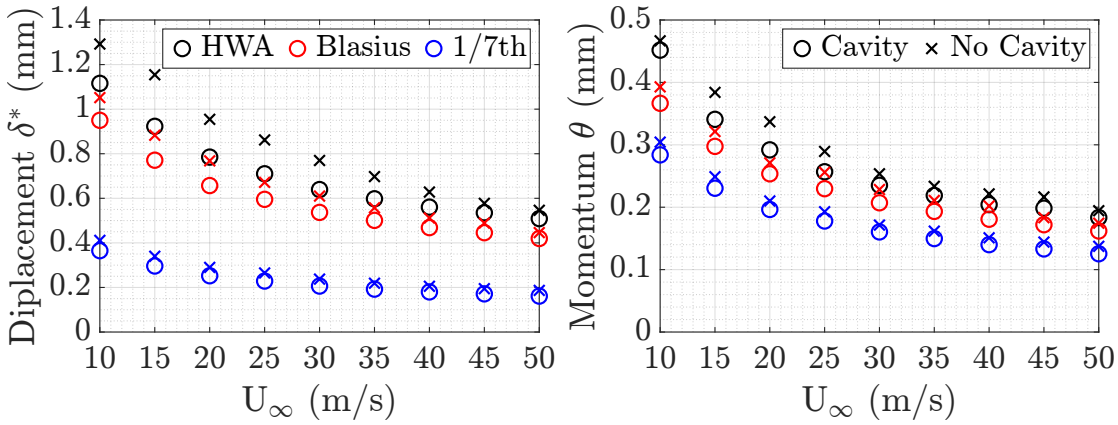

Figure 4.16: HWA: Parabola Nose Boundary Layer Thicknesses

4.3.4 Boundary Layer Flow with a Cavity Downstream

Table 4.2-4.4 show an increase in τ_w, and $dp/dx < 0$, with a reduction in BL δ, when the cavity is open. Implying cavity presence induces or amplifies $dp/dx < 0$ on U/S flow, which has not been documented. External acoustic propagation has been measured, however the U/S effect has not. Therefore, cavity feedback U/S beyond the LE, is assessed in Chapter 5.

4.4 Unsteady Surface Pressure

This section details method used to transform USP data, into meaningful cavity surface pressure maps. Data is produced for each cavity internal geometry, with each external geometry U/S nose cone, compared to the baseline flat-plate, at U_∞ = 1-65m/s, as presented in Section 6.1.

4.4.1 Data Reduction

Each pressure tap was given a number, with distance to the cavity LE CL origin; $+x$ streamwise, $+y$ vertical, and $+z$ right spanwise facing D/S. Port number was assigned to each tap, to align transducer volume V_t in post-processing, as each Scanivalve port has a different volume per Fig. 3.18, and V_t is required to correct tube distortion in Section 4.4.2.

All raw data was imported, and aligned x, y, z, tap, case and port number. Then an output file was written with cells per case, and rows per U_∞ with pressure and time aligned to tap, port number, and ambient conditions per case, as given in Appendix A.1.

Pressure coefficient C_p was computed using Eqn. 4.58. The numerator is given by the MPS, where p_∞ is FS pressure, p is pressure at the point of interest, and q_∞ in the denominator is FS dynamic pressure. Lastly, an output file is generated per case, with a cell per U_∞, matrix values at each port, and time step with normalised coordinates; x/L, and y/D.

Time averaged $C_{p,rms}$ is also computed, or Root-Mean Square (RMS) of C_p over time t, the square root of the mean of a set of N values, with discrete distribution x_i, x_{i+1}..., squared x_i^2 per Eqn. 4.59. $C_{p,rms}$ allows for identification of peaks in oscillatory intensity, and aligned dominant structures. Here, $N = 5000$ time steps over $t = 10$s. Appendix F.1.1 provides the algorithm.

$$C_p = \frac{p - p_\infty}{q_\infty} \qquad (4.58)$$

$$C_{p,rms} = \sqrt{\frac{\sum_{i=1}^{N} C_{p,i}^2}{N}} \qquad (4.59)$$

4.4.2 Tube Distortion Error

An error caused by change in pressure applied at one end of a tube (interest pressure), as it develops through the tube, or series of N tubes, toward tube(s) end, where measured. The error is prevalent in this set-up, as the Scanivalve, located outside the WT, measures pressure at a point in the WT, with tubes between. The Scanivalve also has a series of tubes internally, directing flow to the pressure sensor, see Fig. 3.18. Tube distortion has three primary effects; resonance, pressure wave phase shift, and amplitude distortion [86].

Tube length L_j, and radius R_j, are primary to pneumatic frequency response. As they increase amplitude distortion, and phase shift. Tube material and layout is also important. However, the associated error can be removed by following design rules of Tijdeman & Spiering [120], Rajan et al [121] and Rofail et al [122], and using flexible soft PVC tubes. Ambient conditions $(T_\infty, p_\infty, \mathrm{V_{v_j}}, \mathrm{a}_\infty, \gamma, \alpha_j)$ per Appendix A.1 also alter response, if not accurately considered.

Iberall [123] developed a method to correct tube distortion effects, which was applied by Bergh & Tijdeman [124,125], using incompressible NS equations, with a recursion formula. This approach updates dynamic pressure and phase response of the Scanivalve to model set-up, with a series-connection of j thin tubes and j volumes in Fig. 4.17. The method relates sinusoidal pressure disturbance in volume $\mathrm{V_{v_j}}$, to preceding volume $\mathrm{V_{v_{j-1}}}$, and following volume $\mathrm{V_{v_{j+1}}}$, to derive pressure input by successive $j = N, N-1, ...2, 1$, as follows. This method was used over a transfer function approach, as Scanivalve recommend the method, and WT access was limited.

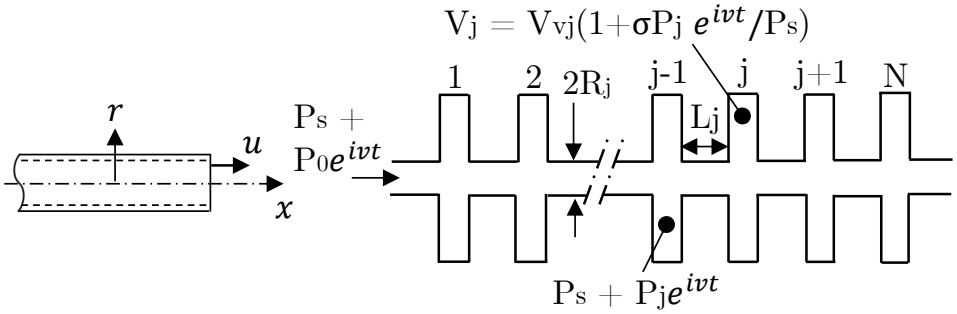

Figure 4.17: USP: Series Connection of Tubes and Transducers

Given L_j, a wide tube, produces higher resonant peaks than a narrow tube. Given R_j, a long tube, produces lower resonant peaks, at smaller frequencies, than a short tube. Therefore, certain L_j, R_j, remove resonant effects [124], and are determined by finding Eqn. 4.60 false. Phase shift occurs, as pressure oscillates through the tube(s), altering wave time correlation, and magnitude between the beginning and end of tube(s), thus false spectra. It can not be eliminated, only minimised and corrected. Eqn. 4.62 [124] outputs phase shift in degrees, converted to velocity per; $\bar{u} = u \cdot e^{iut}$. Pressure wave amplitude distortions can not be eliminated, only minimised and corrected with Eqn. 4.61 [124]. Equations 4.60-4.61 form Eqn. 4.63 [124], to correct pressure.

$$\cot g \left\langle \frac{fL_j}{\mathrm{a}_\infty} \right\rangle = \gamma \frac{\mathrm{V_{v_j}}}{\mathrm{V_{t_j}}} \left(\sigma + \frac{1}{k}\right) \left(\frac{fL_j}{\mathrm{a}_\infty}\right) \quad (4.60) \qquad p = (a+b) \exp\left[\frac{vx}{\mathrm{a}_\infty} \sqrt{\frac{\gamma}{n} \frac{J_0\langle\alpha\rangle}{J_2\langle\alpha\rangle}}\right] \quad (4.61)$$

$$u = \frac{i}{\mathrm{a}_\infty \rho_\infty} \sqrt{\frac{\gamma}{n} \frac{J_0\langle\alpha\rangle}{J_2\langle\alpha\rangle}} \left\{ \frac{J_0\langle\alpha\rangle}{J_2\langle\alpha\rangle} - 1 \right\} \left\{ (a-b) \exp\left[\frac{fx}{\mathrm{a}_\infty} \sqrt{\frac{\gamma}{n} \frac{J_0\langle\alpha\rangle}{J_2\langle\alpha\rangle}}\right] \right\} \quad (4.62)$$

$$\frac{p_j}{p_{j-1}} = \left[\cosh\langle\phi_j L_j\rangle + \frac{\mathrm{V_{v_j}}}{\mathrm{V_{t_j}}}\left(\sigma_j + \frac{1}{k_j}\right) n_j \phi_j L_j \sinh\langle\phi_j L_j\rangle + \right.$$
$$\left. \frac{\mathrm{V_{t_{j+1}}}\phi_{j+1} L_j J_0\langle\alpha_j\rangle J_2\langle\alpha_{j+1}\rangle}{\mathrm{V_{t_j}}\phi_j L_{j+1} J_0\langle\alpha_{j+1}\rangle J_2\langle\alpha_j\rangle} \frac{\sinh\langle\phi_j L_j\rangle}{\sinh\langle\phi_{j+1} L_{j+1}\rangle}\left\{\cosh\langle\phi_{j+1} L_{j+1}\rangle - \frac{p_{j+1}}{p_j}\right\}\right]^{-1} \tag{4.63}$$

Symbols:

- $\mathrm{V_{t_j}}$, and $\mathrm{V_{v_j}}$ are tube and transducer volume per Table 4.5 and 4.6 respectively
- σ is dimensionless increase in transducer volume due to diaphragm deflection
- k is polytropic constant based on volume; $k = p \cdot \mathrm{V^j}$
- $n_j = \left[1 + \frac{\gamma-1}{\gamma}\frac{J_2\langle\alpha_j\sqrt{\mathrm{P_r}}\rangle}{J_0\langle\alpha_j\sqrt{\mathrm{P_r}}\rangle}\right]^{-1}$ polytropic index for expansion/compression due to heat transfer
- J_j is Bessel functions of first kind of order j,
- $\alpha_j = R_j\sqrt{i^3}\sqrt{\rho_{\infty_j} f/\mu_j}$ is shear wave number, dependent on FS conditions
- $\mathrm{P_r} = \mu g c_p/\lambda$ is Prandtl No.; c_p is constant pressure specific heat, λ is thermal conductivity
- r is radial and x is axial coordinate, and a, b are constants refer [124]
- $\phi_j = \left(f/a_{\infty_j}\right)\sqrt{J_0\langle\alpha_j\rangle/J_2\langle\alpha_j\rangle}\sqrt{\gamma/n_j}$

Data is given by Scanivalve in [86], derivation by [120, 124, 125], theory by [123] and the algorithm in Appendix F.1.2. Also using ambient data to account $T_\infty, p_\infty, \mathrm{a}_\infty, \gamma$, shear wave number α, and transducer volumes V_v per Table 4.6 and Fig. 3.18. Fig. 4.18 and 4.19 provide an examples of the change from original to corrected data, as a result of tube distortion.

Table 4.5: USP: Tube Volume for each Port in Scanivalve MPS 4264

Transfer Function No. and Component		L_j (mm)	R_j (mm)	$\mathrm{V_t}$ ($\mathrm{mm^3}$)
1	Plastic Tube Model	750	0.40	377
1	Plastic Tube Tunnel Floor	500	0.40	251
2	Scanivalve Port Tube	6.86	0.53	25

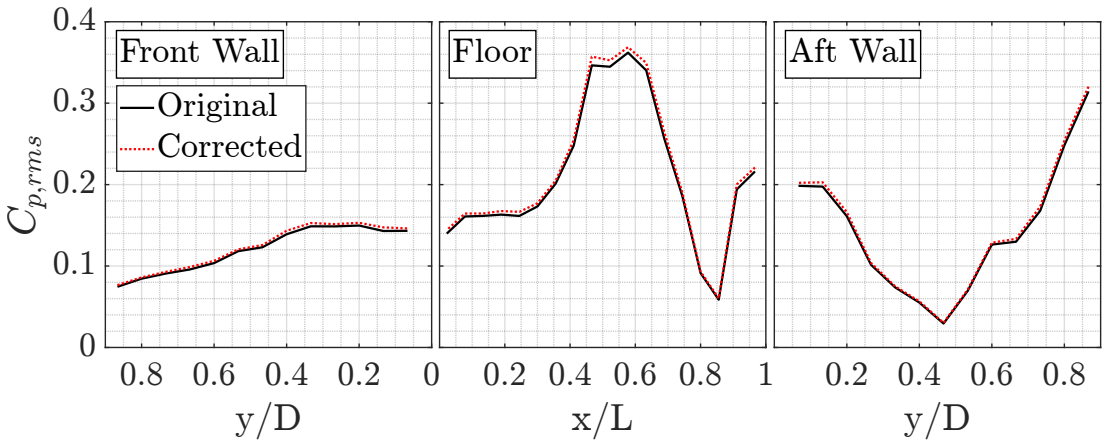

Figure 4.18: USP: Tube Distortion on $C_{p,rms}$ of C5: L/D = L/W = 3, Conic U/S, $\mathrm{U_\infty}$ = 50m/s

Table 4.6: USP: Transducer Volume for each Port in Scanivalve MPS 4264

Scanivalve MPS 4264 Port No.																V_v (mm^3)
1	5	9	13	17	21	25	29	33	37	41	45	49	53	57	61	15.1
2	6	10	14	18	22	26	30	34	38	42	46	50	54	58	62	10
3	7	11	15	19	23	27	31	35	39	43	47	51	55	59	63	7.49
4	8	12	16	20	24	28	32	36	40	44	48	52	56	60	64	12.5
Reference Cavity for all 64 Channels																1884

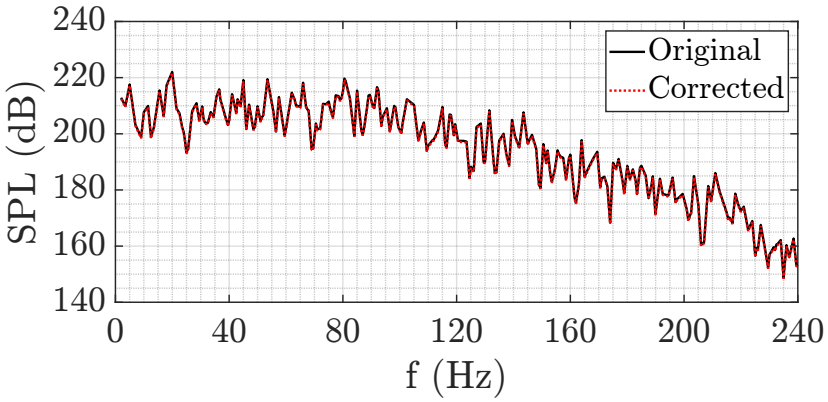

Figure 4.19: USP: Tube Distortion on Cavity Spectra of C6: L/D = 3, L/W = 6, Conic U/S, U_∞ = 50m/s from a Pressure Tap on the floor at x/L = 0.5, z/W = 0.3

4.5 Signal Analysis

This section details conversion of temporal data to the frequency domain, using Fast Fourier Transform (FFT), and Dynamic Mode Decomposition (DMD), to extract spectral characteristics from the BL and internal cavity flow. USP and HWA data are both temporal, but their sample and spatial distributions vary. USP has a low frequency range, but measures efficiently in space, requiring DMD to re-construct the spatial modes. HWA has a high frequency range, ideal for turbulent BL structures, but is not measured over large spatial areas. Therefore, DMD is applied to USP with cavity spatial distribution, and FT to HWA for turbulent BL spectra. See Appendix C for further information on theory, method, and algorithm construction.

4.5.1 Fast Fourier Transform

FFT was performed for amplitude p and frequency f on USP and HWA signals per sample rates (sR); 500Hz and 2^{15}Hz respectively, to observe sR/2 per Nyquist [126]. SPL is used to non-dimensionalise amplitude; SPL $= 20\log_{10}\left(p/p_{\text{ref}}^2\right)$, where $p_{\text{ref}} = 20\mu$Pa is the limit of human perception. A band-pass filter reduced the HWA signal, due to its large range. A moving-average filter is used on both data sets. Gaussian, Blackman, and multiple-pass [126] were tried, however, output difference was null. Thence, moving-average was used for simplicity, with a rational transfer function in Eqn. 4.64 [126]. See Appendix C for detail and F.3 the algorithm.

$$Y(z) = \frac{b(1) + b(2)z^{-1} + ... + b(n_b+1)z^{-n_b}}{1 + a(2)z^{-1} + ... + a(n_a+1)z^{-n_a}} X(z)$$

$$\rightarrow \qquad y(n) = \frac{x(n) + x(n-1) + ... + x(n-(wS-1))}{wS} \tag{4.64}$$

- $X(z)$ and $Y(z)$ are the Z-transform of input and output signals $x(n)$ and $y(n)$ respectively
- $a = 1$ is normalisation factor, $b = (1/\text{wS})\times$1-by-wS matrix of ones, and wS = window size
- n_a and n_b are feedback and feedforward filters respectively

4.5.2 Dynamic Mode Decomposition

DMD is performed to extract dominant cavity spatial modes, by algorithmically regressing dynamic system state snapshots $\mathbf{x}_k$ of pressure, at time t_k for $k = 1, 2, ...m$, onto a locally linear dynamic system; $\mathbf{x}_{k+1} = \mathbf{A}\mathbf{x}_k$. The architecture was developed per [127–130], with reference to [69, 71] for cavity flow, further detailed in Appendix C.2. The DMD solution gives: eigenvalues λ_k, and vectors ϕ_k of $\mathbf{A}$ in Eqn. 4.66. To reduce error, m snapshots are allocated to data matrix $\mathbf{X}, \mathbf{X'}$ in Eqn. 4.65. Then using dynamic samples, are decomposed to an optimal linear approximation where; $\mathbf{X'} \approx \mathbf{A}\mathbf{X}$ with $\mathrm{A} = \mathrm{X'X}^{\dagger}$; † is the Moore-Penrose pseudo inverse, minimising error to $\|\mathbf{X'} - \mathbf{A}\mathbf{X}\|_F$, where $\|\cdot\|_F$ is the Frobenius norm in Eqn. 4.67[130].

$$\mathbf{X} = \begin{bmatrix} | & | & & | \\ \mathbf{x}_1 & \mathbf{x}_2 & ... & \mathbf{x}_{m-1} \\ | & | & & | \end{bmatrix} \qquad \mathbf{X'} = \begin{bmatrix} | & | & & | \\ \mathbf{x}_2 & \mathbf{x}_3 & ... & \mathbf{x}_{m} \\ | & | & & | \end{bmatrix} \tag{4.65}$$

$$\mathbf{x}_k = \sum_{r}^{j=1} \phi_j \lambda_j^k b_j = \mathbf{\Phi}\mathbf{\Lambda}^k\mathbf{b} \tag{4.66}$$

$$\|\mathbf{X}\|_F = \sqrt{\sum_{j=1}^{n}\sum_{k=1}^{m} X_{jk}^2} \tag{4.67}$$

Steps below summarises DMD implementation[130], with detail in Appendix C.2:

(1) Singular Value Decomposition (SVD) $\mathbf{X} \approx \mathbf{U\Sigma V}^*$: `[U,S,V] = svd(X,'econ')`

(2) Rank Reduction: SVD output matrices $\mathbf{X} \approx \mathbf{U\Sigma V}^* \rightarrow$ `[U,S,V]` are truncated by rank-r, which is the index when 99% of dynamic system energy is captured.

(3) Dynamic Reduction: time linear dynamics $\mathbf{A}$, reduce to the POD subspace $\tilde{\mathbf{A}}$, with pseudo-inverse $\mathbf{X}$ from SVD, and $r \times r$ projection of $\mathbf{A}$ to POD modes in Eqn. 4.68.

$$\mathbf{A} = \mathbf{X'V\Sigma^{-1}U}^* \qquad \rightarrow \qquad \tilde{\mathbf{A}} = \mathbf{U}^*\mathbf{AU} = \mathbf{U}^*\mathbf{X'V\Sigma^{-1}} \tag{4.68}$$

(4) Eigendecomposition: $\tilde{A} \rightarrow \tilde{\mathbf{A}}\mathbf{W} = \mathbf{W}\mathbf{\Lambda}$ with `[W,D] = eig(Atilde)` for: eigenvector $\mathbf{W}$ columns, and eigenvalue λ_k diagonal matrix $\mathbf{\Lambda} =$ `D`.

(5) Dynamic Reconstruction: for eigenvalues λ_k `= diag(D)`, frequencies $\omega_k = \log(\lambda_k)/2\pi\Delta t$, and DMD modes $\mathbf{\Phi} = \mathbf{X'V\Sigma^{-1}W}$ as `phi = X'*Vr/Sr*W` in eigenvector ϕ_k columns.

Symbols:

- $\mathbf{A}$ is matrix of discrete linear dynamics, and $\tilde{\mathrm{A}}$ is reduced dynamics on POD subspace
- $\mathbf{b}$ is vector of DMD mode amplitudes
- r is truncated SVD rank, m is number of data snapshots, n is state dimension; $\mathbf{x} \in \mathbb{R}^n$.
- $\mathbf{U}$ is left singular vectors (POD modes) of $\mathbf{X}$, as `U` in the algorithm.
- $\mathbf{V}$ is right singular vectors of $\mathbf{X}$, as `V` in the algorithm.
- $\mathbf{X} \in \mathbb{R}^{n\times(m-1)}$ is data matrix with $\mathbf{X'} \in \mathbb{R}^{n\times(m-1)}$ the shifted data matrix, as `X,X'` in the algorithm, and state snapshots x_k of data at time t_k.

- $\mathbf{W}$ is eigenvector of $\tilde{A}$, as `W` in the algorithm.
- $\mathbf{\Lambda}$ is diagonal matrix of DMD eigenvalues in discrete time, as `D` in the algorithm.
- λ_j is DMD eigenvalue, with ω_j the continuous-time eigenvalue, $\omega \equiv \log(\lambda_j)/\Delta t$.
- $\mathbf{\Sigma}$ is matrix of singular values, as `S` in the algorithm.
- $\mathbf{\Phi}$ is matrix of DMD modes; $\mathbf{\Phi} \equiv \mathbf{X'V\Sigma^{-1}W}$, with ϕ_j the DMD mode (eigenvector).

Two issues arise when applying DMD to experimental data. Firstly, DMD requires high spatial resolution to map system dynamics, at the risk of interfering with flow dynamics. However, pressure taps were densely distributed in space, and mounted surface flush, to reduce error. Secondly, complex conjugate pairs are produced, as the spectrum is symmetric with respect to temporal frequencies[127], incurring an output of either non-oscillatory and purely real, or complex conjugates of a mode oscillating about the real axis.

Due to the oscillatory nature of cavity flow, DMD modes are mostly complex conjugates. Therefore, conjugate combination is executed, by checking if adjacent eigenvectors and values share absolute value and removing the secondary if equal[127,130,131]. Fig. 4.20 is an eigencircle example of the combination, for the cavity with; L/D = L/W = 3, and conic nose U/S at U_∞ = 50m/s. Singh et al[71] produced a similar result, with DMD of experimental open cavity data.

Dominant modes ϕ are the largest eigenvector norm in space, with corresponding eigenvalues closest to unity in an eigencircle, i.e., The red mode in eigencircle Fig. 4.20, and the DMD norm plot in Fig. 4.21. The norm plot x-axis is eigenvector column index of DMD matrix Φ, with modes 1-6 in order of dominance (not increasing frequency). DMD assumes 2D spatial distribution, thence, was executed on cavity walls individually; LE, Floor and TE.

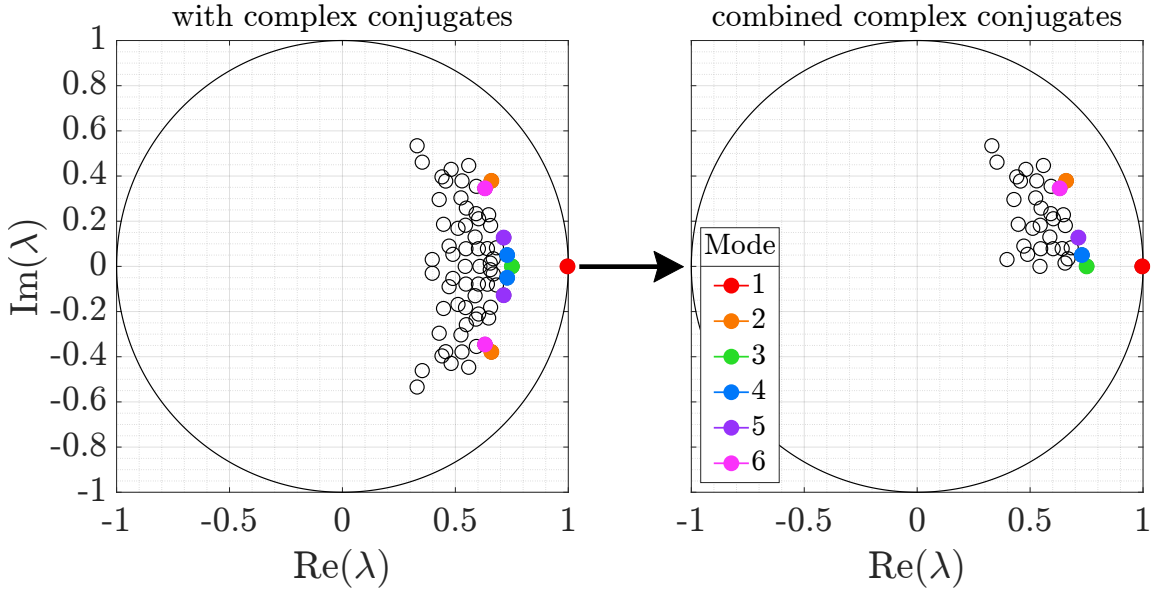

Figure 4.20: USP: Conjugate Combination of C5 TE: L/D = L/W = 3, Conic U/S, U_∞ = 50m/s

Fig. 4.22 is an example of the DMD solution output, across walls of the cavity with; L/D = L/W = 3, and the conic nose U/S at U_∞ = 50m/s. Each surface has a different amount of pressure taps per Section 3.4, thus spatially distributed points. Therefore, based on DMD architecture, each dominant mode may arise in a different eigenvector column index of DMD matrix Φ. This

does not necessarily attribute to a different frequency, just a different location, with respect to global space based derivation. As comparison of results across the walls, consistently implicate 3-4 dominant frequencies within the top six dominant modes.

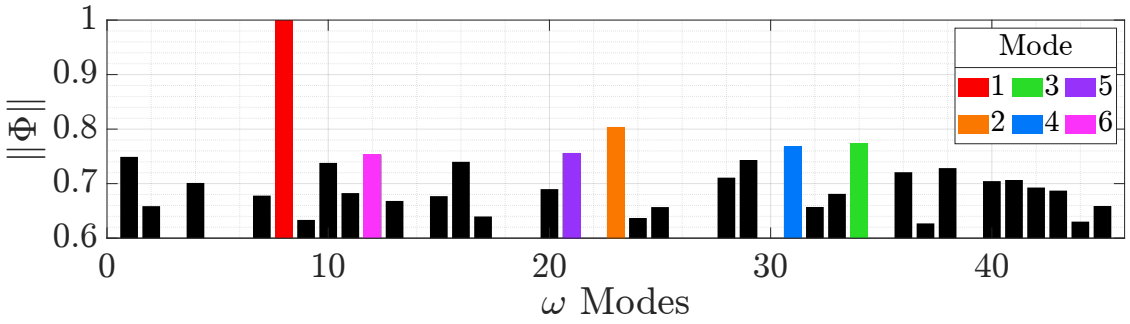

Figure 4.21: USP: Modes of C5 Floor: L/D = L/W = 3, Conic U/S, $U_\infty = 50$m/s

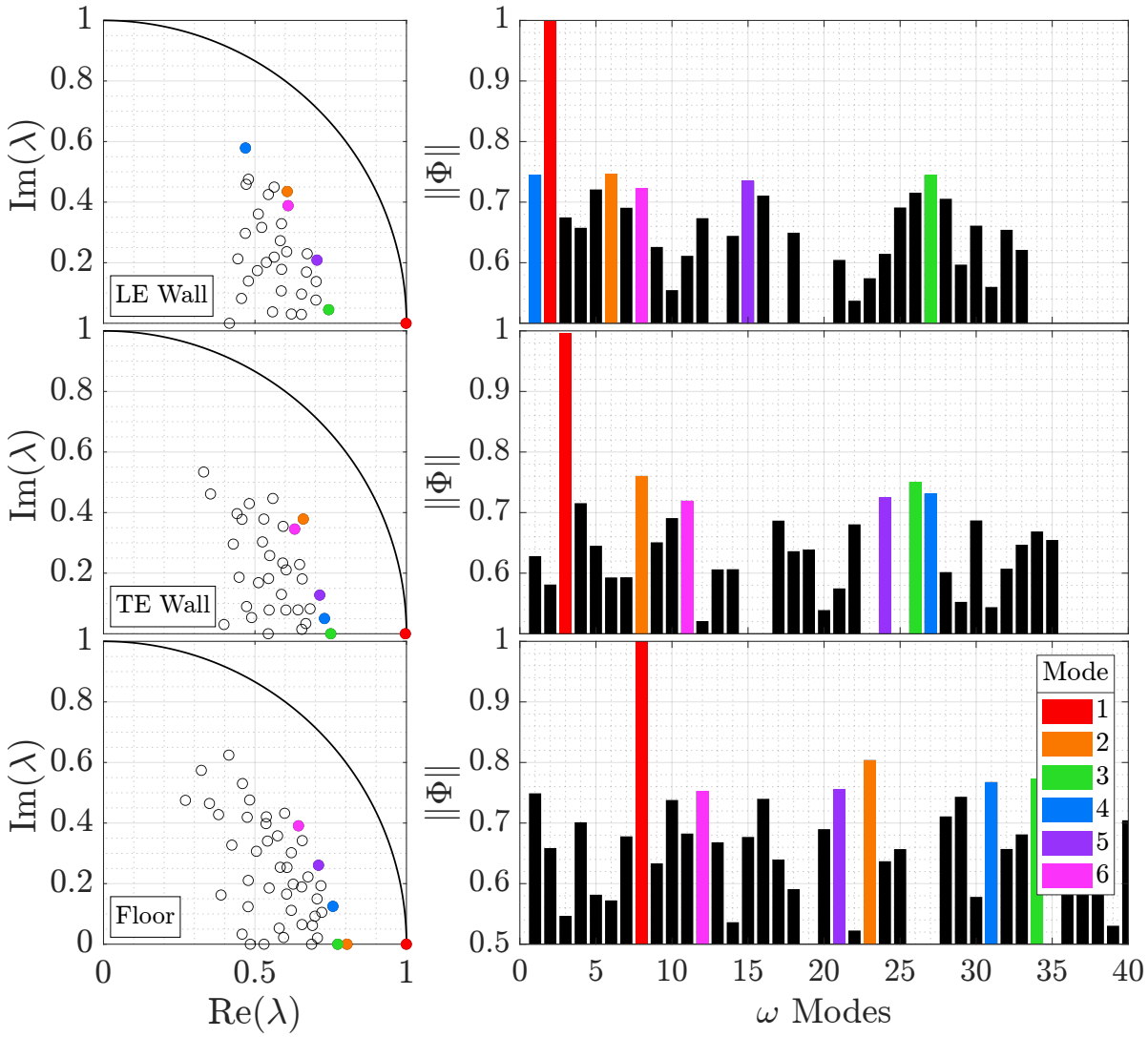

Figure 4.22: USP: Modes of C5: L/D = L/W = 3, Conic U/S, $U_\infty = 50$m/s

Dominant DMD mode 1-4 data aligned with FFT in areas of high $C_{p,rms}$, as discerned from contour plots in Section 6.1. Also, when compared to most recurrent occurrence of a frequency, in a vector of FFT frequencies in space. Most recurrent, doesn't account temporal intervals in space like DMD, nonetheless, it provides a sanity check. Results were also compared to

literature in Section 2, for a sanity check. As expected, regardless of width, for L/D > 1, mode 2 or 3 was dominant, and for L/D $= 1$, mode 1 was dominant. Frequency shifts slightly with U_∞, and U/S geometry thus BL profile, and SPL increases with increasing U_∞, width, and when BL δ decreases. Dominant mode output for each cavity case, is given in Table D.1-D.24 of Appendix D.2, with the algorithm in Appendix F.3.3, and results analysed in Section 6.2.

Mode shapes were reconstructed from $\mathbf{\Phi}$, by contouring values ϕ_k at respective spatial coordinates to observe mode distribution. Appendix C Fig. C.1 is an example of the mode shapes for the cavity with L/D = L/W = 1, and the conic nose U/S at $U_\infty = 50$m/s. However, due to the large swathe of data generated by the USP campaign, and resultant DMD, decomposed modes were generally used to determine dominant spectral characteristics, rather than observe shapes.

4.5.3 Strouhal Number Prediction

Strouhal number (St) in Eqn. 4.69 is used to non-dimensionalise cavity frequency response, due to the abundance of vorticity in the flow-field, with cavity length for the length scale. Numerous models exist to predict cavity St, based on; geometry, M_∞ and constants of vorticity phase γ_v, and SL convection κ (see Section 2.3). These models do not include viscid metrics, or an account of external geometry, and lack alignment for incompressible cavity flow.

This thesis observes the BL effect on cavity response, whilst varying incompressible M_∞, and U/S external geometry. And the BL has been observed, to hold a powerful role in cavity response, along with an induced favourable pressure gradient $dp/dx < 0$ effect, from external geometry. Therefore, a new model is to be proposed for incompressible flow, including viscosity, which is more abundant in the incompressible realm of experiments conducted.

Dominant DMD frequencies are used to compute St number, from spatially distributed USP data, to confirm accuracy of the proposed model. Along with accrued BL δ, δ^* and pressure gradients dp/dx, extracted from HWA. The model is also compared to existing models, and experimental data, extracted from research in the incompressible to supersonic flow regimes.

$$\mathrm{St} = \frac{f\mathrm{L}}{\mathrm{U}_\infty} \tag{4.69}$$

St prediction models by Rossiter[2], Heller et al[13] and Block[6], deviate as flow becomes incompressible $M_\infty < 0.3$, due to lack of modal line curvature. East[8] mapped the curve for deep cavity mode 1, excluding BL metrics, which over predicted for L/D > 1. Viscosity is more abundant in incompressible flow, due to lack of compressibility. Thus expected to have a larger impact on cavity response, compared to $M_\infty > 0.3$, where prior models were derived, and fairly accurate. BL metrics are thus theorised to improve modal prediction for incompressible flow.

This thesis updates East's[8] model, by accounting for the BL, with its thickness to cavity depth ratio; δ/D, to scale vorticity. δ/D is considered effective depth, with respect to external and internal flow interaction. This approach starts at lower St for higher M_∞, and converges through a curved profile, toward higher St, as flow becomes incompressible. δ/D provides an inverse relation to U_∞, as δ reduces when $M_\infty < 0.3$ increases, with cavity depth D constant. Moreover, in favourable pressure gradient $dp/dx < 0$ cases, the BL is thin and laminar, shifting

dominant frequencies, compared to the flat-plate baseline. Therefore, dimensionless pressure gradient for the incline surface of the conic nose, and convex curved surface of the ogive and parabola, is included in the new approach, to shift St based on observed phenomena.

4.6 Data Processing and Analysis Summary

In this chapter, HWA and USP data was post-processed. HWA data was calibrated and converted to velocity. Signal statistics have been assessed, and uncertainty calculated for a maximum of $u_{i,tot} = 3.05 \times 10^{-2}$m/s, and both are within expected behaviour of Dantec Systems.

Velocity profiles were constructed, and BL data calculated. Implementing similar BL solutions of the 1/7th power law for a flat-plate, Falkner-Skan[22,105] for wedge flow, and an extended Falkner-Skan[7,23] for curved flow, to model flow over variable U/S geometry of; the flat-plate baseline, conic, ogive, and parabola respectively, using HWA data to validate BCs, ICs and assumptions. BL data calculated includes; disturbance thickness δ, displacement thickness δ^*, momentum thickness θ, wall shear stress τ_w, pressure gradient dp/dx, and Re_x, to determine if flow is laminar or turbulent, dependant on the point of transition $\mathrm{Re}_{x,crit}$.

Following, USP data was processed to allocate case number and spatial coordinates, relative to each cavity geometry, and calculate non-dimensional quantities C_p, and time-averaged $C_{p,rms}$, to determine oscillatory intensity. The results are presented in Section 6, as contour and streamwise magnitude plots, to assess effects of changed variables. Tube distortion effects, as a result of experimental set-up were corrected for, including; resonance, pressure wave phase shift, and amplitude distortion. Lastly, signal analysis using FFT was performed on both HWA and USP results, to provide their frequency spectra, and response magnitude. DMD was additionally applied on USP results to account for spatial distribution over the cavity surfaces.

Results accumulated by this section, are presented in Chapter 5 for HWA velocity profiles, BL data and spectra, and Chapter 6 for pressure response maps and spectra. Both are then correlated in Chapter 7, where major findings are developed and summarised.

Chapter 5

Hot-Wire Results & Discussion

This chapter presents hot-wire anemometry (HWA) results, including; reconstructed velocity profiles, corresponding boundary layer (BL) data of disturbance δ, displacement δ^* and momentum θ thickness, wall shear stress τ_w, pressure gradient dp/dx, and respective FFT spectra, at $+y$ points in the velocity profile. Free-stream (FS, ∞) Reynolds number Re_∞/m, and U/S geometry effects are assessed. Followed by how presence of a cavity downstream (D/S) alters velocity U/S. Chapter 7 cross-correlates these and USP results in Chapter 6, where a relationship is formulated between the BL and cavity response, to highlight BL structural dependence.

5.1 Velocity Profiles

This section observes velocity profiles measured 5mm U/S of the cavity LE ($x = -5$mm) over $y = 0 - 270$mm. Corresponding BL δ, δ^*, θ, τ_w, and $dp/dx < 0$ in Section 5.2, and Table 4.2-4.14 are considered. Effects of Re_∞/m, U/S geometry (conic, ogive, parabola, flat-plate) and a cavity D/S are assessed. The latter by comparing profiles when the cavity is open (L/D = L/W = 3) vs closed. Temperature T_∞ thus kinematic ν_∞ and dynamic μ_∞ viscosity remain relatively constant. Therefore, Re_∞/m is considered $\propto \mathrm{U}_\infty$, and $\tau_w \propto du/dy$. Profile axis are non-dimensionalised for comparison. The x-axis is local velocity u, normalised by U_∞. The y-axis is distance from the wall y, normalised by the baseline flat-plate δ_f. Each profile captures the BL, and accelerated flow regions ($dp/dx < 0$) in nose cone U/S geometry cases.

5.1.1 Effect of Free-Stream Reynolds Number Re_∞

Fig. 5.1 presents Re_∞/m effects on the velocity profile 5mm U/S of the cavity LE ($x = -5$mm), for each U/S geometry. For the flat-plate, as Re_∞/m increases, u/U_∞ values increase toward unity, $\propto \tau_w$ increase, and δ decrease at $u/\mathrm{U}_\infty \approx 1$. The effect appears small as flat-plate δ_f is the baseline. However, Table 4.2 showed increased τ_w and reduced δ as Re_∞/m increases.

For nose cases, velocity profiles invert about $u/\mathrm{U}_\infty = 1$, due to local flow acceleration $dp/dx < 0$, which alters location of BL δ compared to the flat-plate. Instead Falkner-Skan wedge flow [22] was used for the conic, and an extended Falkner-Skan [7] for curved ogive and parabola [23] (See Section 4.3.2 and 4.3.3 respectively). In these solutions, δ is at a point in the velocity profile where flow becomes inviscid, by satisfying stream function ψ. In this case, increasing Re_∞/m

increases dp/dx, which increases acceleration of local velocity u relative to the FS; $u > U_\infty$, further toward the δ point. Therefore, τ_w increases and BL δ[7,23] decreases.

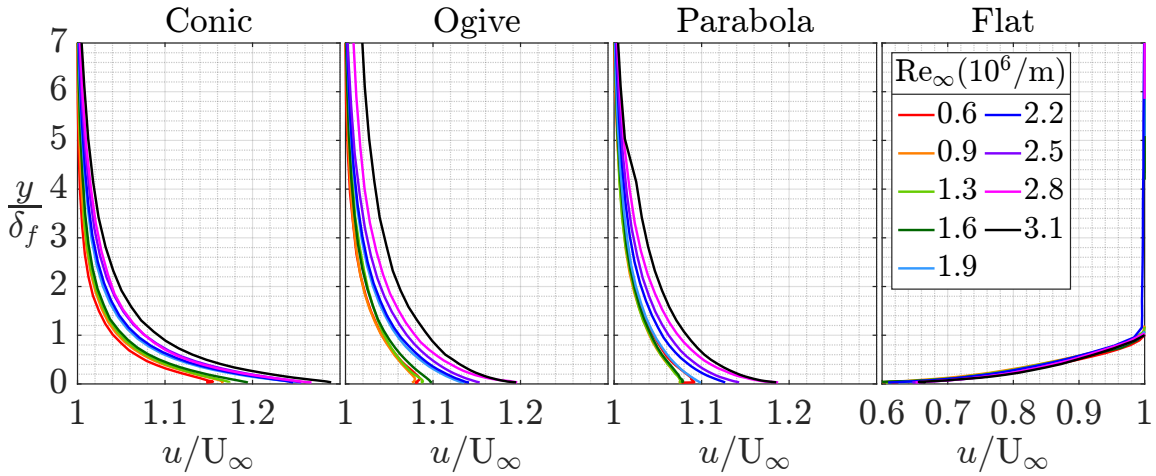

Figure 5.1: HWA: Velocity Profile ΔRe_∞/m Effect: $x = -5$mm from cavity LE, $y = 0 - 270$mm

Overall, increasing Re_∞/m increases u/U_∞ values close to the wall, relative to a FS datum. This is $\propto \tau_w$ increase and dp/dx increase when nose cones are present, for net δ decrease. This is expected per Prandtl BL formulation[88], as Re_∞ is inversely proportional to vertical or y-axis displacement, which represents BL δ per viscous boundary conditions (BCs). Because increasing U_∞, induces a larger force per unit area of flow past the wall, for more fluid present at a higher rate, leading to more efficient BL mixing, which reduces δ, as observed.

5.1.2 Effect of Upstream Geometry

Fig. 5.2 presents effects of U/S geometry, on the velocity profile 5mm U/S of the cavity LE ($x = -5$mm). Results highlight a distinct difference in BL structure due to U/S geometry variation, with respect to turbulent, and laminar flow, and varying degrees of $dp/dx < 0$.

The flat-plate produces a typical flat-plate turbulent profile $dp/dx = 0$, due to large $x \approx 1.8$m from the start of the test-section (TS); $Re_x = 1.8 - 9.3 \times 10^6 > Re_{x,crit} \approx 5{\times}10^5$, where $Re_{x,crit}$ represents transition from a laminar to turbulent BL. This creates a thick turbulent BL at the cavity LE, which is apparent as significantly larger $du/dy \propto \tau_w$, when compared to laminar BL values in noses cases. This occurs because turbulent viscosity is significantly higher than laminar viscosity, triggering turbulent fluctuations, which rapidly change direction, increasing the velocity gradient near the wall, thus tangential force exerted on the wall τ_w.

Nose cases instead have an accelerated laminar BL profile, due to incoming laminar flow, which is sustained by favourable $dp/dx < 0$ over small x, from the nose LE to TE; $x = 0.14$m for $Re_x = 0.72 - 3.72 \times 10^5 < Re_{x,crit} \approx 5{\times}10^5$. For flow acceleration through favourable $dp/dx < 0$, resulting $u >> U_\infty$, also increases $Re_{x,crit}$, which further supports laminar BL conditions, producing magnitude smaller $du/dy \propto \tau_w$, than turbulent BL conditions. Moreover, increasing $dp/dx < 0$, increases local flow rate u thus τ_w, pushing the profile further forward; $u/U_\infty >> 1$. As the conic nose produces the largest $dp/dx < 0$, flow accelerates the furthest, with higher τ_w, and lower δ, compared to ogive and parabola noses, with slightly thicker laminar δ, and lower τ_w, of correlative profile curvature due to their geometric similarity.

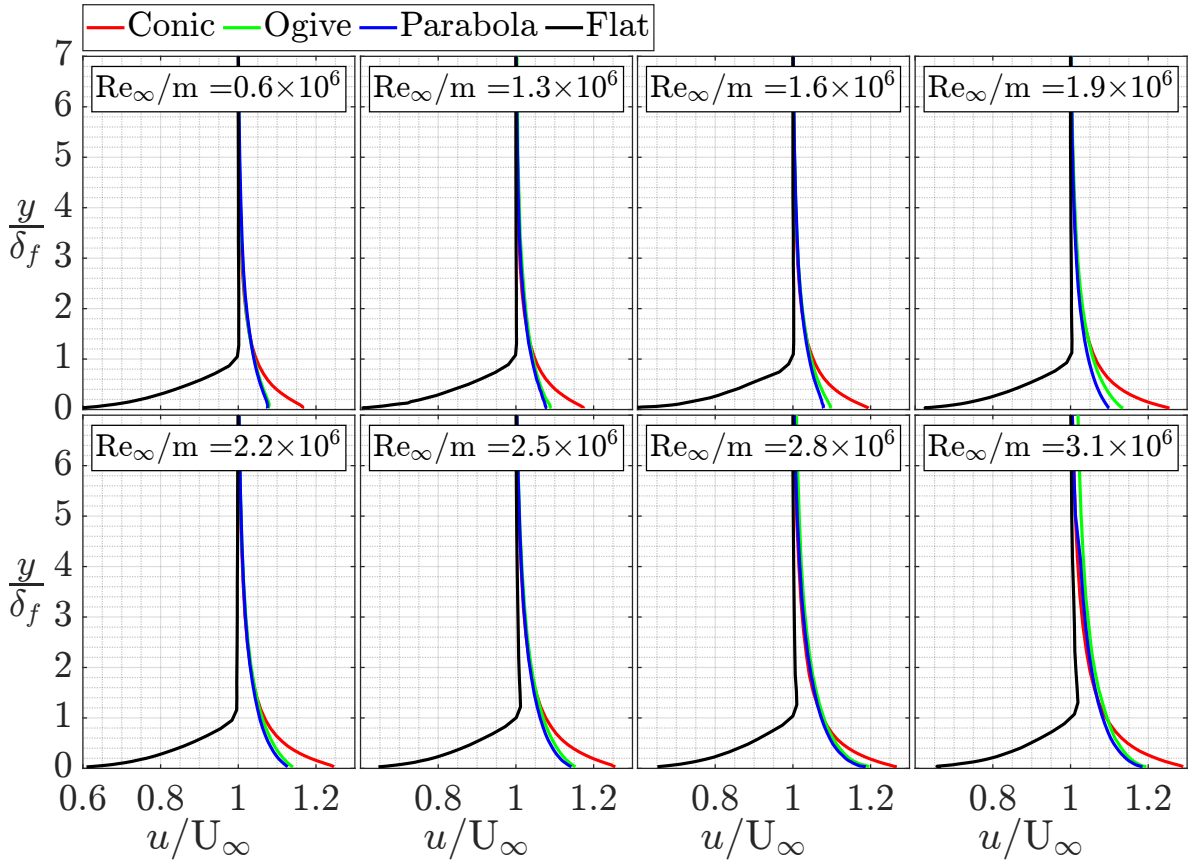

Figure 5.2: HWA: Velocity Profile Geometry Effect: $x = -5$mm from cavity LE, $y = 0 - 270$mm

Overall, the flat-plate baseline BL is turbulent with large τ_w, and δ, due to large x, and turbulent viscosity, triggering more rapid gradient change. Nose BLs are laminar with comparatively small τ_w and δ, due to small x, and $dp/dx < 0$, which accelerates flow over the wall. The larger dp/dx increasing τ_w relative. Lastly, Prandtl's BL theory conserved above, assumes;

(1) Flat-plate τ_w is effective streamwise dx in increments dy for a BL with $dp/dx = 0$.

(2) Laminar to Turbulent BL transition occurs when $\mathrm{Re}_{\mathrm{x_{crit}}} = 5 \times 10^5$, however laminar incoming flow is sustained by $dp/dx < 0$, whilst also decreasing δ in x.

(3) External forces are small compared to $O(\delta)$, thus neglected by order of magnitude analysis.

However, if a disturbance is present D/S producing periodic feedback U/S, τ_w and $\mathrm{Re}_{\mathrm{x_{crit}}}$ change, due to an external force, if $\geq O(\delta)$. Based on Stokes 2$^{\mathrm{nd}}$ problem, the force renders $dp/dx = 0$ false for flat-plate flow with discontinuity i.e., cavity D/S, due to altered dynamics, per below.

5.1.3 Effect of Cavity Downstream

Fig. 5.3 presents effects of a cavity D/S, on the velocity profile 5mm U/S of the cavity LE ($x = -5$mm). For the flat-plate, u/U_∞ values $\propto \tau_w$ increase and δ decreases. For laminar BL nose cases, $u/\mathrm{U}_\infty \propto \tau_w$ and dp/dx increase for net δ decrease, indicating amplified $dp/dx < 0$. Therefore, a cavity D/S modifies velocity U/S, altering viscous and dp/dx force at the wall.

The feedback effect is less abundant in the flat-plate case, as δ_f is the normalised baseline. Also because a turbulent BL, is known to weaken periodicity in the cavity response, which is responsible for feedback U/S. Karamcheti[15] likened the effect to a low pass filter, which was

similarly observed by [43, 51, 68, 69, 73, 80], as a reduction in response due to a turbulent BL δ U/S. In some cases shifting, or completely removing cavity response, if overwhelmed by incoming random turbulent buffet or far-field broadband noise. In nose cases, the BL is laminar, due to small x, sustained by $dp/dx < 0$, which creates a distinct periodic response, that strengthens feedback[15,28,43]. Moreover, increasing $dp/dx < 0$ with Re_∞/m or geometry U/S, is $\propto \tau_w$ increase, and δ[7,23] decrease, as observed when the cavity is open. Therefore, cavity presence D/S increases local velocity u U/S, by increasing or introducing $dp/dx < 0$.

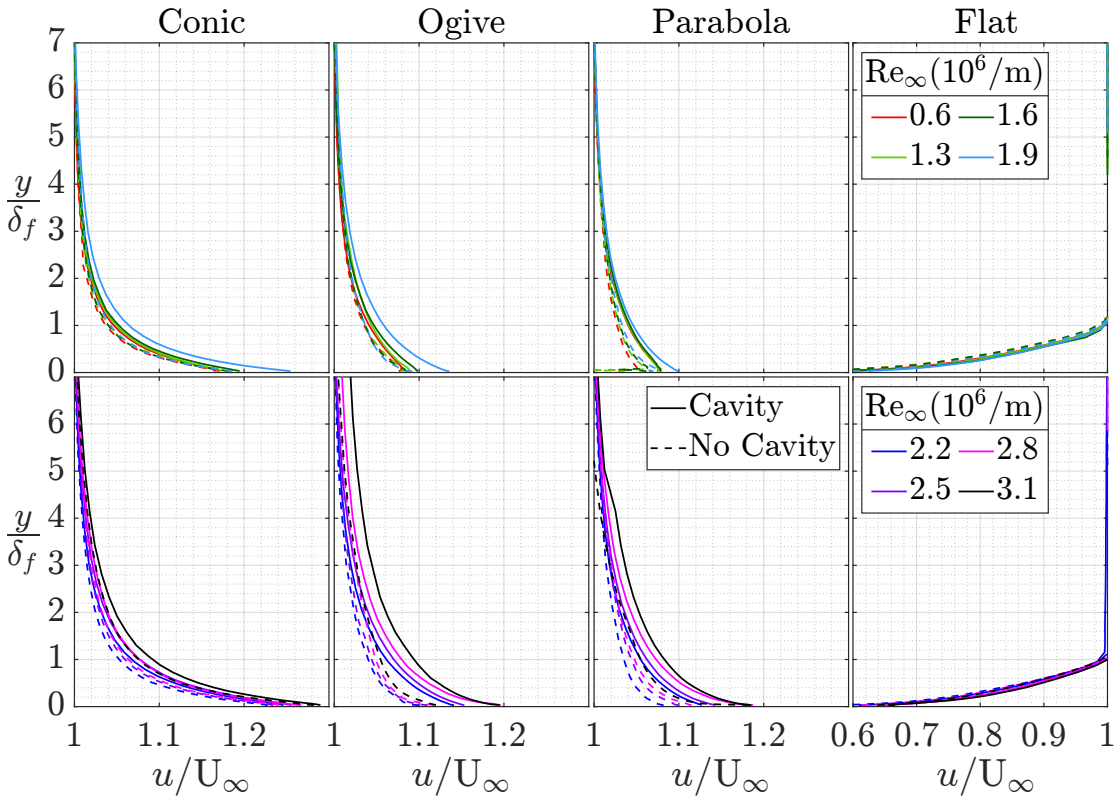

Figure 5.3: HWA: Velocity Profile Cavity Effect: $x = -5$mm from cavity LE, $y = 0 - 270$mm

5.1.4 Integral Time Scale

ITS (τ_i) indicates how long a fluid structure is influenced by its past, prior to significant change. Large τ_i, indicates persistent large-scale structures, with slow dynamic decay. Small τ_i, indicates rapid decay from past correlation, which is characteristic of turbulent flow; rapid direction change/mixing, with high τ_w. Fig. 5.4 presents ITS (calculated in Section 4.2.1) for increasing Re_∞/m of each U/S geometry, when the cavity is open (L/D = L/W = 3) verse closed. Similar trends with increasing Re_∞/m are apparent, however vary from the near wall to FS.

In the FS, τ_i increases with Re_∞/m, indicating increased flow stability. This is expected, as higher velocity stabilises streamlines at low-speed, dampening irregular fluctuations, due to growing dominance of inertia, and reduced WT buoyancy[89]. Near the wall, as Re_∞/m increases, τ_i reduces, thus structures decay faster, indicating higher τ_w in BL or accelerated flow, as expected. For the flat-plate turbulent BL, $\Delta\tau_i$ for $\Delta\mathrm{Re}_\infty$/m is larger than laminar nose cases, as turbulent τ_w is larger, thus increases more relative, compared to small laminar τ_w.

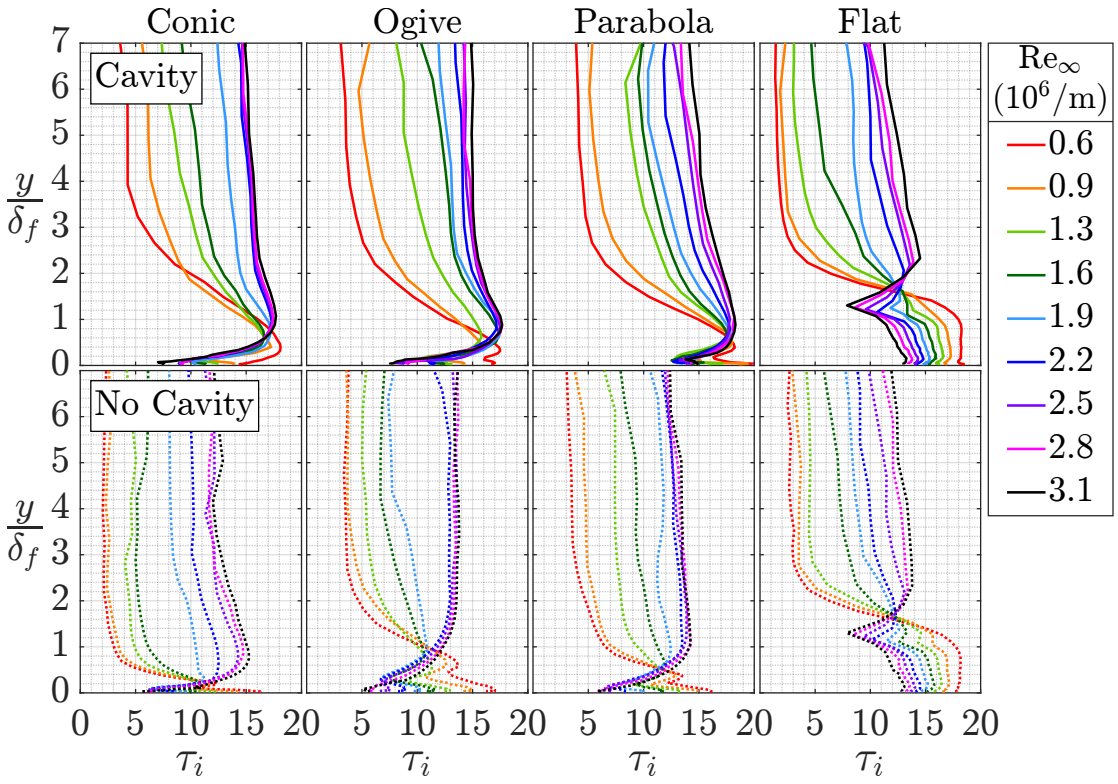

Figure 5.4: HWA: Integral Time Scale τ_i at Δ Re_∞/m: $x = -5$mm from cavity LE, $y = 0 - 270$mm

5.2 The Boundary Layer

From velocity profiles above, BL data; disturbance δ, displacement δ^*, momentum θ thickness, wall shear stress τ_w, and pressure gradient $dp/dx < 0$ were derived. Using Blasius and turbulent flat-plate BL theory for the flat-plate baseline, Falkner-Skan for the conic, and extended Falkner-Skan for curved ogive and parabola (See Section 4.3). Results in Table 4.2- 4.4 are presented in Fig. 5.5-5.8 for increasing Re_∞. Note: the left plot is flat turbulent BL results, distinguished from laminar nose BL $dp/dx < 0$ cases on the right, due to magnitude difference. Fig. 5.9 presents dp/dx results for $\Delta\mathrm{Re}_\infty$ in nose cases. Primary observations are listed below:

(1) As Re_∞ increases, τ_w increases and BL δ reduces.

(2) The flat-plate baseline has a thick turbulent BL as $\mathrm{Re}_x >> \mathrm{Re}_{x,\mathrm{crit}}$, and magnitude larger δ, τ_w than laminar BL nose cases with $dp/dx < 0$, where $\mathrm{Re}_x < \mathrm{Re}_{x,\mathrm{crit}}$.

(3) Conic $dp/dx < 0$ is largest and δ smallest, due to a steeper physical gradient, increasing acceleration of local $u \propto \tau_w$ increase for δ decrease. Followed by ogive then parabola.

(4) In nose cases, with a laminar BL, as Re_∞ increases dp/dx grows, increasing local u acceleration and τ_w relative to net δ decrease.

(5) Cavity presence increases τ_w, reduces δ, and increases $dp/dx < 0$ in nose cases.

Observations (1-4) were expected based on Prandtl BL theory and formulation [23,99] for Re_∞, U/S geometry, and $dp/dx < 0$ effects. However, the effect of cavity presence D/S is a point of interest, considering $\mathrm{U}_\infty, \mu_\infty$, and length scale are constant, when the cavity is open and closed. Nonetheless, τ_w increases, and δ reduces, when the cavity is present D/S. This implies an

increase in local velocity u U/S, due to a force from the cavity ($dp/dx < 0$), increasing velocity into the cavity. The effect also grows with Re_∞, akin to increasing $dp/dx < 0$ magnitude.

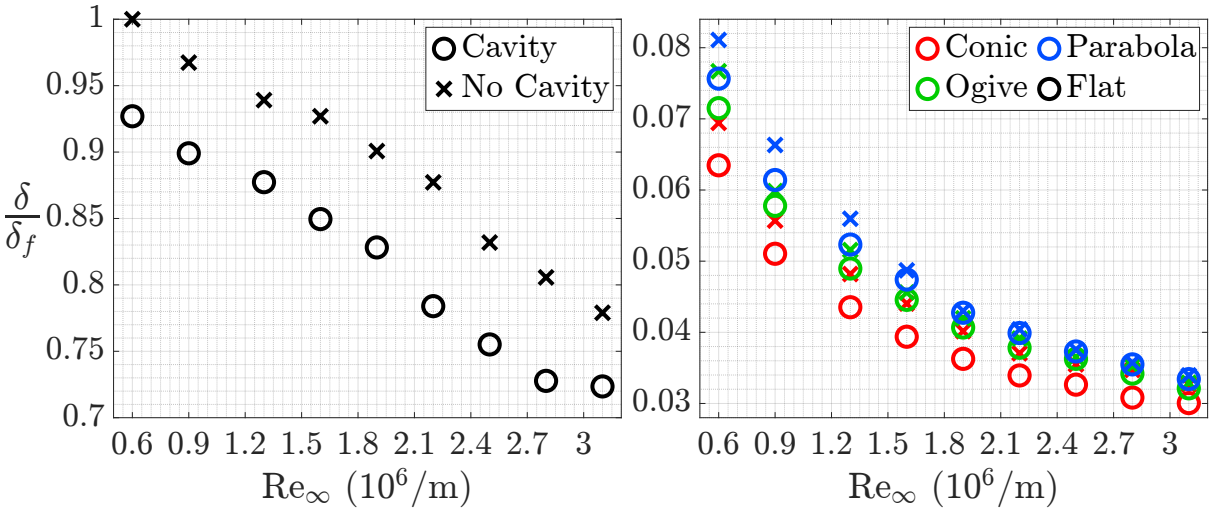

Figure 5.5: HWA: BL Disturbance Thickness δ at $x = -5$mm from cavity LE

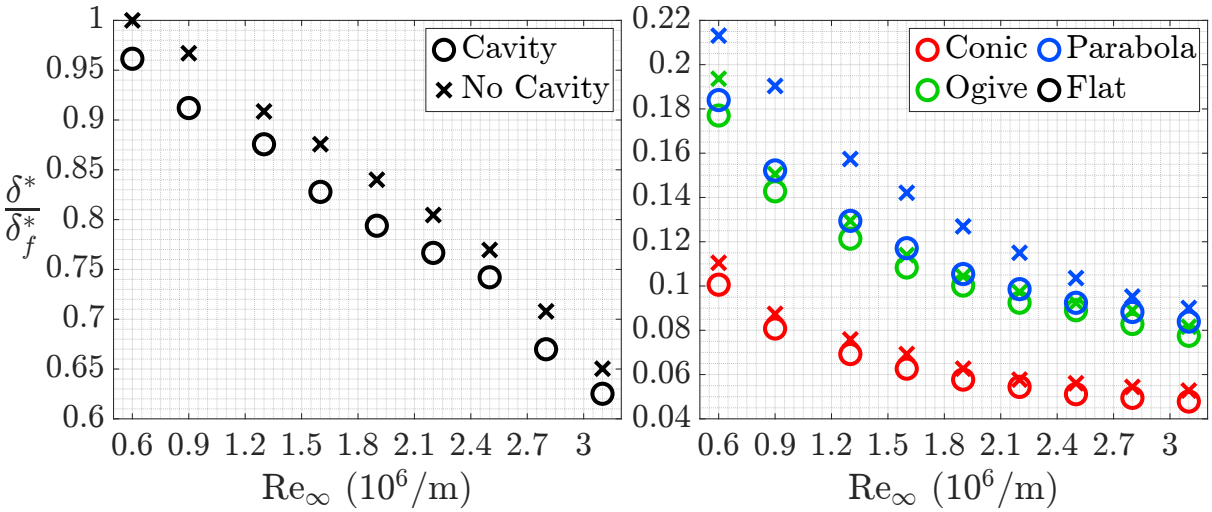

Figure 5.6: HWA: BL Displacement Thickness δ^* at $x = -5$mm from cavity LE

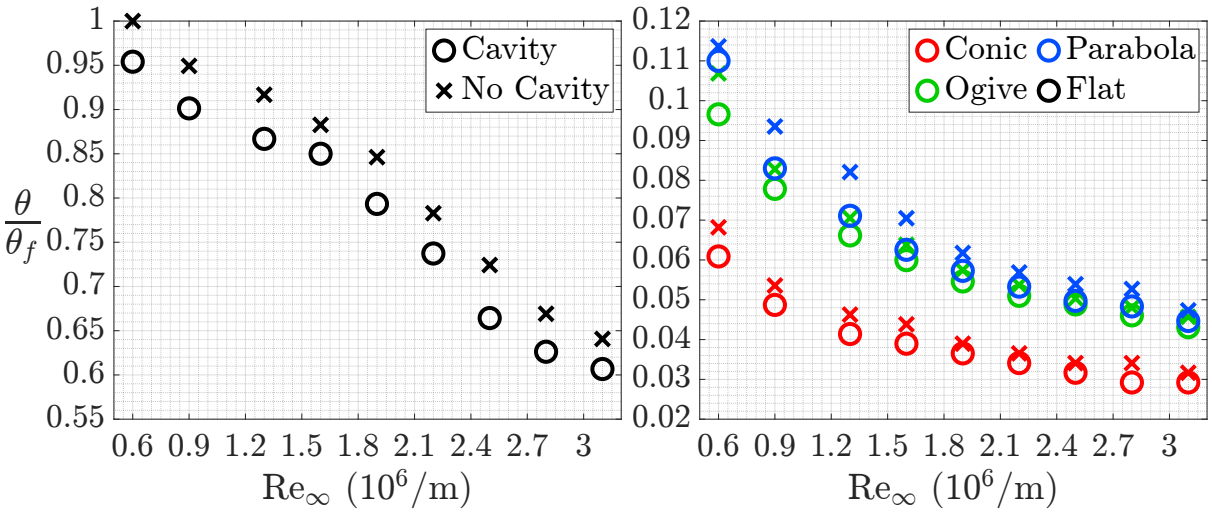

Figure 5.7: HWA: BL Momentum Thickness θ at $x = -5$mm from cavity LE

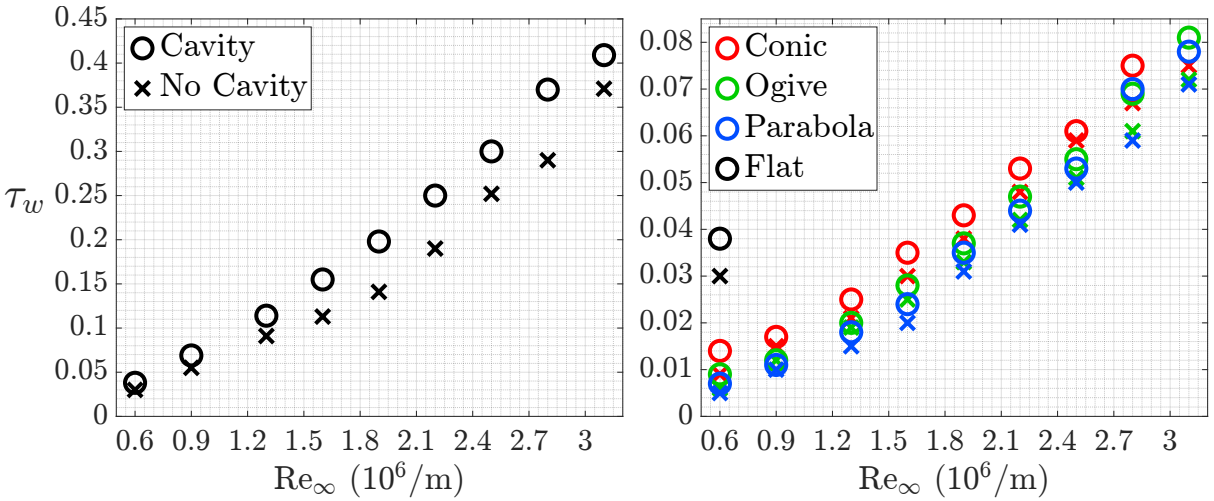

Figure 5.8: HWA: Wall Shear Stress τ_w (Pa) at $x = -5$mm from cavity LE

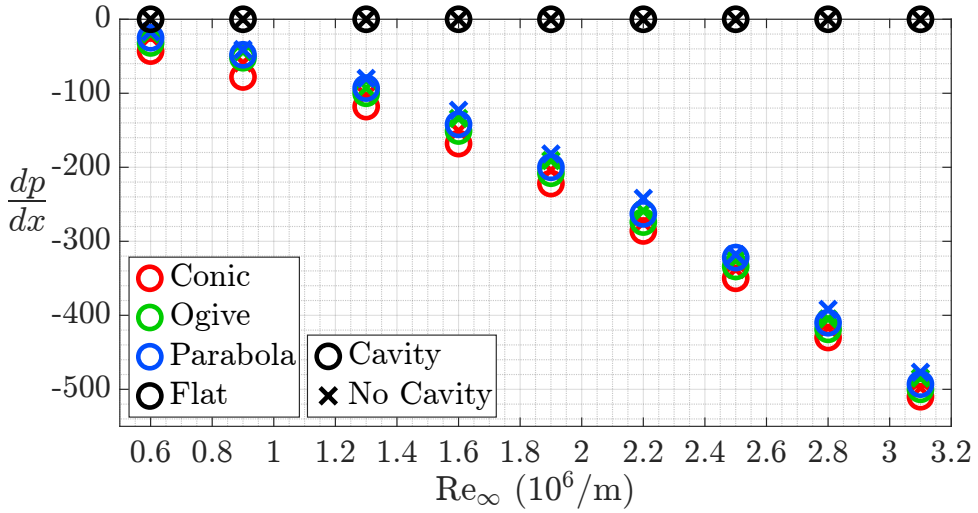

Figure 5.9: HWA: Favourable Pressure Gradient dp/dx (Pa/m) at $x = -5$mm from cavity LE

5.3 Velocity Spectra

This section assesses the HWA FFT results of velocity profile measurements taken 5mm U/S of the cavity LE ($x = -5$mm) at logarithmically distributed points in $y = 1 - 270$mm, over $t =$ 60s at $f = 2^{15}$Hz. Effects of Re_∞, U/S geometry, cavity presence and $+y$mm from the wall are observed. Parabola results are considered proxy of ogive due to correlative geometry per Fig. 5.12. Table 5.1 provides peak SPL reference values for overall trends.

5.3.1 Effect of Free-Stream Reynolds Number Re_∞

Fig. 5.10 and 5.11 present velocity spectra for $\Delta\mathrm{Re}_\infty$ at $+y = 1.2$ and 32.3mm from the wall for U/S conic, ogive (parabola by proxy) and flat geometry, with no cavity D/S. Table 5.1 provides further indication of SPL change for $\Delta\mathrm{Re}_\infty$. $+y = 1.2$mm is within all BLs, and $+y = 32.3$mm is in the FS. As expected, SPL increases with Re_∞. OASPL converges $\mathrm{Re}_\infty/m \approx 2.5 \times 10^6$, as WT fluid heats up due to work-to-fluid transfer from the fan, returning smaller increase in $\mathrm{U}_\infty/\nu_\infty$, compared to lower Re_∞. However, peak SPL per Table 5.1 increases. Frequency f (kHz) observations align to typical BL spectra; near-wall smaller high-f structures, and larger lower-f

structures away from the wall. Peak f increases slightly, with Re_∞, as expected. Additional peaks are also introduced, due to added structures in higher Re_∞ flow. Especially in nose cases outside the BL per Fig. 5.11, reflecting an accelerated flow region.

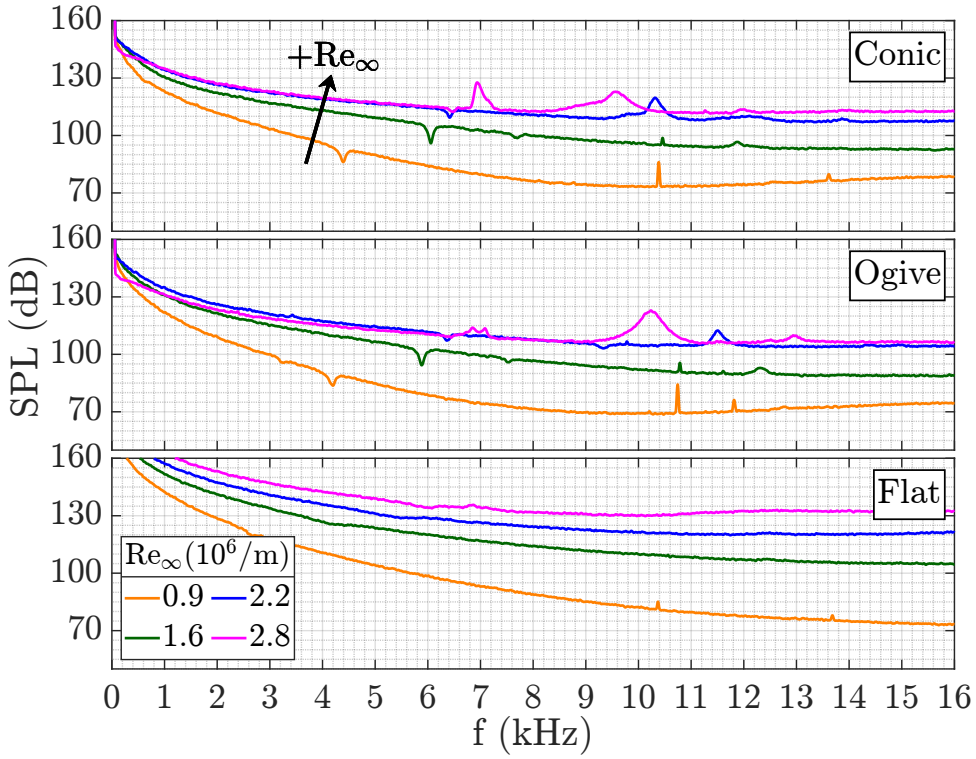

Figure 5.10: HWA: ΔRe FFT: $y = 1.2$mm, $x = -5$mm from cavity LE

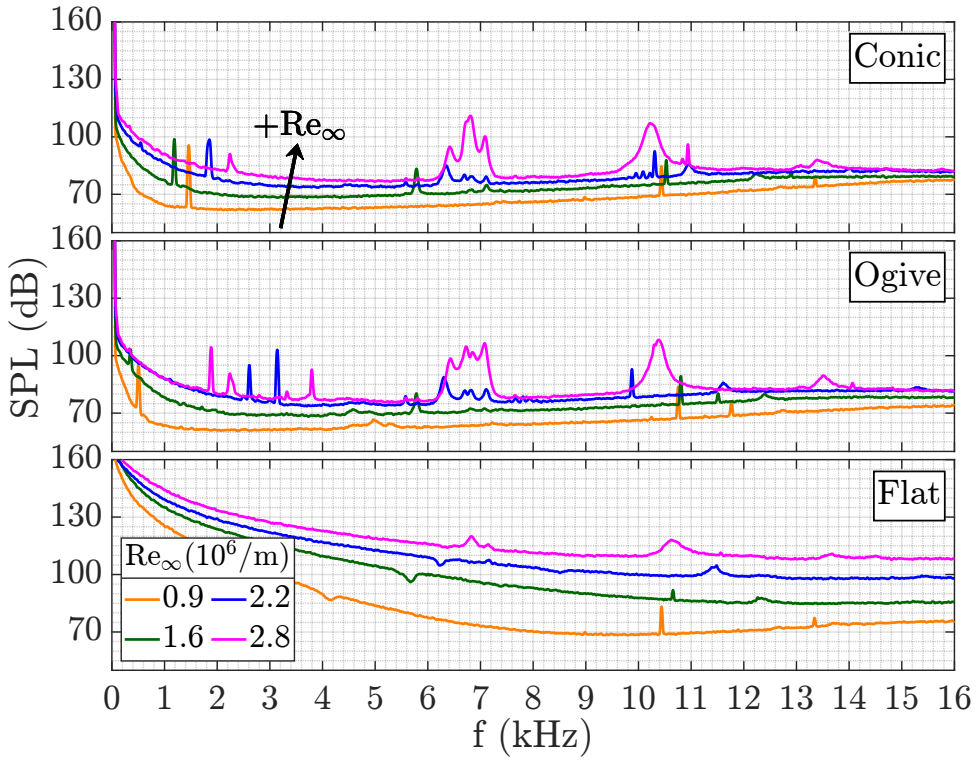

Figure 5.11: HWA: ΔRe FFT: $y = 32.3$mm, $x = -5$mm from cavity LE

5.3.2 Effect of Upstream Geometry

Fig. 5.12 compares U/S geometry at $U_\infty = 40$m/s $\propto Re_\infty/m = 2.5 \times 10^6$, for various $+y$ from the wall, with no cavity D/S. $y = 1.2$mm is within the BL for all, $y = 3.2$mm is outside the BL for all except the flat-plate, whilst in the accelerated region for nose cases, and $y = 32.3$mm is outside the BL for all, and in the accelerated region for nose cases. At $y = 32.3$mm, FS structures start to interact with accelerated flow, enhancing distinct peaks due to a coupling effect. Table 5.1 provides further indication of SPL change with U/S geometry.

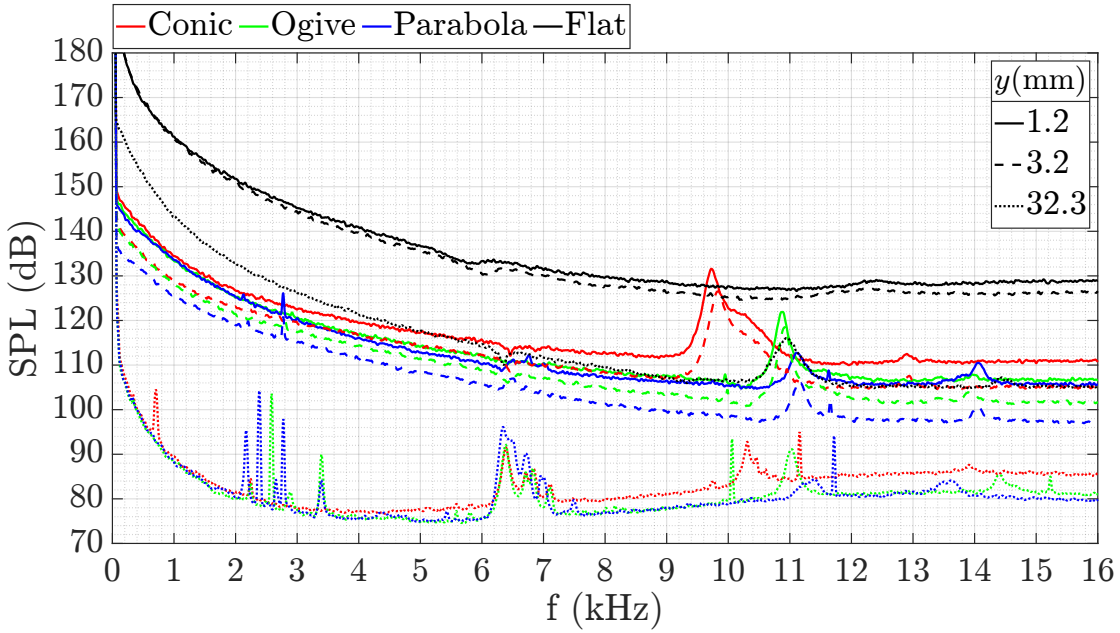

Figure 5.12: HWA: ΔU/S Geometry FFT: $x = -5$mm from cavity LE, $Re_\infty/m = 2.5\times10^6$

Flat-plate spectra has higher SPL, as the BL is turbulent, attributed to higher broadband noise. There are however, no distinct spectral peaks, which would typically be expected in a turbulent BL, likely due to broadband noise. Nose spectra share similar SPL, the conic is slightly higher, and closer to the wall. Due to a higher accelerated flow magnitude, raising relative flow momentum. Furthest from the wall in nose cases, more distinct peaks are apparent. These are a function of FS structures coupled to dp/dx as aforementioned, due to presence of the model accelerating flow relative to the FS. They are not in the flat case, as the model is in the floor, outside the TS, reducing relative fluid structure complexity.

5.3.3 Effect of Distance from the Wall $+y$

Fig. 5.13 shows the effect of increasing distance $+y$ from the wall at $U_\infty = 40$m/s $\propto Re_\infty/m = 2.5 \times 10^6$. Table 5.1 provides further indication of SPL change. Overall, regardless of U/S geometry, increasing y reduces SPL, as expected. Because relative turbulence reduces away from the wall, as viscosity, and $dp/dx < 0$ effects dwindle. For the flat case, reduced SPL is delayed until larger $+y$, due to a thick turbulent BL having larger influence, further from the wall. Moreover, in the flat case, a small peak emerges at $f = 11$kHz, becoming more distinct as $+y$ increases. This suggests a turbulent BL structure, enhanced by transition into the FS. In every case, a cluster of peaks emerge from $f \approx$ 6-8kHz representing FS flow, as they do not appear in the near wall region. Similarly at $f < 2$kHz. Nose cases have a distinct frequency for;

conic at $f \approx 9$kHz, then ogive (parabola by proxy) at $f \approx 9.6$kHz closest to the wall, becoming more distinct as y increases. Then at a point merges with a FS peak. This peak aligns with $dp/dx < 0$, which grows, and eventually couples to FS flow, amplifying the response.

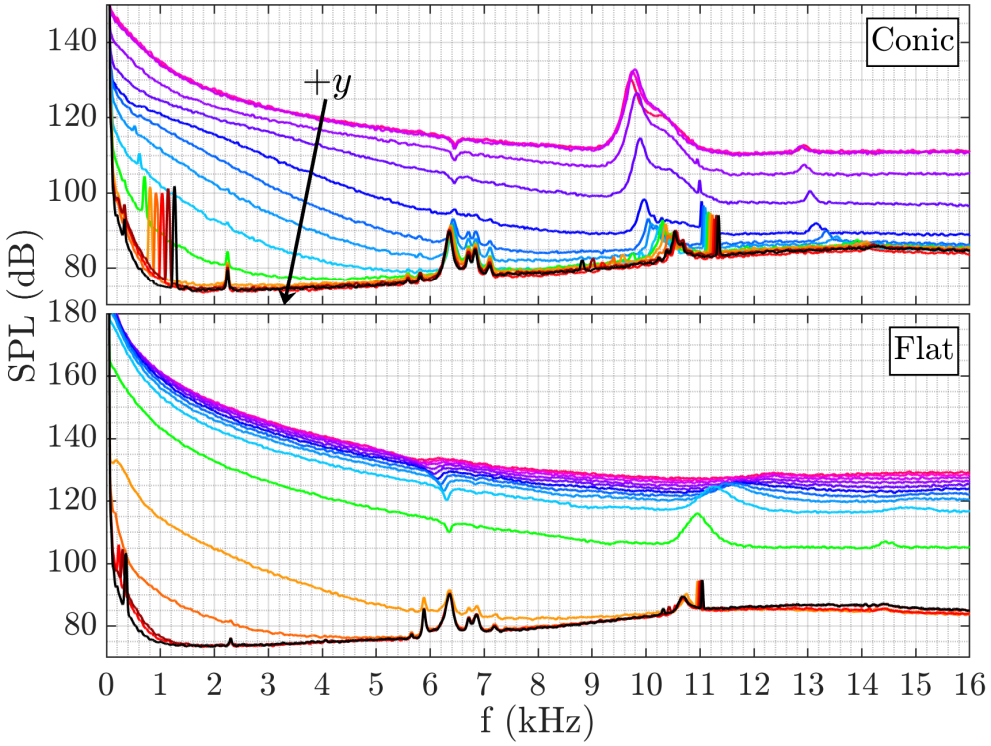

Figure 5.13: HWA: $+y$ FFT: $x = -5$mm from cavity LE, $\mathrm{Re}_\infty/\mathrm{m} = 2.5{\times}10^6$

5.3.4 Effect of the Cavity Downstream

Fig. 5.14 presents the effect of a cavity D/S on U/S velocity spectra, for conic, ogive (parabola by proxy) and flat U/S geometry at $\mathrm{U}_\infty = 40$m/s $\propto \mathrm{Re}_\infty/m = 2.5 \times 10^6$, and various $+y$. For the flat-plate, inside the BL $y < 32$mm, there is negligible difference. Outside the BL $y > 32$mm, there is a shift in peak $f \approx 11 \rightarrow 10.6$. In nose cases, there is an abundant shift in spectra, regardless of y. Not only an increase in OASPL, but new peaks also arise when the cavity is present, with large increase in SPL, compared to peaks in cavity absence.

For the conic nose, two peaks arise for $f \approx 6.4 - 7.2$kHz jumping by $\approx$ 25-50dB from the no cavity baseline, and three for $f \approx 13 - 14.3$kHz jumping by $\approx$ 10-30dB. The jump is larger at y = 32.3mm, due to reduced nose $dp/dx < 0$ effects. Thus, cavity presence also effects the wider region. Furthermore, a peak at $f \approx 9.75$kHz when no cavity is present, disappears when the cavity is D/S. Implying a BL structure, suppressed by the cavity D/S.

For the ogive nose (parabola by proxy), additional peaks also occur, and OASPL increases from the no cavity baseline. Large impact further away from the wall alike the conic nose, is not apparent, instead OASPL decreases, aside from peaks. Therefore, must be a factor of $dp/dx < 0$, which is larger for the conic, amplifying cavity presence, further away from the wall. Overall, cavity presence D/S effects velocity spectra U/S of the cavity. The effect is only a small shift in peak frequency for the flat case. In nose cases, amplified $dp/dx < 0$ is implied.

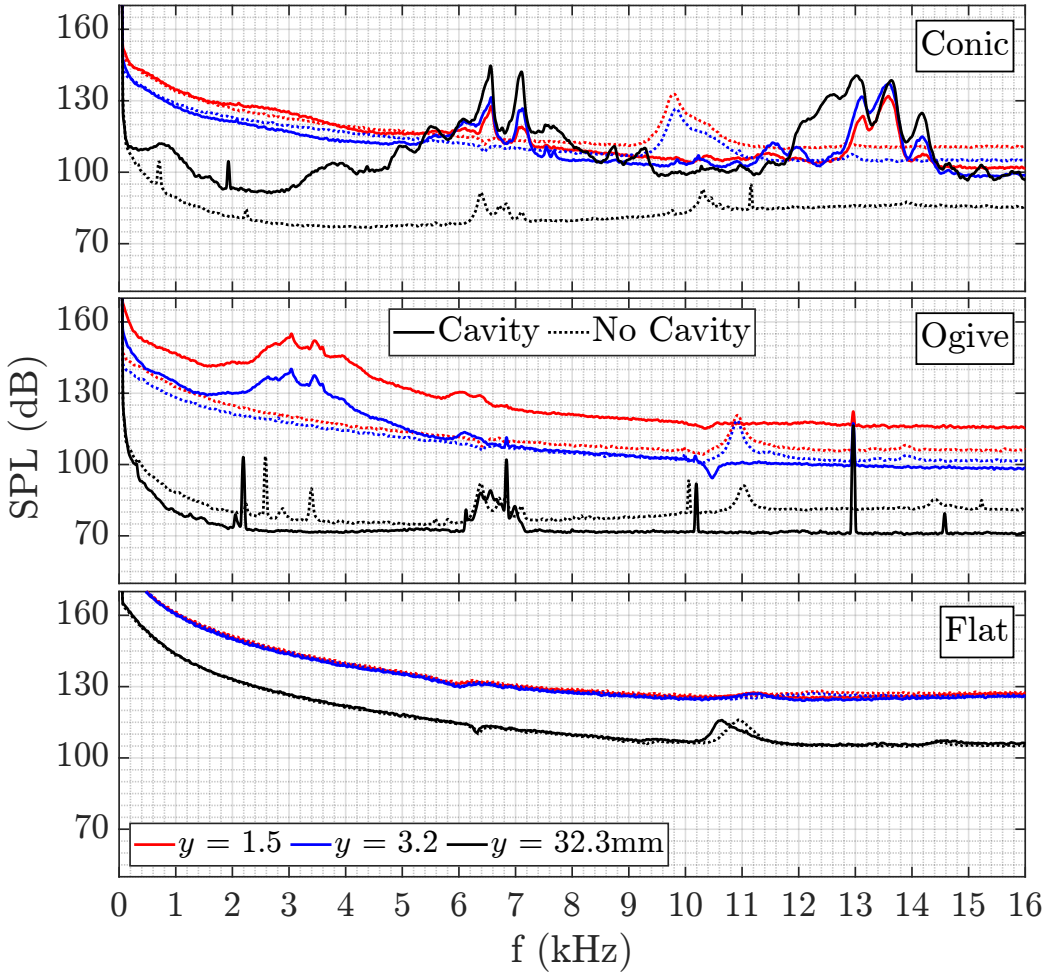

Figure 5.14: HWA: Cavity Effect FFT: $x = -5$mm from cavity LE, $\mathrm{Re}_\infty/\mathrm{m} = 2.5{\times}10^6$

5.3.5 Summary of Magnitude Response

Table 5.1 and Fig. 5.15 present peak SPL, which support the overall trend of spectral magnitude observed above. Increasing $\mathrm{Re}_\infty/\mathrm{m}$, increases SPL. Increasing distance further from the wall $+y$, decreases SPL. Decreasing laminar BL δ, through increasing dp/dx, with geometry U/S increases SPL. The flat case has no distinct peaks until further away from the wall, where turbulent BL sustains highest SPL. At this point nose cases are outside the BL in the accelerated region.

5.4 Hot-Wire Results Summary

From results above, several key findings are attributed, to support hypothesis in Chapter 7. The flat-plate baseline geometry produces a thick turbulent BL, with $\mathrm{Re}_x >> \mathrm{Re}_{x,\mathrm{crit}}$, and magnitude larger τ_w and δ, compared to thin laminar BL nose cases, with $\mathrm{Re}_x < \mathrm{Re}_{x,\mathrm{crit}}$ and $dp/dx < 0$, resulting in very thin δ. Increasing $\mathrm{Re}_\infty/\mathrm{m}$, $dp/dx < 0$ through U/S geometry, and cavity presence D/S, resulted in increased τ_w, and $dp/dx < 0$ in nose cases, for net δ decrease.

Increasing $\mathrm{Re}_\infty/\mathrm{m}$, increased overall magnitude and peak SPL, shifting peak frequencies, as expected with δ decrease. Flat-plate SPL is higher due to its turbulent BL. Nose cases share similar SPL, their peak frequency dependant on $dp/dx < 0$. The conic nose has highest overall magnitude, and peak SPL near the wall. Cavity presence D/S increased magnitude, and peak

SPL by $10 - 50dB$, dependant on peak frequency. When increasing distance $+y$ from the wall, high frequency peaks reduced in SPL before shifting to a low frequency peak in the FS.

Table 5.1: HWA: SPL (dB) for $\Delta \mathrm{Re}_\infty/\mathrm{m}$, ΔGeometry and Δy

y (mm)	Re_∞/m	0.6	0.9	1.3	1.6	1.9	2.2	2.5	2.9	3.1
1.2	Conic	90.6	100.3	103.3	112.1	113.3	119.7	131.6	133.6	135.9
	Ogive	86.2	90.7	97.9	109.8	111.9	113.9	125.8	127.8	131.7
	Parabola	81.2	86.5	94.8	97.9	106.1	110.6	121.9	123.7	129.2
	Flat	73.8	84.8	-	-	-	-	-	-	-
3.2	Conic	89.7	94.7	100.1	101.2	109.5	114.7	117.6	122.1	126.5
	Ogive	83.7	86.9	95.6	99.5	105.4	112.4	116.7	120.5	121.5
	Parabola	83.3	83.4	92.7	96.1	104.1	108.4	114.8	118.5	120.9
	Flat	74.3	84.2	92.0	-	-	-	-	-	-
32.3	Conic	89.7	94.7	100.1	101.2	109.5	114.7	117.6	122.1	126.5
	Ogive	83.7	86.9	95.6	99.5	105.4	112.4	116.7	120.5	121.5
	Parabola	83.3	83.4	92.7	96.1	104.1	108.4	114.8	118.5	120.9
	Flat	74.3	84.2	92.0	-	-	-	-	-	-

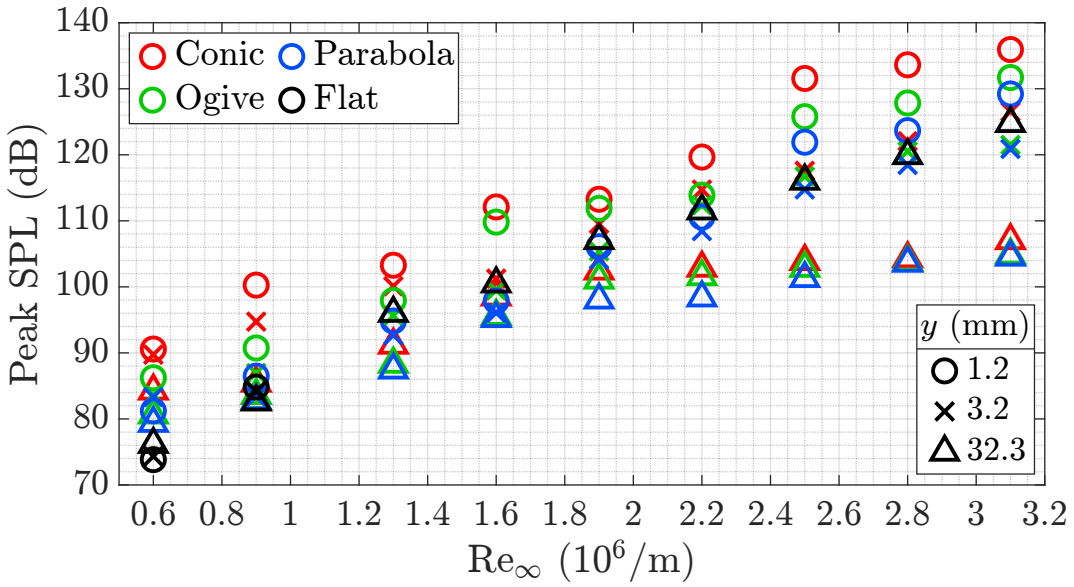

Figure 5.15: HWA: SPL (dB) for $\Delta \mathrm{Re}_\infty/\mathrm{m}$, Δy, and different U/S geometry

Chapter 6

Pressure Results & Discussion

This chapter presents unsteady surface pressure (USP) results, including; contour surface plots of $C_{p,rms}$, to assess the oscillatory magnitude response, aligned x, y streamwise plots, to highlight effects of; length (L, L/D), width (W, L/W), airspeed $U_\infty \sim Re_\infty$/m, and the upstream (U/S) boundary layer (BL), through variation of geometry thus pressure gradient $dp/dx < 0$, with spectra for areas of interest. Final analysis is executed in Section 7 with correlation to hot-wire anemometry (HWA) results, where a relationship is formed between the BL, and cavity response. Table 6.1 provides U/S and cavity case numbers, to serve as a result road map.

Table 6.1: USP: Cavity Case Reference Table

CASE	U/S	L (mm)	D (mm)	W (mm)	L/D	L/W
1	Conic	60	60	60	1	1
2	Conic	60	60	30	1	2
3	Conic	120	60	60	2	2
4	Conic	120	60	30	2	4
5	Conic	180	60	60	3	3
6	Conic	180	60	30	3	6
7	Ogive	60	60	60	1	1
8	Ogive	60	60	30	1	2
9	Ogive	120	60	60	2	2
10	Ogive	120	60	30	2	4
11	Ogive	180	60	60	3	3
12	Ogive	180	60	30	3	6
13	Parabola	60	60	60	1	1
14	Parabola	60	60	30	1	2
15	Parabola	120	60	60	2	2
16	Parabola	120	60	30	2	4
17	Parabola	180	60	60	3	3
18	Parabola	180	60	30	3	6
19	Flat	60	60	60	1	1
20	Flat	60	60	30	1	2

21	Flat	120	60	60	2	2
22	Flat	120	60	30	2	4
23	Flat	180	60	60	3	3
24	Flat	180	60	30	3	6

6.1 Surface Pressure Distributions

This section presents contour surface plots of cavity wall $C_{p,rms}$, with aligned centre line (CL) streamwise plots from USP data per Section 4.4. Effects of Reynolds number Re_∞, internal cavity geometry (length, width), and external U/S geometry thus BL, are assessed. Normalised coordinates are used to compare geometry; streamwise (x/L), vertical (y/D), and spanwise (z/W), with x (mm) for length effects, to show relative cavity size. Data has been mirrored data about the cavity CL $z = 0$, assuming symmetrical flow. Cavity flow is not inherently symmetrical, however prior research [46,81,132,133] in this incompressible flow range tended toward symmetry for $C_{p,rms}$, with only very small asymmetries were observed in visualisation [46,53,58,81,134]. Therefore, for observation of $C_{p,rms}$ magnitude trends, symmetry is considered acceptable.

6.1.1 Effect of Internal Cavity Geometry: Length and Width

Increasing cavity length at fixed depth transforms open cavity flow (L/D $<$ 5) to closed (L/D $>$ 12). Length is increased; L = 60 $\rightarrow$ 120 $\rightarrow$ 180mm, at fixed depth D = 60mm, for L/D = 1, 2 and 3, thus flow remains open. Reducing width at fixed length transforms wide cavity flow (L/W $<$ 1), to narrow (L/W $>$ 1), inducing spanwise 3D flow. Less is known about reducing width when flow is narrow (L/W $>$ 1), as assessed below, for; W = 60 $\rightarrow$ 30mm at L/W $>$ 1.

Fig. 6.1 shows C1, C3, and C5, with W = 60mm for L = 60, 120 and 180mm respectively, and the conic nose U/S. Fig. 6.2 is corresponding C2, C4, and C6, for narrower W = 30mm. Fig. 6.3 is the corresponding streamwise CL plot, to magnify dp/dx. Short wider conic C1 $C_{p,rms}$, is high on all surfaces, with slight dp/dx toward peaks, implying a balanced standing wave, as expected for L/D = 1. Narrower C2 $C_{p,rms}$ is similar, with lower $C_{p,rms}$, less spanwise flow, and sharper adverse $dp/dx \propto$ separation at the upper TE corner.

Increasing length to conic C3, $C_{p,rms}$ reduces on the leading edge (LE) and trailing edge (TE), as a floor peak emerges. Either side of the floor peak in x, $C_{p,rms}$ reduces, with steeper adverse dp/dx aft, implying sharper flow separation. This behaviour aligns with the primary recirculation mechanism of open cavity flow [2,15,43], which is driven by BL separation propagated through shear layer (SL) oscillation, triggering flow separation off internal walls, and into recirculation.

Spanwise flow is apparent on the floor, as distinct eyelet nodes (x = 40-80mm, z/W = $\pm$ 0.25), followed by tail-like nodes downstream (D/S) (x = 80-90mm, z/W = $\pm$ 0.3), which align to TE spanwise nodes ($\approx$ y/D = 0.4-0.6). Motion of C_p in time was observed to understand this feature. And, oscillation was identified between floor and TE spanwise nodes, shed in sequence, from the streamwise floor peak, whose oscillation dominated, suggesting, the primary recirculation mechanism [15] aforementioned, sheds energy spanwise sequentially. Narrower C4 is similar, with less spanwise flow, with sharper dp/dx, toward more distinct floor and TE peaks.

Increasing length to C5, $C_{p,rms}$ reduces further on the LE and TE, as the floor peak $C_{p,rms}$ grows streamwise, thus primary recirculation strengthens. Spanwise flow is sustained, with coincident nodes on the floor, and TE at $z/\mathrm{W} = \pm 0.3$. The floor peak also thickens, indicating interaction of span and streamwise flow. For narrower C6, the floor peak also grows streamwise, $C_{p,rms}$ and spanwise flow is lower, but dp/dx increases on the TE.

Overall, wider cases have spanwise flow, while narrower have larger adverse dp/dx toward the TE corner. Implying wider flow moves spanwise, while narrower oscillates close to the cavity mouth, with stronger SL flapping causing flow to separate from the TE, thence larger $dp/dx > 0$.

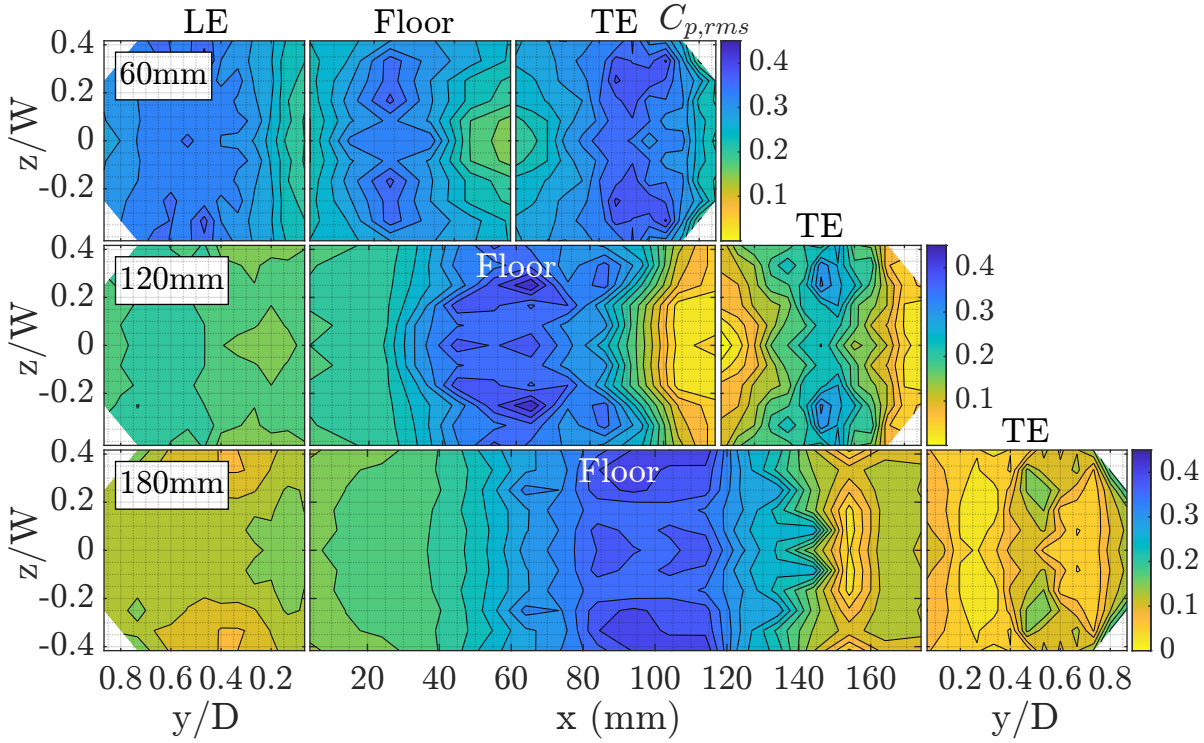

Figure 6.1: USP: ΔL for C1, C3, C5: Conic Nose U/S, W = 60mm, $\mathrm{Re}_\infty/\mathrm{m} = 3.1{\times}10^6$

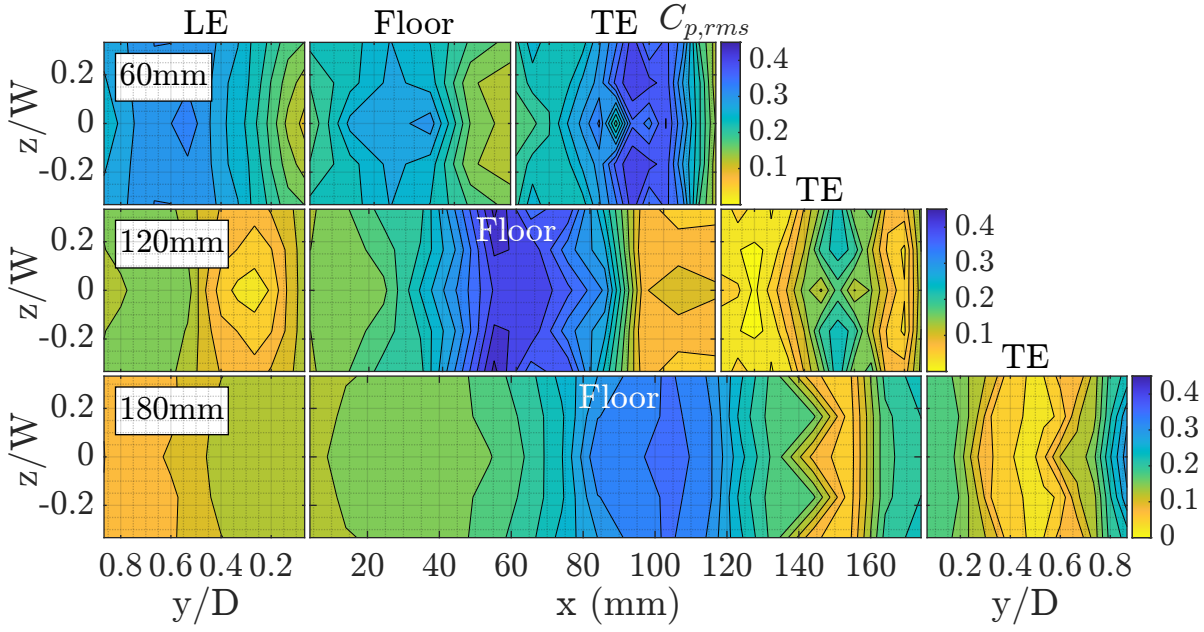

Figure 6.2: USP: ΔL for C2, C4, C6: Conic Nose U/S, W = 30mm, $\mathrm{Re}_\infty/\mathrm{m} = 3.1{\times}10^6$

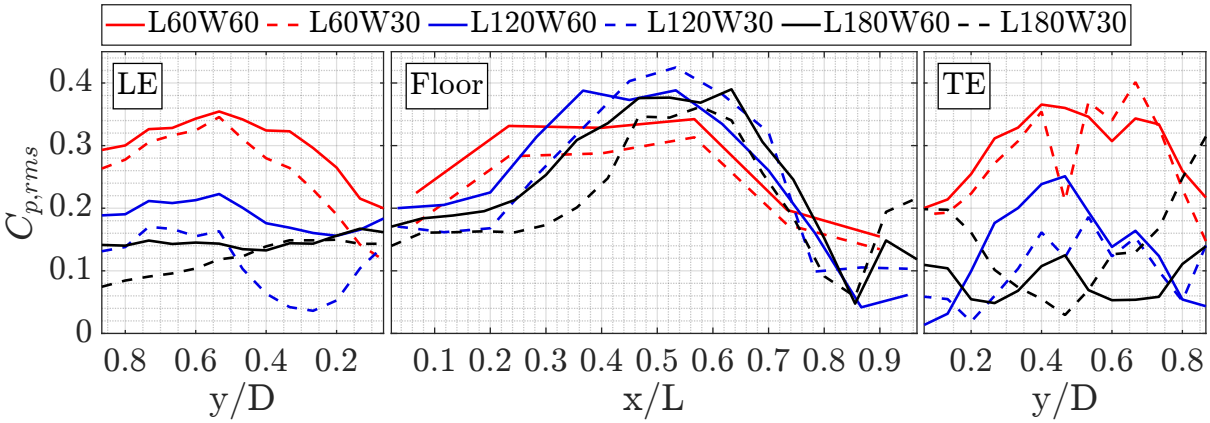

Figure 6.3: USP: ΔL and ΔW: Conic Nose U/S at $\mathrm{Re}_\infty/\mathrm{m} = 3.1{\times}10^6$

Fig. 6.4 presents C7, C9, and C11, of wider W = 60mm for L = 60, 120 and 180mm respectively, when the ogive nose is U/S. Fig. 6.5 is corresponding C8, C10, C12, for narrower W = 30mm, and Fig. 6.6 is the streamwise plot, to magnify dp/dx, comparing both length and width. Short wider ogive C7 $C_{p,rms}$ magnitude and gradients are evenly distributed, implying a balanced standing wave for L/D = 1, alike the conic case. Narrower C8 is similar, with lower $C_{p,rms}$, less spanwise flow, and sharper adverse dp/dx on the upper TE wall $\propto$ flow separation.

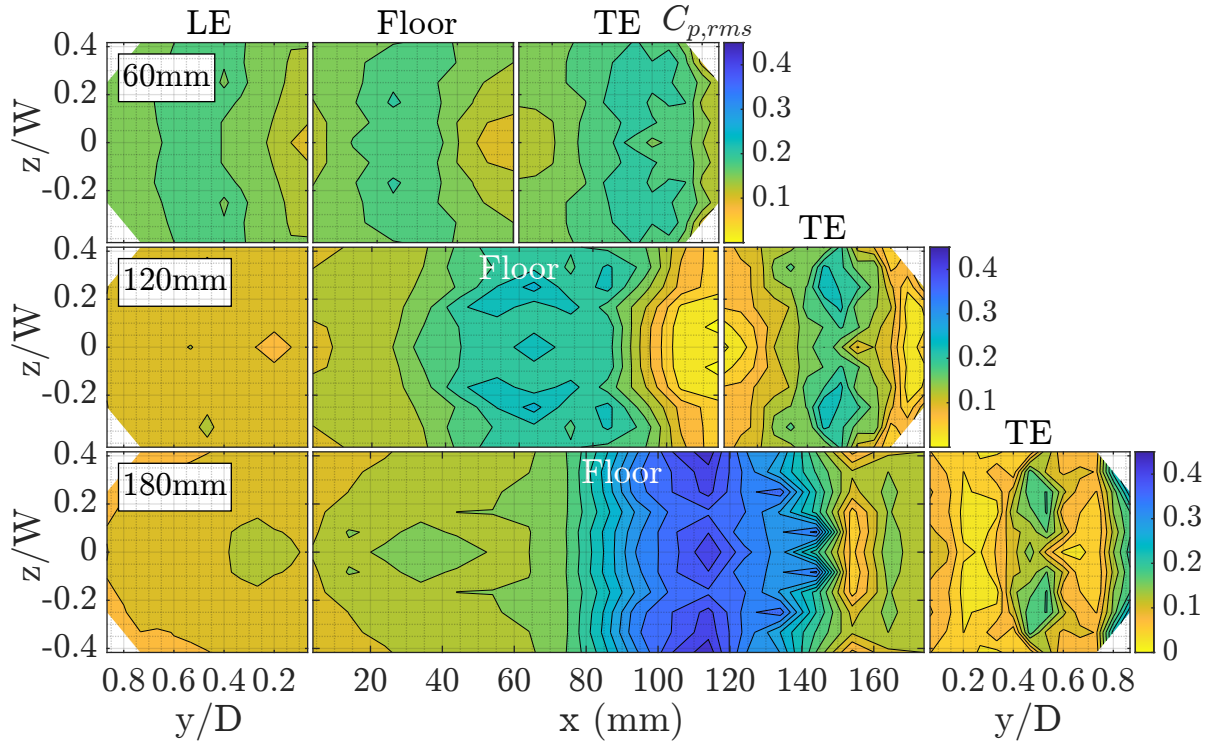

Figure 6.4: USP: ΔL for C7, C9, C11: Ogive Nose U/S, W = 60mm, $\mathrm{Re}_\infty/\mathrm{m} = 3.1{\times}10^6$

Increasing length to mid-length ogive C9, $C_{p,rms}$ reduces on the LE and TE, as a floor peak emerges with spanwise nodes aligned to the TE at $z/\mathrm{W} = \pm 0.3$. Either side of the peak in x, $C_{p,rms}$ reduces, with steeper $dp/dx > 0$ aft $\propto$ flow separation, alike the conic case, suggesting a primary recirculation mechanism. Narrower C10, is similar, with lower $C_{p,rms}$, and less spanwise flow. Increasing length to long C11, LE and TE $C_{p,rms}$ reduce further, as floor peak $C_{p,rms}$ increases, with steeper dp/dx, and spanwise flow for x = 130-150mm, before increased adverse $dp/dx \propto$ flow separation, reflecting increase in recirculation strength. Narrower C12 is similar,

with lower $C_{p,rms}$, and less spanwise flow. Overall, as length increases high pressure centralises to a primary recirculation peak on the floor, with increasing dp/dx either side. From wider to narrower geometry, spanwise flow and $C_{p,rms}$ reduce, while dp/dx toward the upper TE increases, implying narrower flow oscillates closer to the mouth, and wider disperses spanwise.

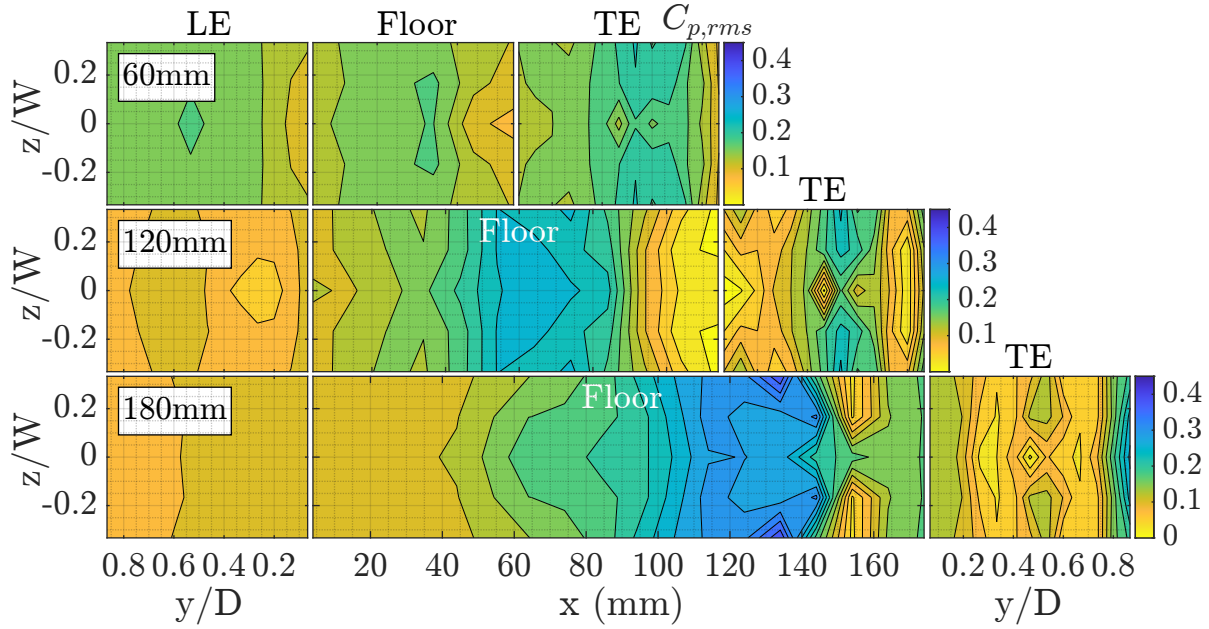

Figure 6.5: USP: ΔL for C8, C10, C12: Ogive Nose U/S, W = 30mm, Re_∞/m = 3.1×10^6

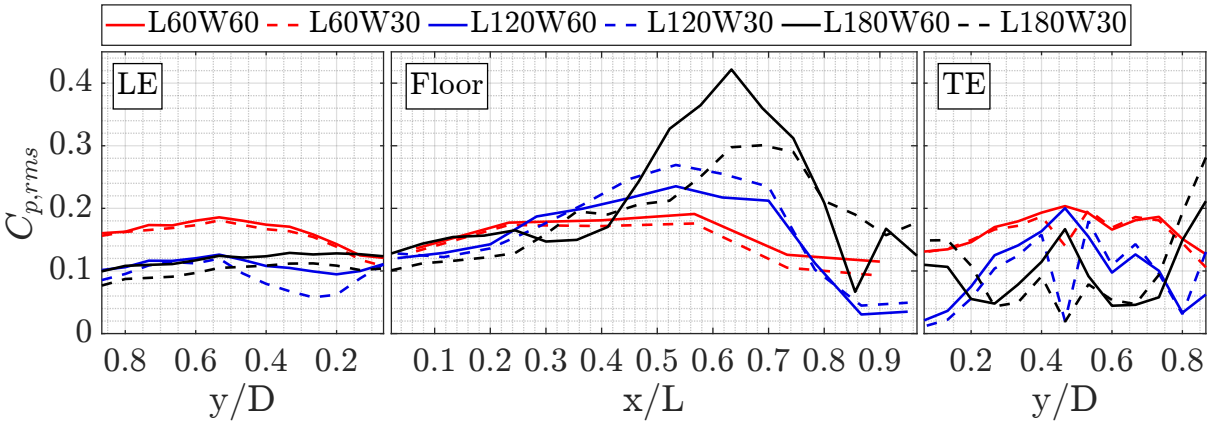

Figure 6.6: USP: ΔL and ΔW: Ogive Nose U/S at Re_∞/m = 3.1×10^6

Parabola C13-C18 are identical to ogive C7-C12, with slight $C_{p,rms}$ decrease. Flat C19-C24 has a similar but very lulled response. Refer to Fig. D.1-D.5 in Appendix D.1. Per Section 5.2 the parabola has a thicker BL than the ogive, and the flat-plate BL is very thick compared to nose cones, thence lower $C_{p,rms}$, further detailed in Section 6.1.3.

Overall, for increased length, a floor peak emerged with steepening dp/dx either side, as LE and TE $C_{p,rms}$ reduced. Based on [2, 15], a primary recirculation mechanism is implied, drawing flow in from separation off walls thus increased $dp/dx > 0$, to feed SL oscillation. The LE is comparatively lull, thus the mechanism is closer to the TE, moving closer as L/D increases, as expected for open flow. Moreover, as L/D increases, length-wise vortical oscillations take-over depth-wise standing waves[3,8,15]. Standing waves move back and forth between the LE and TE[3], producing more balanced wall pressure. Lengthwise oscillations instead move up and

down from the floor, triggering primary recirculation with incoming flow[2], which presents as a discrete floor peak[43], moving and stretching D/S with increasing L/D, as observed.

Spanwise flow is apparent in wider cases, on the floor and TE. The floor peak, or primary recirculation characteristic, thickens and stretches D/S as length increases, suggesting stream and spanwise flow interaction. Viewing C_p in time, confirmed this, as spanwise nodes were observed to shed sequentially from the primary streamwise peak. These spanwise patterns coincide with Crook et al[56–58,135]; "*centrally located saddle point*" or primary recirculation, "*flanked by a pair of spanwise nodes*" near y/D = 0.5 and z/W = ±0.3 on the TE wall, and aft centre on the floor. Spanwise features reduced in narrower cases. However, higher gradient density arose on the upper TE wall, indicating increased flow separation, likely due to SL flapping. Effectively, narrower flow oscillates closer to the mouth, and wider develops spanwise.

6.1.2 Effect of Free-Stream Reynolds Number Re_∞

Experiments were performed at incompressible airspeeds; U_∞ = 10-65m/s ∝ Re_∞/m = 0.6-4.1×10^6. Fig. 6.7-6.16 exhibit $C_{p,rms}$ contour surface plots at Re_∞/m ≈ 4.1×10^6, with a streamwise CL plot for ΔRe_∞/m to magnify dp/dx. For short wider conic C1 in Fig. 6.7, $C_{p,rms}$ increases as Re_∞ increases proportionally increasing dp/dx, improving peak clarity, thus pressure wave periodicity. Narrower C2 is similar, with less spanwise flow per Appendix D.1 Fig. D.7.

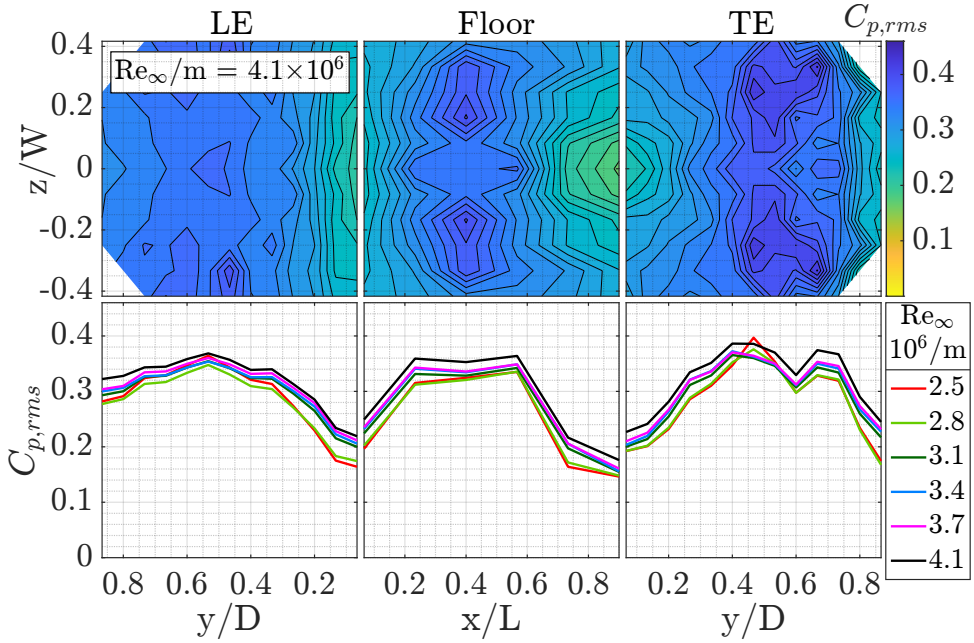

Figure 6.7: USP: ΔRe_∞/m for C1: L/D = 1, L/W = 1, Conic Nose U/S

For mid-length wider conic C3 in Fig. 6.8, $C_{p,rms}$ increases relative to Re_∞ on each wall. Aside from the floor between x/L = 0.54-0.85, where large adverse dp/dx implies flow separation, increasing slightly with Re_∞, thus reducing $C_{p,rms}$ at the tail end relative. For narrower C4 in Fig. 6.9, $C_{p,rms}$ also increases with Re_∞. However, adverse dp/dx on the floor (x/L = 0.54-0.78) is sharper than wider C3 (x/L = 0.54-0.85), and split into sections; (1) x/L = 0.54-0.7, where dp/dx remains consistent for Re_∞ increase, and (2) x/L = 0.7-0.77, which is steeper, and has slight dp/dx increase with Re_∞. Therefore, increased Re_∞, increases $C_{p,rms}$, and dp/dx ∝ flow separation, to improve peak clarity, thus pressure wave periodicity.

For long wider conic C5 in Fig. 6.10, $C_{p,rms}$ and dp/dx increase slightly with Re_∞, across each surface. Aside from the floor region of large adverse dp/dx (x/L = 0.64-0.86), where dp/dx increases slightly with Re_∞, aft which ($x/\mathrm{L} > 0.88$) $C_{p,rms}$ reduces with increasing Re_∞. This is expected aft large dp/dx, where higher Re_∞ increases flow separation, and reduces relative pressure aft separation. This improves peak clarity, for increased pressure wave periodicity. A similar feature is apparent on the TE, where higher Re_∞ induces higher peak $C_{p,rms}$ and steeper dp/dx, improving peak clarity. Narrower C6 has a similar trend per Appendix D.1 Fig. D.8.

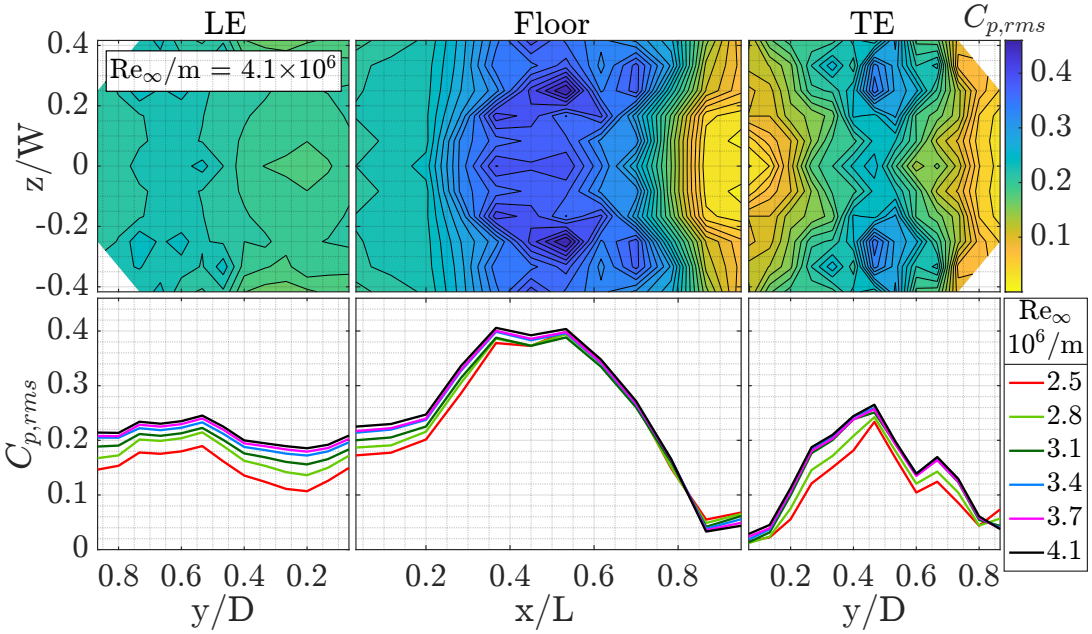

Figure 6.8: USP: $\Delta\mathrm{Re}_\infty$/m for C3: L/D = 2, L/W = 2, Conic Nose U/S

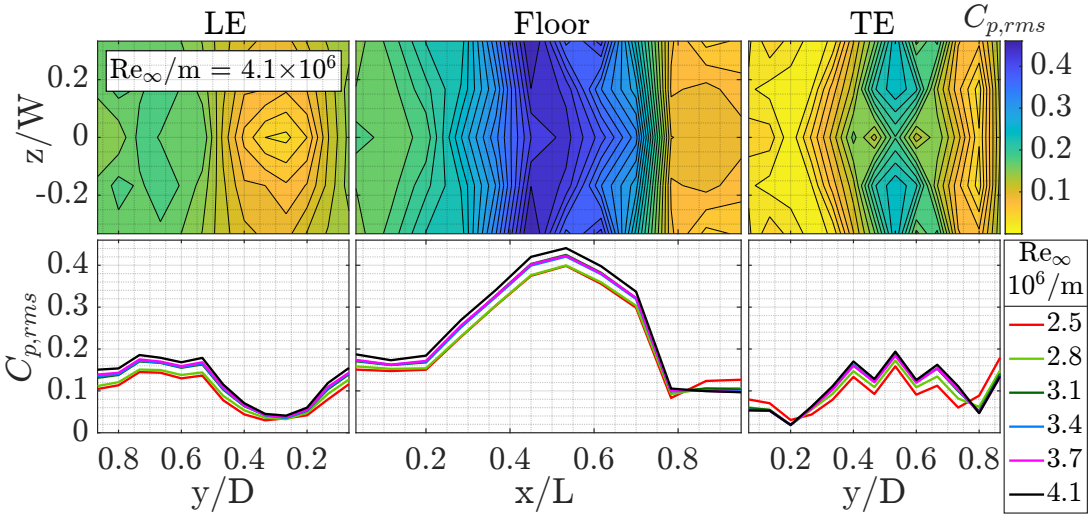

Figure 6.9: USP: $\Delta\mathrm{Re}_\infty$/m for C4: L/D = 2, L/W = 4, Conic Nose U/S

For short wider ogive C7 in Fig. 6.11, $C_{p,rms}$ and dp/dx increase proportional to Re_∞, especially in the adverse dp/dx region on the aft floor. Effectively, the dominant standing wave, growing in strength. Narrower C8 in Fig. D.9 of Appendix D.1 has an analogous response. Mid-length wider C9 in Fig. 6.12, and narrower C10 in Fig. D.10 of Appendix D.1, also show increase in $C_{p,rms}$ and dp/dx with Re_∞, with length-wise recirculation growth instead of a standing wave. For long wider ogive C11 in Fig. 6.13, the size of high $C_{p,rms}$ regions, and $C_{p,rms}$ overall

increase with Re_∞. Especially in the peak floor region, with increased dp/dx before and aft. Adverse dp/dx aft the floor peak, and on the TE upper wall, indicate flow separation, which also increases with Re_∞, resulting in lower $C_{p,rms}$ aft separation for higher Re_∞. Narrower ogive C12 in Fig. D.11 of Appendix D.1 is similar. This peak behaviour represents enhancement of primary recirculation. Its strength growing with Re_∞, for increased oscillatory magnitude, through peak $C_{p,rms}$, as recirculation tightens about its centre, pulling more flow in, and thus increasing flow separation. Note: the ogive nose is a proxy to the parabola, as contour plots are very similar, with only slightly smaller $C_{p,rms}$, refer Fig. D.12-D.17 of Appendix D.1.

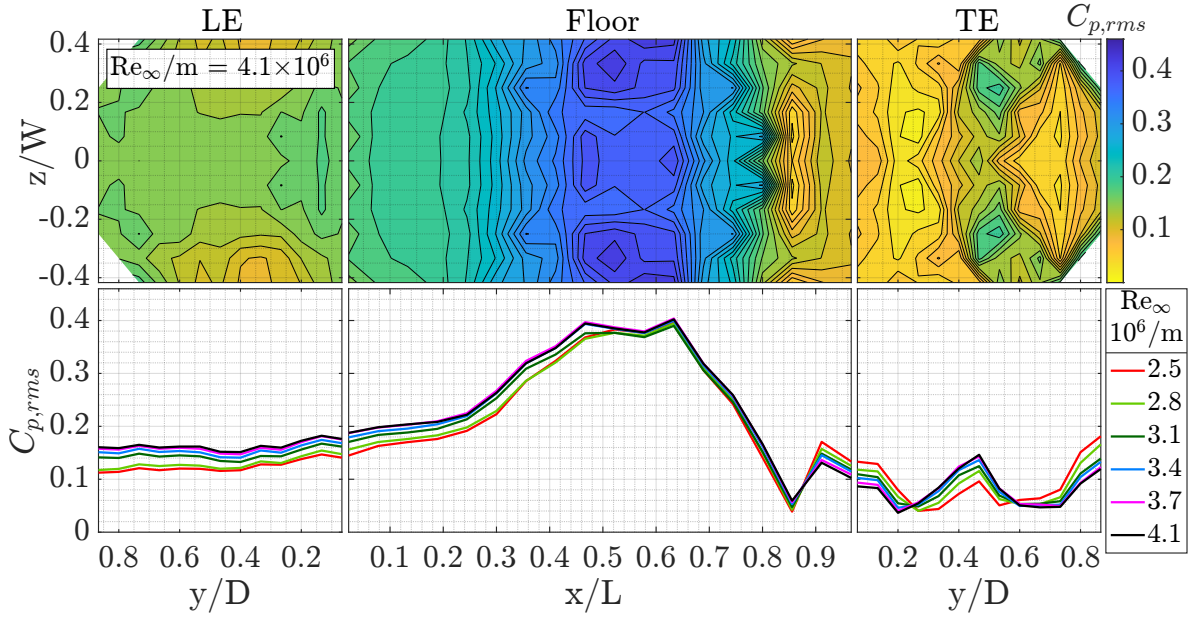

Figure 6.10: USP: $\Delta\mathrm{Re}_\infty$/m for C5: L/D = 3, L/W = 3, Conic Nose U/S

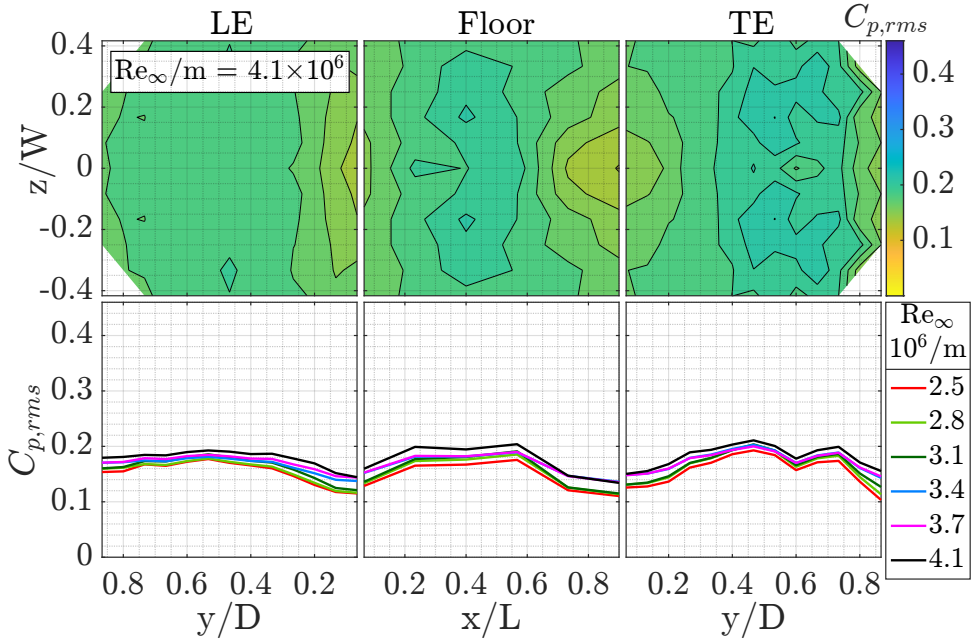

Figure 6.11: USP: $\Delta\mathrm{Re}_\infty$/m for C7: L/D = 1, L/W = 1, Ogive Nose U/S

For flat-plate U/S geometry with a thick turbulent BL, $C_{p,rms}$ is significantly reduced from maxima $C_{p,rms} = 0.45$ in cases with a nose U/S to $C_{p,rms} = 0.18$ for flat-plate cases. Therefore, $C_{p,rms}$ scale was adjusted. For short wider flat C19 in Fig. 6.14, $C_{p,rms}$ increases with Re_∞

due to growth of higher $C_{p,rms}$ and dp/dx regions on each wall. Narrower C20 in Fig. D.18 of Appendix D.1, presents the same trend, with a slightly larger increase in $C_{p,rms}$.

For mid-length flat cases C21 and C22, wider C21 goes null on the floor aft $x/\mathrm{L} = 0.5$, which was a measurement issue. Thus narrower C22 in Fig. 6.15 is proxy, with wider C21 in Fig. 6.15 of Appendix D.1. Overall, as Re_∞ increases, there is no abundant change in $C_{p,rms}$ magnitude or gradient. Aside from small increase in $C_{p,rms}$, and dp/dx on the aft floor ($x/\mathrm{L} > 0.7$), and upper TE wall ($y/D > 0.55$). For long wider flat C23 in Fig. 6.16, $C_{p,rms}$ increases with Re_∞, and dp/dx in higher $C_{p,rms}$ regions, especially aft the floor peak. Increasing adverse dp/dx, indicates sharper flow separation, improving peak clarity due to strengthened wave periodicity thus higher $C_{p,rms}$. Narrower C24 in Fig. D.19 in Appendix D.1 is similar.

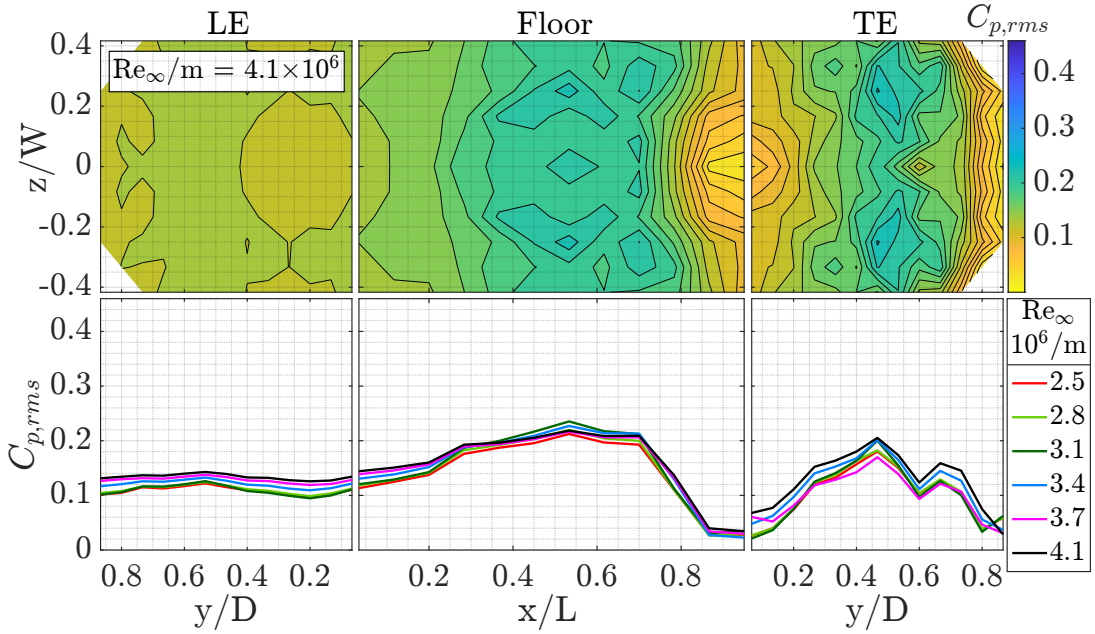

Figure 6.12: USP: $\Delta\mathrm{Re}_\infty/\mathrm{m}$ for C9: L/D = 2, L/W = 2, Ogive Nose U/S

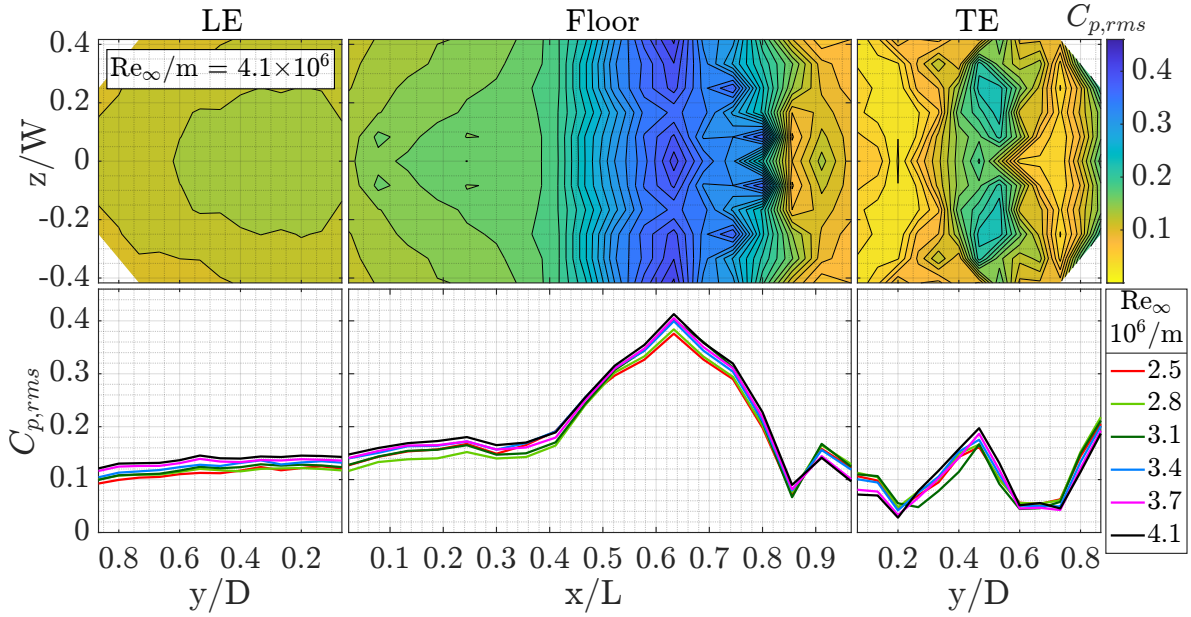

Figure 6.13: USP: $\Delta\mathrm{Re}_\infty/\mathrm{m}$ for C11: L/D = 3, L/W = 3, Ogive Nose U/S

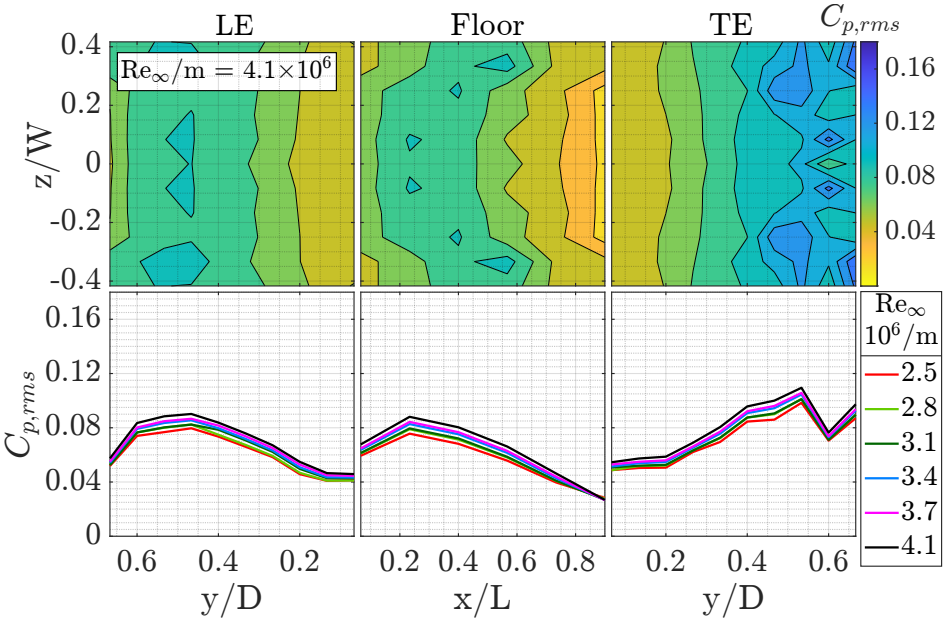

Figure 6.14: USP: $\Delta\mathrm{Re}_\infty/\mathrm{m}$ for C19: L/D = 1, L/W = 1, Flat-plate U/S

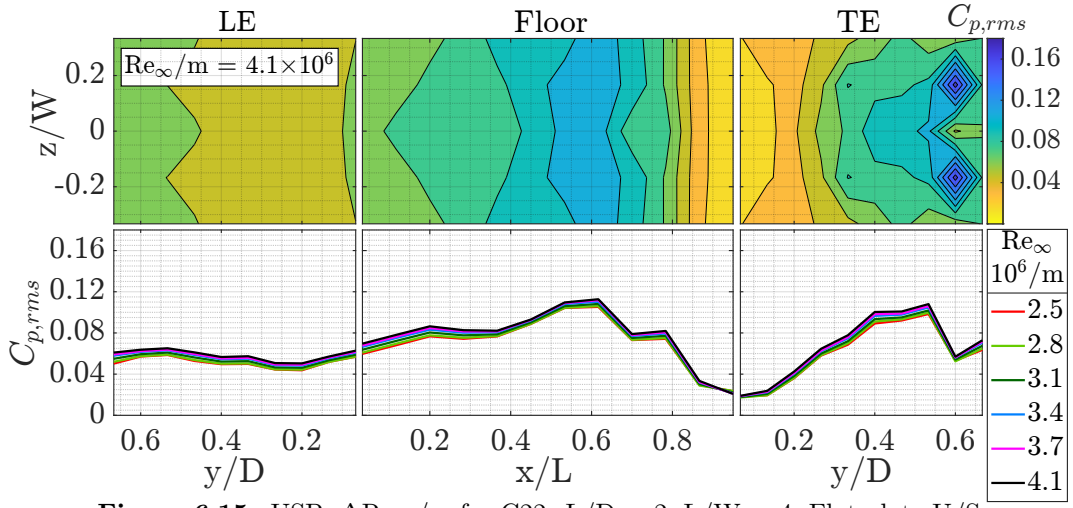

Figure 6.15: USP: $\Delta\mathrm{Re}_\infty/\mathrm{m}$ for C22: L/D = 2, L/W = 4, Flat-plate U/S

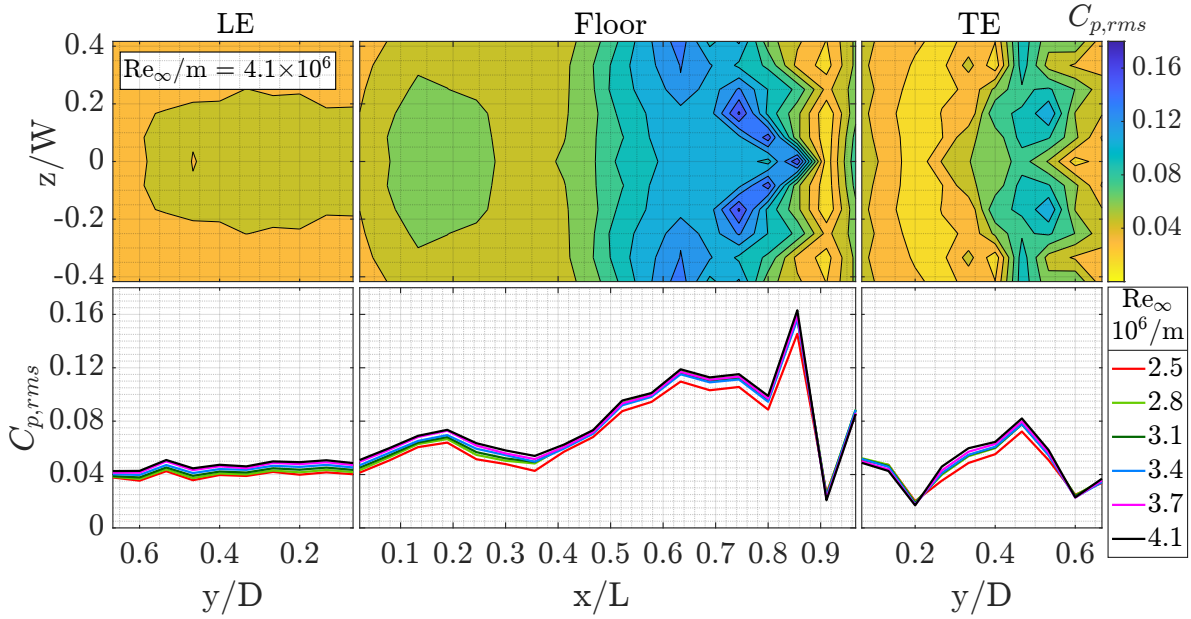

Figure 6.16: USP: $\Delta\mathrm{Re}_\infty/$ for C23: L/D = 3, L/W = 3, Flat-plate U/S

Overall, increasing Re_∞ slightly increased $C_{p,rms}$, and dp/dx in regions of high $C_{p,rms}$, especially adverse dp/dx aft the floor peak indicating sharper flow separation. This implies increased strength of the internal oscillating mechanism. For short cases (L/D = 1), a balanced standing wave, and long cases (L/D = 2, and 3), a primary recirculation mechanism, pulling more fluid into oscillation. For this range, Re_∞ impact is small[49] compared to internal geometry in Section 6.1.1, and U/S BL in Section 6.1.3. When comparing low and high $Re_\infty/m = 0.6$ and 4.1×10^6 results, $C_{p,rms}$ increase is more notable. Pressure at $U_\infty = 70m/s \propto Re_\infty/m = 4.5\times10^6$ was too large for the Scanivalve to measure, indicating further increase of Re_∞ increases $C_{p,rms}$. Larger Re_∞ range would provide a better manifest, however, range is within facility limit.

6.1.3 Effect of Upstream Geometry

Four U/S geometry profiles listed below were observed, to assess the effect of altering BL δ and dp/dx. Fig. 6.17-6.22 present the flow response of each internal cavity geometry to differing BL profiles. Velocity profiles are in Section 5.1, and BL data is in Section 4.3, and 5.2 for reference.

(1) Flat-plate baseline: $dp/dx = 0$, thick turbulent BL: $\delta \approx 39 \rightarrow 28$mm.

(2) Conic: 45° angle, $dp/dx < 0$ for a thin laminar BL at the cavity LE: $\delta \approx 2.68 \rightarrow 1.16$mm.

(3) Ogive: K = 1.43, $dp/dx < 0$ for a thin laminar BL at the cavity LE: $\delta \approx 2.96 \rightarrow 1.24$mm.

(4) Parabola: K = 6.44, $dp/dx < 0$, for a thin laminar BL at the cavity LE: $\delta \approx 3.13 \rightarrow 1.31$mm.

Short wider cavity $C_{p,rms}$ response (L/D = L/W = 1), to varied U/S geometry, thus BL, is in Fig. 6.17. The conic with the thinnest BL, and largest $dp/dx < 0$ at the cavity LE, produces higher $C_{p,rms}$ and dp/dx on internal cavity surfaces. Ogive and parabola with thicker δ and smaller $dp/dx < 0$, produce lower $C_{p,rms}$ and dp/dx, almost equal due to correlative BL curvature. And lastly, response to the flat-plate thick turbulent BL is comparatively null.

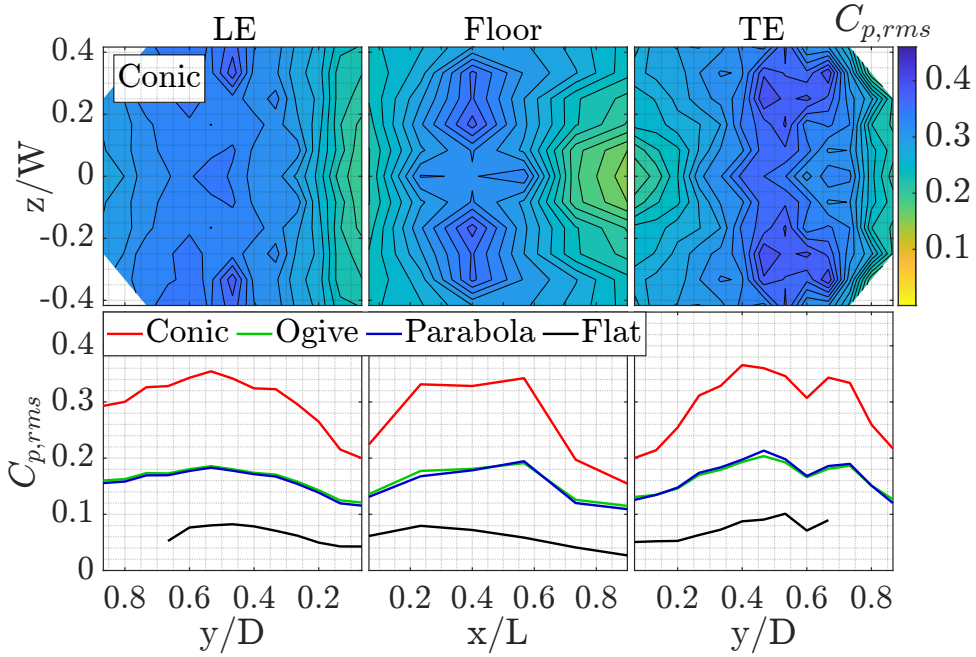

Figure 6.17: USP: ΔBL for L/D = 1, L/W = 1, $Re_\infty/m = 3.1\times10^6$

The short narrower cavity response (L/D = 1, L/W = 2) in Fig. 6.18 is similar with more notable increase in cavity surface dp/dx as BL δ decreases, and U/S $dp/dx < 0$ increases. More

so on the aft floor, and upper TE wall in adverse dp/dx regions, representing sharper flow separation, due to higher fluctuation intensity, heightened by lower BL δ and larger $dp/dx < 0$.

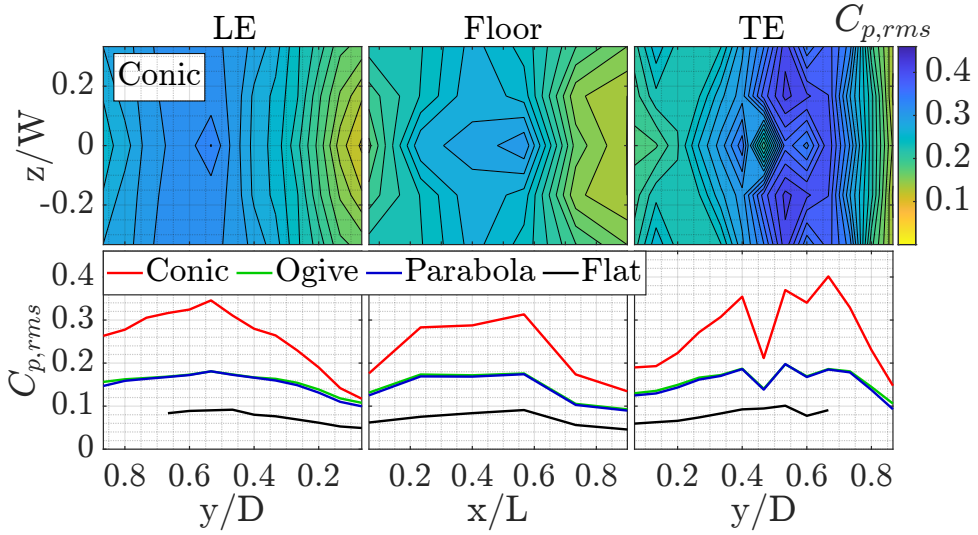

Figure 6.18: USP: ΔBL for L/D = 1, L/W = 2, Re_∞/m = 3.1×10^6

Mid-length wider cavity pressure response (L/D = L/W = 2), to varied U/S geometry thus BL is in Fig. 6.19. The conic nose produces higher $C_{p,rms}$ and dp/dx on internal cavity surfaces, followed by ogive and parabola, which are all much larger than response to the flat-plate U/S. This is proportional to increasing BL δ and decreasing $dp/dx < 0$, as aforementioned. Nose cases also induce more abundant spanwise flow in the central floor peak, trailed D/S by spanwise nodes on the floor outboard (x/L = 0.4-0.7), matched to the TE (y/D = 0.4-0.6). Ogive and parabola spanwise shapes are less distinct with lower $C_{p,rms}$ and dp/dx compared to the conic nose. These shapes are however absent in response to the flat-plate BL.

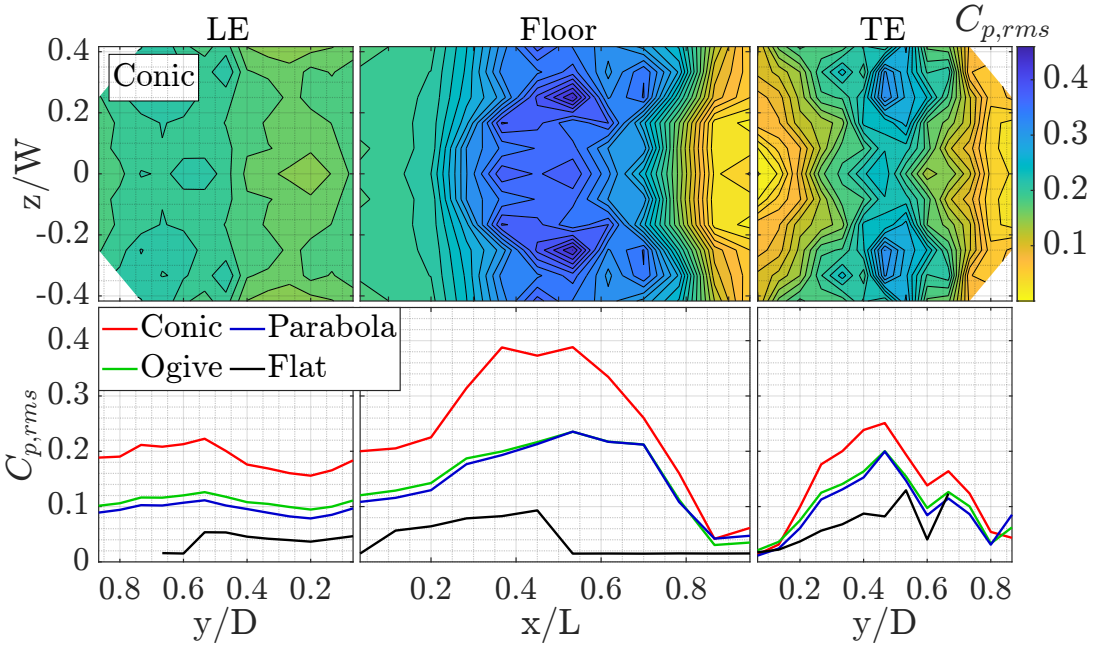

Figure 6.19: USP: ΔBL for L/D = 2, L/W = 2, Re_∞/m = 3.1×10^6

The mid-length narrower cavity response (L/D = 2, L/W = 4) in Fig. 6.20, presents the same trend as the wider, aside from spanwise flow, which is largely mute. Therefore, based on BL

data at the cavity LE for nose cases, its apparent cavity surface $C_{p,rms}$ and dp/dx increase for mid-length cavities, proportional to decreasing BL δ, and increasing U/S $dp/dx < 0$. Especially, considering the thick turbulent BL response is comparatively null.

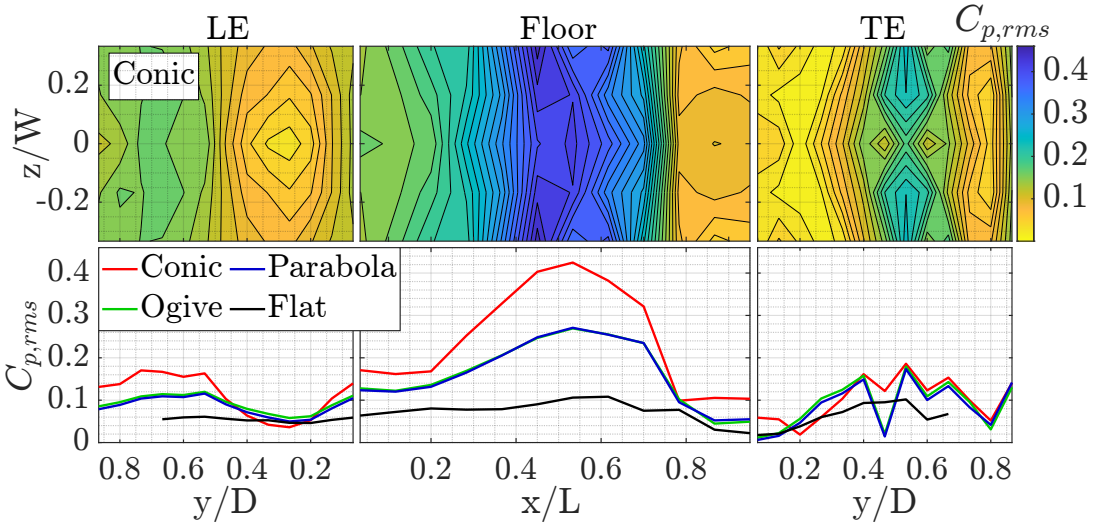

Figure 6.20: USP: ΔBL for L/D = 2, L/W = 4, $\mathrm{Re}_\infty/\mathrm{m} = 3.1{\times}10^6$

The long wider cavity response (L/D = L/W = 3) to varied U/S geometry is in Fig. 6.21. Conic, ogive, and parabola, produce higher $C_{p,rms}$ and dp/dx on cavity walls, than the flat-plate, due to smaller BL δ and $dp/dx < 0$ U/S, alike shorter cases. Peak $C_{p,rms}$ on the floor between nose cases, is consistent at this length, compared to shorter cavities. However, the region increases streamwise from $x/\mathrm{L} = 0.55$-65 for ogive and parabola, to $x/\mathrm{L} = 0.4$-65 for conic, as δ decreases and $dp/dx < 0$ U/S increases. Indicating growth of recirculation spatially. The TE is largely unaffected between noses, however the flat-plate response is comparatively null.

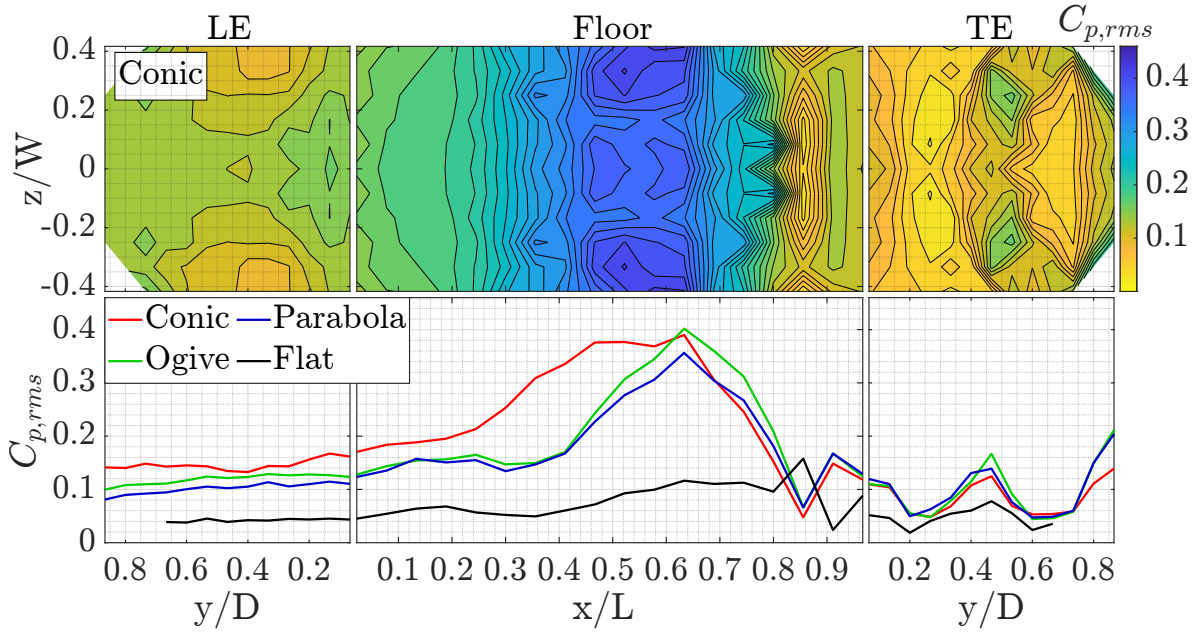

Figure 6.21: USP: ΔBL for L/D = 3, L/W = 3, $\mathrm{Re}_\infty/\mathrm{m} = 3.1{\times}10^6$

The long narrower cavity response (L/D = 3, L/W = 4) in Fig. 6.22 presents the same trend aside from spanwise motion which is largely mute. On the TE wall, the conic nose produces more distinct flow separation and attachment structure due to steeper dp/dx, reflected by the

higher peak $C_{p,rms}$ region on the floor. Effectively, U/S geometry effects, through BL δ, and dp/dx on cavity pressure are sustained for the longer cavity.

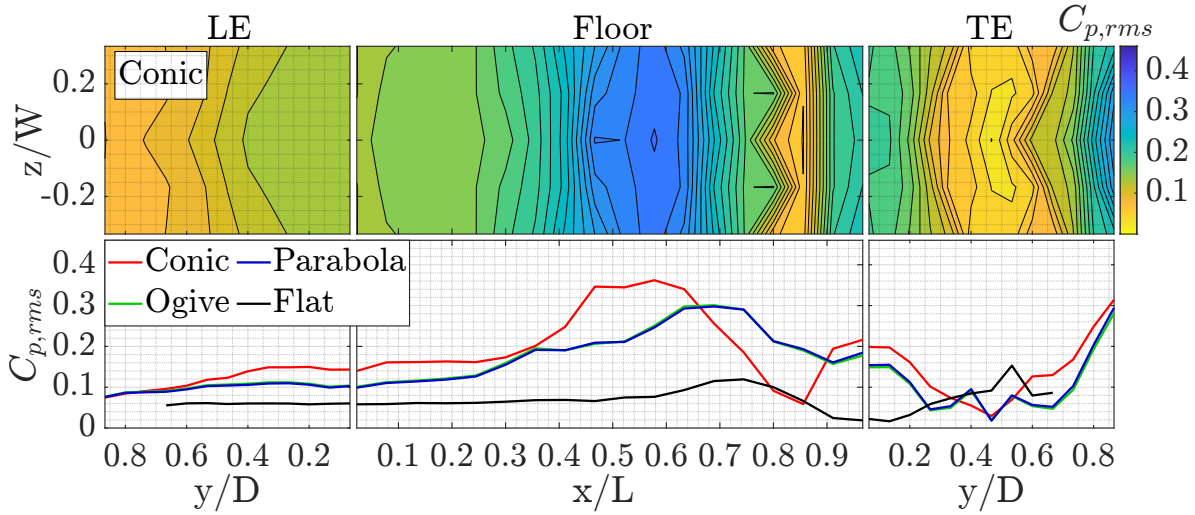

Figure 6.22: USP: ΔBL for L/D = 3, L/W = 6, Re_∞/m = 3.1×10^6

Overall, increasing BL $dp/dx < 0$, and reducing δ, through U/S geometry, increased cavity pressure response. As the thinnest BL $\delta \sim$ 2mm, with the largest $dp/dx < 0$, produced larger $C_{p,rms}$, and steeper dp/dx on each cavity wall, than the thick turbulent BL $\delta \sim$ 40mm, by almost a magnitude. Larger dp/dx on cavity walls, especially $dp/dx > 0 \propto$ flow separation, indicates stronger oscillation. As it implies, more momentum is pulled away from walls, into recirculation. Thus smaller BL δ, and larger U/S $dp/dx < 0$, increase cavity oscillation periodicity.

Regarding frequency response. Whilst $C_{p,rms}$ is a measure of magnitude, representing the effective value of an oscillating pressure, with respect to C_p. When plotted in space, change in its gradient density $\partial\rho/\partial x$, reflects change in occurrence of effective C_p in space. Therefore, higher $\partial\rho/\partial x$, suggests larger change in pressure. Whilst this is not directly related to frequency, it does indicate a shift in dynamic response, which would imply a shift in frequency response.

Prior research has investigated the BL effect, observing variation in laminar and turbulent BL δ, and also observed a thin BL to increase cavity pressure response, but no effect on frequency. This led to BL neglect in common place Strouhal (St) models, to predict cavity frequency response. However, between U/S case, $C_{p,rms}$ regions change size, with varying gradient density. The conic nose with the thinnest BL, and largest $dp/dx < 0$ U/S, produced a broader peak on the cavity floor, with higher dp/dx either side, compared to curved noses. In this case, internal cavity geometry is sustained, however U/S BL δ decreased and $dp/dx < 0$ increased. Therefore, U/S BL altered system dynamics, suggesting shift in frequency response through space, which is further investigated with spectral response below, for inclusion in a St model in Section 7.

6.2 Pressure Spectra

This section assesses internal cavity pressure spectra from USP data per Section 4.5. Effects of Re_∞, internal, and external U/S geometry thus BL structure, are assessed. Cavity floor spectra is observed in the peak region of stream and spanwise flow (x/L = 0.6, z/W = 0.3), aligned to dominant DMD frequencies. Data for Mode 1-4 f(Hz) and SPL(dB) is given in Appendix D.2.

6.2.1 Effect of Internal Geometry

Fig. 6.23 provides an example of the effect of length at W = 60, and Fig. 6.24 the effect of width at L = 120mm. Overall, increasing length, or reducing width increased SPL, however, noise also increased. Three distinct peaks are apparent; $f \approx$ 18-40, 50 and 199Hz, varying in magnitude and clarity with geometry, and in some cases, a fourth at $f \approx$ 100Hz. Further detailed below.

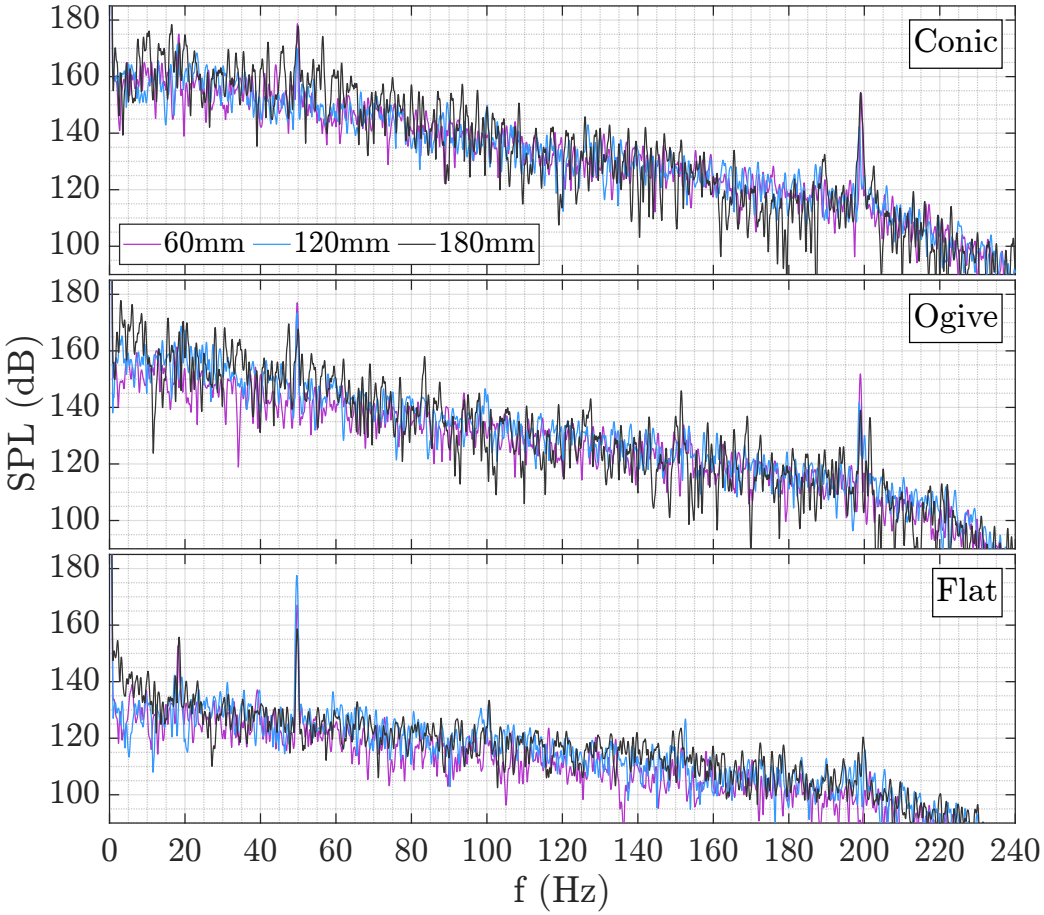

Figure 6.23: USP: ΔL FFT: W = 60mm, Re_∞/m = 0.6×10^6, x/L = 0.6, z/W = 0.3

Mode 1 ($f \approx$ 20-30Hz), the normal mode, based on St number for length L = 60, 120, 180mm at 10m/s; St_L = 0.11, 0.22, and 0.32, aligns to Disimile et al,[50], Block[6] and East's[8] experimental data for the mode. Therefore, its implied, the peak is a normal cavity mode, usually dominant in deeper open cavities, and 2nd or 3rd dominant in shallower open cavities.

Mode 2 (f = 50-70Hz), is SL mode 2; 2nd in the spectra, changes magnitude with length, and St at 10m/s of; St_L = 0.3, 0.6, 0.9, aligned to data from [15, 44, 50, 51]. There is no width effect. SPL is effected by U/S geometry thus BL, returning higher clarity for the flat case, likely due to reduction in spanwise flow from fuselage and nose geometry.

Mode 3 (f = 80-105Hz), is SL mode 3, 3rd in the spectra, with St = 0.6, 1.2, 1.8 at 10m/s, aligned to data from[2, 15, 44, 50, 51]. It first appears at L = 120mm for the flat plate U/S at both widths, and in curved U/S cases (ogive, parabola) when W = 30mm. It is sustained at L = 180mm, for both width with the flat-plate U/S, and curved U/S cases, however lulled. There is no appearance in conic cases. Therefore, this mode is dampened by a thin U/S BL, or $dp/dx < 0$, its formation dependant on a relationship between BL, cavity length and width.

Mode 4 (f = 152-199Hz), or **Mode 3** in laminar BL cases, it is present in every spectral plot. The peak holds SPL with length and width, only decreasing proportional to increase in δ, and reduction in dp/dx. Therefore, this mode is manipulated by U/S geometry thus BL, with its dominance as mode 3 dependant also on length and the BL.

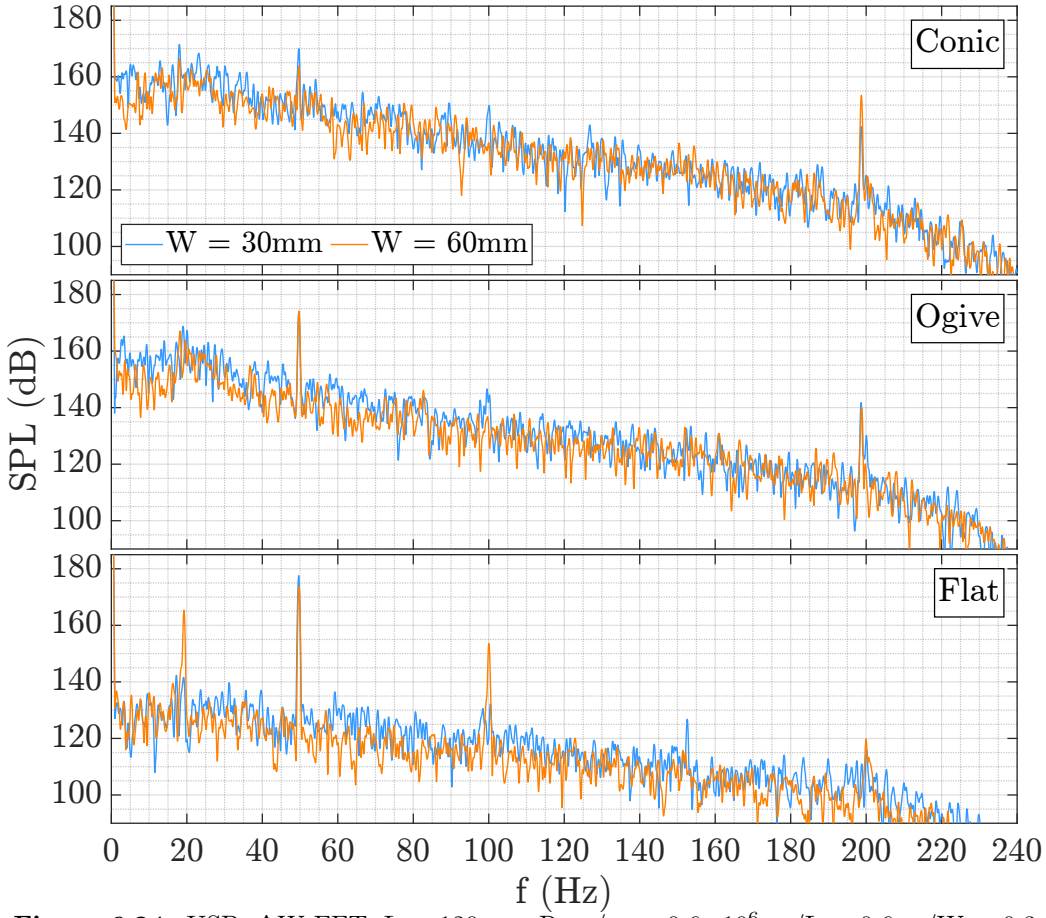

Figure 6.24: USP: ΔW FFT: L = 120mm, $Re_\infty/m = 0.6\times10^6$, $x/L = 0.6$, $z/W = 0.3$

6.2.2 Effect of Free-Stream Reynolds Number Re_∞

Fig. 6.25 shows increase in SPL, with increasing $Re_\infty \propto U_\infty$, for L/D = L/W = 1. Mode 1 (f = 20-30Hz), and Mode 2 (f = 50Hz) at $Re_\infty/m = 0.6\times10^6$, shift higher as Re_∞ increases, and tentative mode 3 ≈100Hz at $Re_\infty/m = 0.6\times10^6$ is enhanced, also shifting higher as Re_∞ increases. However, Mode 3 or 4 (f = 199Hz), hold until $Re_\infty/m \approx 3.1\times10^6$, in most cases. In others, f = 199Hz shifts to higher f, or disappears as broadband noise.

As mode 1 shifts from f = 16-22Hz to 40-50Hz, for higher Re_∞, mode 1 closes in on mode 2. They eventually overlap, as mode 2 becomes mode 1, while a new mode 2 and 3 arise, as f = 100Hz becomes consistent. At higher Re_∞, mode 2 shifts to 51-54 then 56-73, and 81-89Hz. As mode 1's low f encroaches mode 2's previous f = 50Hz, mode 2 then increases in f, with increasing Re_∞. Similarly for 100Hz and 199Hz modes, however due to noise at higher Re_∞, modes became indistinguishable from general WT noise, for reasons discussed, as follows.

Data was corrected to remove WT noise using empty WT data. However, higher $U_\infty \propto Re_\infty$ data became difficult to filter, due to mechanical WT noise, where anechoic equipment is required. This wasn't previously a poignant issue. However, shortly after testing, the WT suffered

a mechanical failure, impacting higher U_∞, reducing the maximum to 50m/s. The fault likely pre-existed time of failure, impacting higher U_∞ results, thus assumed responsible for noisy higher U_∞ data, undetected, thus uncorrected for with empty WT data. Full U_∞ range has not been restored, thus re-reruns were not possible above 50m/s.

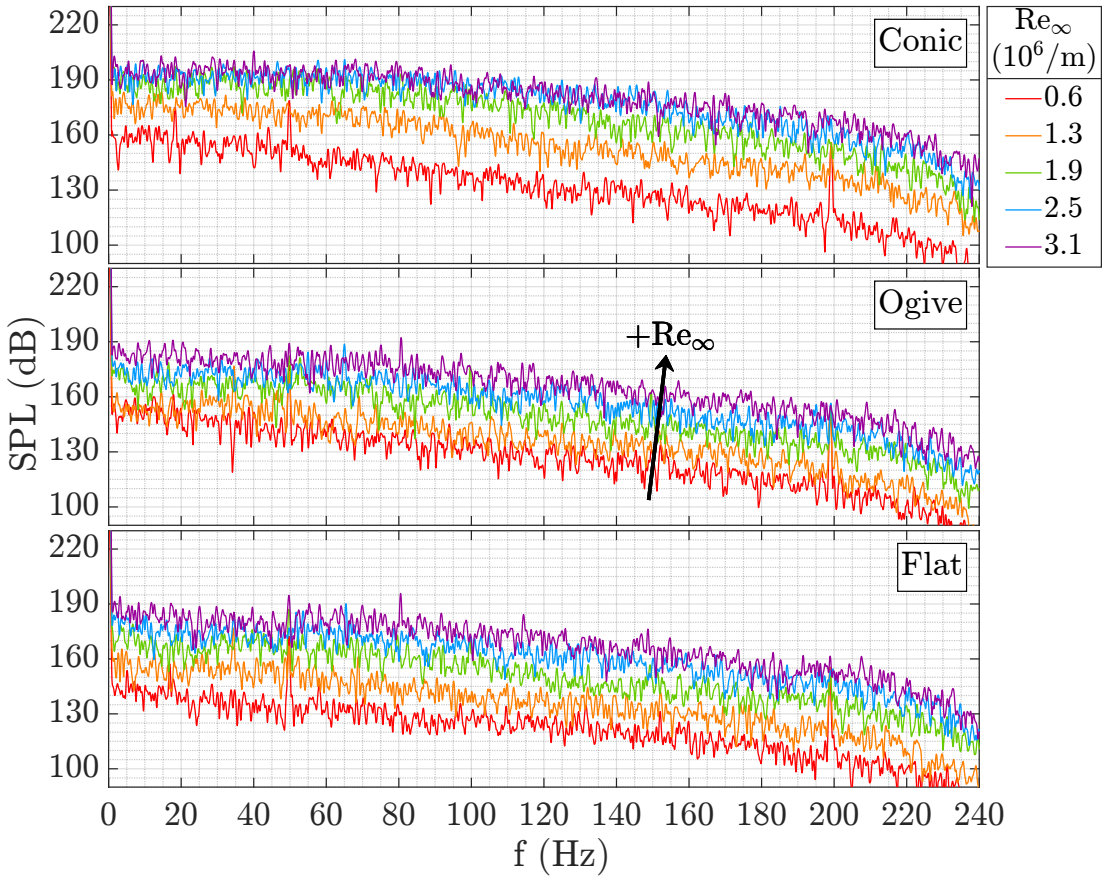

Figure 6.25: USP: ΔRe FFT: L/D = 1, L/W = 1, x/L = 0.6, z/W = 0.3

6.2.3 Effect of Upstream Geometry

Fig. 6.26 shows change in spectra, for varied U/S geometry, thus BL δ and $dp/dx < 0$ at W = 60mm (trends are similar at W = 30mm). Between thin laminar BL nose cases, SPL reduces from conic, to ogive then parabola geometry, proportional to increase in BL δ, and decrease in U/S $dp/dx < 0$. From laminar BL nose cases, to the thick turbulent BL of the flat U/S case a larger reduction in SPL results, corresponding to larger increase in BL δ and $dp/dx = 0$.

Mode 1 ($f \approx$ 20-30Hz) and 2 ($f \approx$ 50Hz) peak frequencies in nose cases, are reduced in the flat case. Mode 3 at $f \approx$ 100Hz, is more abundant in the flat case, otherwise lulled by noses, which have mode 3 at f = 199Hz. Frequency also shifts higher, for mode 1, 3 and 4, however mode 2 sustains. Mode 2 is a dominant SL mode, based on cavity length, and as length does not change, mode frequency would not change, its SPL can however change with BL δ, as observed.

Plumblee[3], East[8] and Block[6], observed mode 1 dependence on cavity depth, thus included it in their St models. Research following[50,135] visualised cavity flow with PIV or Schlieren, and observed dynamic changes, in response to effective depth $\Delta(\delta/\text{D})$. In this thesis, depth was fixed, and mode 1 frequency shifted with δ. Therefore, by recognising δ/D as the controlling

depth parameter. Mode 1 frequency appears driven by depth at fixed δ, or δ at fixed depth. Consequently, for St prediction based on cavity length St_L, effective depth; δ/D is instead proposed to predict mode 1, as an update to East's[8] model. This reduces St_L, introduces curvature, and brings frequency prediction for incompressible flow within experimental results of this thesis, and those where δ data was given[15,44,50,51], per Chapter 7.

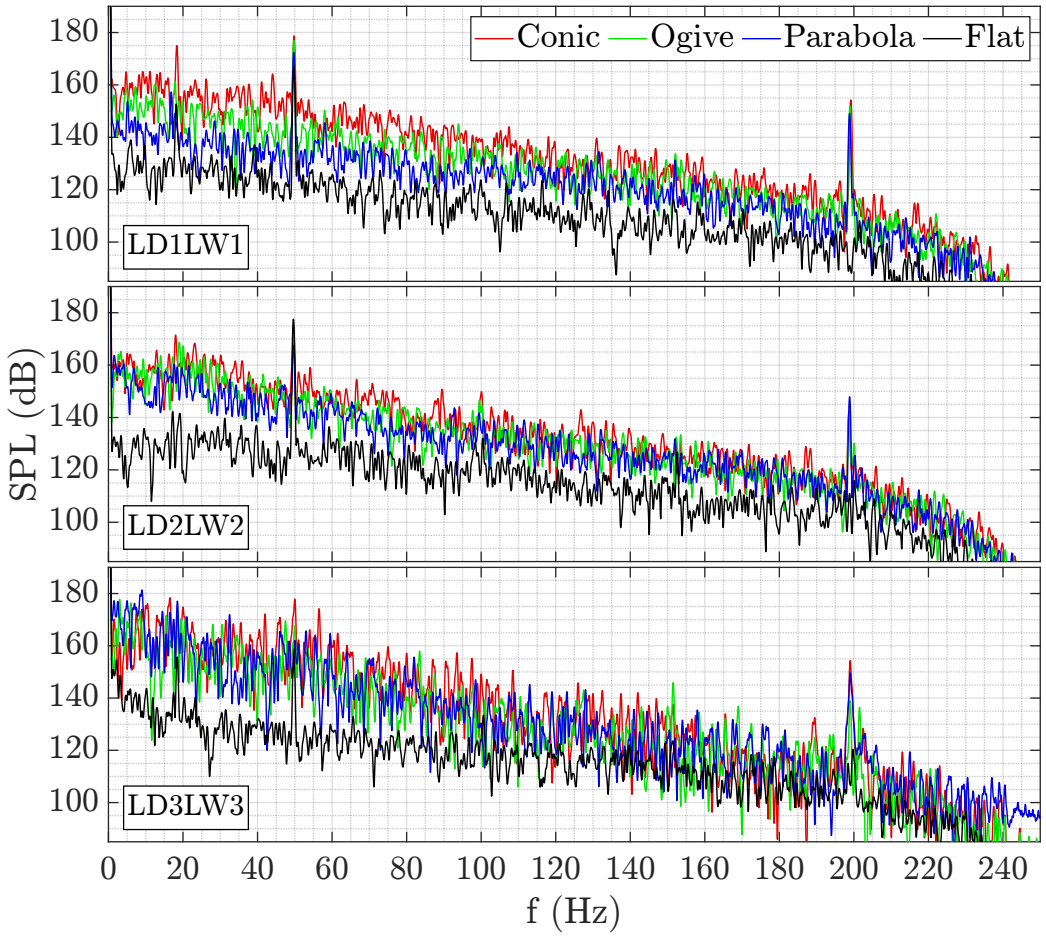

Figure 6.26: USP: ΔBL FFT: W = 60mm, Re_∞/m = 0.6×10^6, x/L = 0.6, y/D = 1, z/W = 0.3

Flat-plate mode 3 f = 100Hz, is observed to dampen in short cavities, with a thin U/S BL, and $dp/dx < 0$. This is poignant, regarding not only the BL, and dp/dx effects on cavity flow response. But also, and particularly of note, a potential indication of causation for dominant mode switching. A phenomena observed in cavity flow spectra, between SL modes 2 and 3, when increasing U_∞. The origin of which, is a known mystery[18,28,50,75,136–141].

In these results, mode 3 location and magnitude is manipulated by U/S geometry, through the BL, and dp/dx. It only appears, when the cavity is long enough, BL thick enough, and $dp/dx < 0$ low enough. Otherwise, it is weak, or null. BL structure defines flow separation, and vorticity into the cavity. And as U_∞ increases, for these nose cases, BL δ decreases, as $dp/dx < 0$ increases, which influences mode 3 presence. Therefore, it is proposed, mode switching in cavity flow, between SL mode 2 and 3, is a function of mode 3. As the mode is manipulated by U/S BL δ, and $dp/dx < 0$, in contribution to BL separation from the cavity LE, which drives SL formation through propagated vorticity, the foundation of cavity response.

Gharib & Roshko[28] non-dimensionalised cavity geometry, with SL momentum thickness θ_{SL}, and identified a hysteresis region for mode 3, linked to θ_{SL}. The SL and its momentum θ_{SL}, are structurally defined by BL separation, thus δ, and dp/dx, at separation, which is observed to change with U/S geometry, in this thesis. Gharib & Roshko[28] similarly performed experiments in incompressible flow, observing a cavity with curvature U/S, to ensure a laminar BL. This indicates, the effect is magnified by incompressible flow, where viscous effects have more influence over the dynamics than compressible flow. Therefore, Gharib & Roshko[28] provide supporting evidence, surrounding impact of BL δ and $dp/dx < 0$ U/S, as an insight to mode switching, and a means to predict dominant frequencies, and potentially amplitude.

6.3 Pressure Results Summary

(1) Cavity Length: A balanced standing wave is implied by equal $C_{p,rms}$ on each cavity wall at L/D = 1. For L/D = 2-3, energy moved to a floor peak with steeper dp/dx each side, especially aft, with $dp/dx > 0 \propto$ flow separation. Past research implies recirculation, pulling flow in, thus separation on the floor, to feed SL oscillation thus cavity response.

(2) Cavity Width: spanwise nodes in the wider cavity (W = 60mm), shed outboard serially alike [56–58, 135]; a primary streamwise recirculation mechanism, "*flanked by a pair of spanwise nodes*" on the floor, reflected off the TE. They disappear at W = 30mm, as gradient density increases on the upper TE, indicating sharper flow separation, likely due to SL flapping. Thus, narrower flow oscillates closer to the mouth, and wider develops spanwise.

(3) Increasing $\mathrm{Re}_\infty \propto \mathrm{U}_\infty$, increased $C_{p,rms}$, and dp/dx on each cavity surface. The impact is small compared to changes in cavity geometry, and the U/S BL, per below.

(4) Smaller BL δ and larger $dp/dx < 0$ U/S, increased $C_{p,rms}$ and dp/dx on each cavity surface, especially $dp/dx > 0$ aft the floor peak, indicating sharper flow separation, thus stronger recirculation. The peak region also grew, as BL δ decreased, and $dp/dx < 0$ increased U/S, supporting stronger recirculation, and indicating frequency shift in space.

(5) Between U/S cases, the high $C_{p,rms}$ regions size, and gradient density change. The thinnest BL, and largest $dp/dx < 0$ U/S, produces a broader peak on the cavity floor, with higher dp/dx either side. Internal cavity geometry is sustained, only U/S BL δ decreased, and $dp/dx < 0$ increased. Thus, U/S BL altered system dynamics, implying a spatial shift in frequency response, to be adjusted for in St number prediction.

(6) OASPL and peak SPL increase with increasing cavity length, Re_∞ and decreasing U/S BL δ, more notably for the latter, by up to 40dB, from a turbulent to laminar BL U/S.

(7) Four dominant modes are apparent, their occurrence, and frequency (Hz) dependant on cavity geometry, and U/S BL. The Re_∞ effect is comparatively small.

(8) Mode 1 is the normal mode. Its amplitude and frequency shifting with δ.

(9) Modes 2-4 are SL modes. Mode 2-3 shift dominance, dependant on U/S geometry thus δ. Mode 3 frequency, is especially dependant on δ. For a thick turbulent BL, $f \approx 100$Hz, for thin laminar BL $f \approx 199$Hz. The latter as mode 4 for the flat plate, lower in SPL. Suspected to be the SSO mode, which is much stronger for a laminar BL.

Chapter 7

Physical Cavity Model

This chapter converges hot-wire anemometry (HWA), and unsteady surface pressure (USP) results, to derive a new open cavity flow model, including viscosity, in contrast to past models[2,6,8]. Disturbance δ, and displacement δ^* thickness of the boundary layer (BL), and pressure gradient dp/dx upstream (U/S) are considered, in formation of the shear layer (SL), through shed vorticity from the cavity leading edge (LE), which propagates over the cavity, with respect to cavity geometry, $\mathrm{Re}_\infty, \mathrm{a}_\infty$, and dp/dx into the cavity, to predict frequency and amplitude.

The model is formulated from past research of the open cavity flow phenomena, which is reviewed in Chapter2, and experimental investigation in this thesis, observing effects of; cavity length, depth, width, $\mathrm{Re}_\infty/\mathrm{m} \propto \mathrm{U}_\infty$, and most importantly viscosity, through BL δ, δ^* and dp/dx U/S. Cavity response was reconstructed from USP data of $C_{p,rms}$, dynamic mode decomposition (DMD), and the U/S BL profile from HWA and USP, considering U/S geometry in BL formulae.

7.1 Dimensionless Frequency

Evidence highlights the principle characteristics of cavity flow periodic pressure oscillations, and how they are driven, with respect to viscosity. This has provided a basis to model cavity viscid response, through BL δ, and mass displaced δ^*, for turbulent to laminar BLs, also $dp/dx < 0$, with respect to effective cavity geometry $\sim \delta/\mathrm{L}, \delta^*/\mathrm{L}, \delta^*/\mathrm{D}$. Dimensionless frequency is thus composed, as an update to Rossiter's[2] model, from the viscid physical model in Fig. 7.1, considering [3, 6, 8] for incompressible effects. A full derivation is provided in Appendix E.

First, we consider the number of periodic components, or modes m. In cavity flow, three distinct factors coalesce; m_f and m_v, phased by γ_v. Here, m_f represents feedback modes from the cavity TE, and m_v represents cavity LE shed vorticity modes, a core feature of the pressure oscillation, empirically phased to m_f by γ_v, as defined by Rossiter[2]. A value of $\gamma_v = 0.25$, is generally accepted for best fit in the L/D range[2,6,13]. To give cavity modes per:

$$m - \gamma_v = (m_f + m_v) - \gamma_v \tag{7.1}$$

Secondly, based on Crocco's theorem[142,143], vorticity is assumed proportional to mass displaced δ^* by $\mathrm{e}^{\bar{p}_x}$, feedback phase lag $\gamma_v\lambda_v$, and its propagation in time; $(\delta/\mathrm{L})\kappa\mathrm{U}_\infty\Delta t$. Feedback waves are assumed proportional to travel U/S in time; $(\delta/L)\mathrm{a_c}\Delta t$, through distance in the cavity,

represented by a ratio of cavity length by $e^{\bar{p}_x}$, to effective mass depth δ^*/D. Here, $\kappa = 0.57$ is Rossiter's[2] empirical ratio of SL vorticity convection to U_∞. δ/L is effective disturbance length, representing traversability of the viscid disturbance, over cavity length. a_c is speed of sound in the cavity, and $\bar{p}_x$ is an empirically derived dimensionless dp/dx U/S, as follows:

$$\frac{a_\infty}{a_c} = \left(1 + \frac{\delta}{L}\right) \qquad (7.2) \qquad\qquad \bar{p}_x = \frac{dp}{dx}\frac{1}{\rho U_\infty^2}\frac{L}{\delta^*/D} \qquad (7.3)$$

Then, as cavity oscillations per Eqn. 7.1, are periodically shed LE vorticity, propagated D/S at wavelength λ_v, by κU_∞ [144], and TE reflected feedback travelling U/S at wavelength λ_f by a_c [2] they must be related in frequency:

$$\frac{fL}{\delta} = \frac{\kappa U_\infty}{\lambda_v} = \frac{a_c}{\lambda_f} \qquad (7.4)$$

Using Eqn. 7.4, dimensionless frequency St, can be determined as a function of vorticity shed through mass displaced δ^*, and feedback over cavity length by effective mass depth δ^*/D, both by $e^{\bar{p}_x}$, through combination of wave equations for vorticity m_v and feedback m_f as follows:

$$m_v\lambda_v = \delta^* e^{\bar{p}_x} + \gamma_v\lambda_v + \kappa U_\infty \frac{\delta}{L}\Delta t \qquad (7.5) \qquad\qquad m_f\lambda_f = \frac{Le^{\bar{p}_x}}{\delta^*/D} - a_c\frac{\delta}{L}\Delta t \qquad (7.6)$$

Re-arranging Eqn. 7.5 for Δt, and substituting into Eqn. 7.6 returns:

$$m_f\lambda_f = \frac{Le^{\bar{p}_x}}{\delta^*/D} - \frac{a_c}{\kappa U_\infty}\left(m_v\lambda_v - \delta^* e^{\bar{p}_x} - \gamma_v\lambda_v\right) \qquad (7.7)$$

Re-arranging Eqn. 7.7, to group modes on the LHS, and other variables on the RHS gives:

$$\kappa\frac{U_\infty}{a_c}m_f\lambda_f + \lambda_v\left(m_v - \gamma_v\right) = \kappa\frac{U_\infty}{a_c}\frac{Le^{\bar{p}_x}}{\delta^*/D} + \delta^* e^{\bar{p}_x} \qquad (7.8)$$

Substituting λ_v and λ_f from Eqn. 7.4 into Eqn. 7.8 we find:

$$\kappa\frac{U_\infty}{f}\frac{\delta}{L}\left(m_f + m_v - \gamma_v\right) = \kappa\frac{U_\infty}{a_c}\frac{Le^{\bar{p}_x}}{\delta^*/D} + \delta^* e^{\bar{p}_x} \qquad (7.9)$$

Expanding Eqn. 7.9 to Eqn. 7.10, considering a_∞/a_c in Eqn. 7.2 with $M_\infty = U_\infty/a_\infty$, leads to:

$$\kappa\frac{U_\infty}{f}\frac{\delta}{L}\left(m_f + m_v - \gamma_v\right) = \kappa Le^{\bar{p}_x}\left(\frac{U_\infty}{a_\infty}\frac{a_\infty}{a_c}\frac{D}{\delta^*} + \frac{\delta^*}{\kappa L}\right) \qquad (7.10)$$

$$\downarrow$$

$$\frac{U_\infty}{f}\frac{\delta}{L}\left(m_f + m_v - \gamma_v\right) = Le^{\bar{p}_x}\left(\frac{M_\infty}{\delta^*/D}\left(1 + \frac{\delta}{L}\right) + \frac{\delta^*}{\kappa L}\right) \qquad (7.11)$$

Finally rearranging Eqn. 7.11 for St number; fL/U_∞ gives viscous dimensionless frequency:

$$\frac{\delta}{L}\left(m_f + m_v - \gamma_v\right) = \frac{fL}{U_\infty}e^{\bar{p}_x}\left(\frac{M_\infty}{\delta^*/D}\left(1 + \frac{\delta}{L}\right) + \frac{\delta^*}{\kappa L}\right)$$

$$\downarrow$$

$$\frac{fL}{U_\infty} = \frac{\delta}{Le^{\bar{p}_x}}\left(m_f + m_v - \gamma_v\right)\left[\frac{M_\infty}{\delta^*/D}\left(1 + \frac{\delta}{L}\right) + \frac{\delta^*}{\kappa L}\right]^{-1}$$

$$\downarrow$$

$$St_{HS} = \frac{fL}{U_\infty} = \frac{\delta}{e^{\bar{p}_x}}\left(m - \gamma_v\right)\left[\frac{M_\infty}{\delta^*/D}\left(L + \delta\right) + \frac{\delta^*}{\kappa}\right]^{-1} \qquad (7.12)$$

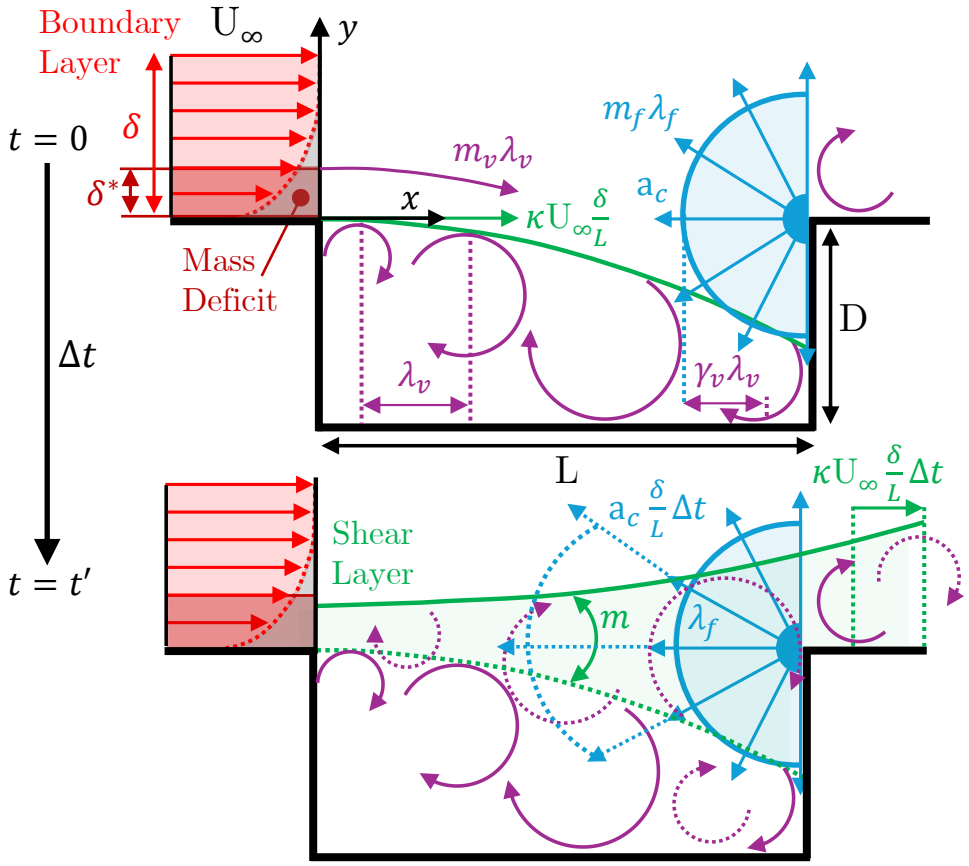

Figure 7.1: Viscid Incompressible Open Cavity Flow Model

Examining Eqn. 7.12 for the flat-plate U/S with $dp/dx = 0$, Eqn. 7.12 simplifies to:

$$\mathrm{St_{HS}} = \delta\,(m - \gamma_v)\left[\frac{\mathrm{M_\infty}}{\delta^*/\mathrm{D}}\,(\mathrm{L} + \delta) + \frac{\delta^*}{\kappa}\right]^{-1} \tag{7.13}$$

Now assuming a Blasius flat-plate relationship of $\delta^* = 0.34\delta$ [99] for Eqn. 7.13, Fig. 7.2 shows St number convergence toward the limit of inviscid flow $\delta \to 0$, $\mathrm{St_{HS}} \to 0$. In this case, lack of viscosity in the flow, prevents vorticity shedding from the cavity LE, resulting in no SL or oscillation. Hence, the equation gives consistent physical characteristics.

Previous models [2,3,6,8,97], assumed inviscid flow, or an infinitely thin SL, introducing the SL artificially with κ, to account vorticity. However, from Crocco's theorem [142,143], vortex formation and propagation, is a function of viscosity, and when ignored, creates D'Alembert's paradox [99]. This contradicts observation of viscid driven roll-up, to form the SL over a cavity. D'Alembert's paradox can be resolved by considering viscous propagation of the BL, with no-slip BCs per Eqn. 7.13, to form the SL, between external and internal flow, where vorticity rolls-up.

For comparison to Rossiter's formula, order of magnitude analysis is applied to Eqn. 7.13. In this case, assuming inertial dominance $O(\rho \mathrm{U_\infty})$ over viscosity $O(\delta)$, such that viscous terms of effective mass depth δ^*/D, disturbance and mass length $\delta/L, \delta^*/L$ attain zero order of magnitude $O(\delta) \to 10^0$. Further, assuming $\mathrm{a_c} = \mathrm{a_\infty}$ per Rossiter [2], the substitution from Eqn. 7.10 to 7.11 returns $\mathrm{M_\infty}$. Thus Eqn. 7.14, simplifies to Rossiter's Eqn. 2.2 for $0.4 < \mathrm{M_\infty} < 1.2$, explaining why higher speed flow is modelled well with Rossiter's inviscid formula, but also why this approach falls short for incompressible flow, where viscid effects are more dominant.

$$\mathrm{St_{HS}} = \frac{\delta}{L}(m-\gamma_v)\left[\frac{\mathrm{M}_\infty}{\delta^*/D}\left(1+\frac{\delta}{L}\right)+\frac{1}{\kappa}\frac{\delta^*}{L}\right]^{-1} \rightarrow \quad \frac{m-\gamma_v}{\mathrm{M}_\infty+\kappa^{-1}} \tag{7.14}$$

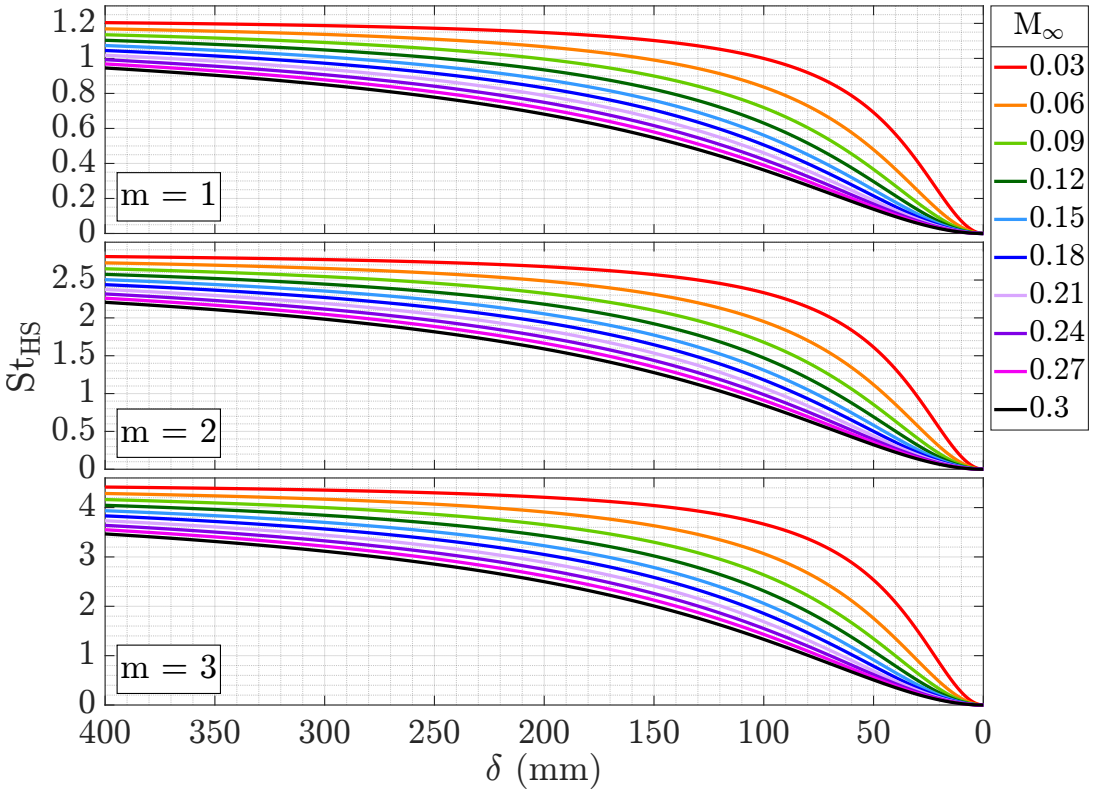

Figure 7.2: Strouhal Number $\mathrm{St_{HS}}$ vs Boundary Layer Thickness δ

In nose cases, δ was notably reduced by $dp/dx < 0$, along the wedge, or curve before the cavity. Thus Eqn. 7.12 is prevalent, with dimensionless $dp/dx \propto \bar{p}_x$ U/S in Eqn. 7.3: dp/dx is pressure gradient, with dp nondimensionalised by $\rho \mathrm{U}_\infty$ [99], and dx by effective L/D = L/(δ^*/D). As viscid stream geometry defines vorticity [15] and feedback, altering dp/dx U/S.

The physical characteristic of exponential exponent implementation, for $\bar{p}_x \neq 0$ in Eqn. 7.12, represents a response to adverse $dp/dx > 0$, which is induced by the cavity, with respect to change in velocity through dp/dx. If dp/dx is favourable U/S, acceleration decays with adverse dp/dx, as flow moves into the cavity. If dp/dx is adverse U/S, deceleration instead grows.

In this study, nose geometry produced $dp/dx < 0$ U/S, accelerating flow before the cavity, which then decays through $dp/dx > 0$ into the cavity. Moreover, larger $dp/dx < 0$ U/S, increased cavity magnitude response. This is because, larger $dp/dx < 0$ U/S, requires more decay by $dp/dx > 0$ into the cavity, through vorticity shed, due to larger Δp external to internal, forcing a faster rate of change along the pressure path, which increases oscillatory pressure. If $dp/dx > 0$ U/S, extant deceleration would grow into the cavity, and thus vorticity shed, and oscillatory magnitude would be much lower. Per definition, $\bar{p}_x$ is a constant of U/S geometry alike Falkner-Skan [22], as dp/dx increases $\propto \mathrm{U}_\infty$, and decreases δ^* giving: $\bar{p}_x \approx$ -6.3, -5.8 and -5.6 for conic, ogive and parabola. However, as vorticity is a function of $dp/dx < 0$, and δ^*/D, $e^{\bar{p}_x}$ effectively cancels δ^*/D in Eqn. 7.12's denominator, to simplify calculation if dp/dx isn't available.

Fig. 7.3 compares modal lines predicted by Eqn. 7.13 in black, for the baseline cavity with a flat-plate U/S thus $dp/dx = 0$, and thick turbulent BL $\delta \approx 35$mm, to Rossiter's[2] Eqn. 2.2 in green, Block's[6] Eqn. 2.5 in blue, East's[8] Eqn. 2.3 in red, and USP data from this thesis, to track against experimental results. Similarly, Fig. 7.4 presents modal prediction lines by Eqn. 7.12 for the conic nose U/S, with $dp/dx < 0$, and a thin laminar BL $\delta \approx 2$mm. Corresponding plots for curved ogive, and parabola noses U/S are presented in Fig. E.1 and E.2 of Appendix E.3. On comparing Fig. 7.3 and 7.4, model accuracy deviates slightly for the thinner conic BL with $dp/dx < 0$, as BL δ approaches the inviscid limit $\delta = 0$ from $\delta \approx 35 \rightarrow 2$mm.

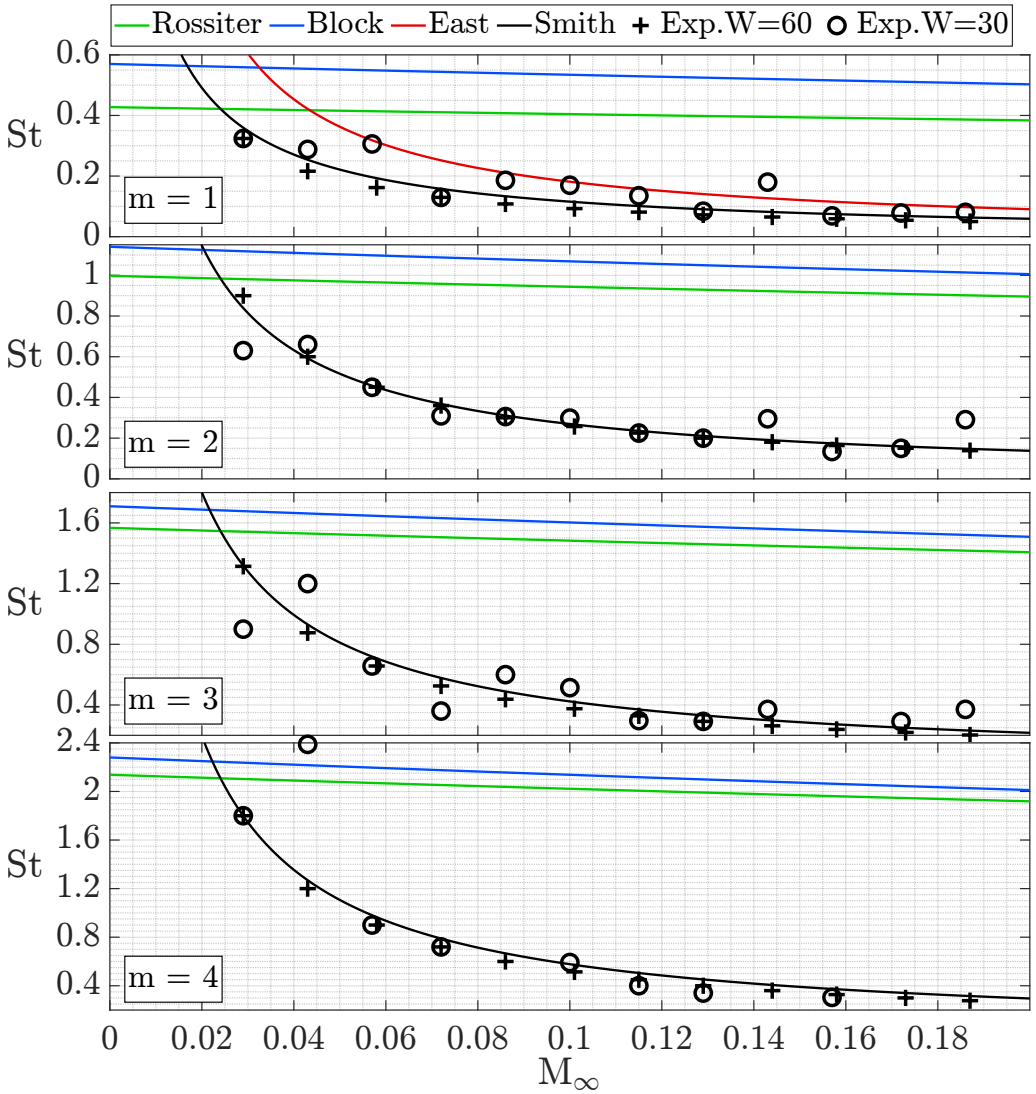

Figure 7.3: Strouhal Number: Flat-Baseline U/S

Fig. 7.5 compares modal lines predicted by Eqn. 7.13 in black, to Rossiter's[2] experimental data, used to derive their model in Eqn. 2.2, represented in green. Similarly, Fig. 7.6 compares modal lines predicted by Eqn. 7.13 in black, to Block's[6] experimental data, used to derive their model in Eqn. 2.5, represented in blue. Fig. 7.7 then makes further comparison to experimental data, from a series of well cited subsonic open cavity flow studies in [17, 36, 97, 145, 146]. Overall, Eqn. 7.13 proves reasonably robust against a variety of L/D, and M_∞, with higher accuracy for open incompressible cavity flow (L/D ≤ 5, $M_\infty < 0.3$), where the model was derived.

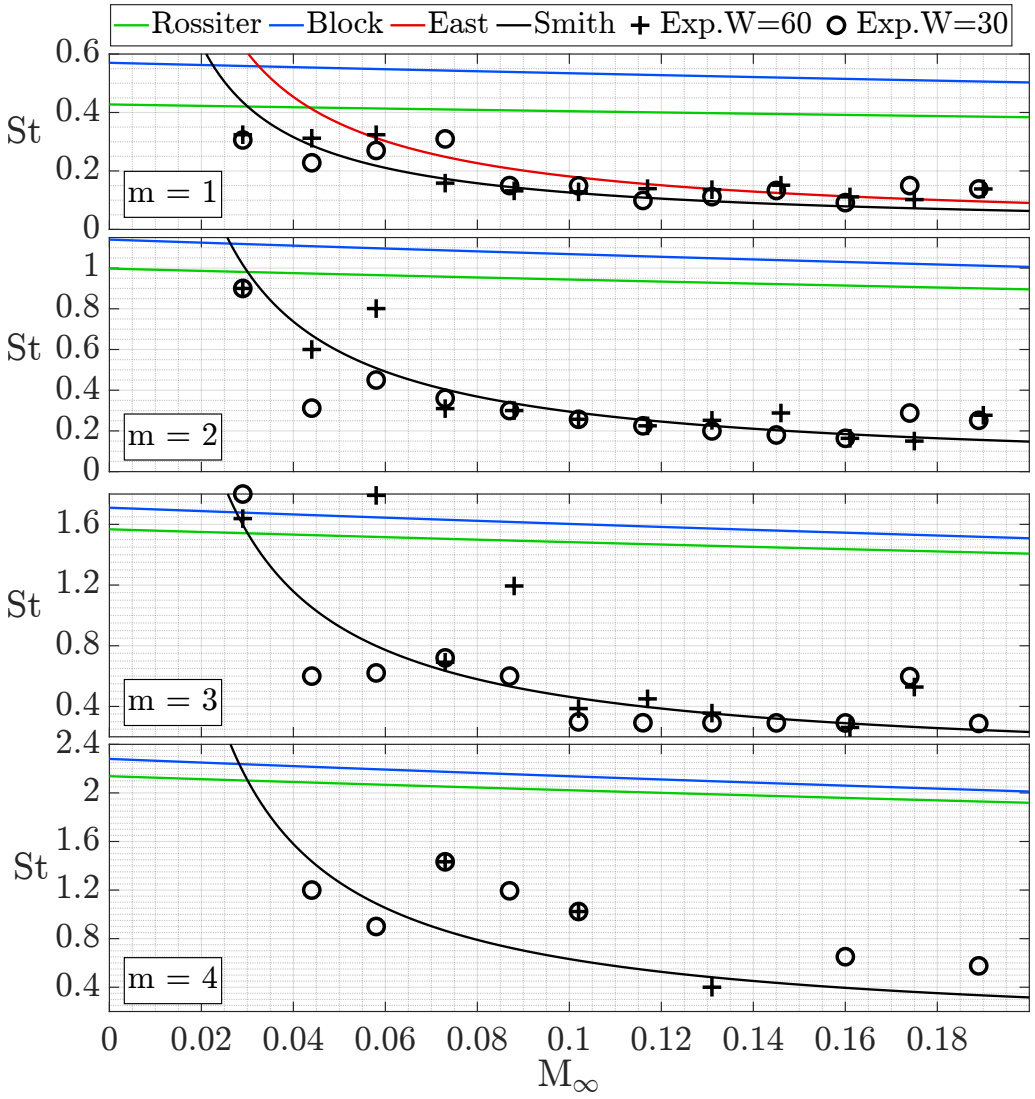

Figure 7.4: Strouhal Number: Conic Nose U/S

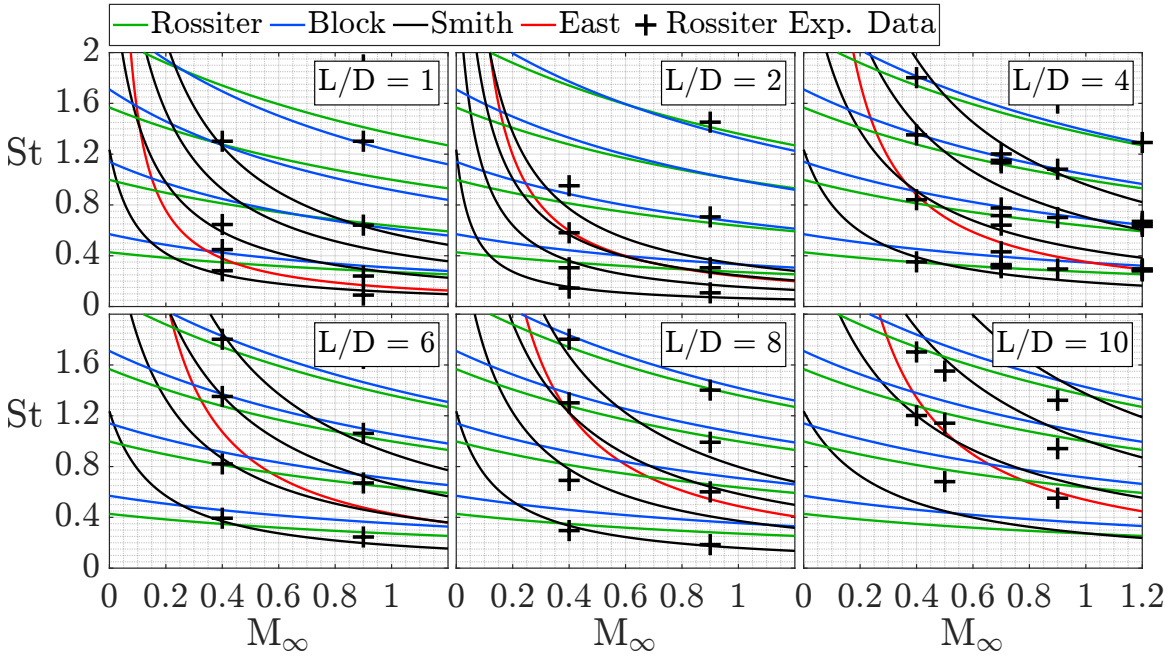

Figure 7.5: Strouhal Number: Comparison to Rossiter's[2] Experimental Data

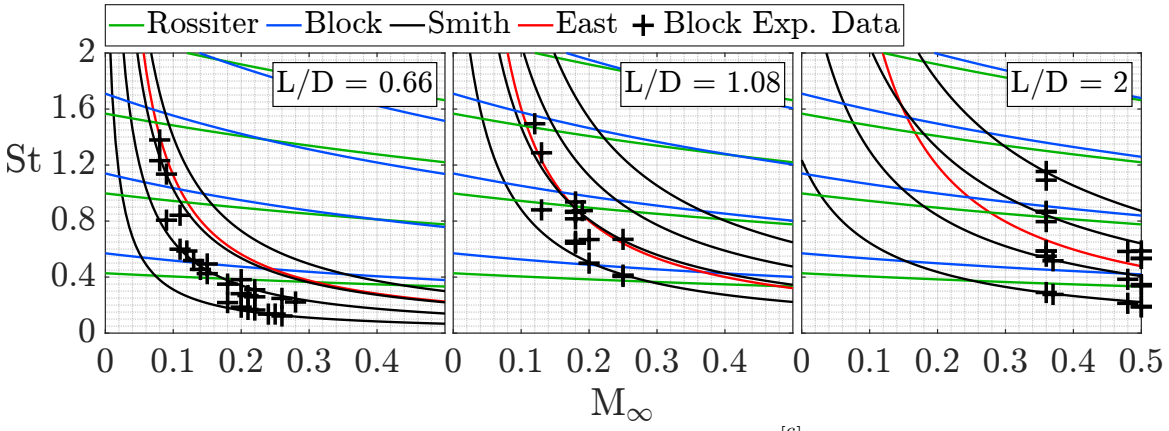

Figure 7.6: Strouhal Number: Comparison to Block's[6] Experimental Data

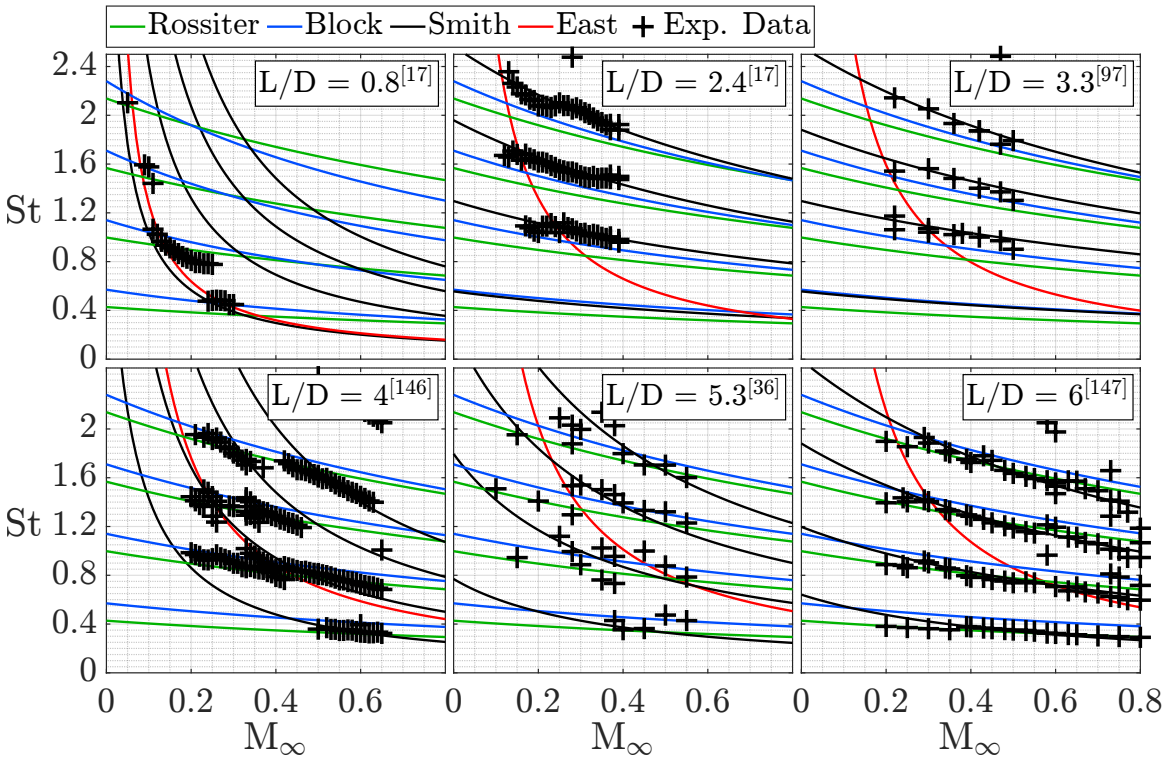

Figure 7.7: Strouhal Number: Comparison to Various Subsonic Experimental Data

7.2 Dimensionless Pressure Amplitude

Evidence further suggests, cavity magnitude response is dependant on the BL U/S. The derivation for dimensionless frequency St references thus, with effective cavity geometry respective to BL δ and mass displaced δ^* prevalent; $\delta/\mathrm{L}, \delta^*/\mathrm{D}, \delta^*/\mathrm{D}$. Therefore, Plumblee at al's[3] amplification model is updated, accounting effective geometry, wave number and frequency above, to predict amplitude response. The model is a theoretical radiative impedance treatment, for cavity pressure oscillations, using enclosure response functions by Morse[147]. Here, impedance is cavity fluid resistance to incoming flow, as a function of required pressure amplitude, to create a frequency, dependant on; fluid density, viscosity, wave speed, and geometry.

Morse's[147] function depends on; enclosure dimensions, boundary impedance, source location, and strength. Enclosure dimensions are cavity length, depth and width. Boundary impedance

is SL fluid resistance to incoming flow. Source location, and strength depend on location in the cavity with respect to LE shed vorticity, and feedback from the TE. Oscillation is assumed to form, from flow over the cavity, radiated into space by a piston-like SL with impedance; $Z \propto R_z + iX_z$, using subsonic radiation resistance R_z and reactance X_z in Eqn. 7.15 and 7.16 [3].

$$
\begin{aligned}
R_z = -\frac{\beta^3}{\pi\bar{k}}\Bigg[& \int_0^{\tan^{-1}\beta\zeta}\left(\frac{\sec\theta\sin\left(\bar{k}(\sec\theta+M)/\beta^2\right)}{(\sec\theta+M)^2}+\frac{\sec\theta\sin\left(\bar{k}(\sec\theta-M)/\beta^2\right)}{(\sec\theta-M)^2}\right)d\theta \\
& -\int_0^{\cot^{-1}\beta\zeta}\left(\sin\theta-\frac{\cos\theta}{\beta\zeta}\right)\left(\frac{\sin\left(\bar{k}\zeta\sec\theta(1+M\sin\theta)/\beta\right)}{(1+M\sin\theta)^2}+\frac{\sin\left(\bar{k}\zeta\sec\theta(1-M\sin\theta)/\beta\right)}{(1-M\sin\theta)^2}\right)d\theta \\
& -\int_0^{\cot^{-1}\beta\zeta}\left(\frac{2\beta\sin\theta\cos\theta}{\bar{k}\zeta}\right)\left(\frac{\cos\left(\bar{k}\zeta\sec\theta(1+M\sin\theta)/\beta\right)}{(1+M\sin\theta)^3}+\frac{\cos\left(\bar{k}\zeta\sec\theta(1-M\sin\theta)/\beta\right)}{(1-M\sin\theta)^3}\right)d\theta \\
& +\frac{\beta}{\bar{k}\zeta}\left[\frac{\cos\left(\bar{k}\left(\sqrt{1+(\beta\zeta)^2}+M\right)/\beta^2\right)}{\left(\sqrt{1+(\beta\zeta)^2}+M\right)^2}+\frac{\cos\left(\bar{k}\left(\sqrt{1+(\beta\zeta)^2}-M\right)/\beta^2\right)}{\left(\sqrt{1+(\beta\zeta)^2}-M\right)^2}\right] \\
& -\frac{\beta}{\bar{k}\zeta}\left[\frac{\cos\left(\bar{k}\,(1+M)/\beta^2\right)}{(1+M)^2}+\frac{\cos\left(\bar{k}\,(1-M)/\beta^2\right)}{(1-M)^2}\right]+\frac{\beta}{\bar{k}\zeta}\left[\frac{1}{(1+M)^2}+\frac{1}{(1-M)^2}\right] \\
& -\frac{2\bar{k}}{\beta^3}\left[\tan^{-1}\left(\frac{1-M}{\beta}\right)+\tan^{-1}\left(\frac{1+M}{\beta}\right)\right]\Bigg]
\end{aligned}
\tag{7.15}
$$

$$
\begin{aligned}
X_z = \frac{\beta^3}{\pi\bar{k}}\Bigg[& -\int_0^{\tan^{-1}\beta\zeta}\left(\frac{\sec\theta\cos\left(\bar{k}(\sec\theta+M)/\beta^2\right)}{(\sec\theta+M)^2}+\frac{\sec\theta\cos\left(\bar{k}(\sec\theta-M)/\beta^2\right)}{(\sec\theta-M)^2}\right)d\theta \\
& +\int_0^{\cot^{-1}\beta\zeta}\left(\sin\theta-\frac{\cos\theta}{\beta\zeta}\right)\left(\frac{\cos\left(\bar{k}\zeta\sec\theta(1+M\sin\theta)/\beta\right)}{(1+M\sin\theta)^2}+\frac{\cos\left(\bar{k}\zeta\sec\theta(1-M\sin\theta)/\beta\right)}{(1-M\sin\theta)^2}\right)d\theta \\
& -\int_0^{\cot^{-1}\beta\zeta}\left(\frac{2\beta\sin\theta\cos\theta}{\bar{k}\zeta}\right)\left(\frac{\sin\left(\bar{k}\zeta\sec\theta(1+M\sin\theta)/\beta\right)}{(1+M\sin\theta)^3}+\frac{\sin\left(\bar{k}\zeta\sec\theta(1-M\sin\theta)/\beta\right)}{(1-M\sin\theta)^3}\right)d\theta \\
& +\frac{\beta}{\bar{k}\zeta}\left[\frac{\sin\left(\bar{k}\left(\sqrt{1+(\beta\zeta)^2}+M\right)/\beta^2\right)}{\left(\sqrt{1+(\beta\zeta)^2}+M\right)^2}+\frac{\sin\left(\bar{k}\left(\sqrt{1+(\beta\zeta)^2}-M\right)/\beta^2\right)}{\left(\sqrt{1+(\beta\zeta)^2}-M\right)^2}\right] \\
& -\frac{\beta}{\bar{k}\zeta}\left[\frac{\sin\left(\bar{k}\,(1+M)/\beta^2\right)}{(1+M)^2}+\frac{\sin\left(\bar{k}\,(1-M)/\beta^2\right)}{(1-M)^2}\right]+\frac{1}{\beta\zeta}\left[\frac{1}{1+M}+\frac{1}{1-M}\right] \\
& +\frac{2}{\beta^2}-\frac{2M}{\beta^3}\left[\tan^{-1}\left(\frac{1-M}{\beta}\right)+\tan^{-1}\left(\frac{1+M}{\beta}\right)\right]\Bigg]
\end{aligned}
\tag{7.16}
$$

where, $\beta = \sqrt{1-{M_\infty}^2}$, θ is cylindrical coordinate radiation, $\zeta = W/L$ accounts cavity aspect ratio, and $\bar{k}$ is normal wave number. Per Eqn. 7.4, cavity vorticity and feedback are related in frequency, thus contribute to amplitude as; $k = k_v + k_f$: $k_v = 2\pi f L/\kappa U\delta$, and $k_f = 2\pi f L/a_c\delta$ normal as $\bar{k}_v = k_v\delta^*$ and $\bar{k}_f = k_f L(\delta^*/D)^{-1}$. The algorithm is in Appendix F.4.2.

R_z and X_z were derived based on: a cavity of five walls with infinite impedance, and a sixth of finite impedance, representing a SL over the cavity mouth, through $\zeta = W/L$. Here, oscillation

wave speed is altered by $\mathrm{U}_\infty, \mathrm{a}_\infty$, through Eqn. 7.17, with retarded potential theory to account velocity, and BL propagation delay, as transient elements, with respect to a stationary cavity.

$$\bar{\mathrm{V}}_p^2 = \frac{p_{p,m}}{\mathrm{a}^2}\left(\frac{\partial}{\partial t} + \mathrm{U}_\infty \frac{\partial}{\partial x}\right) \tag{7.17}$$

A simplified solution for normal depth mode $m = 1$ is in Eqn. 7.18 [3], with respect to pressure at the cavity mouth p_0. For dominant lengthwise vortical or SL modes $m > 1$, a more complex form is required, including cavity length, depth, and width as follows.

$$p_{p,m} = p_0\left[(\mathrm{R_z}\sin k\mathrm{D})^2 + (\mathrm{X_z}\sin k\mathrm{D} - \cos k\mathrm{D})^2\right]^{-1/2} \tag{7.18}$$

Morse's enclosure characteristic response function, in Eqn. 7.19 [147], is used to model cavity response at a point of interest (x, y, z): m is mode number, and g_m in Eqn. 7.20 is the Morse boundary function [147], representing the cavity mouth SL with finite impedance.

$$\phi_m = \cos\left(\frac{\pi m x}{\mathrm{L}}\right)\cosh\left(\frac{\pi \mathrm{g}_m y}{\mathrm{D}}\right)\cos\left(\frac{\pi z}{\mathrm{W}}\right) \tag{7.19}$$

$$\mathrm{g}_m \tanh(\pi \mathrm{g}_m) = i\left[\frac{\bar{k}\mathrm{D}}{\pi\mathrm{L}\,(\mathrm{R_z} + i\mathrm{X_z})}\right] \tag{7.20}$$

Boundary function g_m is given a solution $\mathrm{g}_n = \xi_m + i\eta_m$, with complex roots ξ_m and η_m derived by separating Eqn. 7.20 into real and imaginary parts:

$$\cot(\pi\eta_m) = \frac{\eta_m \cosh(\pi\xi_m) - \left(\bar{k}\mathrm{DR_z}/\pi\mathrm{L}\left(\mathrm{R_z^2} + \mathrm{X_z^2}\right)\right)\sinh(\pi\xi_m)}{\xi_m \sinh(\pi\xi_m) - \left(\bar{k}\mathrm{DX_z}/\pi\mathrm{L}\left(\mathrm{R_z^2} + \mathrm{X_z^2}\right)\right)\cosh(\pi\xi_m)}$$

$$i\cot(\pi\eta_m) = -\frac{\xi_m \cosh(\pi\xi_m) - \left(\bar{k}\mathrm{DX_z}/\pi\mathrm{L}\left(\mathrm{R_z^2} + \mathrm{X_z^2}\right)\right)\sinh(\pi\xi_m)}{\eta_m \sinh(\pi\xi_m) - \left(\bar{k}\mathrm{DX_z}/\pi\mathrm{L}\left(\mathrm{R_z^2} + \mathrm{X_z^2}\right)\right)\cosh(\pi\xi_m)}$$

Re-arranging above, forms an expression for η_m with respect to ξ_m:

$$\eta_m = \frac{\bar{k}\mathrm{DR_z}\coth(2\pi\xi_m)}{\pi\mathrm{L}\,(\mathrm{R_z^2} + \mathrm{X_z^2})} \pm \sqrt{\left(\frac{\bar{k}\mathrm{DR_z}\coth(2\pi\xi_m)}{\pi\mathrm{L}\,(\mathrm{R_z^2} + \mathrm{X_z^2})}\right)^2 + \frac{2\bar{k}\mathrm{DX_z}\xi_m\coth(2\pi\xi_m)}{\pi\mathrm{L}\,(\mathrm{R_z^2} + \mathrm{X_z^2})} - \frac{\left(\bar{k}\mathrm{D}/\pi\mathrm{L}\right)^2}{\mathrm{R_z^2} + \mathrm{X_z^2}} + \xi_m^2} \tag{7.21}$$

A numerical iterative method is then applied. Selecting ξ_m, to sub into radical Eqn. 7.21, and resolve $\pm\eta_m$, which is subbed into forcing function $F_m\pm$:

$$\begin{aligned} F_m\pm = {} & \cos(\pi\eta_m)\left[\xi_m\sinh(\pi\xi_m) - \left(\frac{\bar{k}\mathrm{DX_z}}{\pi\mathrm{L}\,(\mathrm{R_z^2} + \mathrm{X_z^2})}\right)\cosh(\pi\xi_m)\right] \\ & - \sin(\pi\eta_m)\left[\eta_m\cosh(\pi\xi_m) - \left(\frac{\bar{k}\mathrm{DR_z}}{\pi\mathrm{L}\,(\mathrm{R_z^2} + \mathrm{X_z^2})}\right)\sinh(\pi\xi_m)\right] \end{aligned} \tag{7.22}$$

This process is iterated for $\xi_m \sim 0 \to 1$, resolving $\pm\eta_m$ until convergence of $F_m \to 0$ with a pair of ξ_m, η_m, as a solution to Eqn. 7.20 of $\mathrm{g}_m = \xi_m + \eta_m i$. Due to the numerical nature of this approach, $F_m \approx 10^{-8}$ is adequate for convergence. Using the characteristic response function $\phi_m(x, y, z)$ at a point of interest, $\phi'_m(x', y'z')$ at the source, and converged boundary function g_m. Mode amplitude is numerically resolved with Eqn. 7.23. ρ_∞ is fluid density, $V_m = \kappa\mathrm{U}_\infty + \mathrm{a_c}$ is superimposed wave velocity, $m = 1 - 6$, and Q_m is source strength, as defined following.

$$p_{p,m} = \frac{16i\pi\rho V_m Q_m \bar{k}}{\mathrm{DWe}^{\bar{p}_x}} \sum_m \frac{\mathrm{g}_m \phi_m \phi'_m}{\sinh(2\pi\mathrm{g}_m) + 2\pi\mathrm{g}_m}\left[\bar{k}^2 - (\pi\mathrm{L})^2\left(\frac{m^2}{\mathrm{L}^2} + \frac{1}{\mathrm{W}^2} - \frac{\mathrm{g}_m^2}{\mathrm{D}^2}\right)\right]^{-1} \tag{7.23}$$

Plumblee at al[3] defined Q_m empirically, as done here, with observed drivers of amplitude change in Section 6.2. Mode 1 is a classic resonator or normal depth mode: $Q_1 = a_c D^2$. The 2nd is a SL mode, as a function of length, and depth: $Q_2 = V_2 LD$. The 3rd is a SL mode, based on length, and δ: $Q_3 = U_\infty L\delta$. The 4th also alters with U/S BL δ for $Q_4 = U_\infty L\delta^*$. These definitions are arbitrary, based on observation, however, overall provide best fit.

Fig. 7.8-7.10 compare numerical to experimentally attained SPL of flat U/S cases, with a 5% error bar $\varepsilon_{5\%}$ for total mean: $\varepsilon_m = 3.4\%$ at L/D = L/W = 1, $\varepsilon_m = 3.5\%$ at L/D = L/W = 2, and $\varepsilon_m = 3.9\%$ at L/D = L/W = 3. Appendix E.2 provides data for remaining cases.

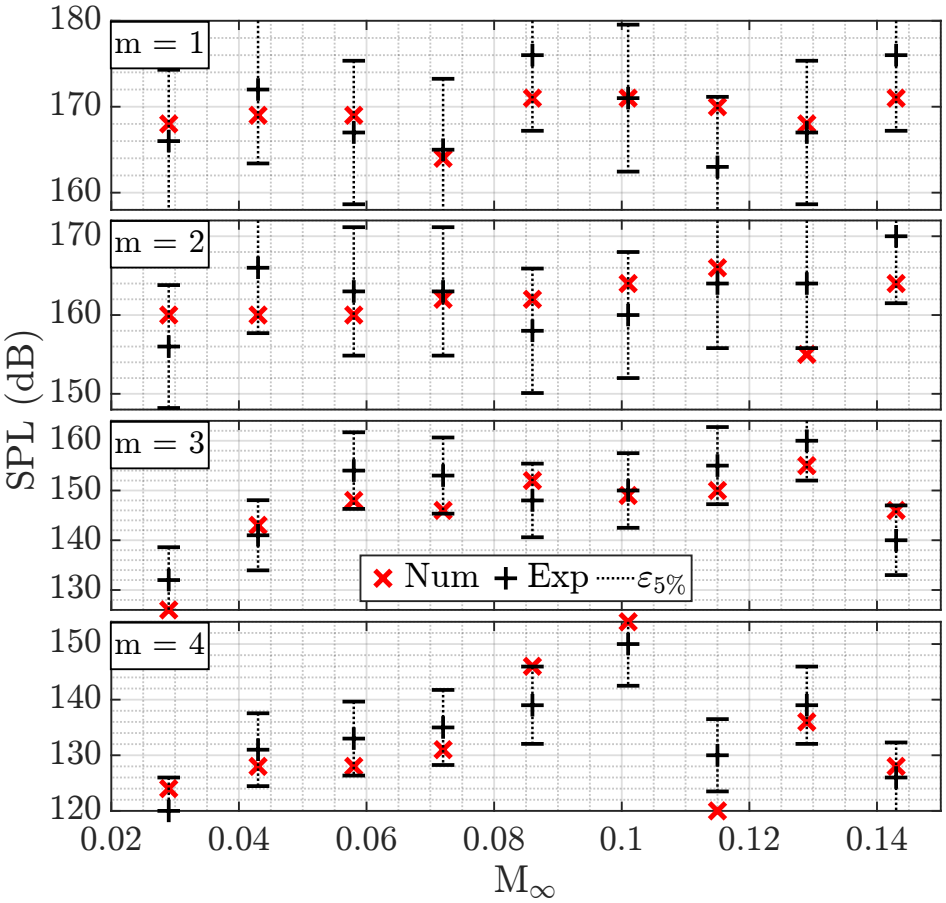

Figure 7.8: Amplitude Experimental vs. Numerical: Flat-plate U/S C19: L/D = L/W = 1

Mean error remains <5%, with outliers <10%. Outliers are assumed a function of convergence for g_m, or inaccurate frequency from experiment or prediction. An iterative step of $\xi_m = 10^{-9}$ to converge on $F_m\pm = 10^{-8}$, was implemented, but a smaller step to converge $F\pm = 0$, would likely improve accuracy. The model is also sensitive to $k \propto f$, such that inaccurate frequency, increases error. Moreover, as cavity L/D increases, $\%\varepsilon$ increases slightly. This was expected, as model physics depend on a strong feedback effect, to interact with LE shed vorticity, which decreases in strength as L/D increases. Plumblee at al's[3] original model, similarly presented an increase in error, as cavity L/D increased from unity, however more notably, due to lack of viscosity. Nonetheless, an overall average error of $< 5\%$, with maximum outliers $< 10\%$, is considered decent for a preliminary amplitude pressure model, given the empirical nature of this study, and unsteady, oscillatory and rotational nature of viscid incompressible cavity flow[148].

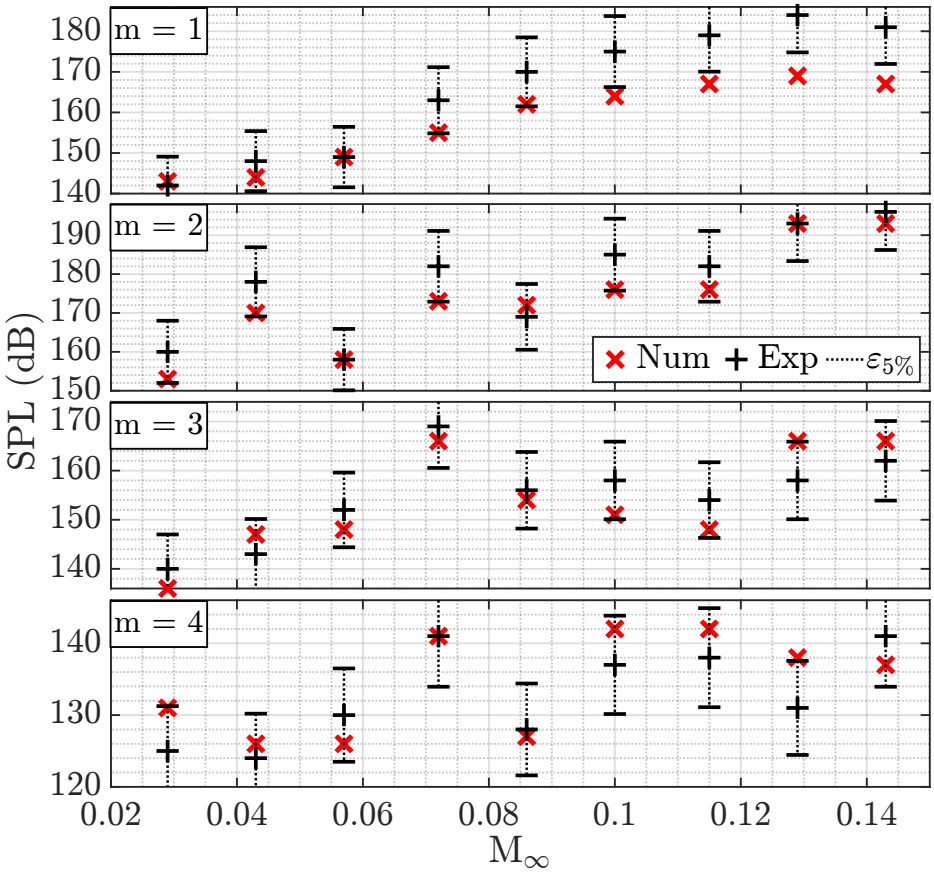

Figure 7.9: Amplitude Experimental vs. Numerical: Flat-plate U/S C21: L/D = L/W = 2

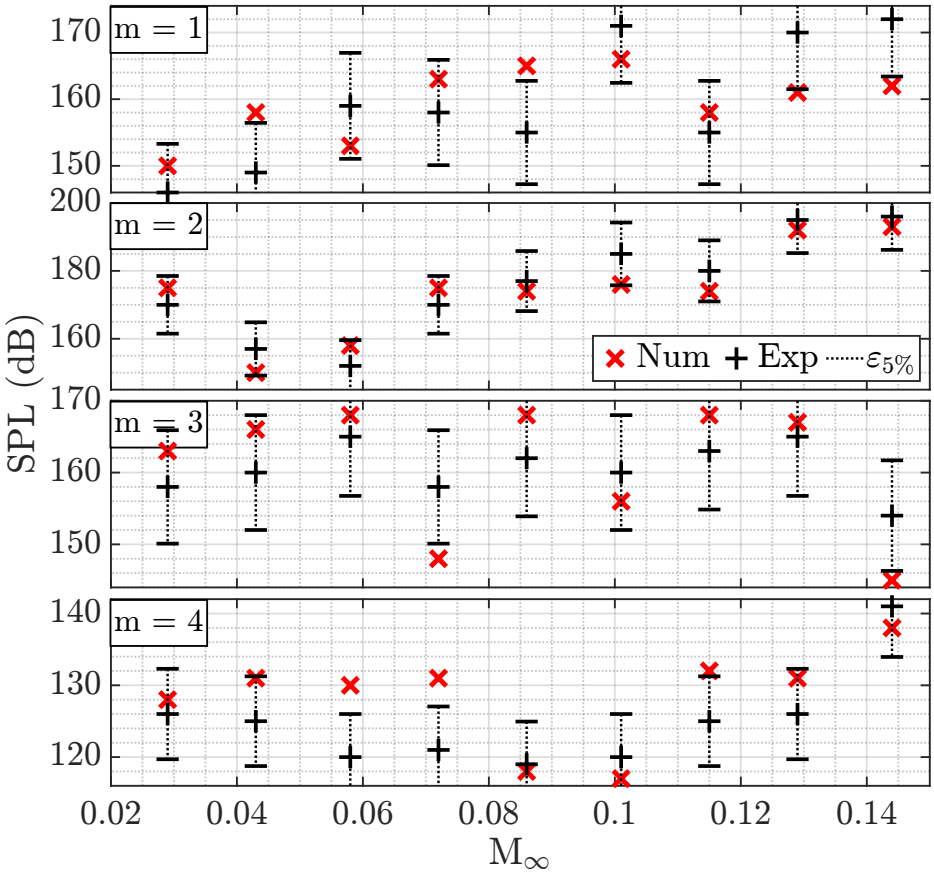

Figure 7.10: Amplitude Experimental vs. Numerical: Flat-plate U/S C23: L/D = L/W = 3

Chapter 8

Conclusions & Recommendations

8.1 Conclusion

Experimental investigation presented in this thesis, allowed for derivation of a viscid physical model for incompressible open cavity flow. The model estimates empirical dimensionless frequency $\mathrm{St_{HS}}$, derived with respect to the U/S BL for responding oscillatory cavity vorticity and feedback modes:

$$\mathrm{St_{HS}} = \frac{f\mathrm{L}}{\mathrm{U}_\infty} = \frac{\delta}{\mathrm{e}^{\bar{p}_x}}\left(m - \gamma_v\right)\left[\frac{\mathrm{M}_\infty}{\delta^*/\mathrm{D}}\left(\mathrm{L}+\delta\right) + \frac{\delta^*}{\kappa}\right]^{-1} \tag{8.1}$$

The model also estimates pressure amplitude, at a specified location (x, y, z) in the cavity $p_{p,m}$, with respect to corresponding TE source $\mathrm{Q}(x', y', z')$ and excitation frequency f through wave number k, as an update to Plumblee et al's[3] radiative impedance model, including the U/S BL, for responding oscillatory cavity vorticity and feedback wave modes:

$$p_{p,m} = \frac{16i\pi\rho V_m Q_m \bar{k}}{\mathrm{DWe}^{\bar{p}_x}} \sum_m \frac{\mathrm{g}_m \phi_m \phi'_m}{\sinh\left(2\pi \mathrm{g}_m\right) + 2\pi \mathrm{g}_m}\left[\bar{k}^2 - (\pi\mathrm{L})^2\left(\frac{m^2}{\mathrm{L}^2} + \frac{1}{\mathrm{W}^2} - \frac{\mathrm{g}_m^2}{\mathrm{D}^2}\right)\right]^{-1} \tag{8.2}$$

- f, m are cavity oscillation frequency, mode, and L,D,W are cavity length, depth, width
- δ, δ^* are boundary layer disturbance and mass displacement thickness
- $\bar{p}_x = (dp/dx)(\rho \mathrm{U}^2)_\infty^{-1}(\mathrm{LD}/\delta^*)$ is dimensionless dp/dx U/S of the cavity
- U_∞, M_∞, ρ_∞ are free-stream velocity, Mach number and density
- $\gamma_v = 0.25$ is Rossiter's[2] empirical constant for phase lag between vorticity and feedback.
- $\kappa = 0.57$ is Rossiter's[2] empirical ratio constant, for SL convection over the cavity to U_∞.
- $V_m = \kappa \mathrm{U}_\infty + \mathrm{a_c}$ is superimposed wave velocity for SL vorticity $\kappa \mathrm{U}_\infty$ and feedback a_c
- $Q_m(x', y', z')$ is source strength, dependant on mode, for cavity flow at the TE
- $\bar{k} = \bar{k}_v + \bar{k}_a$ is superimposed dimensionless wave number; $\bar{k}_v = k_v\delta^*$, $\bar{k}_a = k_a \mathrm{L}(\delta/\mathrm{D})^{-1}$
- $k_v = 2\pi f \mathrm{L}/\kappa \mathrm{U}\delta$ is vorticity wave number, and $k_f = 2\pi f \mathrm{L}/\mathrm{a_c}\delta$ for feedback wave number..
- $\mathrm{g}_m = \xi_m + i\eta_m$ is the Morse[147] boundary function
- $\phi_m(x, y, z)$ is characteristic response function at interest point, and $\phi'_m(x', y', z')$ at source

Further specific findings from experimental work, completed on a range of cavity geometries ,and BL profiles, generated by a novel upstream nose geometry, include:

(1) **Open Cavity Flow L/D $\lessapprox$ 5**

(a) Deep Open L/D $\leq$ 1: supports oscillation of depth-wise stand waves, back and forth between the LE and TE wall, driven from an oscillatory point central to the cavity. This induces overall high pressure in the cavity, with less distinct modality, and more resonant buffet, akin to a classic resonator, previously observed by [3, 6, 8].

(b) Shallow Open 1 < L/D $\lessapprox$ 5: instead supports the oscillation of length-wise vortical waves, fed by a central recirculation system, governed by external flow through the SL, which impinges the TE wall, and is pushed, and pulled, in and out of the cavity, in a dynamic steady state. Its location driven by internal cavity geometry.

(2) **Cavity Length (L) and Streamwise Flow**

(a) For L/D = 1 $\rightarrow$ 2: a discrete floor peak forms, with gradients toward a low pressure region either side, energy reduces on the LE and TE wall proportionally. The TE impingement peak remains, moving slightly down, and reducing in magnitude.

(b) For L/D = 2 $\rightarrow$ 3: floor peak and gradients increase, and low pressure reduces.

(b) Increasing gradients either side of the peak toward a low pressure region, suggest flow is being pulled to the peak, by a central force; the primary recirculation mechanism.

(d) Based on prior research, increasing length further, should move primary recirculation U/S, as impingement moves down on the TE toward open-transitional type flow.

(3) **Cavity Width (W) and Spanwise Flow**

(a) Based on prior research, wide flow L/W << 1 has no distinct sign of spanwise flow as features disperse. Then in transition to narrow flow L/W $\rightarrow$ 1 spanwise features become apparent, and more distinct at L/W = 1.

(b) For narrow flow L/W = 1, 2, and 3 at fixed W = 60mm: spanwise vorticity is suggested on the floor and TE wall close to side walls. The floor peak, thickens as it stretches D/S when length increases, suggesting interaction of stream and spanwise flow.

(c) Spanwise patterns coincide with Crook et al[56–58,135]; "*centrally located saddle point*" or the primary recirculation region, "*flanked by a pair of spanwise nodes*".

(d) For reduced W = 30mm narrow flow L/W = 2, 4, and 6: distinct spanwise flow morphs to uniform streamwise drag spanwise, with increased gradient density on the TE, toward the cavity mouth, indicating increased rate of SL flapping at the TE corner.

(e) Wider narrow flow develops spanwise, narrower flow moves toward the mouth, due to internal momentum build up as cavity volume reduces, forcing high to low pressure.

(4) **Reynolds Number Re_∞**: increasing Re_∞, increased internal cavity surface pressure. Largely as a function of U_∞ and the BL, where increasing Re_∞ reduces BL δ, with even larger reduction in BL δ inducing a larger effect, as follows.

(5) **The Boundary Layer**:

(a) $dp/dx < 0$ grows with increasing U_∞, accelerating flow relative, inducing laminarity on turbulent flow, thus reducing BL δ from thick turbulent to thin laminar.

(b) Internal cavity surface pressure $C_{p,rms}$ doubles, when the U/S BL is thin due to $dp/dx < 0$, compared to a thick flat-plate turbulent BL with $dp/dx = 0$

(c) Reducing δ of a thin laminar BL due to increasing $dp/dx < 0$, by increasing structural gradient from a curved to wedge incline surface, also increases internal surface $C_{p,rms}$.

(d) Peak modes shift to higher frequency as δ increases when the BL is thin and laminar.

(e) Away from the wall, SPL reduces to low FS turbulent modes, non-existent close to the surface in a BL or accelerated flow region, whose modes instead dominate the flow.

(7) **Cavity Feedback Effect on Velocity Profile U/S**:

(a) Amplifies $dp/dx < 0$ if present, increasing local velocity, acceleration, OASPL and peak SPL, whilst proportionally reducing viscosity δ. This is also apparent in the flat-plate case, with $dp/dx = 0$, suggesting very slight induced $dp/dx < 0$.

(b) Peak frequencies shift, with additional peaks also appearing, likely cavity feedback modes, suggesting an overall change in turbulent structure.

(6) **Cavity Modes**:

(a) Mode 1, distinctly the cavity normal or depth mode.

(b) Mode 2, a SL mode, dominant in nose cases.

(c) Mode 3, a SL mode, its presence requiring certain length and U/S BL δ. Its frequency alters with U/S BL; lower in the flat-plate case with a thick turbulent BL, which is dampened by a thin U/S BL $dp/dx < 0$, shifting Mode 3 frequency higher.

(c) Mode 4, a SL mode, its frequency altering with U/S BL δ, apparent as Mode 3 for the thin BL, and 4th for a turbulent thick BL.

It is thus suggested, dominant modes switch between Mode 2 and 3, due to altering location and or strength of Mode 3, dependant on the U/S BL, and cavity length. As opposed to change in Mode 2, which sustains consistent f (Hz) for these open type flow geometries.

8.2 Further Recommended Work

This thesis concludes viscid effects are a primary governing facet of cavity flow, especially at low subsonic Mach. Based on past research, and present experimental findings, a viscid physical model was derived, to predict cavity dimensionless frequency. The model was built in a confine, attuned to open narrow cavity geometry; L/D = 1-3, and L/W = 1-6, subject to M_∞ = 0.03-0.18, and four BL profiles U/S. Error is expected to emerge outside the confine, thus further work should strengthen the model, by observing isolated discrete change in U/S BL δ, and dp/dx, then cavity geometry and U_∞ at fixed δ and dp/dx, as follows.

For isolated BL δ, a 2D flat-plate rig with fixed cavity geometry, and Re_∞, moving the cavity D/S in x, to increase δ, δ^* and test Eqn. 8.1. This removes effects of BL dp/dx, spanwise

curvature, and controls Re_∞, L/D and L/W. To test $dp/dx \neq 0$, a flat-plate incline would then be increased before the cavity for $dp/dx < 0$, and decreased for $dp/dx > 0$, similarly with convex curvature for $dp/dx < 0$, and concave $dp/dx > 0$, tracking δ decrease and increase respectively. Then, discrete alteration of; L/D, and L/W separately, at fixed $\delta, dp/dx$, to observe altered St. It is important each facet be observed independently, to ensure the effect is accurately observed.

These tests would also improve amplitude prediction, using the model in this thesis. As based on USP results, the primary driver of amplitude response is BL δ, and dp/dx. As the thinnest BL of larger $dp/dx < 0$, produced the highest amplitude response, and cavity geometry instead only altered cavity flow type; deep to shallow open or closed, narrow or wide. Therefore, a more accurate update to amplitude prediction, requires isolated discrete study of δ and dp/dx.

Moreover, HWA results observed a feedback effect in the U/S velocity profile, when comparing profiles of a cavity D/S, to no cavity D/S. The effect was similar to presence of $dp/dx < 0$ U/S, effectively decreasing BL δ. This suggests pressure amplification D/S by the cavity, imparts $dp/dx < 0$ U/S. Due to the oscillating nature of cavity flow, the effect would also oscillate, implicating Stokes 2$^{\text{nd}}$ problem; "*Oscillating Pressure Gradient Near a Rigid Plane*" [103], formulated in Eqn. 8.3 [103], to model effects of a flow disturbance D/S on velocity U/S. U(x) is stream velocity at x along a plane. $u_1(y,t)$ is velocity due to the oscillator: cavity with $\omega = 2\pi f$, based on y normal to x, in time t. η is the disturbance similar parameter in Eqn. 8.4 [103].

$$u(y,t) = \mathrm{U}_\infty e^{-\eta} \cos(\omega t - \eta) \qquad (8.3) \qquad \eta = y\sqrt{\omega/2\nu} \qquad (8.4)$$

Using this approach, it is theorised, velocity oscillation U/S of the cavity can be modelled with Eqn. 8.3, using dominant cavity frequencies, to determine the impact on external flow. And vice versa, when velocity oscillation U/S is known, to quantify dominant cavity frequency response. More discrete velocity profile data in x and y is required for such a model. Thus it is recommended further study extract such, in the range of cavity frequencies, to determine if Stokes 2$^{\text{nd}}$ problem can predict the effect of cavity flow U/S, or in the broadband environment.

Lastly, this study identified simple cavity geometry of a flat-plate U/S, and either side, produced a significantly lulled response, compared to the fuselage model, which produced over double the magnitude, especially at a peak. Therefore, more research is recommended to observe vehicle effects, which clearly alter cavity response. The proposed studies above will assist. However, it is recommended to independently perform volume based assessment as well, with respect to the BL. That is, fixed cavity L/D, and L/W, whilst increasing volume.

It is expected, BL effects will become more apparent, as based on the present model, effective cavity mass depth δ^*/D, disturbance, and mass length $\delta/L, \delta^*/L$ are powerful ratios, which decrease with increasing volume. Suggesting cavity flight scalability requires knowledge of the viscid environment U/S. Furthermore, amplification is dependant on cavity volume, as a function of energy capacitance, to model boundary impedance in the cavity radiation model.

Bibliography

[1] C.O.L. Hamilton Smith, N. Lawson, and G.A. Vio. History, review and summary of the cavity flow phenomena. *European Journal of Mechanics - B/Fluids*, 108:32–72, 2024. doi: 10.1016/j.euromechflu.2024.07.005.

[2] J.E. Rossiter. Wind Tunnel Experiments on the Flow over Rectangular Cavities at Subsonic and Transonic Speeds. Technical report, Ministry of Aviation: Aeronautical Research Council, London, UK, Oct. 1964. ARC-RM-3438.

[3] H.E. Plumblee, J.S Gibson, and L.W. Lassiter. A Theoretical and Experimental Investigation of the Acoustic Response of Cavities in an Aerodynamic Flow. Technical report, Air Force Flight Dynamics Laboratory, Wright-Patterson AFB, OH, USA, Mar. 1962. WADD TR 61-75.

[4] D. Rockwell and E. Naudascher. Review: Self Sustaining Oscillations of Flow Past Cavities. *ASME Journal of Engineering*, 100(2):152–165, Jun. 1978. doi: 10.1115/1.3448624.

[5] Scani-valve: MPS4264 Miniature Pressure Scanner. `http://scanivalve.com/products/pressure-measurement/miniature-ethernet-pressure-scanners/mps4264`, 2018.

[6] P.J.W. Block. Noise Response of Cavities of Varying Dimensions at Subsonic Speeds. Technical report, NASA Langley, VA, USA, Dec. 1976. NASA-TN-D-8351.

[7] J.S. Murphy. Some Effects of Surface Curvature on Laminar Boundary-Layer Flow. *Aeronautical Sciences Archive*, 20(5):338–344, May. 1953. doi: 10.2514/8.2638.

[8] L.F. East. Aerodynamically Induced Resonance in Rectangular Cavities. *Journal of Sound and Vibrations*, 3(3):277–287, May. 1966. doi: 10.1016/0022-460X(66)90096-4.

[9] J.E. Rossiter and A.G. Kurn. Wind Tunnel Measurements of the Unsteady Pressures in and behind a Bomb Bay (Canberra). Technical report, Ministry of Aviation, Aeronautical Research Council, London, UK, Mar. 1965. ARC-CP-0728.

[10] D.L. Carr. An Experimental Investigation of Open Cavity Pressure Oscillation. Technical report, Air Force Flight Dynamics Laboratory, Wright-Patterson AFB, OH, USA, Sep. 1974. AD-787 700.

[11] L.L. Shaw and D.L. Smith. Prediction of the Pressure Oscillations in Cavities exposed to Aerodynamic Flow. Technical report, Air Force Flight Dynamics Laboratory, Wright-Patterson AFB, OH, USA, Oct. 1975. AFFDL-TR-75-34.

[12] R.C. Bauer and R.E. Dix. Engineering Modal of Unsteady Flow in a Cavity. Technical report, Arnold Engineering Development Center, Tennessee Air Force Systems Command, United States Air Force, Arnold AFB, TN, USA, Dec. 1991. AEDC-TR-91-17.

[13] H. Heller, D.G. Holmes, and E.E. Covert. Flow Induced Pressure Oscillations in Shallow Cavities. *Journal of Sound and Vibration*, 18(4):545–553, Oct. 1971. doi: 10.1016/0022-460X(71)90105-2.

[14] L.G. Kaufman II and R.L. Clark. Mach 0.6 to 3.0 flows over Rectangular Cavities. Technical report, Air Force Flight Dynamics Laboratory, Wright-Patterson AFB, OH, USA, May. 1983. AFWAL-TR-82-3112.

[15] K. Karamcheti. Acoustic Radiation from Two-Dimensional Rectangular Cutouts in Aerodynamic Surfaces. Technical report, NACA, D.C. USA., Aug. 1955. NACA-TN-3487.

[16] V. Sarohia. Experimental Investigation of Oscillations in Flows over Shallow Cavities. *AIAA Journal*, 15(7):984–991, Jul. 1977. doi: 10.2514/3.60739.

[17] C.K.W. Tam and P.J.W. Block. On the Tones and Pressure Oscillations Induced by Flow over Rectangular cavities. *Journal of Fluid Mechanics*, 89(2):373–399, Nov. 1978. doi: 10.1017/S0022112078002657.

[18] C. W. Rowley and D.R. Williams. Dynamics and Control of High-Reynolds-Number Flow over Open Cavities. *Annual Review of Fluid Mechanics*, 38(1):251–276, Jan. 2006. doi: 10.1146/annurev.fluid.38.050304.092057.

[19] L.N. Cattafesta III, O. Song, D.R. Williams, C.W. Rowley, and F.S. Alvi. Active Control of Flow Induced Cavity Oscillations. *Progress in Aerospace Sciences*, 44(7-8):471–502, Oct. 2008. doi: 10.1016/j.paerosci.2008.07.002.

[20] S.J. Lawson and G.N. Barakos. Review of Numerical Simulations for High-Speed, Turbulent Cavity Flows. *Progress in Aerospace Sciences*, 47(3):186–216, Apr. 2011. doi: 10.1016/j.paerosci.2010.11.002.

[21] H. Blasius. Grenzschicluen in flüssigkeiten mit kleiner reibung. *Zeitschrift Angewandte Maihemalik Physik*, 56:1–37, 1908.

[22] S.W. Falkner, V.M. & Skan. Approximate Solutions of Boundary Layer Equations. *Philosophical Magazine*, 12(80):865–896, Jan. 1931. doi: 10.1080/14786443109461870.

[23] S. Goldstein. A note on the Boundary Layer equations. *Mathematical Proceedings of the Cambridge Philosophical Society*, 35(2):338–233409, Apr. 1939.

[24] A.F. Charwat, J.N. Roos, F.C. Dewey, Jr, and J.A. Hitz. An Investigation of Separated Flows - Part 1: The Pressure Field. *Journal of Aerospace Sciences*, 28(6):457–470, 1961.

[25] R.L. Stallings and F.J. Wilcox. Experimental Cavity Pressure Distributions at Supersonic Speeds. Technical report, NASA Langley, VA, USA, Jun. 1987. NASA-TP-2683.

[26] E.B. Plentovich, J. Chu, and M.B. Tracy. Experimental Cavity Pressure Measurements at

Subsonic and Transonic Speeds. Technical report, NASA Langley, VA, USA, Dec. 1993. NASA-TP-3358.

[27] E.B. Plentovich, Jr. R.L. Stallings, and M. B. Tracy. Experimental Cavity Pressure Measurements at Subsonic and Transonic Speeds-Static-Pressure Results. Technical report, NASA Langley, VA, USA, Dec. 1993. NASA-TP-3358.

[28] M. Gharib and A. Roshko. The Effect of Flow Oscillations on Cavity Drag. *Journal of Fluid Mechanics*, 177(4):501–530, Apr. 1987. doi: 10.1017/S002211208700106X.

[29] I. Bassioni, M. Abdelkhalek, Z. Ghoneim, M. Daoud, and A.M. Naguib. Microphone-Array Measurements of Acoustic and Hydrodynamic Wall-Pressure Fluctuations in a Low-Speed Cavity Flow. In *38th AIAA Fluid Dynamics Conference and Exhibit*, Portland, OR, USA, Jun. 2004. AIAA-2004-2655. doi: 10.2514/6.2004-2655.

[30] M. Daoud, A.M. Naguib, I. Bassioni, M. Abdelkhalek, and Z. Ghoniem. Microphone-Array Measurments of the Floor Pressure im a Low-Speed Cavity Flow. *AIAA Journal*, 44(9):2018–2023, Sep. 2006. doi: 10.2514/1.18129.

[31] V. Strouhal. Ueber eine besondere Art der Tonerregung. *Annalen der Physik*, 241(10): 216–251, Feb. 1878. doi: 10.1002/andp.18782411005.

[32] P.J.W. Block. Measurements of the Tonal Component of Cavity Noise and Comparison with Theory. Technical report, NASA Langley, VA, USA, Nov. 1977. NASA-TP-1013.

[33] L.L. Shaw. Suppression of Aerodynamically Induced Cavity Pressure Oscillations. *Journal of Acoustical Society of America*, 66(3):880–884, Sep. 1979. doi: 10.1121/1.383242.

[34] A.D. Vakili and C. Gauthier. Control of Cavity Flow by Upstream Mass-Injection. *Journal of Aircraft*, 31(1):169–174, Jan. 1994. doi: 10.2514/3.46470.

[35] L.N. Cattafesta III, S. Garg, M. Choudhari, and F. Li. Active Control of Flow-Induced Cavity Resonance. In *28th Fluid Dynamics Conference*, Snowmass Village, CO, USA, Jun. 1997. AIAA-97-1804. doi: 10.2514/6.1997-1804.

[36] D.R. Williams and D. Fabris. Experiments on Controlling Multiple Acoustic Modes in Cavities. In *6th AIAA/CEAS Aeroacoustics Conference*, Lahaina, HI, USA, Jun. 2000. AIAA-2000-1903. doi: 10.2514/6.2000-1903.

[37] M.A. Kegerise, L.N. Cattafesta III, and C. Ha. Adaptive Identification and Control of Flow Induced Cavity Oscillations. In *1st Flow Control Conference*, St. Louis, MO, USA, Jun. 2002. AIAA-2002-3158. doi: 10.2514/6.2002-3158.

[38] M.C. Harrington and W.H. Dunham. Studies of the Mechanism for the Flow-Induced Cavity Resonance. *The Journal of the Acoustical Society of America*, 32(7):921, Jul. 1960. doi: 10.1121/1.1936469.

[39] W.H. Dunham. Flow-Induced Cavity Resonance in Viscous Compressible and Incompressible Fluids. In *4th Symposium on Naval Hydrodynamics*, volume 3, pages 1057–1081, DC, USA, Aug. 1962. Office of Naval Research.

[40] A.F. Charwat, J.N. Roos, F.C Dewey, Jr, and J.A. Hitz. An Investigation of Separated Flows- Part 2 : Flow in the Cavity and Heat Transfer. *Journal of Aerospace Sciences*, 28 (7):513–527, Jul. 1961. doi: 10.2514/8.9099.

[41] R.L. Goldman, M.N. Morkovin, and R.N. Schumacher. Unsteady Control Surface Loads of Lifting Re-Entry Vehicles at Very High Speeds. *AIAA Journal*, 6(1):44–50, Jan. 1968. doi: 10.2514/3.4439.

[42] K. Karamcheti. *Sound Radiated from Surface Cutouts in High-Speed Flows*. PhD thesis, Caltech, Pasadena, CA, USA, 1956.

[43] A. Roshko. Some Measurements of Flow in Rectangular Cutout. Technical report, NACA, Washington, D.C. USA., Aug. 1955. NACA-TN-3488.

[44] X. Zhang and J.A. Edwards. An Investigation of Supersonic Oscillatory Cavity Flows drive by Thick Shear Layers. *The Aeronautical Journal*, 94(940):355–364, Dec. 1990. doi: 10.1017/S0001924000023319.

[45] K. Wieghardt and W. Tillman. On the Turbulent Friction Layer for Rising Pressure. Technical report, NACA, Washington, D.C. USA., Oct. 1951. NACA-TM-1314.

[46] D.J. Maull and L.F. East. Three-Dimensional Flow in Cavities. *Journal of Fluid Mechanics*, 16(4):620–632, Aug. 1963. doi: 10.1017/S0022112063001014.

[47] P.J.W. Block and H. Heller. Measurements of Far-Field Sound Generation from Flow-Excited Cavity. Technical report, NASA Langley, VA, USA, Dec. 1975. TM-X-3292.

[48] M.B. Tracy, E.B. Plentovich, and J. E.B. Chu. Measurements of Fluctuating Pressure in a Rectangular Cavity in Transonic Flow at High Reynolds Number. Technical report, NASA Langley, VA, USA, Jun. 1992. NASA TM-4363.

[49] M.B. Tracy and E.B. Plentovich. Cavity Unsteady-Pressure Measurements at Subsonic and Transonic Speeds. Technical report, NASA Langley, VA, USA, Dec. 1997. TP-3669.

[50] P.J. Disimile, N. Toy, and E. Savory. Effect of Planform Aspect Ratio on Flow Oscillations in Rectangular Cavities. *Journal of Fluids Engineering*, 122(1):32–38, Mar. 2000. doi: 10.1115/1.483223.

[51] K.K. Ahuja and J. Mendoza. Effects of Cavity Dimensions, Boundary Layer and Temperature on Cavity Noise with Emphasis on Benchmark Data to Validate Computational Aeroacoustic Codes. Technical report, Georgia Tech, Apr. 1995. NASA CP-4653.

[52] K.M. Chung. Three-Dimensional Effect on Transonic Rectangular Cavity Flows. *Experiments in Fluids*, 30:531–536, May. 2001. doi: 10.1007/s003480000232.

[53] T.M. Faure, P.A. Adrianos, F. Lusseyran, and L. Pastur. Visualizations of Flow inside an Open Cavity at Medium range Reynolds Numbers. *Experiments in Fluids*, 42(2):169–184, Feb. 2007. doi: 10.1007/s00348-006-0188-8.

[54] H. Gortler. On the Three-Dimensional Instability of Laminar Boundary Layers on Concave Walls. Technical report, NACA, Washington, D.C. USA., Jan. 1954. NACA-TM-1375.

[55] K. Zhang and A.M. Naguib. Effect of Cavity Width on Self-Sustained Oscillations in a Low-Mach-Number Cavity Flow. In *38th Fluid Dynamics Conference & Exhibit*, pages AIAA–2008–4376, Seattle, WA, USA, Jun. 2008. AIAA. doi: 10.2514/6.2008-4376.

[56] S.D. Crook, E.R. Hassan, and R.M. Kelso. Low Speed Cavity Flows: Principle Flow Features. In *5th Australian Conference on Laser Diagnostics in Fluid Mechanics and Combustion*, Crawley, AUS, Dec. 2008.

[57] S.D. Crook, E.R. Hassan, and R.M. Kelso. Low Speed Cavity Flows: Shear Layer Growth. In *5th Australian Conference on Laser Diagnostics in Fluid Mechanics and Combustion*, Crawley, WA, AUS, Dec. 2008.

[58] S.D. Crook, E.R. Hassan, and R.M. Kelso. Low Speed Cavity Flows Part ii: Presentation of Piv Results. In *5th Australian Conference on Laser Diagnostics in Fluid Mechanics and Combustion*, page ., Crawley, WA, AUS, Dec. 2008. UWA.

[59] L.F. Richardson. IX.The Approximate Arithmetical Solution by Finite Differences of Physical Problems involving Differential Equations, with an Application to the Stresses in a Masonry Dam. *Philosophical Transactions of the Royal Society A: Mathematical, Physical and Engineering Sciences*, 210:307–357, Jan. 1911. doi: 10.1098/rsta.1911.0009.

[60] S.J. Beresh, J.L. Wagner, and B.O. Pruett. Particle Image Velocimetry of a Three-Dimensional Supersonic Cavity Flow. In *50th AIAA Aerospace Sciences Meeting including the New Horizons Forum and Aerospace Exposition*, Nashville, TN, USA, Jan. 2012. AIAA-2012-0030. doi: 10.2514/6.2012-30.

[61] S.J. Beresh, J.L. Wagner, and Pruettm B.O.M. Supersonic Flow over a Finite-Width Rectangular Cavity. In *51st AIAA Aerospace Sciences Meeting*, Grapevine, TX, USA, Jan. 2013. AIAA-2013-0389. doi: 10.2514/6.2013-389.

[62] J.L. Wagner, K.M. Casper, S.J. Beresh, P.S. Hunter, R.W. Spillers, J.F. Henfling, and R.L. Mayes. Experimental Investigation of Fluid Structure Interactions in Compressible Cavity Flows. In *43rd Fluid Dynamics Conference*, San Diego, CA, USA, Jun. 2013. AIAA-2013-3172. doi: 10.2514/6.2013-3172.

[63] J.L. Wagner, S.J. Beresh, K.M. Casper, B. Pruett, R. Spillers, and J. Henfling. Experimental Investigation of Aspect-Ratio Effects in Transonic and Subsonic Rectangular Cavity Flows. In *52nd Aerospace Sciences Meeting*, National Harbour, MD, USA, Jun. 2013. AIAA-2013-3172. doi: 10.2514/6.2014-1446.

[64] S. Arunajatesan, M.F. Barone, J.L. Wagner, K.M. Casper, and S.J. Beresh. Joint Experimental/Computational Investigation into the Effects of Finite width on Transonic Cavity Flow. In *32nd AIAA Applied Aerodynamics Conference*, Atlanta, GA, USA, Jun. 2014. AIAA-2014-3027. doi: 10.2514/6.2014-3027.

[65] S.J. Beresh, J.L. Wagner, E.P. Demauro, J. Henfling, and R. Spillers. Resonance Characteristics of Transonic Flow over a Rectangular Cavity using Pulse-Burst PIV. In *54th AIAA Aerospace Sciences Meeting*, San Diego, CA, USA, Jan. 2016. AIAA-2016-1344. doi: 10.2514/6.2016-1344.

[66] Y. Sun, Y. Zhang, K. Taira, L.N. Cattafesta III, B. George, and L. Ukeiley. Width and Sidewall Effects on High Speed Cavity Flows. In *54th AIAA Aerospace Sciences Meeting*, San Diego, CA, USA, Jan. 2016. AIAA-2016-1343. doi: 10.2514/6.2016-1343.

[67] M.B. Jones and J. Watmuff. Aero-Acoustic Measurements of a Deep Cavity in Low-Speed Flow. Technical report, Australian Government Department of Defence, DST Operation, Electronic Warfare and Radar Division, Edinburgh, SA, AUS, Oct. 2016.

[68] S.M. Grace, W.G. Dewar, and D.E. Wroblewski. Experimental Investigation of the Flow Characteristics within a Shallow Wall Cavity for both Laminar and Turbulent Upstream Boundary Layers. *Experiments in Fluids*, 36(5):728–740, Mar. 2004. doi: 10.1007/s00348-003-0761-3.

[69] A. Seena and H.J. Sung. Dynamic Mode Decomposition of Turbulent Cavity Flows for Self-Sustained Oscillations. *International Journal of Heat and Fluid Flow*, 32(6):1098–1110, Oct. 2011. doi: 10.1016/j.ijheatfluidflow.2011.09.008.

[70] K.M. Casper and S. Arunajatesan. Modal Decomposition of Pressure Data in Cavity Flows. In *45th AIAA Fluid Dynamics Conference*, Dallas, TX, USA, Jun. 2015. AIAA-2015-2938. doi: 10.2514/6.2015-2938.

[71] S. Singh, L.S. Ukeiley, L.N. Cattafesta III, and K. Taira. Extraction of DMD modes from Pulse-Burst PIV data of Flow over an Open Cavity. In *AIAA Scitech 2020 Forum*, Orlando, FL, USA, Jan. 2020. AIAA-2020-1068. doi: 10.2514/6.2020-1068.

[72] Y. Sun, K. Taira, L.N. Cattafesta III, and L. Ukeiley. Bi-global Instabilities of Compressible Open-Cavity Flows. *Journal of Fluid Mechanics*, 826:270–301, Sep. 2017. doi: 10.1017/jfm.2017.416.

[73] J. Scheiman. Acoustic Measurements of a Large Cavity in a Wind Tunnel. Technical report, Langley Research Center, VA, USA, May. 1978. NASA-TM-78658.

[74] E.B. Plentovich. Three-Dimensional Cavity Flow Fields at Subsonic and Transonic Speeds. Technical report, NASA Langley, VA, USA, Sep. 1990. NASA TM-4209.

[75] S.A. Ritchie. *Non-Instrusive Measurements and Computations of Transonic Cavity Flows with Applications to Aircraft Store Release*. PhD thesis, Department of Aerospace Power and Sensors, Cranfield University, Swindon, England, UK, Sep. 2005.

[76] T. Colonius. An Overview of Simulation, Modelling, and Active Control of Flow/Acoustic Resonance in Open Cavities. In *39th Aerospace Sciences Meeting and Exhibit*, Reno, NV, USA, Jan. 2001. AIAA-2001-0076. doi: 10.2514/6.2001-76.

[77] C. Haigermoser, L. Vesely, M. Novara, and M. Onorato. Visualizations of the Flow Inside an Open Cavity at Medium range Reynolds Numbers. *Physics of Fluid*, 20(10):105101, Oct. 2008. doi: 10.1063/1.2990043.

[78] T. Colonius, A.J. Basu, and C.W. Rowley. Numerical Investigation of the Flow Past a Cavity. In *5th AIAA/CEAS Aeroacoustics Conference and Exhibit*, Bellevue, WA, USA, May. 1999. AIAA-99-1912. doi: 10.2514/6.1999-1912.

[79] R. W. Rowley, T. Colonius, and A.J. Basu. On Self-Sustained Oscillations in Two-Dimensional Compressible Flow over Rectangular Cavities. *Journal of Fluid Mechanics*, 455:315–346, Mar. 2002. doi: 10.1017/S0022112001007534.

[80] J. Milbank. *Investigation of Fluid-Dynamic Cavity Oscillations and the Effects of Flow Angle in an Automotive Context using an Open-Jet Wind Tunnel*. PhD thesis, School of AMME, RMIT University, Melbourne, VIC, AUS, Aug. 2004.

[81] K. Chang, G. Constantunescu, and S-O. Park. Analysis of the Flow and Mass Transfer Process for the Incompressible Flow Past an Open Cavity with a Laminar and Fully Turbulent incoming Boundary Layer. *Journal of Fluid Mechanics*, 561:113–145, Aug. 2006. doi: 10.1017/S0022112006000735.

[82] F.E. Jørgensen. How to Measure Turbulence with Hot-Wire Anemometers. Technical report, Dantec Dynamiucs A/S, Skovlunde, DNK, Jun. 2004. 9040U6152.

[83] H.H Bruun. *Hot-Wire Anemometry: Principles and Signal Analysis*. Oxford Academic, May. 1995. doi: 10.1093/oso/9780198563426.001.0001.

[84] 9040U49236. *Dantec Dynamics: StreamWare Pro: Installation and User Guide*, 2020.

[85] Tygon e-3603: Tubing for laboratory and vacuum applications. `https://www.ics.saint-gobain.com/tygon-tubing-accessories/thermoplastic-elastomer-flexible-tubing/tygon-e-3603`, Accessed 19/04/2024.

[86] R. Pemberton. An Overview of Dynamic Pressure Measurement Considerations. Technical report, Scanivalve Corporation, Liberty Lake, WA, USA, Mar. 2010.

[87] Howard Austerlitz. Chapter 4 - analog/digital conversions. In *Data Acquisition Techniques Using PCs*, pages 51–77. Academic Press, San Diego, CA, USA, 2nd edition, 2003. doi: 10.1016/B978-012068377-2/50004-8.

[88] L. Prandtl. Über Flüssigkeitsbewegung bei sehr kleiner Reibung. In *Verhandlungen des III: Internationalen Mathematiker Kongresses*, pages 485–491, Heidelberg, GER, Aug. 1904. B. G. Teubner, Leipzig.

[89] B.F.R. (Editor) Ewald. Wind Tunnel Wall Corrections. Technical report, Advisory Group for Aerospace Research & Development (AGARD), BP 25, 7 Rue Ancelle, F-92201 Neuilly-Sur-Seine Cedex, FR, Nov. 1998. GARD-AD-336.

[90] K.M. Wagner, J.L. aand Caspa, S.J. Beresh, J.F. Henfling, R.W. Spillers, and B.O.M Pruett. Mitigation of Wind Tunnel Wall Interactions in Subsonic Cavity Flows. *Experiments in Fluids*, 56(59):198–206, Mar. 2015. doi: 10.1007/s00348-015-1924-8.

[91] O.W. McGregor and White R.A. Drag of Rectangular Cavities in Supersonic and Transonic Flow including the Effects of Cavity Resonance. *AIAA Journal*, 8(11):277–287, Nov. 1970. doi: 10.2514/3.6032.

[92] J.B. Barlow, W.H.Jr. Rae, and A. Pope. Boundary Corrections I. In *Low Speed Wind Tunnel Testing*, chapter 9, page 329. John Wiley & Sons, NY, USA, Jun. 1966.

[93] J.B. Barlow, W.H.Jr. Rae, and A. Pope. Boundary Corrections II. In *Low Speed Wind Tunnel Testing*, chapter 10, pages 368–375. John Wiley & Sons, NY, USA, Jun. 1966.

[94] E.C. Maskell. A Theory of the Blockage Effects on Bluff Bodies and Stalled Wings in a Closed Wind Tunnel. Technical report, Ministry of Aviation: Aeronautical Research Council, Her Majesty's Stationery Office, London, UK, Nov. 1963. ARC-RM-3400.

[95] Dr.-Ing. S.F. Hoerner. Pressure Drag. In *Fluid Dynamic Drag*, chapter 3, pages 3–18. Hoerner Fluid Dynamics, Bakersfield, CA, USA, 1965.

[96] C.F. Heddleson, D.L. Brown, and R.T. Cliffe. Summary of Drag Coefficients of Various Shaped Cylinders. Technical report, General Electric, Atomic Products Division, Aircraft Nuclear Propulsion Department, Cincinnati, OH, USA, Apr. 1957. APEX-299.

[97] H.H. Heller and D.B. Bliss. The Physical Mechanism of Flow Induced Pressure Fluctuations in Cavities and Concepts for their Suppression. In *AIAA 2nd Aero-Acoustic Conference*, VA, USA, Mar. 1975. AIAA-75-491. doi: 10.2514/6.1975-491.

[98] K.M. Talluru, V. Kulandaivelu, N. Hutchins, and I. Marusic. A Calibration Technique to Correct Sensor Drift Issues in Hot-Wire Anemometry. *Measurement Science and Technology*, 25(105304), Jun. 2014. doi: 10.1088/0957-0233/25/10/105304.

[99] H. Schlichting and H. Gersten. *Boundary-Layer Theory*. Springer-Verlag Berlin Heidelberg, Berlin, GER, 9th edition, 2017.

[100] P.K. Kundu, I.M. Cohen, and D.R. Dowling. Turbulence. In *Fluid Mechanics*, chapter 12, pages 541–620. Academic Press, Boston, 5th edition, 2012. doi: 10.1016/B978-0-12-382100-3.10012-5.

[101] A.N. Kolmogorov. Local Structure of Turbulence in Incompressible Viscous Fluid for Very Large Reynolds Numbers. *Mathematical and Physical Sciences*, 434(1890):9–13, Jul. 1991. doi: 10.1098/rspa.1991.0075.

[102] M. Hansen. Velocity Distribution in the Boundary Layer of a Submerged Plate. Technical report, NACA, Washington, D.C. USA., Oct. 1930. NACA-TM-585.

[103] F.M. White. *Viscous Fluids*. McGraw-Hill, 3rd edition, 2006.

[104] A. Asaithambi. On solving the Nonlinear Falner-Skan Boundary-Value Problem: a Review. *Fluids*, 6(4):153, Apr. 2021. doi: 10.3390/fluids6040153.

[105] T. Cebeci and H.B. Keller. Shooting and Parallel Shooting Methods for Solving the Falkner-Skan Boundary-Layer Equation. *Journal of Sound and Vibration*, 18(4):545–553, Oct. 1971. doi: 10.1016/0022-460X(71)90105-2.

[106] H.B. Keller. *Numerical Methods for Two-point Boundary-Value Problems*. Ginn-Blaisdell Pub. Co.,, Waltham, MA, USA, 1968.

[107] J.S. Murphy. Extensions of the Falkner-Skan Similar Solutions to Flows with Surface Curvature. *AIAA Journal*, 3(11):2043–2049, Nov. 1965. doi: 10.2514/3.3313.

[108] P. Bradshaw. The analogy between Streamline Curvature and Buoyancy in Turbulent Shear Flow. *Journal of Fluid Mechanics*, 36(1):177–191, Mar. 1969. doi: 10.1017/S0022112069001583.

[109] V.C. Patel. The Effects of Curvature on the Turbulent Boundary Layer. Technical report, Ministry of Technology, Aeronautical Research Council, Cambridge University Engineering Deparment, Aug. 1968. R.M.No.3599.

[110] R.M.C. So and G.L. Mellor. An Experimental Investigation of Turbulent Boundary Layers along Curved Surfaces. Technical report, Princeton University, Lewis Research Center, NACA, Princeton, NJ, Cleveland, OH, Washington, D.C. USA., Apr. 1972. CR-1940.

[111] P. Bradshaw. Effects of Streamline Curvature on Turbulent Flow. Technical report, Department of Aeronautics, Imperial College of Science and Technology, London, England, Aug. 1973. AGARD Report No. 169.

[112] R.M.C. So and G.L. Mellor. Experiment on Convex Curvature Effects in Turbulent Boundary Layers. *Journal of Fluid Mechanics*, 60(1):43–62, Jan. 1973. doi: 10.1017/S002211208500297X.

[113] R.N. Meroney and P. Bradshaw. Turbulent Boundary-Layer growth over a Longitudinally Curved Surface. *AIAA Journal*, 13(11):1448–1453, Nov. 1975. doi: 10.2514/3.7014.

[114] J.C. Gillis and J.P. Johnston. Turbulent Boundary-Layer Flow and Structure on a Convex Wall and its Redevelopment on a Flat Wall. *Journal of Fluid Mechanics*, 135:123–153, Oct. 1983. doi: 10.1017/S0022112083002992.

[115] M.M. Gibson, W.P.. Jones, and B.A. Younis. Calculation of Turbulent Boundary Layers on Curved Surfaces. *Physics of Fluids*, 24:386–395, Mar. 1981. doi: 10.1063/1.863383.

[116] J.C. Gillis, J.P. Johnston, W.M. Kays, and R.J. Moffat. Turbulent Boundary Layer on a Convex Curved Surface. Technical report, Heat Transfer and Turbulence Mechanics Group, Thermosciences Division, Department of Mechanical Engineering, Stanford University, NASA, Stanford, CA, U.S., Feb. 1981. Report No. HMT-31.

[117] K.C. Muck, P.H. Hoffman, and P. Bradshaw. The Effect of Convex Surface Curvature on Turbulent Boundary Layers. *Journal of Fluid Mechanics*, 161:347–369, Jul. 1985. doi: 10.1017/S002211208500297X.

[118] V.C. Patel and F. Sotiropoulos. Longitudinal Curvature in Turbulent Boundary Layers. *Progress Aerospace Sciences*, 33(1-2):1–70, 1997. doi: 10.1016/S0376-0421(96)00001-2.

[119] M. Ramirez and G. Araya. Falkner-Skan Similarity Flow Solutions Subject to Wall Curvature and Passive Scalar Transport. In *7th Thermal and Fluids Engineering Conference, ASTFE*, May. 2022. doi: 10.1088/1742-6596/1786/1/012047. TFEC-2022-40936.

[120] H. Tijdeman and R.M.E.J. Spiering. A System for Unsteady Pressure Measurements Revisited. In *International Forum on Aeroelasticity and Structural Dynamics*, Amsterdamn, NL, Jun. 2003. Nederlandse Vereniging voor Luchtvaarttechniek.

[121] S.S. Rajan, N. Lakshmanan, S. Arunachalam, M. H. Angelin, and S. Krishnankumar. Development of a Dynamic Pressure Calibrator Model for Wind Tunnel studies. *Journal of Instrumentation Society of India*, 38(3):190–197, 2008.

[122] A.W. Rofail, R. Tonin, and D. Hanafi. Sensitivity of Frequency Response to a Type of Tubing. In *Australasian Wind Engineering Workshop*, Darwin, NT, AUS, Jun. 2004.

[123] A.S. Iberall. Attenuation of Oscillatory Pressures in Instrument Lines. *Journal of Research of National Bureau of Standards*, 45:85–108, Jul. 1950. doi: 10.6028/JRES.045.008.

[124] H. Bergh and H. Tijdeman. Theoretical and Experimental Results for the Dynamic Response of Pressure Measuring System. Technical report, National Aero- and Astronautical Research Institute, Amsterdamn, NETH, Jan. 1965. NLR-TR F.238.

[125] Tigdeman H. and Bergh H. The Influence of the Main Flow on the Transfer Function of Tube-Transducer Systems used for Unsteady Pressure Measurements. Technical report, National Aerospace Laboratory, NLR, Amsterdam, NL, Sep. 1972.

[126] A.V. Oppenheim, R.W. Schafer, and J.R. Buck. *Discrete-Time Signal Processing*. Prentice Hall, Upper Saddle River, NJ, USA, 1999.

[127] P.J. Schmid. Dynamic Mode Decomposition of Experimental Data. In *8th International Symposium on PIV*, Melbourne, VIC, AUS, Aug. 2009. Monash University.

[128] P.J. Schmid. Dynamic Mode Decomposition of Numerical and Experimental Data. *Journal of Fluid Mechanics*, 21(9):5–28, Jul. 2010. doi: 10.1017/S0022112010001217.

[129] P.J. Schmid. Application of the Dynamic Mode Decomposition to Experimental Data. *Experiments in Fluids*, 50:1123–1130, Feb. 2011. doi: 10.1007/s00348-010-0911-3.

[130] J.N. Kutz, S.L. Brunton, B.W. Brunton, and J.L. Proctor. *Dynamic Mode Decomposition: Data-Driven Modeling of Complex Systems*. Society for Industrial and Applied Mathematics, Philadelphia, PA, USA, 2016.

[131] T. Krake, S. Reinhardt, M. Hlawatsch, B. Eberhardt, and D. Weiskopf. Visualisation and Selection of Dynamic Mode Decomposition Components for Unsteady Flow. *Visual Informatics*, 5:15–27, Jun. 2021. doi: 10.1016/j.visinf.2021.06.003.

[132] C.O.L Hamilton-Smith. An Experimental Investigation of Flow Induced Pressure Oscillations in Rectangular Cavities. Master's thesis, School of Aerospace, Mechanical & Mechatronic Engineering, USYD, Darlington, NSW, AUS, 2019.

[133] N.M. Komerath, K.K. Ahuja, and F.W. Chambers. Prediction and Measurement of Flow over Cavities - A Survey. In *25th Aerospace Sciences Meeting*, Reno, NV, USA, Jan. 1987. AIAA-87-0166. doi: 10.2514/6.1987-166.

[134] D. Rockwell and C Knisely. Observations of the Three-Dimensional Nature of Unstable Flow Past a Cavity. *Physics of Fluids*, 23(3):425–431, Mar. 1980. doi: 10.1063/1.863009.

[135] S.D. Crook, R.M. Kelso, and J. Drobik. Aeroacoutics of Aircraft Cavities. In *16th Australasian Fluid Mechanic Conference*, pages 429–435, Gold Coast, QLD, AUS, Dec. 2007.

[136] M.A. Kegerise, E.F. Spina, and L.N. Cattafesta III. An Experimental Investigation of Flow-Induced Cavity Oscillations. In *30th AIAA Fluid Dynamics Conference*, Norfolk, VA, USA, Jun. 1999. AIAA-99-3705. doi: 10.2514/6.1999-3705.

[137] P.J. Disimile, N. Toy, and E. Savory. Pressure Oscillations in a Subsonic Cavity at Yaw. *AIAA Journal*, 36(7):1141–1148, Jul. 1998. doi: 10.2514/2.521.

[138] P.J. Disimile and P.D. Orkwis. Sound Pressure Level Variations in a Supersonic Rectangular Cavity at Yaw. *Journal of Propulsion and Power*, 14(3):392–398, May. 1998. doi: 10.2514/2.5292.

[139] N. Forestier, L. Jacquin, and P. Geffroy. The Mixing Layer over a Deep Cavity at High-Subsonic Speed. *Journal of Fluid Mechanics*, 475:101–145, Jan. 2003. doi: 10.1017/S0022112002002537.

[140] N.E. Murray and L.S. Ukeiley. Modified Quadratic Stochastic Estimation of Resonating Subsonic Cavity Flow. *Journal of Turbulence*, 8(53), Dec. 2007. doi: 10.1080/14685240701656121.

[141] N. Murray, E. Sallstrom, and L. Ukeiley. Properties of Subsonic Open Cavity Flow Fields. *Physics of Fluid*, 21(9):095103, Sep. 2009. doi: 10.1063/1.3210772.

[142] L. Crocco. Eine neue stromfunktion für die erforschung der bewegung der gase mit rotation. *Zeitschrift für Angewandte Mathematik und Mechanik*, 17(1):1–7, Feb. 1937. doi: 10.1002/zamm.19370170103.

[143] A.H. Shapiro. National committee for fluid mechanics films film notes for vorticity. Encyclopædia Britannica Educational Corporation, Chicago, IL, USA, 1969. URL `https://web.mit.edu/hml/ncfmf/09VOR.pdf`.

[144] G.B. Brown. The Vortex Motion causing Edge Tones. *Physical Society*, 49(5):493–507, Jun. 1937. doi: 10.1088/0959-5309/49/5/306.

[145] J. Malone, M. Debiasi, J. Little, and M. Samimy. Analysis of the Spectral Relationships of Cavity Tones in Subsonic Resonant Cavity Flows. *Physics of Fluids*, 21(5):055103, May. 2009. doi: 10.1063/1.3139270.

[146] N.E. Murray and L.S. Ukeiley. Wall Pressure Modes in Subsonic Cavity Flows. In *11th AIAA/CEAS Aeroacoustics Conference (26th AIAA Aeroacoustics Conference)*, Monterey, CA, USA, May. 2005. AIAA-2005-2801. doi: 10.2514/6.2005-2801.

[147] P.M. Morse. *Vibration and Sound*. McGraw-Hill, 2nd edition, 1948.

[148] T. Cebeci and J. Cousteix. Conservation Equations for Mass and Momentum for Incompressible Flows. In *Modeling and Computation of Boundary Layer Flows*, chapter 2, pages 18–23. Horizons Publishing Inc., Long Beach, CA, USA, 2nd edition, 2005.

[149] P.K. Kundu, I.M. Cohen, and D.R. Dowling. Compressible Flows. In *Fluid Mechanics*, chapter 15, pages 729–778. Academic Press, Boston, MA, USA, 5th edition, 2012. doi: 10.1016/B978-0-12-382100-3.10015-0.

[150] K. Heizman. Die grenzschicht an einem in den gleichformigen flussigkeitsstrom eingetauchten geraden kreiszylinder. *Dinglers Polytech Journal*, 326:321–324, 1911.

[151] D.R. Hartree. On an equation occurring in Falkner and Skan's approximate treatment of the equations of the Boundary Layer. *Mathematical Proceedings of the Cambridge Philosophical Society*, 33(2):223–239, Apr. 1937. doi: 10.1017/S0305004100019575.

[152] W Mangler. Zusammenhang zwischen ebenen und rotationssymmetrischen Grenzschichten in kompressiblen Flüssigkeiten. *Journal of Applied Mathmatics and Mechanics*, 28(4):97–103, 1948. doi: 10.1002/zamm.19480280401.

[153] J. Katz and A. Plotkin. *Low-Speed Aerodynamics*. Cambridge Aerospace Series. Cambridge University Press, 2nd edition, 2001.

[154] E. Isaacson and H.B. Keller. *Analysis of Numerical Methods*. John Wiley & Sons, NY, USA, 1966.

[155] W.A. Coppel. On a Differential Equation of Boundary Layer Theory. *Philosophical Transcations of the Royal Society of London, Series A*, 253(1023):101–136, Sep. 1960.

[156] A.H. Craven and L.A. Peletier. On the uniqueness of solutions of the Falkner-Skan equation. *Mathematika*, 19(1):129–133, Jun. 1972. doi: 10.1112/S0025579300005052.

[157] N.S. Asaithambi. A Numerical Method for the Solution of the Falkner-Skan Equation. *Applied Mathematics and Computation*, 81(2-3):259–264, Feb. 1997. doi: 10.1016/S0096-3003(95)00325-8.

[158] J. Zhang and B. Chen. An iterative method for solving Falkner–Skan. *Applied Mathematics & Computation*, 210(1):215–22, Apr. 2009. doi: 10.1016/j.amc.2008.12.079.

[159] H. Temini and M. Ben-Romdhane. Numerical Solutions of Falkner-Skan Equation by Iterative Transformation Method. *Mathematical Modelling and Analysis*, 23(1):139–151, Feb. 2018. doi: 10.3846/mma.2018.009.

[160] I. Sher and A. Yakot. New approach to Solution of the Falkner-Skan Equation. *AIAA Journal*, 39(5):965–967, May. 2001. doi: 10.2514/2.1403.

Appendix A

Wind Tunnel Data

A.1 Ambient Conditions

Ambient conditions are in Tables A.1 - A.24 for USP, and Tables A.25-A.27 for HWA. Velocity U_∞ (m/s), density ρ_∞ (kg/m^3) and temperature T_∞(C°) were recorded, and the rest calculated as follows. Static pressure p_∞ (kPa) in Eqn. A.1 with R = 287.05J/kg.K. Dynamic pressure q_∞ (kPa) in Eqn. A.2. Speed of Sound a_∞(m/s) in Eqn. A.3, with specific heat $\gamma = 1.4$. Mach M_∞ in Eqn. A.4. Dynamic viscosity μ_∞ (kg/ms) with Sutherland's theory[103] in Eqn. A.5; μ_0 = 1.7× 10^{-5}kg/m.s, T_0 = 273K and S_μ = 111.8K. Reynolds Number Re_∞/m in Eqn. A.6.

$$p_\infty = \rho_\infty R T_\infty \qquad \text{(A.1)} \qquad\qquad q_\infty = 0.5\rho_\infty U_\infty^2 \qquad \text{(A.2)}$$

$$a_\infty = \sqrt{\gamma R T_\infty} \qquad \text{(A.3)} \qquad\qquad M_\infty = U_\infty / a_\infty \qquad \text{(A.4)}$$

$$\mu_\infty = \mu_0 \cdot \frac{T_0 + S_\mu}{T_\infty + S_\mu}\sqrt{\left(\frac{T_\infty}{T_0}\right)^3} \qquad \text{(A.5)} \qquad\qquad Re_\infty/m = \frac{U_\infty}{\nu_\infty} \qquad \text{(A.6)}$$

For tube distortion in Section 4.4.2, Prandtl number P_r is calculated with the algorithm in Appendix F.1.3. Pr is kinematic viscosity ($\nu = \mu/\rho$), over thermal diffusivity $\alpha_t = k_t/c_p\rho$, per Eqn. A.7. k_t is thermal conductivity per Sutherland[103] with; $k_0 = 2.4 \times 10^{-2}$kg/ms, T_0 = 273K and S_k = 202K. c_p is specific heat at constant pressure, per Eqn. A.9, using Daubert & Danner correlations for air[103]; A = 28958, B = 9390, C = 3012, D = 7580, and E = 1484.

$$Pr = \frac{\nu}{\alpha} = \frac{\mu}{\rho}\frac{c_p\rho}{k_t} = \frac{c_p\mu}{k} \qquad \text{(A.7)} \qquad\qquad k_t = k_{t_0} \cdot \frac{T_0 + S_k}{T_\infty + S_k}\sqrt{\left(\frac{T_\infty}{T_0}\right)^3} \qquad \text{(A.8)}$$

$$c_p = \frac{1}{MW}\left[A + B\left(\frac{C/T_0}{\sinh(C/T_0)}\right)^2 + D\left(\frac{E/T_0}{\cosh(E/T_0)}\right)^2\right] \qquad \text{(A.9)}$$

Table A.1: USP: Ambient Conditions of C1: L/D = 1, L/W = 1, Conic U/S

U_∞	ρ_∞	μ_∞	T_∞	p_∞	q_∞	a_∞	M_∞	Re_∞
m/s	kg/m^3	kg/ms	C°	kPa	kPa	m/s	-	10^6/m
10	1.198	1.83E-05	21.7	101.4	0.06	344.5	0.03	0.6
15	1.197	1.83E-05	21.8	101.3	0.13	344.5	0.04	0.9

20	1.197	1.83E-05	21.8	101.3	0.24	344.5	0.06	1.3
25	1.196	1.83E-05	21.9	101.3	0.37	344.6	0.07	1.6
30	1.196	1.83E-05	22.0	101.3	0.54	344.7	0.09	1.9
35	1.196	1.83E-05	22.1	101.4	0.73	344.7	0.10	2.2
40	1.196	1.83E-05	22.1	101.4	0.96	344.7	0.12	2.5
45	1.195	1.83E-05	22.2	101.3	1.21	344.8	0.13	2.8
50	1.195	1.83E-05	22.2	101.3	1.49	344.8	0.14	3.1
55	1.195	1.83E-05	22.5	101.4	1.81	344.9	0.16	3.4
60	1.195	1.83E-05	22.5	101.4	2.15	344.9	0.18	3.7
65	1.195	1.83E-05	26.0	102.6	2.52	347.0	0.19	4.0

Table A.2: USP: Ambient Conditions of C2: L/D = 1, L/W = 2, Conic U/S

U_∞	ρ_∞	μ_∞	T_∞	p_∞	q_∞	a_∞	M_∞	Re_∞
m/s	kg/m^3	kg/ms	C°	kPa	kPa	m/s	-	10^6/m
10	1.192	1.84E-05	23.8	101.6	0.06	345.7	0.03	0.6
15	1.192	1.84E-05	23.8	101.6	0.13	345.7	0.04	0.9
20	1.191	1.84E-05	24.0	101.6	0.24	345.8	0.06	1.3
25	1.190	1.84E-05	24.2	101.6	0.37	345.9	0.07	1.6
30	1.190	1.84E-05	24.2	101.6	0.54	345.9	0.09	1.9
35	1.189	1.84E-05	24.4	101.6	0.73	346.0	0.10	2.2
40	1.189	1.84E-05	24.4	101.6	0.95	346.0	0.12	2.5
45	1.189	1.84E-05	24.4	101.6	1.20	346.0	0.13	2.8
50	1.189	1.84E-05	24.4	101.6	1.49	346.0	0.14	3.1
55	1.188	1.84E-05	24.6	101.5	1.80	346.2	0.16	3.4
60	1.188	1.84E-05	24.6	101.5	2.14	346.2	0.18	3.7
65	1.188	1.84E-05	24.6	101.5	2.51	346.2	0.19	4.1

Table A.3: USP: Ambient Conditions of C3: L/D = 2, L/W = 2, Conic U/S

U_∞	ρ_∞	μ_∞	T_∞	p_∞	q_∞	a_∞	M_∞	Re_∞
m/s	kg/m^3	kg/ms	C°	kPa	kPa	m/s	-	10^6/m
10	1.221	1.80E-05	17.0	101.7	0.06	341.7	0.03	0.6
15	1.220	1.80E-05	17.1	101.6	0.14	341.8	0.04	0.9
20	1.219	1.81E-05	17.2	101.6	0.24	341.8	0.06	1.3
25	1.219	1.81E-05	17.2	101.6	0.38	341.8	0.07	1.6
30	1.219	1.81E-05	17.2	101.6	0.55	341.8	0.09	1.9
35	1.219	1.81E-05	17.2	101.6	0.75	341.8	0.10	2.2
40	1.218	1.81E-05	17.3	101.5	0.97	341.9	0.12	2.5
45	1.218	1.81E-05	17.3	101.5	1.23	341.9	0.13	2.8
50	1.218	1.81E-05	17.3	101.5	1.52	341.9	0.14	3.1
60	1.217	1.81E-05	17.4	101.5	2.19	342.0	0.18	3.7
65	1.217	1.81E-05	17.4	101.5	2.57	342.0	0.19	4.1

Table A.4: USP: Ambient Conditions of C4: L/D = 2, L/W = 4, Conic U/S

U_∞	ρ_∞	μ_∞	T_∞	p_∞	q_∞	a_∞	M_∞	Re_∞
m/s	kg/m^3	kg/ms	C°	kPa	kPa	m/s	-	10^6/m
10	1.182	1.85E-05	26.0	101.5	0.06	347.0	0.03	0.6
15	1.182	1.85E-05	26.0	101.5	0.13	347.0	0.04	0.9
20	1.184	1.85E-05	25.9	101.6	0.24	346.9	0.06	1.3
25	1.183	1.85E-05	25.9	101.6	0.37	346.9	0.07	1.6
30	1.183	1.85E-05	25.9	101.6	0.53	346.9	0.09	1.9
35	1.183	1.85E-05	25.9	101.6	0.72	346.9	0.10	2.2
40	1.183	1.85E-05	25.9	101.6	0.95	346.9	0.12	2.5
45	1.183	1.85E-05	25.9	101.6	1.20	346.9	0.13	2.8
50	1.183	1.85E-05	25.9	101.6	1.48	346.9	0.14	3.1
55	1.183	1.85E-05	25.9	101.6	1.79	346.9	0.16	3.4
60	1.182	1.85E-05	26.0	101.5	2.13	347.0	0.18	3.7
65	1.182	1.85E-05	26.0	101.5	2.50	347.0	0.19	4.1

Table A.5: USP: Ambient Conditions of C5: L/D = 3, L/W = 3, Conic U/S

U_∞	ρ_∞	μ_∞	T_∞	p_∞	q_∞	a_∞	M_∞	Re_∞
m/s	kg/m^3	kg/ms	C°	kPa	kPa	m/s	-	10^6/m
10	1.215	1.81E-05	18.0	101.5	0.06	342.3	0.03	0.6
15	1.215	1.81E-05	18.0	101.5	0.14	342.3	0.04	0.9
20	1.215	1.81E-05	18.0	101.5	0.24	342.3	0.06	1.3
25	1.215	1.81E-05	18.0	101.5	0.38	342.3	0.07	1.6
30	1.215	1.81E-05	18.0	101.5	0.55	342.3	0.09	1.9
35	1.215	1.81E-05	18.0	101.5	0.74	342.3	0.10	2.2
40	1.215	1.81E-05	18.0	101.5	0.97	342.3	0.12	2.5
45	1.215	1.81E-05	18.0	101.5	1.23	342.3	0.13	2.8
50	1.215	1.81E-05	18.0	101.5	1.52	342.3	0.14	3.1
55	1.215	1.81E-05	18.0	101.5	1.84	342.3	0.16	3.4
60	1.215	1.81E-05	18.0	101.5	2.19	342.3	0.18	3.7
65	1.215	1.81E-05	18.0	101.5	2.57	342.3	0.19	4.1

Table A.6: USP: Ambient Conditions of C6: L/D = 3, L/W = 6, Conic U/S

U_∞	ρ_∞	μ_∞	T_∞	p_∞	q_∞	a_∞	M_∞	Re_∞
m/s	kg/m^3	kg/ms	C°	kPa	kPa	m/s	-	10^6/m
10	1.201	1.83E-05	21.5	101.6	0.06	344.4	0.03	0.6
15	1.201	1.83E-05	21.5	101.6	0.14	344.4	0.04	0.9
20	1.201	1.83E-05	21.5	101.6	0.24	344.4	0.06	1.3
25	1.201	1.83E-05	21.5	101.6	0.38	344.4	0.07	1.6
30	1.201	1.83E-05	21.5	101.6	0.54	344.4	0.09	1.9
35	1.201	1.83E-05	21.5	101.6	0.74	344.4	0.10	2.2
40	1.201	1.83E-05	21.5	101.6	0.96	344.4	0.12	2.5

45	1.201	1.83E-05	21.5	101.6	1.22	344.4	0.13	2.8
50	1.201	1.83E-05	21.5	101.6	1.50	344.4	0.14	3.1
55	1.201	1.83E-05	21.5	101.6	1.82	344.4	0.16	3.4
60	1.200	1.83E-05	21.4	101.5	2.16	344.3	0.18	3.7
65	1.200	1.83E-05	21.4	101.5	2.54	344.3	0.19	4.1

Table A.7: USP: Ambient Conditions of C7: L/D = 1, L/W = 1, Ogive U/S

U_∞	ρ_∞	μ_∞	T_∞	p_∞	q_∞	a_∞	M_∞	Re_∞
m/s	kg/m^3	kg/ms	C°	kPa	kPa	m/s	-	10^6/m
10	1.203	1.82E-05	21.0	101.6	0.06	344.1	0.03	0.6
15	1.202	1.82E-05	21.2	101.6	0.14	344.2	0.04	0.9
20	1.202	1.82E-05	21.2	101.6	0.24	344.2	0.06	1.3
25	1.201	1.83E-05	21.4	101.5	0.38	344.3	0.07	1.6
30	1.201	1.83E-05	21.4	101.5	0.54	344.3	0.09	1.9
35	1.201	1.83E-05	21.4	101.5	0.74	344.3	0.10	2.2
40	1.200	1.83E-05	21.6	101.5	0.96	344.4	0.12	2.5
45	1.200	1.83E-05	21.6	101.5	1.22	344.4	0.13	2.8
50	1.200	1.83E-05	21.6	101.5	1.50	344.4	0.14	3.1
55	1.199	1.83E-05	22.0	101.6	1.81	344.7	0.16	3.4
60	1.199	1.83E-05	22.0	101.6	2.16	344.7	0.18	3.7
65	1.199	1.83E-05	22.0	101.6	2.53	344.7	0.19	4.1

Table A.8: USP: Ambient Conditions of C8: L/D = 1, L/W = 2, Ogive U/S

U_∞	ρ_∞	μ_∞	T_∞	p_∞	q_∞	a_∞	M_∞	Re_∞
m/s	kg/m^3	kg/ms	C°	kPa	kPa	m/s	-	10^6/m
10	1.188	1.84E-05	24.0	101.3	0.06	345.8	0.03	0.6
15	1.187	1.84E-05	24.2	101.3	0.13	345.9	0.04	0.9
20	1.187	1.84E-05	24.2	101.3	0.24	345.9	0.06	1.3
25	1.186	1.84E-05	24.3	101.3	0.37	346.0	0.07	1.6
30	1.186	1.84E-05	24.3	101.3	0.53	346.0	0.09	1.9
35	1.186	1.84E-05	24.3	101.3	0.73	346.0	0.10	2.2
40	1.185	1.84E-05	24.6	101.3	0.95	346.2	0.12	2.5
45	1.185	1.84E-05	24.6	101.3	1.20	346.2	0.13	2.8
50	1.185	1.84E-05	24.6	101.3	1.48	346.2	0.14	3.1
55	1.185	1.84E-05	24.6	101.3	1.79	346.2	0.16	3.4
60	1.184	1.84E-05	24.8	101.3	2.13	346.3	0.18	3.7
65	1.184	1.84E-05	24.8	101.3	2.50	346.3	0.19	4.1

Table A.9: USP: Ambient Conditions of C9: L/D = 2, L/W = 2, Ogive U/S

U_∞	ρ_∞	μ_∞	T_∞	p_∞	q_∞	a_∞	M_∞	Re_∞
m/s	kg/m^3	kg/ms	C°	kPa	kPa	m/s	-	10^6/m
10	1.206	1.82E-05	20.0	101.5	0.06	343.5	0.03	0.6
15	1.206	1.82E-05	20.0	101.5	0.14	343.5	0.04	0.9
20	1.205	1.82E-05	20.2	101.5	0.24	343.6	0.06	1.3
25	1.205	1.82E-05	20.2	101.5	0.38	343.6	0.07	1.6
30	1.205	1.82E-05	20.2	101.5	0.54	343.6	0.09	1.9
35	1.205	1.82E-05	20.2	101.5	0.74	343.6	0.10	2.2
40	1.205	1.82E-05	20.2	101.5	0.96	343.6	0.12	2.5
45	1.205	1.82E-05	20.2	101.5	1.22	343.6	0.13	2.8
50	1.205	1.82E-05	20.2	101.5	1.51	343.6	0.14	3.1
55	1.205	1.82E-05	20.2	101.5	1.82	343.6	0.16	3.4
60	1.205	1.82E-05	20.2	101.5	2.17	343.6	0.18	3.7
65	1.204	1.82E-05	20.3	101.4	2.54	343.7	0.19	4.1

Table A.10: USP: Ambient Conditions of C10: L/D = 2, L/W = 4, Ogive U/S

U_∞	ρ_∞	μ_∞	T_∞	p_∞	q_∞	a_∞	M_∞	Re_∞
m/s	kg/m^3	kg/ms	C°	kPa	kPa	m/s	-	10^6/m
10	1.195	1.83E-05	22.5	101.4	0.06	344.9	0.03	0.6
15	1.194	1.83E-05	22.6	101.4	0.13	345.0	0.04	0.9
20	1.194	1.83E-05	22.6	101.4	0.24	345.0	0.06	1.3
25	1.194	1.83E-05	22.6	101.4	0.37	345.0	0.07	1.6
30	1.193	1.83E-05	22.7	101.3	0.54	345.1	0.09	1.9
35	1.193	1.83E-05	22.7	101.3	0.73	345.1	0.10	2.2
40	1.193	1.83E-05	22.7	101.3	0.95	345.1	0.12	2.5
45	1.190	1.83E-05	23.3	101.3	1.20	345.4	0.13	2.8
50	1.190	1.83E-05	23.3	101.3	1.49	345.4	0.14	3.1
55	1.190	1.83E-05	23.3	101.3	1.80	345.4	0.16	3.4
60	1.190	1.83E-05	23.3	101.3	2.14	345.4	0.18	3.7
65	1.190	1.83E-05	23.3	101.3	2.51	345.4	0.19	4.1

Table A.11: USP: Ambient Conditions of C11: L/D = 3, L/W = 3, Ogive U/S

U_∞	ρ_∞	μ_∞	T_∞	p_∞	q_∞	a_∞	M_∞	Re_∞
m/s	kg/m^3	kg/ms	C°	kPa	kPa	m/s	-	10^6/m
10	1.192	1.84E-05	23.7	101.6	0.06	345.6	0.03	0.6
15	1.192	1.84E-05	23.7	101.6	0.13	345.6	0.04	0.9
20	1.192	1.84E-05	23.7	101.6	0.24	345.6	0.06	1.3
25	1.192	1.84E-05	23.7	101.6	0.37	345.6	0.07	1.6
30	1.192	1.84E-05	23.7	101.6	0.54	345.6	0.09	1.9
35	1.192	1.84E-05	23.7	101.6	0.73	345.6	0.10	2.2
40	1.192	1.84E-05	23.7	101.6	0.95	345.6	0.12	2.5

45	1.192	1.84E-05	23.7	101.6	1.21	345.6	0.13	2.8
50	1.192	1.84E-05	23.7	101.6	1.49	345.6	0.14	3.1
55	1.192	1.84E-05	23.7	101.6	1.80	345.6	0.16	3.4
60	1.192	1.84E-05	23.7	101.6	2.15	345.6	0.18	3.7
65	1.192	1.84E-05	23.7	101.6	2.52	345.6	0.19	4.1

Table A.12: USP: Ambient Conditions of C12: L/D = 3, L/W = 6, Ogive U/S

U_∞	ρ_∞	μ_∞	T_∞	p_∞	q_∞	a_∞	M_∞	Re_∞
m/s	kg/m^3	kg/ms	C°	kPa	kPa	m/s	-	10^6/m
10	1.200	1.82E-05	21.0	101.3	0.06	344.1	0.03	0.6
15	1.200	1.82E-05	21.0	101.3	0.14	344.1	0.04	0.9
20	1.199	1.82E-05	21.1	101.3	0.24	344.1	0.06	1.3
25	1.199	1.82E-05	21.1	101.3	0.37	344.1	0.07	1.6
30	1.199	1.82E-05	21.1	101.3	0.54	344.1	0.09	1.9
35	1.199	1.82E-05	21.1	101.3	0.73	344.1	0.10	2.2
40	1.198	1.82E-05	21.3	101.3	0.96	344.2	0.12	2.5
45	1.198	1.82E-05	21.3	101.3	1.21	344.2	0.13	2.8
50	1.198	1.82E-05	21.3	101.3	1.50	344.2	0.14	3.1
55	1.198	1.82E-05	21.3	101.3	1.81	344.2	0.16	3.4
60	1.198	1.82E-05	21.3	101.3	2.16	344.2	0.18	3.7
65	1.198	1.82E-05	21.3	101.3	2.53	344.2	0.19	4.1

Table A.13: USP: Ambient Conditions of C13: L/D = 1, L/W = 1, Parabola U/S

U_∞	ρ_∞	μ_∞	T_∞	p_∞	q_∞	a_∞	M_∞	Re_∞
m/s	kg/m^3	kg/ms	C°	kPa	kPa	m/s	-	10^6/m
10	1.193	1.82E-05	21.0	100.7	0.06	344.1	0.03	0.6
15	1.193	1.82E-05	21.2	100.8	0.13	344.2	0.04	0.9
20	1.193	1.82E-05	21.2	100.8	0.24	344.2	0.06	1.3
25	1.193	1.83E-05	21.4	100.9	0.37	344.3	0.07	1.6
30	1.193	1.83E-05	21.4	100.9	0.54	344.3	0.09	1.9
35	1.193	1.83E-05	21.4	100.9	0.73	344.3	0.10	2.2
40	1.193	1.83E-05	21.6	100.9	0.95	344.4	0.12	2.5
45	1.193	1.83E-05	21.6	100.9	1.21	344.4	0.13	2.8
50	1.193	1.83E-05	21.6	100.9	1.49	344.4	0.14	3.1
55	1.193	1.83E-05	22.0	101.1	1.80	344.7	0.16	3.4
60	1.193	1.83E-05	22.0	101.1	2.15	344.7	0.18	3.7
65	1.193	1.83E-05	22.0	101.1	2.52	344.7	0.19	4.1

Table A.14: USP: Ambient Conditions of C14: L/D = 1, L/W = 2, Parabola U/S

U_∞	ρ_∞	μ_∞	T_∞	p_∞	q_∞	a_∞	M_∞	Re_∞
m/s	kg/m^3	kg/ms	C°	kPa	kPa	m/s	-	10^6/m
10	1.184	1.85E-05	26.0	101.7	0.06	347.0	0.03	0.6
15	1.183	1.85E-05	26.1	101.6	0.13	347.0	0.04	0.9
20	1.183	1.85E-05	26.1	101.6	0.24	347.0	0.06	1.3
25	1.183	1.85E-05	26.1	101.6	0.37	347.0	0.07	1.6
30	1.183	1.85E-05	26.1	101.6	0.53	347.0	0.09	1.9
35	1.183	1.85E-05	26.1	101.6	0.72	347.0	0.10	2.2
40	1.182	1.85E-05	26.4	101.6	0.95	347.2	0.12	2.5
45	1.182	1.85E-05	26.4	101.6	1.20	347.2	0.13	2.8
50	1.182	1.85E-05	26.4	101.6	1.48	347.2	0.14	3.1
55	1.182	1.85E-05	26.4	101.6	1.79	347.2	0.16	3.4
60	1.182	1.85E-05	26.4	101.6	2.13	347.2	0.18	3.7
65	1.182	1.85E-05	26.4	101.6	2.50	347.2	0.19	4.1

Table A.15: USP: Ambient Conditions of C15: L/D = 2, L/W = 2, Parabola U/S

U_∞	ρ_∞	μ_∞	T_∞	p_∞	q_∞	a_∞	M_∞	Re_∞
m/s	kg/m^3	kg/ms	C°	kPa	kPa	m/s	-	10^6/m
10	1.203	1.82E-05	20.4	101.4	0.06	343.7	0.03	0.6
15	1.203	1.82E-05	20.4	101.4	0.14	343.7	0.04	0.9
20	1.201	1.82E-05	20.7	101.3	0.24	343.9	0.06	1.3
25	1.201	1.82E-05	20.7	101.3	0.38	343.9	0.07	1.6
30	1.201	1.82E-05	20.7	101.3	0.54	343.9	0.09	1.9
35	1.200	1.82E-05	21.0	101.3	0.74	344.1	0.10	2.2
40	1.200	1.82E-05	21.0	101.3	0.96	344.1	0.12	2.5
45	1.200	1.82E-05	21.0	101.3	1.22	344.1	0.13	2.8
50	1.200	1.82E-05	21.0	101.3	1.50	344.1	0.14	3.1
55	1.200	1.82E-05	21.0	101.3	1.82	344.1	0.16	3.4
60	1.199	1.82E-05	21.2	101.3	2.16	344.2	0.18	3.7
65	1.199	1.82E-05	21.2	101.3	2.53	344.2	0.19	4.1

Table A.16: USP: Ambient Conditions of C16: L/D = 2, L/W = 4, Parabola U/S

U_∞	ρ_∞	μ_∞	T_∞	p_∞	q_∞	a_∞	M_∞	Re_∞
m/s	kg/m^3	kg/ms	C°	kPa	kPa	m/s	-	10^6/m
10	1.190	1.84E-05	23.5	101.3	0.06	345.5	0.03	0.6
15	1.190	1.84E-05	23.5	101.3	0.13	345.5	0.04	0.9
20	1.189	1.84E-05	23.7	101.3	0.24	345.6	0.06	1.3
25	1.189	1.84E-05	23.7	101.3	0.37	345.6	0.07	1.6
30	1.189	1.84E-05	23.7	101.3	0.54	345.6	0.09	1.9
35	1.188	1.84E-05	24.0	101.3	0.73	345.8	0.10	2.2
40	1.187	1.84E-05	24.2	101.3	0.95	345.9	0.12	2.5

45	1.187	1.84E-05	24.2	101.3	1.20	345.9	0.13	2.8
50	1.187	1.84E-05	24.2	101.3	1.48	345.9	0.14	3.1
55	1.187	1.84E-05	24.2	101.3	1.80	345.9	0.16	3.4
60	1.186	1.84E-05	24.4	101.3	2.13	346.0	0.18	3.7
65	1.186	1.84E-05	24.4	101.3	2.51	346.0	0.19	4.1

Table A.17: USP: Ambient Conditions of C17: L/D = 3, L/W = 3, Parabola U/S

U_∞	ρ_∞	μ_∞	T_∞	p_∞	q_∞	a_∞	M_∞	Re_∞
m/s	kg/m^3	kg/ms	C°	kPa	kPa	m/s	-	10^6/m
10	1.204	1.82E-05	21.0	101.3	0.06	344.1	0.03	0.6
15	1.204	1.82E-05	21.0	101.3	0.14	344.1	0.04	0.9
20	1.204	1.82E-05	21.0	101.3	0.24	344.1	0.06	1.3
25	1.204	1.82E-05	21.0	101.3	0.38	344.1	0.07	1.6
30	1.204	1.82E-05	21.0	101.3	0.54	344.1	0.09	1.9
35	1.204	1.82E-05	21.0	101.3	0.74	344.1	0.10	2.2
40	1.204	1.82E-05	21.0	101.3	0.96	344.1	0.12	2.5
45	1.204	1.82E-05	21.0	101.3	1.22	344.1	0.13	2.8
50	1.204	1.82E-05	21.0	101.3	1.50	344.1	0.14	3.1
55	1.204	1.82E-05	21.0	101.3	1.82	344.1	0.16	3.4
60	1.204	1.82E-05	21.0	101.3	2.16	344.1	0.18	3.7
65	1.204	1.82E-05	21.0	101.3	2.54	344.1	0.19	4.1

Table A.18: USP: Ambient Conditions of C18: L/D = 3, L/W = 6, Parabola U/S

U_∞	ρ_∞	μ_∞	T_∞	p_∞	q_∞	a_∞	M_∞	Re_∞
m/s	kg/m^3	kg/ms	C°	kPa	kPa	m/s	-	10^6/m
10	1.198	1.82E-05	21.0	101.2	0.06	344.1	0.03	0.6
15	1.198	1.82E-05	21.0	101.2	0.13	344.1	0.04	0.9
20	1.197	1.82E-05	21.1	101.1	0.24	344.1	0.06	1.3
25	1.196	1.82E-05	21.1	101.0	0.37	344.1	0.07	1.6
30	1.196	1.82E-05	21.1	101.0	0.54	344.1	0.09	1.9
35	1.195	1.82E-05	21.1	100.9	0.73	344.1	0.10	2.2
40	1.195	1.83E-05	21.3	101.0	0.96	344.2	0.12	2.5
45	1.195	1.83E-05	21.3	101.0	1.21	344.2	0.13	2.8
50	1.194	1.83E-05	21.3	100.9	1.49	344.2	0.14	3.1
55	1.194	1.83E-05	21.3	100.9	1.81	344.2	0.16	3.4
60	1.194	1.83E-05	21.3	100.9	2.15	344.2	0.18	3.7
65	1.194	1.83E-05	21.3	100.9	2.52	344.2	0.19	4.1

Table A.19: USP: Ambient Conditions of C19: L/D = 1, L/W = 1, Flat U/S

U_∞	ρ_∞	μ_∞	T_∞	p_∞	q_∞	a_∞	M_∞	Re_∞
m/s	kg/m^3	kg/ms	C°	kPa	kPa	m/s	-	10^6/m
10	1.171	1.85E-05	26.8	100.9	0.06	347.4	0.03	0.6
15	1.170	1.85E-05	27.1	100.9	0.13	347.6	0.04	0.9
20	1.170	1.85E-05	27.3	100.9	0.23	347.8	0.06	1.3
25	1.168	1.86E-05	27.7	100.9	0.37	347.9	0.07	1.6
30	1.168	1.86E-05	27.7	100.9	0.53	348.0	0.09	1.9
35	1.168	1.86E-05	27.8	100.9	0.72	348.0	0.10	2.2
40	1.167	1.86E-05	27.8	100.8	0.93	348.0	0.12	2.5
45	1.167	1.87E-05	29.9	101.5	1.18	349.2	0.13	2.8
50	1.167	1.87E-05	29.9	101.5	1.46	349.2	0.14	3.1
55	1.167	1.86E-05	28.0	100.9	1.76	348.2	0.16	3.4
60	1.166	1.86E-05	28.1	100.8	2.10	348.2	0.18	3.7
65	1.165	1.86E-05	28.4	100.9	2.46	348.4	0.19	4.1

Table A.20: USP: Ambient Conditions of C20: L/D = 1, L/W = 2, Flat U/S

U_∞	ρ_∞	μ_∞	T_∞	p_∞	q_∞	a_∞	M_∞	Re_∞
m/s	kg/m^3	kg/ms	C°	kPa	kPa	m/s	-	10^6/m
10	1.180	1.85E-05	26.9	101.6	0.059	347.5	0.03	0.6
15	1.180	1.85E-05	26.9	101.6	0.133	347.5	0.04	0.9
20	1.180	1.85E-05	26.9	101.6	0.236	347.5	0.06	1.3
25	1.180	1.85E-05	26.9	101.6	0.369	347.5	0.07	1.6
30	1.180	1.85E-05	27.0	101.7	0.531	347.6	0.09	1.9
35	1.179	1.85E-05	27.0	101.6	0.722	347.6	0.10	2.2
40	1.179	1.85E-05	27.1	101.6	0.943	347.6	0.12	2.5
45	1.179	1.85E-05	27.1	101.6	1.194	347.6	0.13	2.8
50	1.179	1.85E-05	27.1	101.6	1.474	347.6	0.14	3.1
55	1.179	1.85E-05	27.2	101.6	1.783	347.7	0.16	3.4
60	1.178	1.85E-05	27.3	101.6	2.120	347.7	0.18	3.7
65	1.177	1.85E-05	27.5	101.6	2.486	347.8	0.19	4.1

Table A.21: USP: Ambient Conditions of C21: L/D = 2, L/W = 2, Flat U/S

U_∞	ρ_∞	μ_∞	T_∞	p_∞	q_∞	a_∞	M_∞	Re_∞
m/s	kg/m^3	kg/ms	C°	kPa	kPa	m/s	-	10^6/m
10	1.166	1.86E-05	28.4	100.9	0.058	348.4	0.03	0.6
15	1.166	1.86E-05	28.4	100.9	0.131	348.4	0.04	0.9
20	1.166	1.86E-05	28.4	100.9	0.233	348.4	0.06	1.3
25	1.165	1.86E-05	28.5	100.9	0.364	348.4	0.07	1.6
30	1.165	1.86E-05	28.5	100.9	0.524	348.4	0.09	1.9
35	1.165	1.86E-05	28.5	100.9	0.714	348.4	0.10	2.2
40	1.165	1.86E-05	28.6	100.9	0.932	348.5	0.12	2.5

45	1.164	1.86E-05	28.7	100.9	1.179	348.6	0.13	2.8
50	1.163	1.86E-05	29.0	100.9	1.454	348.7	0.14	3.1
55	1.163	1.86E-05	29.1	100.9	1.759	348.8	0.16	3.4
60	1.162	1.86E-05	29.2	100.8	2.092	348.8	0.18	3.7
65	1.161	1.86E-05	29.4	100.8	2.453	348.9	0.19	4.1

Table A.22: USP: Ambient Conditions of C22: L/D = 2, L/W = 4, Flat U/S

U_∞	ρ_∞	μ_∞	T_∞	p_∞	q_∞	a_∞	M_∞	Re_∞
m/s	kg/m^3	kg/ms	C°	kPa	kPa	m/s	-	10^6/m
10	1.163	1.87E-05	31.1	101.6	0.058	349.9	0.03	0.6
15	1.163	1.87E-05	31.0	101.5	0.131	349.9	0.04	0.9
20	1.164	1.87E-05	30.9	101.6	0.233	349.8	0.06	1.3
25	1.164	1.87E-05	30.9	101.6	0.364	349.8	0.07	1.6
30	1.164	1.87E-05	30.8	101.6	0.524	349.8	0.09	1.9
35	1.165	1.87E-05	30.8	101.6	0.714	349.8	0.10	2.2
40	1.165	1.87E-05	30.8	101.6	0.932	349.8	0.12	2.5
45	1.165	1.87E-05	30.8	101.6	1.180	349.8	0.13	2.8
50	1.165	1.81E-05	30.8	101.6	1.456	349.8	0.14	3.1
55	1.165	1.87E-05	30.9	101.6	1.762	349.8	0.16	3.4
60	1.164	1.87E-05	30.9	101.6	2.095	349.8	0.18	3.7
65	1.164	1.87E-05	31.1	101.6	2.459	349.9	0.19	4.1

Table A.23: USP: Ambient Conditions of C23: L/D = 3, L/W = 3, Flat U/S

U_∞	ρ_∞	μ_∞	T_∞	p_∞	q_∞	a_∞	M_∞	Re_∞
m/s	kg/m^3	kg/ms	C°	kPa	kPa	m/s	-	10^6/m
10	1.187	1.85E-05	26.7	102.1	0.059	347.4	0.03	0.6
15	1.187	1.85E-05	26.7	102.1	0.134	347.4	0.04	0.9
20	1.187	1.85E-05	26.7	102.1	0.237	347.4	0.06	1.3
25	1.187	1.85E-05	26.7	102.2	0.371	347.4	0.07	1.6
30	1.187	1.85E-05	26.7	102.2	0.534	347.4	0.09	1.9
35	1.186	1.85E-05	26.8	102.1	0.727	347.4	0.10	2.2
40	1.186	1.85E-05	26.8	102.1	0.949	347.4	0.12	2.5
45	1.186	1.85E-05	26.8	102.2	1.201	347.5	0.13	2.8
50	1.186	1.85E-05	26.8	102.2	1.483	347.5	0.14	3.1
55	1.186	1.85E-05	26.9	102.2	1.794	347.5	0.16	3.4
60	1.186	1.85E-05	26.9	102.2	2.135	347.5	0.18	3.7
65	1.186	1.85E-05	26.9	102.1	2.505	347.5	0.19	4.1

Table A.24: USP: Ambient Conditions of C24: L/D = 3, L/W = 6, Flat U/S

U_∞	ρ_∞	μ_∞	T_∞	p_∞	q_∞	a_∞	M_∞	Re_∞
m/s	kg/m^3	kg/ms	C°	kPa	kPa	m/s	-	10^6/m
10	1.167	1.87E-05	29.7	101.5	0.058	349.1	0.03	0.6
15	1.167	1.86E-05	29.6	101.4	0.131	349.1	0.04	0.9
20	1.167	1.86E-05	29.6	101.4	0.233	349.1	0.06	1.3
25	1.167	1.87E-05	29.7	101.5	0.365	349.1	0.07	1.6
30	1.167	1.87E-05	29.7	101.5	0.525	349.1	0.09	1.9
35	1.167	1.87E-05	29.7	101.5	0.715	349.1	0.10	2.2
40	1.167	1.87E-05	29.7	101.5	0.934	349.1	0.12	2.5
45	1.167	1.87E-05	29.8	101.5	1.182	349.2	0.13	2.8
50	1.167	1.87E-05	29.8	101.5	1.459	349.2	0.14	3.1
55	1.166	1.87E-05	30.0	101.5	1.764	349.3	0.16	3.4
60	1.166	1.87E-05	30.1	101.5	2.098	349.3	0.18	3.7
65	1.165	1.87E-05	30.3	101.5	2.461	349.5	0.19	4.1

Table A.25: HWA: Ambient Conditions of C5, C11, C17, C23: Cavity Open

U/S	U_∞	ρ_∞	μ_∞	T_∞	p_∞	q_∞	a_∞	M_∞	Re_∞
-	m/s	kg/m^3	kg/ms	C°	kPa	kPa	m/s	-	10^6/m
Conic	10	1.158	1.86E-05	29.6	100.6	0.058	349.1	0.03	0.6
Conic	15	1.158	1.86E-05	29.6	100.6	0.130	349.1	0.04	0.9
Conic	20	1.157	1.85E-05	25.5	101.1	0.236	346.7	0.06	1.3
Conic	25	1.156	1.85E-05	27.4	101.1	0.366	347.8	0.07	1.6
Conic	30	1.156	1.86E-05	28.0	101.1	0.527	348.1	0.09	1.9
Conic	35	1.156	1.86E-05	27.7	101.0	0.717	348.0	0.10	2.2
Conic	40	1.156	1.87E-05	29.7	101.0	0.930	349.1	0.12	2.5
Conic	45	1.155	1.87E-05	31.4	101.0	1.169	350.1	0.13	2.8
Conic	50	1.147	1.88E-05	33.5	101.0	1.434	351.3	0.14	3.1
Ogive	10	1.177	1.85E-05	25.8	101.0	0.059	346.9	0.03	0.6
Ogive	15	1.176	1.85E-05	25.9	101.0	0.132	346.9	0.04	0.9
Ogive	20	1.174	1.85E-05	26.1	100.8	0.235	347.0	0.06	1.3
Ogive	25	1.171	1.85E-05	26.7	100.8	0.366	347.4	0.07	1.6
Ogive	30	1.169	1.85E-05	27.3	100.8	0.526	347.7	0.09	1.9
Ogive	35	1.163	1.86E-05	28.6	100.7	0.712	348.5	0.10	2.2
Ogive	40	1.155	1.88E-05	31.9	101.1	0.924	350.4	0.12	2.5
Ogive	45	1.162	1.86E-05	29.6	101.0	1.177	349.1	0.13	2.8
Ogive	50	1.155	1.88E-05	32.3	101.3	1.444	350.6	0.14	3.1
Parabola	10	1.204	1.84E-05	23.7	102.6	0.060	345.6	0.03	0.6
Parabola	15	1.203	1.84E-05	23.9	102.6	0.135	345.8	0.04	0.9
Parabola	20	1.202	1.84E-05	24.3	102.6	0.240	346.0	0.06	1.3
Parabola	25	1.200	1.84E-05	24.9	102.7	0.375	346.3	0.07	1.6
Parabola	30	1.197	1.85E-05	25.6	102.7	0.539	346.7	0.09	1.9

Parabola	35	1.193	1.85E-05	26.7	102.7	0.731	347.4	0.10	2.2
Parabola	40	1.188	1.86E-05	27.9	102.7	0.950	348.1	0.12	2.5
Parabola	45	1.181	1.87E-05	30.0	102.8	1.196	349.3	0.13	2.8
Parabola	50	1.212	1.83E-05	22.5	102.9	1.515	344.9	0.14	3.1
Flat	10	1.151	1.87E-05	30.6	100.4	0.058	349.6	0.03	0.6
Flat	15	1.152	1.87E-05	29.8	100.2	0.130	349.2	0.04	0.9
Flat	20	1.149	1.87E-05	30.5	100.2	0.230	349.6	0.06	1.3
Flat	25	1.146	1.87E-05	31.0	100.1	0.358	349.9	0.07	1.6
Flat	30	1.144	1.87E-05	31.6	100.1	0.515	350.2	0.09	1.9
Flat	35	1.140	1.88E-05	32.7	100.1	0.698	350.8	0.10	2.2
Flat	40	1.135	1.88E-05	33.7	100.0	0.908	351.4	0.12	2.5
Flat	45	1.131	1.89E-05	34.8	100.0	1.145	352.0	0.13	2.8
Flat	50	1.124	1.90E-05	36.5	99.9	1.405	353.0	0.14	3.1

Table A.26: HWA: Ambient Conditions of C25-28: Cavity Closed

U/S	U_∞	ρ_∞	μ_∞	T_∞	p_∞	q_∞	a_∞	M_∞	Re_∞
-	m/s	kg/m^3	kg/ms	C°	kPa	kPa	m/s	-	10^6/m
Conic	10	1.160	1.88E-05	31.8	101.5	0.058	350.3	0.03	0.6
Conic	15	1.163	1.87E-05	30.8	101.5	0.131	349.8	0.04	0.9
Conic	20	1.163	1.87E-05	30.7	101.4	0.233	349.7	0.06	1.3
Conic	25	1.162	1.87E-05	30.7	101.3	0.363	349.7	0.07	1.6
Conic	30	1.168	1.86E-05	27.6	100.8	0.526	347.9	0.09	1.9
Conic	35	1.159	1.87E-05	29.8	100.8	0.710	349.2	0.10	2.2
Conic	40	1.152	1.87E-05	31.5	100.7	0.922	350.2	0.12	2.5
Conic	45	1.144	1.88E-05	33.4	100.7	1.158	351.2	0.13	2.8
Conic	50	1.138	1.89E-05	34.8	100.6	1.423	352.0	0.14	3.1
Ogive	10	1.172	1.87E-05	30.0	102.0	0.059	349.3	0.03	0.6
Ogive	15	1.173	1.87E-05	29.8	102.0	0.132	349.2	0.04	0.9
Ogive	20	1.173	1.87E-05	29.7	102.0	0.235	349.1	0.06	1.3
Ogive	25	1.172	1.87E-05	29.9	102.0	0.366	349.2	0.07	1.6
Ogive	30	1.181	1.85E-05	26.8	101.7	0.531	347.4	0.09	1.9
Ogive	35	1.174	1.86E-05	28.6	101.7	0.719	348.5	0.10	2.2
Ogive	40	1.169	1.87E-05	29.9	101.7	0.935	349.2	0.12	2.5
Ogive	45	1.163	1.87E-05	31.4	101.7	1.178	350.1	0.13	2.8
Ogive	50	1.156	1.88E-05	33.0	101.6	1.445	351.0	0.14	3.1
Parabola	10	1.204	1.84E-05	23.7	102.6	0.060	345.6	0.03	0.6
Parabola	15	1.203	1.84E-05	23.9	102.6	0.135	345.8	0.04	0.9
Parabola	20	1.202	1.84E-05	24.3	102.6	0.240	346.0	0.06	1.3
Parabola	25	1.200	1.84E-05	24.9	102.7	0.375	346.3	0.07	1.6
Parabola	30	1.197	1.85E-05	25.6	102.7	0.539	346.7	0.09	1.9
Parabola	35	1.193	1.85E-05	26.7	102.7	0.731	347.4	0.10	2.2

Parabola	40	1.188	1.86E-05	27.9	102.7	0.950	348.1	0.12	2.5
Parabola	45	1.181	1.87E-05	30.0	102.8	1.196	349.3	0.13	2.8
Parabola	50	1.212	1.83E-05	22.5	102.9	1.515	344.9	0.14	3.1
Flat	10	1.158	1.86E-05	29.6	100.6	0.058	349.1	0.03	0.6
Flat	15	1.154	1.87E-05	30.5	100.6	0.130	349.6	0.04	0.9
Flat	20	1.153	1.87E-05	30.9	100.6	0.231	349.8	0.06	1.3
Flat	25	1.152	1.87E-05	31.2	100.6	0.360	350.0	0.07	1.6
Flat	30	1.148	1.88E-05	32.1	100.6	0.517	350.5	0.09	1.9
Flat	35	1.130	1.90E-05	32.7	100.6	0.692	353.3	0.10	2.2
Flat	40	1.146	1.88E-05	32.8	100.6	0.917	350.9	0.12	2.5
Flat	45	1.128	1.90E-05	37.5	100.6	1.142	353.6	0.13	2.8
Flat	50	1.130	1.89E-05	34.3	99.7	1.413	351.8	0.14	3.1

Table A.27: HWA: Ambient Conditions of Empty WT Streamwise Traverse

x	U_∞	ρ_∞	μ_∞	T_∞	p_∞	q_∞	a_∞	M_∞	Re_∞
m	m/s	kg/m^3	kg/ms	C°	kPa	kPa	m/s	-	10^6/m
0.02	10	1.217	1.82E-05	20.3	102.5	0.06	343.7	0.03	0.6
0.02	15	1.216	1.82E-05	20.4	102.5	0.14	343.7	0.04	0.9
0.02	20	1.214	1.82E-05	20.8	102.4	0.24	344.0	0.06	1.3
0.02	25	1.212	1.83E-05	21.3	102.4	0.38	344.2	0.07	1.6
0.02	30	1.209	1.83E-05	22.0	102.4	0.54	344.7	0.09	1.9
0.02	40	1.202	1.84E-05	23.7	102.4	0.96	345.6	0.12	2.5
0.02	50	1.190	1.85E-05	26.7	102.4	1.49	347.4	0.14	3.1
0.07	10	1.209	1.82E-05	19.9	101.7	0.06	343.4	0.03	0.6
0.07	15	1.207	1.82E-05	20.1	101.6	0.14	343.5	0.04	0.9
0.07	20	1.205	1.82E-05	20.4	101.5	0.24	343.7	0.06	1.3
0.07	25	1.202	1.82E-05	21.0	101.5	0.38	344.1	0.07	1.6
0.07	30	1.198	1.83E-05	21.8	101.4	0.54	344.5	0.09	1.9
0.07	40	1.183	1.85E-05	25.8	101.5	0.95	346.9	0.12	2.5
0.07	50	1.176	1.86E-05	27.6	101.5	1.47	347.9	0.14	3.1
0.12	10	1.217	1.82E-05	19.2	102.1	0.06	343.0	0.03	0.6
0.12	15	1.217	1.82E-05	19.4	102.2	0.14	343.1	0.04	0.9
0.12	20	1.215	1.82E-05	19.7	102.1	0.24	343.3	0.06	1.3
0.12	25	1.213	1.82E-05	20.3	102.2	0.38	343.7	0.07	1.6
0.12	30	1.208	1.82E-05	21.1	102.0	0.54	344.1	0.09	1.9
0.12	40	1.197	1.84E-05	23.4	101.9	0.96	345.5	0.12	2.5
0.12	50	1.183	1.85E-05	26.6	101.8	1.48	347.3	0.14	3.1
0.17	10	1.208	1.82E-05	19.7	101.6	0.06	343.3	0.03	0.6
0.17	15	1.205	1.82E-05	20.2	101.5	0.14	343.6	0.04	0.9
0.17	20	1.203	1.82E-05	20.5	101.4	0.24	343.8	0.06	1.3
0.17	25	1.198	1.83E-05	21.5	101.3	0.37	344.4	0.07	1.6

0.17	30	1.193	1.83E-05	22.6	101.3	0.54	345.0	0.09	1.9
0.17	40	1.186	1.84E-05	24.3	101.3	0.95	346.0	0.12	2.5
0.17	50	1.180	1.84E-05	24.2	100.7	1.48	345.9	0.14	3.1
0.22	10	1.178	1.85E-05	26.4	101.3	0.06	347.2	0.03	0.6
0.22	15	1.176	1.86E-05	27.6	101.5	0.13	347.9	0.04	0.9
0.22	20	1.192	1.83E-05	23.1	101.4	0.24	345.3	0.06	1.3
0.22	25	1.192	1.83E-05	23.1	101.4	0.37	345.3	0.07	1.6
0.22	30	1.218	1.81E-05	18.4	101.9	0.55	342.5	0.09	1.9
0.22	40	1.218	1.81E-05	18.1	101.8	0.97	342.4	0.12	2.5
0.22	50	1.203	1.83E-05	21.7	101.8	1.50	344.5	0.14	3.1
0.27	10	1.187	1.85E-05	25.6	101.8	0.06	346.8	0.03	0.6
0.27	15	1.195	1.84E-05	23.6	101.8	0.13	345.6	0.04	0.9
0.27	20	1.198	1.83E-05	22.9	101.8	0.24	345.2	0.06	1.3
0.27	25	1.199	1.83E-05	22.8	101.9	0.37	345.1	0.07	1.6
0.27	30	1.199	1.83E-05	22.9	101.9	0.54	345.2	0.09	1.9
0.27	40	1.198	1.83E-05	23.3	101.9	0.96	345.4	0.12	2.7
0.27	50	1.192	1.84E-05	24.8	102.0	1.49	346.3	0.14	3.1
0.33	10	1.219	1.81E-05	18.7	102.1	0.06	342.7	0.03	0.6
0.33	15	1.218	1.81E-05	19.0	102.1	0.14	342.9	0.04	0.9
0.33	20	1.216	1.82E-05	19.3	102.1	0.24	343.1	0.06	1.3
0.33	25	1.212	1.82E-05	19.9	102.0	0.38	343.4	0.07	1.6
0.33	30	1.208	1.82E-05	20.5	101.8	0.54	343.8	0.09	1.9
0.33	40	1.202	1.83E-05	21.7	101.7	0.96	344.5	0.12	2.5
0.33	50	1.184	1.85E-05	26.2	101.7	1.48	347.1	0.14	3.1
0.39	10	1.211	1.82E-05	20.8	102.2	0.06	344.0	0.03	0.6
0.39	15	1.210	1.82E-05	20.9	102.1	0.14	344.0	0.04	0.9
0.39	20	1.208	1.82E-05	21.1	102.0	0.24	344.1	0.06	1.3
0.39	25	1.205	1.83E-05	21.7	102.0	0.38	344.5	0.07	1.6
0.39	30	1.201	1.83E-05	22.5	101.9	0.54	344.9	0.09	1.9
0.39	40	1.197	1.84E-05	23.5	101.9	0.96	345.5	0.12	2.5
0.39	50	1.183	1.85E-05	26.9	101.9	1.48	347.5	0.14	3.1
0.54	10	1.174	1.86E-05	29.1	101.9	0.06	348.8	0.03	0.6
0.54	15	1.184	1.85E-05	26.5	101.8	0.13	347.3	0.04	0.9
0.54	20	1.188	1.85E-05	25.8	102.0	0.24	346.9	0.06	1.3
0.54	25	1.188	1.85E-05	25.5	101.8	0.37	346.7	0.07	1.6
0.54	30	1.226	1.81E-05	18.2	102.5	0.55	342.4	0.09	1.9
0.54	40	1.219	1.82E-05	19.8	102.5	0.98	343.4	0.12	2.5
0.54	50	1.209	1.83E-05	21.9	102.4	1.51	344.6	0.14	3.1

A.2 Empty Wind Tunnel Boundary Layer Data

Hot-wire anemometry (HWA) was performed in the empty wind tunnel (WT) test section (TS), to map flow quality, and boundary layer (BL) profile growth, and development. Logarithmic velocity profiles, with 50 points over y = 0-450mm, were measured at nine streamwise x (m) locations, from the 2nd TS plate LE ($x = 0$) to cavity LE ($x = 0.54$m). The WT has two 4ft long TS's per Fig. 3.2, the 2nd TS was used, as it provides an established BL. Data was acquired per Section 3.3, post-processed per Section 4.2 and 4.3, using the algorithm in Appendix F.2.3.

BL thickness is defined per $\delta \sim u/U_\infty \approx 0.99$, with displacement thickness δ^*, momentum thickness θ, and turbulent intensity (TI) calculated per Eqn. 4.25, 4.26 and 4.6 respectively, with results presented in Table A.28-A.31. Fig. A.1 is δ^*, θ in x (m), against Blasius's laminar flat-plate BL model[21], and the flat-plate 1/7th turbulent power law[99]. Fig. A.2 and A.3 present effects of x (m), and Fig. A.4 and A.5 present effects of U_∞. Overall, BL behaviour follows theory, where increasing U_∞ reduces δ and TI, and increasing x increases δ and TI.

Table A.28: HWA: Boundary Layer Disturbance Thickness δ (mm)

x	U_∞ (m/s)								
(m)	10	15	20	25	30	35	40	45	50
0.02	37.0	36.6	35.7	35.6	34.9	34.4	34.2	33.4	31.7
0.07	37.4	36.9	36.3	36.3	35.2	34.9	34.5	33.4	31.9
0.12	39.9	37.4	37.0	36.7	35.8	35.0	35.0	33.8	33.0
0.17	40.4	39.4	38.1	36.8	36.0	-	35.0	-	33.3
0.22	41.7	42.1	40.5	39.7	36.3	-	35.2	-	33.4
0.27	42.3	42.2	40.8	39.9	37.3	-	35.6	-	33.8
0.33	42.3	42.5	40.9	39.9	37.3	-	36.1	-	34.0
0.39	43.7	42.3	41.3	40.6	39.8	-	36.9	-	34.9
0.54	48.8	45.7	43.7	42.8	40.7	-	39.8	-	36.0

Table A.29: HWA: Boundary Layer Displacement Thickness δ^* (mm)

x	U_∞ (m/s)								
(m)	10	15	20	25	30	35	40	45	50
0.02	6.2	5.8	5.7	5.6	5.5	5.3	4.9	4.9	4.0
0.07	6.3	6.0	6.0	5.9	5.7	5.4	5.0	5.0	4.1
0.12	6.5	6.3	6.1	6.0	5.7	5.6	5.2	5.0	4.3
0.17	6.6	6.3	6.2	6.2	5.8	-	5.2	-	4.3
0.22	6.8	6.6	6.5	6.2	5.9	-	5.2	-	4.4
0.27	6.9	6.7	6.6	6.3	5.9	-	5.4	-	4.5
0.33	7.3	6.9	6.7	6.3	5.9	-	5.4	-	4.6
0.39	7.7	7.1	6.7	6.4	6.0	-	5.5	-	4.9
0.54	7.9	7.5	7.1	6.9	6.2	-	5.6	-	5.0

Table A.30: HWA: Boundary Layer Momentum Thickness θ (mm)

Streamwise	U_∞ (m/s)								
x (m)	10	15	20	25	30	35	40	45	50
0.02	4.7	4.4	4.4	4.2	4.2	3.9	3.6	3.6	2.8
0.07	4.8	4.6	4.5	4.4	4.2	4.0	3.7	3.6	2.9
0.12	4.9	4.7	4.6	4.5	4.3	4.2	3.8	3.7	3.1
0.17	4.9	4.7	4.6	4.6	4.3	-	3.9	-	3.1
0.22	5.1	5.0	4.9	4.7	4.3	-	3.9	-	3.2
0.27	5.2	5.0	4.9	4.7	4.4	-	4.0	-	3.2
0.33	5.5	5.2	5.0	4.7	4.4	-	4.0	-	3.3
0.39	5.9	5.4	5.0	4.8	4.5	-	4.1	-	3.5
0.54	6.0	5.7	5.4	5.2	4.6	-	4.2	-	3.7

Table A.31: HWA: Free-Stream Turbulence Intensity (%)

x	U_∞ (m/s)								
(m)	10	15	20	25	30	35	40	45	50
0.02	0.11	0.10	0.10	0.11	0.13	0.16	0.11	0.12	0.22
0.07	0.11	0.10	0.11	0.11	0.13	0.18	0.11	0.12	0.22
0.12	0.11	0.11	0.11	0.12	0.13	0.18	0.12	0.12	0.24
0.17	0.11	0.11	0.11	0.12	0.13	-	0.12	-	0.24
0.22	0.12	0.12	0.11	0.12	0.14	-	0.14	-	0.24
0.27	0.12	0.12	0.11	0.12	0.14	-	0.14	-	0.25
0.33	0.12	0.13	0.12	0.13	0.14	-	0.14	-	0.26
0.39	0.12	0.13	0.12	0.13	0.14	-	0.18	-	0.27
0.54	0.14	0.14	0.12	0.13	0.15	-	0.18	-	0.29

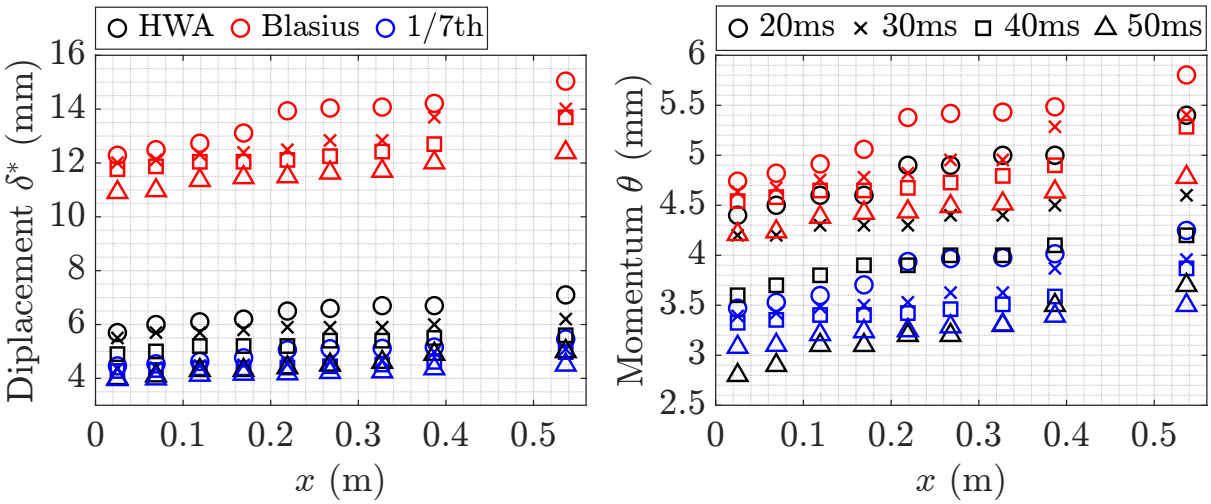

Figure A.1: HWA: Empty WT Flat-Plate Boundary Layer Thicknesses

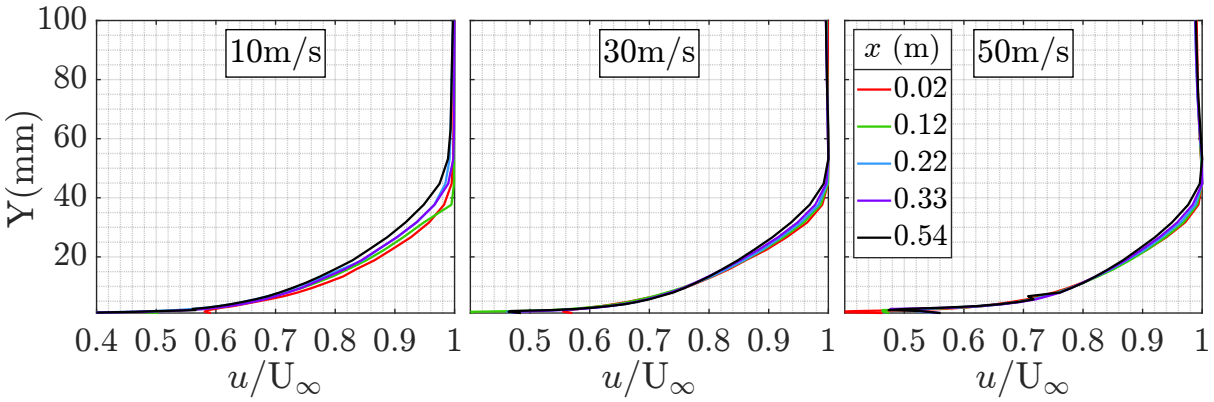

Figure A.2: HWA: BL U_M for ΔX at each Airspeed (airflow moves left to right)

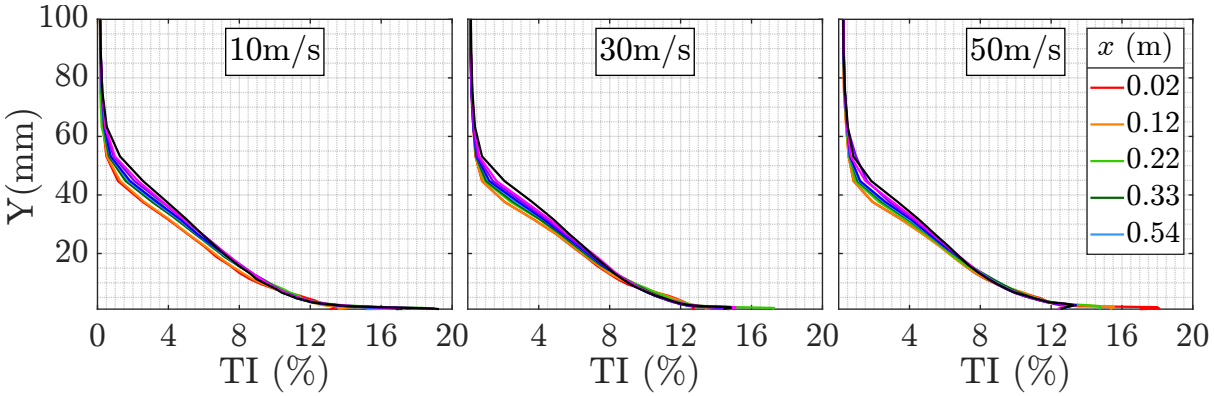

Figure A.3: HWA: BL TI for ΔX at each Airspeed (airflow moves left to right)

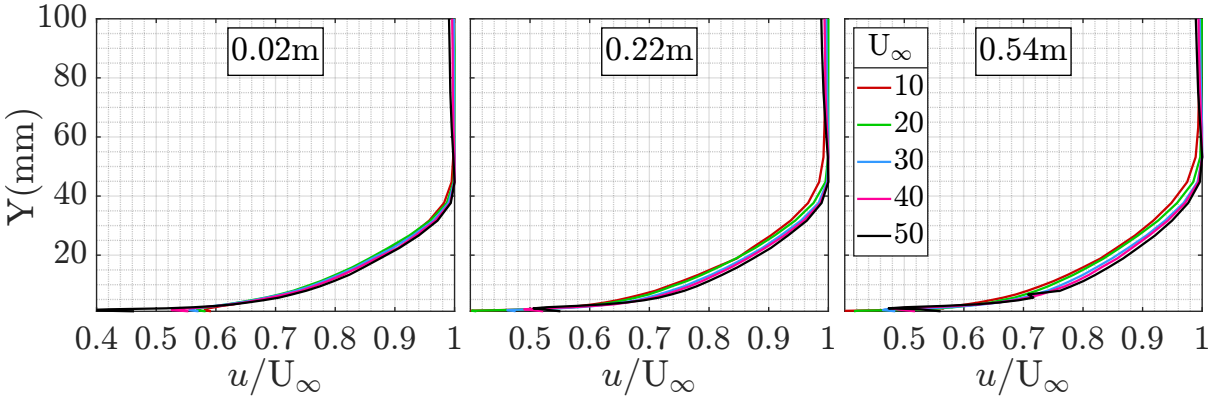

Figure A.4: HWA: BL U_M for ΔU_∞ at each Stream-wise Location (airflow moves left to right)

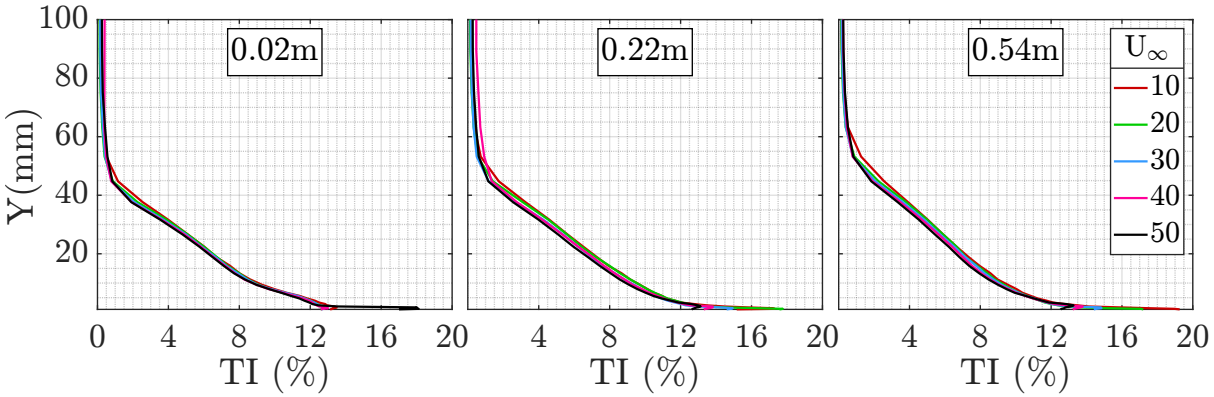

Figure A.5: HWA: BL TI for ΔU_∞ at each Stream-wise Location (airflow moves left to right)

Appendix B

Boundary Layer Theory

The boundary layer (BL) is a viscous layer, in fluid travelling across a surface, between the bulk moving fluid, and surface, per Fig. B.1. It accounts for fluid viscosity μ, as a factor of skin friction c_f, to satisfy velocity transition, from the limiting finite value solution close to the wall, to zero at the wall (no-slip condition [88,99]), relating change in fluid momentum due to viscosity. There are three primary BL metrics, as a function of inertial and viscous forces; disturbance δ, displacement δ^* and momentum θ thickness per Fig. B.2.

Disturbance thickness δ, accounts physical viscous forces induced on the fluid from the surface, due to adjacent fluid motion, proportional to viscosity μ_∞ as a function of momentum. δ is located in y, where inertial and viscous force per unit volume become equivalent; $\rho u(\partial u/\partial x) = \partial\tau/\partial y$, thus $\delta = y$ when $u = 0.99 \cdot \mathrm{U}_\infty$: u = local velocity at y in the velocity profile.

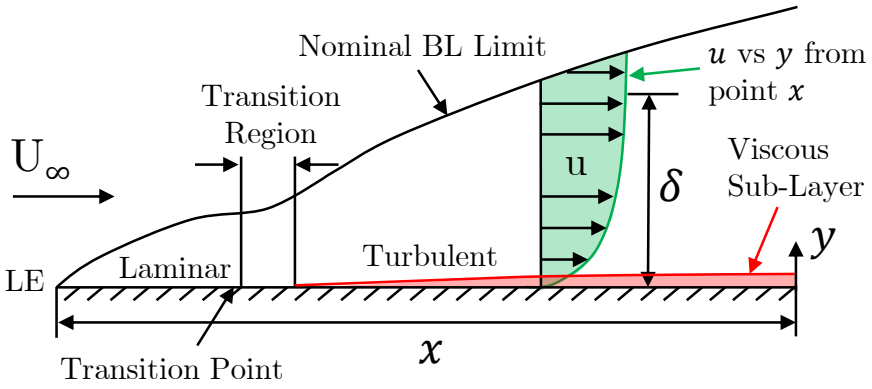

Figure B.1: Boundary Layer Schematic

Displacement thickness δ^* is the mass flux deficit. A measure of displaced inviscid external flow outward, due to viscous effects on fluid against the surface, causing a drop in local velocity. Effectively, the distance external fluid moves, as a reduction of volume flux, due to viscosity. It is equivalent to mass flux loss, compared to the uniform FS flow.

Momentum thickness θ is the momentum flux deficit. The distance a surface would move parallel to itself, towards the reference plane of the inviscid uniform flow U_∞, to establish the same momentum. It exists between the wall, and reference plane in a fluid. BL theory was formulated by Prandtl [88] from continuity and momentum NS equations, further detailed below.

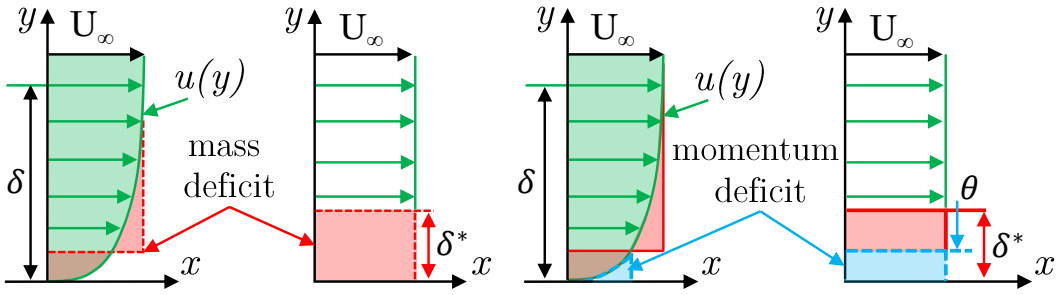

Figure B.2: Boundary Layer Thicknesses: Disturbance δ, Displacement δ^*, Momentum θ

B.1 Boundary Layer Equations of Motion

This thesis observes incompressible flow; $M_\infty < 0.3$ [149]. Appropriate Navier-Stokes (NS) equations of motion (EOM) to conserve mass and momentum are given in differential form by Eqn. B.1-B.4, from the infinitesimal control volume approach, along a streamline of velocity $\vec{V}(u, v, w)$, for flow velocity at each point [148], with Laplacian operator; $\nabla \equiv \partial/\partial x + \partial/\partial y + \partial/\partial z$.

Continuity Equation:

$$\frac{\partial u}{\partial x} + \frac{\partial v}{\partial y} + \frac{\partial w}{\partial z} = 0 \tag{B.1}$$

Momentum Equation:

$$x: \quad -\frac{\partial p}{\partial x} + \rho\nu\nabla^2 + \rho f_x = -\frac{\partial p}{\partial x} + \left(\frac{\partial \sigma_{xx}}{\partial x} + \frac{\partial \sigma_{xy}}{\partial y} + \frac{\partial \sigma_{xz}}{\partial z}\right) + \rho f_x \tag{B.2}$$

$$y: \quad -\frac{\partial p}{\partial y} + \rho\nu\nabla^2 + \rho f_y = -\frac{\partial p}{\partial y} + \left(\frac{\partial \sigma_{yx}}{\partial x} + \frac{\partial \sigma_{yy}}{\partial y} + \frac{\partial \sigma_{yz}}{\partial z}\right) + \rho f_y \tag{B.3}$$

$$z: \quad -\frac{\partial p}{\partial z} + \rho\nu\nabla^2 + \rho f_z = -\frac{\partial p}{\partial z} + \left(\frac{\partial \sigma_{zx}}{\partial x} + \frac{\partial \sigma_{zy}}{\partial y} + \frac{\partial \sigma_{zz}}{\partial z}\right) + \rho f_z \tag{B.4}$$

$$\sigma_{xy} = \sigma_{yx} = \mu\left(\frac{\partial u}{\partial y} + \frac{\partial v}{\partial x}\right) \qquad \sigma_{xz} = \sigma_{zx} = \mu\left(\frac{\partial u}{\partial z} + \frac{\partial w}{\partial x}\right) \qquad \sigma_{yz} = \sigma_{zy} = \mu\left(\frac{\partial w}{\partial y} + \frac{\partial v}{\partial z}\right)$$

$$\sigma_{xx} = 2\mu\frac{\partial u}{\partial x} \qquad \sigma_{yy} = 2\mu\frac{\partial v}{\partial y} \qquad \sigma_{zz} = 2\mu\frac{\partial w}{\partial z}$$

B.1.1 Laminar Flow

Flow is laminar for small δ/L, where terms smaller than governing terms by factor δ/L, are neglected. Order of magnitude analysis, also assumes gradients of u streamwise in x, are larger than other gradients in x, thus neglected. BL EOM for 2D laminar flat-plate flow, thus become a simplified version of 2D NS EOM derived by Prandtl [88] for Eqn. B.5 and B.6 where; $u \sim U_\infty$, $p \sim \rho U_\infty^2$, $x \sim L$, $y \sim \delta$ and $v \sim U_\infty \delta/L$, since $\partial u/\partial x$ is of order U_∞/L.

$$\text{Continuity}: \quad \frac{\partial u}{\partial x} + \frac{\partial v}{\partial y} = 0 \tag{B.5}$$

$$\text{Momentum}: \quad x: \; u\frac{\partial u}{\partial x} + v\frac{\partial u}{\partial y} = -\frac{1}{\rho}\frac{dp}{dx} + \nu\left(\frac{\partial^2 u}{\partial y^2}\right) \qquad y: \; \frac{\partial p}{\partial y} = 0 \tag{B.6}$$

B.1.2 Turbulent Flow

For turbulence, mean flow order of magnitude estimate; $u \sim \mathrm{U}_\infty$, $p \sim \rho \mathrm{U}_\infty^2$, $x \sim \mathrm{L}$, $y \sim \delta$ and $v \sim \mathrm{U}_\infty \delta/\mathrm{L}$, since $\partial u/\partial x$ is of order $\mathrm{U}_\infty/\mathrm{L}$ from 2D continuity, also include fluctuating terms $\overline{u'^2}$, $\overline{u'v'}$ in x, and $\overline{v'^2}$, $\overline{v'u'}$ in y. Pressure variation across the BL in y, is small compared to streamwise values, thus neglected. Giving turbulent BL EOM; continuity in Eqn. B.7 and momentum in Eqn. B.8, with Reynolds shear stress $-\rho\overline{u'v'}$. Note: viscous terms are reduced in x, by neglecting variation of p in y, as p is known, and absorbed into boundary conditions (BCs) via dp/dx as the free-stream (FS) value, where Bernoulli applies; $dp/dx = -\rho \mathrm{U}_\infty (d\mathrm{U}_\infty/dx)$.

$$\text{Continuity :} \qquad \frac{\partial u}{\partial x} + \frac{\partial v}{\partial y} = 0 \tag{B.7}$$

$$\text{Momentum :} \qquad \text{x :}\ u\frac{\partial u}{\partial x} + v\frac{\partial u}{\partial y} = \mathrm{U}_\infty \frac{d\mathrm{U}_\infty}{dx} + \nu\frac{\partial^2 u}{\partial y^2} - \frac{\partial(\overline{u'v'})}{\partial y} \qquad \text{y :}\ \frac{\partial p}{\partial y} = 0 \tag{B.8}$$

B.1.3 Momentum Integral Equations

Integrating momentum and continuity across the BL from $y = 0 \to \delta$, determines BL; displacement δ^*, momentum θ, shear stress $\tau = \mu(\partial u/\partial y) - \rho\overline{u'v'}$, and pressure gradient; $-\rho^{-1}(dp/dx) = \mathrm{U}_\infty(d\mathrm{U}_\infty/dx)$. These reduce NS EOM by adding u times continuity to x-momentum, and integrating in y where $\mathrm{V}_\infty = -\int_0^\delta \partial u/\partial x \cdot dy$ per Eqn. B.9. Then integrating for δ^* and θ in Eqn. B.10. The 2D incompressible momentum integral equation is Eqn. B.11, where skin friction is $c_f = 2\tau_w/\rho \mathrm{U}_\infty^2$, and wall shear stress $\tau_w = \mu(du/dy)$.

$$\text{Continuity :} \quad \frac{\partial u}{\partial x} + \frac{\partial v}{\partial y} = 0 \qquad x\text{−Momentum :} \quad u\frac{\partial u}{\partial x} + v\frac{\partial u}{\partial y} = \mathrm{U}_\infty \frac{d\mathrm{U}_\infty}{dx} + \frac{1}{\rho}\frac{\partial \tau}{\partial y}$$

$$\frac{\partial u^2}{\partial x} + v\frac{\partial uv}{\partial y} = \mathrm{U}_\infty \frac{d\mathrm{U}_\infty}{dx} + \frac{1}{\rho}\frac{\partial \tau}{\partial y} \;\rightarrow\; \int_0^\delta \frac{\partial u^2}{\partial x} dy + \mathrm{U}_\infty \mathrm{V}_\infty = \int_0^\delta \mathrm{U}_\infty \frac{d\mathrm{U}_\infty}{dx} dy - \frac{\tau_w}{\rho} \tag{B.9}$$

$$\int_0^\delta \left(\frac{\partial u^2}{\partial x} - \mathrm{U}_\infty \frac{\partial u}{\partial x} - \mathrm{U}_\infty \frac{\partial \mathrm{U}_\infty}{\partial x} \right) dy \;\rightarrow\; \int_0^\infty \left\{ -\frac{\partial}{\partial x}\left[u(\mathrm{U}_\infty - u)\right] - \frac{d\mathrm{U}_\infty}{dx}(\mathrm{U}_\infty - u) \right\} dy = -\frac{\tau_w}{\rho}$$

$$\frac{d}{dx}\left[\mathrm{U}_\infty^2 \int_0^\delta \frac{u(\mathrm{U}_\infty - u)}{\mathrm{U}_\infty^2} dy \right] + \mathrm{U}_\infty \frac{d\mathrm{U}_\infty}{dx} \int_0^\delta \frac{\mathrm{U}_\infty - u}{\mathrm{U}_\infty} dy = \frac{\tau_w}{\rho}$$

$$\delta^* = \int_0^\delta \left(1 - \frac{u}{\mathrm{U}_\infty}\right) dy \qquad \theta = \int_0^\delta \frac{u}{\mathrm{U}_\infty}\left(1 - \frac{u}{\mathrm{U}_\infty}\right) dy \tag{B.10}$$

$$\frac{d}{dx}(\mathrm{U}_\infty^2 \theta) + \delta^* \mathrm{U}_\infty \frac{d\mathrm{U}_\infty}{dx} = \frac{\tau_w}{\rho} \qquad \rightarrow \qquad \frac{d\theta}{dx} + \left(\frac{\delta^*}{\theta} + 2\right)\frac{\theta}{\mathrm{U}_\infty}\frac{d\mathrm{U}_\infty}{dx} = \frac{c_f}{2} = \frac{\tau_w}{\rho \mathrm{U}_\infty^2} \tag{B.11}$$

B.2 Boundary Layer Similar Solutions

Similar solutions, coalesce multi-dimensional coordinates, into non-dimensional similarity variables, enabling transformation of complex PDEs into a single solution driven ODE. The concept is executed for a BL, from Prandtl's[88] 2D BL EOM. Blasius[21], and Hiemenz[150], obtained flat-plate, and stagnation flow similarity respectively, followed by Falkner & Skan[22] for wedge

flow angles $\beta\pi$. Hartree[151], Goldstein[23] and Mangler[152] assessed the concept for modelling, and Katz & Plotkin[153], and Cebeci & Cousteix[148] detail solutions.

Similarity is derived from 2D incompressible BL EOM; x, y-momentum and continuity in Eqn. B.12-B.15, with BCs; $u(x,0) = v(x,0) = 0$ and $u(x,\infty) = \mathrm{U}_\infty$. Continuity is integrated with stream function ψ, per $u = \partial\psi/\partial y$ and $v = \partial\psi/\partial x$, to form potential momentum Eqn. B.14. Coordinates are then transformed from x, y to similar η and ξ, to reduce BL EOM from a series PDE, to single ODE, for the similar solution in Eqn. B.16[99], dependent on functions $f(\eta)$. Dash denote derivatives of $f(\eta)$, and $\alpha_1, \alpha_2, \alpha_3$ are constants dependent on flow geometry.

$$u\frac{\partial u}{\partial x} + v\frac{\partial v}{\partial y} = \mathrm{U}_\infty\frac{d\mathrm{U}_\infty}{dx} + v\frac{\partial^2 u}{\partial y^2} \qquad \text{(B.12)} \qquad 0 = \frac{\partial p}{dy} \qquad \text{(B.13)}$$

$$\frac{\partial\psi}{\partial y}\frac{\partial^2\psi}{\partial x\partial y} - \frac{\partial\psi}{\partial x}\frac{\partial^2\psi}{\partial y^2} = \mathrm{U}_\infty\frac{d\mathrm{U}_\infty}{dx} + \nu\frac{\partial^3\psi}{\partial y^3} \qquad \text{(B.14)} \qquad \frac{\partial u}{\partial x} + \frac{\partial v}{\partial y} = 0 \qquad \text{(B.15)}$$

$$f''' + \alpha_1 f f'' + \alpha_2 - \alpha_3 f'^2 = 0 \qquad \text{(B.16)}$$

B.2.1 Boundary Layer Flow over a Flat-Plate

Blasius[21] obtained the similar solution for flat-plate BL flow, and the shape of its dimensionless velocity profile; $u/\mathrm{U}_\infty = f(y/\delta)$ or $u/\mathrm{U}_\mathrm{e} = f(x,y)$; U_e is BL edge velocity. Similarity is achieved with variable η in Eqn. B.17, representing coordinate transformation from x, y, to a single variable. Thus, reducing BL EOM from two PDEs, to one solution driven ODE. Stream function ψ given by Eqn. B.18, is then used to derive u, v in Eqn. B.19 and B.20, which substitute into momentum Eqn. B.12, for the Blasius[21] flat-plate BL similar solution; $f''' + ff'' = 0$, thus $\alpha_1 = 1, \alpha_2 = \alpha_3 = 0$. The non-dimensional BL velocity profile is then represented by $f'(\eta)$, and used to determine BL thickness δ, when $u/\mathrm{U}_\mathrm{e} = f'(\eta) \approx 1$.

$$\eta = y\sqrt{\mathrm{U}_\mathrm{e}/2\nu x} \qquad \text{(B.17)} \qquad \psi = f(\eta)\sqrt{2\nu x\mathrm{U}_\mathrm{e}} \qquad \text{(B.18)}$$

$$u = \frac{\partial\psi}{\partial y} = \mathrm{U}_\mathrm{e}f'(\eta) \qquad \text{(B.19)} \qquad v = -\frac{\partial\psi}{\partial x} = \sqrt{\frac{\mathrm{U}_\mathrm{e}\nu}{2x}}\left[\eta f'(\eta) - f(\eta)\right] \qquad \text{(B.20)}$$

B.2.2 Boundary Layer Flow over a Wedge

For BL flow over the conic nose in Fig. B.3, the flat-plate solution no longer holds. Due to presence of a favourable pressure gradient, accelerating flow up the incline $u > \mathrm{U}_\infty$, increasing near wall velocity, thus U_e relative to U_∞. Therefore, δ is no longer at $u/\mathrm{U}_\infty \approx 0.99$, as $\mathrm{U}_\mathrm{e} \neq \mathrm{U}_\infty$ and $\alpha_2, \alpha_3 \neq 0$. The Falkner-Skan[22] similar solution is thus implicated. To resolve BL flow over a wedge, or angled surface, in x, y coordinates, with velocity components u, v, and corresponding more complex PDEs. Falkner-Skan[22] achieves similarity, by adjusting the flat-plate solution for pressure gradient β, dependent on angle $\beta\pi$ per Fig. B.3, and transformation of x, y to similar variable $\xi = x/l$ and η in Eqn. B.21.

To model inviscid flow external to the BL on the wedge surface, a tangential power-law velocity distribution is assumed using potential flow in Eqn. B.22, with the pressure gradient in Eqn. B.23. $m_\beta = \beta/(2-\beta)$ is the Falkner-Skan power-law parameter, with similar pressure gradient

β. C is an integration constant based on ICs. x is along the wedge, y is normal to, and l is wedge length, per Fig. B.3. Stream function ψ is then given by Eqn. B.25, to derive velocity components u, v in Eqn. B.26 and B.27, which substitute into similar potential momentum Eqn. B.12, to give the Falkner-Skan solution in Eqn. B.24. Wall shear stress $\tau_w = \mu(du/dy)$ is derived using similar variables in Eqn. B.28. And per Eqn. B.26, $f'(\eta)$ is the similar velocity profile, where $\delta \propto \eta$, when $f'(\eta) = u/\mathrm{U_e} \approx 0.99$. Therefore, $f'(\eta)$ is required to resolve BL δ.

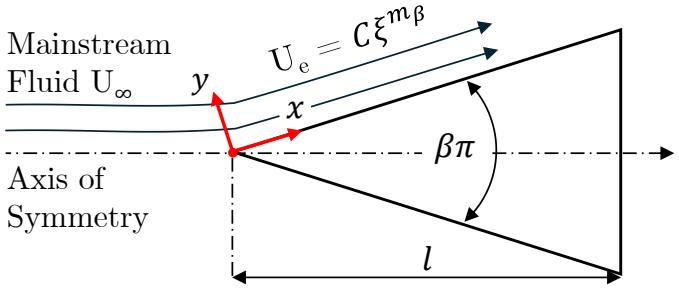

Figure B.3: Wedge Boundary Layer Flow

$$\eta = y\sqrt{\frac{\mathrm{U_e}(1+m_\beta)}{2\nu x}} \quad \text{(B.21)} \qquad \mathrm{U_e} = C\xi^{m_\beta} \quad \text{(B.22)}$$

$$\frac{\partial p}{\partial x} = -\rho \mathrm{U_e}\frac{d\mathrm{U_e}}{d\xi} = -\rho m_\beta C^2 \xi^{2m_\beta - 1} \quad \text{(B.23)} \qquad f''' + ff'' + \beta(1 - f'^2) = 0 \quad \text{(B.24)}$$

$$\psi = f\sqrt{\frac{2\mathrm{U_e}\nu x}{(1+m_\beta)}} \quad \text{(B.25)} \qquad u = \frac{\partial \psi}{\partial y} = \mathrm{U_e} f' \quad \text{(B.26)}$$

$$v = -\frac{\partial \psi}{\partial x} = \sqrt{\frac{\mathrm{U_e}\nu(1+m_\beta)}{2x}}\left[\eta f' \frac{m_\beta - 1}{m_\beta + 1} - f\right] \quad \text{(B.27)} \qquad \tau_w = \mu\sqrt{\frac{\mathrm{U_e}^3(m_\beta+1)}{2\nu x}} f''(0) \quad \text{(B.28)}$$

Falkner-Skan is a numerical 3$^{\mathrm{rd}}$ order, nonlinear boundary value (BVP) problem with BCs;

(1) No slip condition at the wall $y = 0 : u = v = 0 \rightarrow \eta = 0 : f(0) = f'(0) = 0$

(2) Flow outside the BL is tangential toward infinity: $y \rightarrow \infty : u/\mathrm{U_e} = 1 \rightarrow \eta \rightarrow \infty : f'(\infty) = 1$.

The equation has no analytical or closed-form solution [104]. Therefore, a numerical method is required, to approximate the solution. Most popular is the shooting technique [105], using Newton's method [106] to approximate the target, within a 4$^{\mathrm{th}}$ order Runge Kutta scheme, to perform iterative convergence with numerical integration. For the Falkner-Skan equation, this requires a solution to the initial value problem (IVP) of Eqn. B.24 in BC (1), found by shooting at values for $f''(0)$ to satisfy BC (2), and resolve the BVP at $f'(\infty)$.

A shooting method by Cebeci & Keller is applied [105], to numerically solve the BVP per [106]. Newtons Method [154], provides quadratic convergence of the iterations, to decrease time, and create a physically relevent solution [105]. For Newton's method, initial target selection must be close to real, for adequate convergence. This issue is eliminated with parallel shooting [106], if $f''(0) > 0$, or $\beta > 0$. Various applications of this method [105, 154–160], also provide a solid basis to initialise the process, and execute the solution as follows:

(1) Select an array of similar variable η with interval $d\eta$, to capture the region of interest for iterative convergence. Past research [105,154–160] indicates $\eta = 0 - 10$ and $d\eta = 0.01$, as the

BL should exist at $\eta < 4$, with additional values to represent infinity.

(2) Reduce the 3rd-order, two-point nonlinear BVP to a 1st order differential system, to apply 4th order Runge-Kutta[157–160]. A 1st order system, with three variables: x, y, z, three representative ODEs in Eqn. B.29[159], and respective BCs: $x(0) = 0, y(0) = 0, y(\eta = \infty)$. The last becomes finite through truncation of the semi-finite interval limit on η.

$$\begin{bmatrix} f' \\ f'' \\ f''' \end{bmatrix} = \begin{bmatrix} y \\ z \\ -xz - \beta(1 - y^2) \end{bmatrix} \tag{B.29}$$

(3) Shooting: $f''(0) = 2$ is the target upper limit[105], commencing from $f''(0) = 0.0001$. A loop is set to run iterative convergence for each target $f''(0)$, adjusting the value with Newtons method on each loop. Iteration is initialised at $\eta = 0$, for $f(\eta) = f'(\eta) = 0$, then increased $d\eta = 0.01$[105] per iteration, until $f'(\eta) \to 1$, or $\eta_{\max}$.

(4) New $f''(0)$ is selected in the outer loop with Newtons method, and iterative convergence repeats, until $f''(0)$ is within desired error. To assist Newton's method, we also check if:

(i) $f'(\eta) > 1$ at some η, then $f''(0)$ is decreased, and $f'(\eta)$ is evaluated until $f'(\eta) < 1$ at some $f''(0)$, and the asymptotic profile is bracketed.

(ii) $f'(\eta)$ does not cross unity as $\eta \to \eta_{\max}$, because $f'(\eta)$ is negative, then $f''(0)$ is too small, and Newtons method determines a larger value for the next loop.

(5) Find remaining function values: $f(\eta), f'(\eta), f'''(\eta)$ using converged $f''(0)$, and vector definition in Eqn. B.29[159]. Fig. 4.11 provides the functions for different pressure gradients β, to show solution convergence, with data in Table B.1.

$f'(\eta)$ is the similar velocity profile used to find $\delta \propto \eta$, by converging on $f'(\eta) = u/\mathrm{U_e} \approx 0.99$, through iteration of η. When convergence is achieved, the value of converged η, is subbed into Eqn. B.21, which is rearranged for y, representing the BL thickness $y \sim \delta$ in Eqn. B.30.

$$\delta = \eta \left[\frac{\mathrm{U_e}(1 + m_\beta)}{2\nu x} \right]^{-1/2} \tag{B.30}$$

This solution requires several constants, defined based on wedge geometry, and location x of the velocity profile, at the cavity LE/conic TE. The conic has a diameter of $\varnothing$0.1m, incline length $l = 0.121$, pressure gradient $\beta = 0.25$ for $m_\beta = 0.14$, therefore $x = \sqrt{l^2 + 0.05^2} = 0.13$m. The power-law is used to define BL edge velocity; $\mathrm{U_e} = C\xi^{m_\beta}$, with constant C as the IC or velocity at the wall $\mathrm{U_w}$, from HWA data (See the algorithm in Appendix F.2.4).

Table B.1: HWA: Falkner-Skan Similarity Solution Functions

η	$f(\eta)$	$f'(\eta)$	$f''(\eta)$	$f'''(\eta)$	η	$f(\eta)$	$f'(\eta)$	$f''(\eta)$	$f'''(\eta)$
0.00	0.00	0.00	0.55	-0.25	0.60	0.09	0.31	0.46	-0.27
0.02	0.00	0.01	0.55	-0.25	0.70	0.13	0.35	0.45	-0.27
0.04	0.00	0.02	0.54	-0.25	0.80	0.16	0.40	0.43	-0.28
0.06	0.00	0.03	0.54	-0.25	0.90	0.21	0.44	0.41	-0.29
0.08	0.00	0.04	0.54	-0.25	1.00	0.25	0.48	0.40	-0.29

0.10	0.00	0.05	0.54	-0.25	1.20	0.35	0.56	0.36	-0.30
0.12	0.00	0.07	0.53	-0.25	1.40	0.47	0.63	0.33	-0.31
0.14	0.01	0.08	0.53	-0.25	1.60	0.61	0.69	0.29	-0.31
0.16	0.01	0.09	0.53	-0.25	1.80	0.75	0.74	0.26	-0.30
0.18	0.01	0.10	0.52	-0.25	2.00	0.90	0.79	0.22	-0.30
0.20	0.01	0.11	0.52	-0.25	2.20	1.07	0.83	0.19	-0.28
0.22	0.01	0.12	0.52	-0.25	2.40	1.24	0.87	0.16	-0.26
0.24	0.02	0.13	0.52	-0.25	2.60	1.42	0.90	0.13	-0.23
0.26	0.02	0.14	0.51	-0.25	2.80	0.00	0.00	0.00	0.00
0.28	0.02	0.15	0.51	-0.25	3.00	1.79	0.94	0.08	-0.18
0.30	0.02	0.16	0.51	-0.26	3.50	2.17	0.97	0.05	-0.12
0.35	0.03	0.18	0.50	-0.26	4.00	2.76	0.99	0.02	-0.06
0.40	0.04	0.21	0.49	-0.26	4.50	3.26	1.00	0.01	-0.03
0.50	0.07	0.26	0.48	-0.26	5.00	3.76	1.00	0.00	-0.01

B.2.3 Boundary Layer Flow over a Curved Surface

For BL flow over the ogive and parabola nose per Fig. B.4, the flat-plate BL solution also no-longer holds, due to the presence of a favourable pressure gradient. Falkner-Skan too falls short, as the pressure gradient formulation, does not account curvature. However, Murphy [7,107] extended Falkner-Skan for curvature, using incompressible NS EOM with a pressure gradient equated to curved streamlines from Goldstein [23]. The BL EOM is given for x-momentum, y-momentum and continuity respectively in Eqn. B.31-B.33.

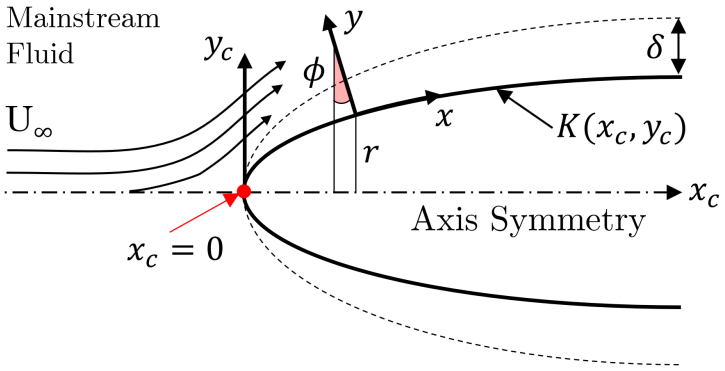

Figure B.4: Curved Boundary Layer Flow

Per Fig. B.4, x is distance along the curve, or arc length with respect to Cartesian coordinates; x_c, y_c in Eqn. B.34, with velocity component u. y is normal to the curve, with velocity component v. K is surface curvature, with respect to x_c, y_c in Eqn. B.35. To find BL thickness in y, at a point x of interest along the curve. K is calculated using an equation of the curve line in x_c, y_c coordinates, to determine derivatives; dy_c/dx_c and d^2y_c/dx_c^2 per Eqn. B.35. At arc length x, which is calculated with the same coordinates x_c, y_c, and equation of the curve line derivative dy_c/dx_c per Eqn. B.34. The curve line equation, is defined from origin of the curve, where flow begins, to the point of interest, where the BL in y, is to be defined, as measured with HWA.

Using the equation for the curve lines in x_c, y_c, at BL location; $x_c = l = +145$mm, K and x are found. For the ogive; K = 1.43, $x = 158.2$mm, and parabola; K = 6.44, and $x = 159.6$mm.

$$\frac{u}{1+\mathrm{K}y}\frac{\partial u}{\partial x} + v\frac{\partial u}{\partial y} + \frac{\mathrm{K}uv}{1+\mathrm{K}y} = -\frac{1}{\rho(1+\mathrm{K}y)}\frac{\partial p}{\partial x} + v\left[\frac{1}{(1+\mathrm{K}y)^2}\frac{\partial^2 u}{\partial x^2} + \frac{\partial^2 u}{\partial y^2} - \frac{y}{(1+\mathrm{K}y)^3}\frac{\partial \mathrm{K}}{\partial x}\frac{\partial u}{\partial x} + \frac{\mathrm{K}}{1+\mathrm{K}y}\frac{\partial u}{\partial y} - \frac{\mathrm{K}^2 u}{(1+\mathrm{K}y)^2} + \frac{2\mathrm{K}}{(1+\mathrm{K}y)^2}\frac{\partial v}{\partial x} + \frac{v}{(1+\mathrm{K}y)^3}\frac{\partial \mathrm{K}}{\partial x}\right] \tag{B.31}$$

$$\frac{u}{1+\mathrm{K}y}\frac{\partial v}{\partial x} + v\frac{\partial v}{\partial y} - \frac{\mathrm{K}u^2}{1+\mathrm{K}y} = -\frac{1}{\rho}\frac{\partial p}{\partial y} + v\left[\frac{1}{(1+\mathrm{K}y)^2}\frac{\partial^2 v}{\partial x^2} + \frac{\partial^2 v}{\partial y^2} - \frac{y}{(1+\mathrm{K}y)^3}\frac{\partial \mathrm{K}}{\partial x}\frac{\partial v}{\partial x} + \frac{\mathrm{K}}{1+\mathrm{K}y}\frac{\partial v}{\partial y} - \frac{\mathrm{K}^2 v}{(1+\mathrm{K}y)^2} - \frac{u}{(1+\mathrm{K}y)^3}\frac{\partial \mathrm{K}}{\partial x} - \frac{2\mathrm{K}}{(1+\mathrm{K}y)^2}\frac{\partial u}{\partial x}\right] \tag{B.32}$$

$$\frac{\partial u}{\partial x} + \frac{\partial v}{\partial y}(1+\mathrm{K}y) = 0 \tag{B.33}$$

$$x = \int_0^{x_c} \sqrt{1 + \left(\frac{dy_c}{dx_c}\right)^2}\, dx_c \tag{B.34}$$

$$\mathrm{K} = \frac{\left|d^2 y_c/dx_c^2\right|}{\sqrt{(1+dy_c/dx_c)^3}} \tag{B.35}$$

Order-of-magnitude analysis[7] is then applied to formulate incompressible BL EOM, for flow over a curved surface, through observed phenomena, and known geometric properties. Due to the convex nature of ogive, and parabola shapes, curvature K is positive, producing a favourable pressure gradient $dp/dx < 0$ over the surface. Therefore, friction terms represented by the BL, and its thickness $1/\delta$, are considered very small compared to the pressure gradient. This means, viscous terms in the EOM, can be neglected, as follows.

For x-momentum in Eqn. B.31, on the RHS, viscous stressors in the square brackets are all very small compared to $\partial^2 u/\partial y^2$, which characterises displacement. Therefore are reduced or removed dependent on large or small curvature. On the LHS, $1+\mathrm{K}y \to 1$ and $\mathrm{K}uv$ are negligible in x for small curvature. Similarly for y-momentum in Eqn. B.32, the pressure gradients, with respect to motion in x, is dominant, and other terms very small. Therefore, BL EOM are created in Eqn. B.36-B.38 for large curvature, and Eqn. B.39-B.41 for small. The latter is used in this case, as both ogive and parabola curvatures are small, per proportionality constant $\mathrm{A_p} << 1$ in Table B.3, a non-dimensional curvature correlation relative to fluid properties in Eqn. B.42.

$$\frac{u}{1+\mathrm{K}y}\frac{\partial u}{\partial x} + v\frac{\partial u}{\partial y} + \frac{\mathrm{K}uv}{1+\mathrm{K}y} = -\frac{1}{\rho(1+\mathrm{K}y)}\frac{\partial p}{\partial x} + v\left(\frac{\partial^2 u}{\partial y^2} + \frac{\mathrm{K}}{1+\mathrm{K}y}\frac{\partial u}{\partial y} - \frac{\mathrm{K}^2 u}{1+\mathrm{K}y^2}\right) \tag{B.36}$$

$$\frac{\mathrm{K}u^2}{1+\mathrm{K}y} = \frac{1}{\rho}\frac{\partial p}{\partial y} \tag{B.37}$$

$$\frac{\partial u}{\partial x} + \frac{\partial v}{\partial y}(1+\mathrm{K}y) = 0 \tag{B.38}$$

$$u\frac{\partial u}{\partial x} + v\frac{\partial u}{\partial y} = -\frac{1}{\rho}\frac{\partial p}{\partial x} + v\frac{\partial^2 u}{\partial y^2} \tag{B.39}$$

$$\mathrm{K}u^2 = \frac{1}{\rho}\frac{\partial p}{\partial y} \tag{B.40}$$

$$\frac{\partial u}{\partial x} + \frac{\partial v}{\partial y} = 0 \tag{B.41}$$

$$\mathrm{A_p} = \mathrm{K}\sqrt{\frac{\nu x}{\mathrm{U_{pw}}}} \tag{B.42}$$

BCs are now implemented;

(1) No-slip condition at the surface; $y = 0 \to u = v = 0$.

(2) Asymptotic transition at the BL edge, from viscous BL conditions, to non-viscous potential flow, which represents external flow as a function of surface curvature.

The no-slip condition satisfies continuity in Eqn. B.41 for small curvature, with the stream function in Eqn. B.43, and similar variable; η in Eqn. B.44 [7]. Asymptotic transition from the BL to external flow is satisfied by potential irrotational condition; $u^{-1} \cdot \partial u/\partial y = -K$, requiring; $\mathrm{U_p} = \mathrm{U_{pw}}^{-\mathrm{K}y}$ for small curvature, and $\mathrm{U_p} = \mathrm{U_{pw}}/(1 + \mathrm{K}y)$ for large curvature. $\mathrm{U_p}$ is potential flow velocity, varying in y. $\mathrm{U_{pw}} = \sqrt{2(p_\infty - p_0)/\rho_\infty}$ is potential flow velocity at the wall $y = 0$, calculated with USP measurement $(p_\infty - p_0)$, where the BL traverse was executed.

Similar velocity components u, v and derivatives, are found in Eqn. B.45-B.47. For coordinate transformation x, y, to similar η and $\xi = x$. u, v and derivatives are then substituted into Eqn. B.40, for pressure gradient $\partial p/\partial \eta$ in Eqn. B.48, $\partial p/\partial \xi = 0$, and wall shear stress τ_w in Eqn. B.49. These functions are for small curvature $\mathrm{A} < \pm 0.05$ [7], refer [7] for large curvature.

$$\psi = f(\eta)\sqrt{\mathrm{U_p}\nu x} \qquad \text{(B.43)} \qquad\qquad \eta = \frac{y}{2}\sqrt{\frac{\mathrm{U_p}}{\nu x}} \qquad \text{(B.44)}$$

$$u = \frac{\partial \psi}{\partial y} = \frac{\mathrm{U_p} f'(\eta)}{2} \qquad \text{(B.45)} \qquad v = -\frac{1}{1 + \mathrm{K}y}\frac{\partial \psi}{\partial x} = \frac{f'(\eta)'\eta - f(\eta)}{2 + 4\mathrm{A_p}\eta}\sqrt{\frac{\mathrm{U_p}\nu}{x}} \qquad \text{(B.46)}$$

$$\frac{\partial u}{\partial x} = -\frac{\mathrm{U_{pw}}\eta f''}{4x} \qquad \frac{\partial u}{\partial y} = \frac{\mathrm{U_{pw}} f''}{4}\sqrt{\frac{\mathrm{U_{pw}}}{\nu x}} \qquad \frac{\partial^2 u}{\partial y^2} = \frac{{\mathrm{U_{pw}}}^2 f'''}{8\nu x} \qquad \text{(B.47)}$$

$$\frac{\partial p}{\partial \eta} = \frac{\rho {\mathrm{U_{pw}}}^2 f'^2}{4 + 4\mathrm{A_p}\eta} \qquad \text{(B.48)} \qquad\qquad \tau_w = \frac{\mu \mathrm{U_{pw}} \mathrm{C_2}}{4}\sqrt{\frac{\mathrm{U_{pw}}}{\nu x}} \qquad \text{(B.49)}$$

The similar solution for BL flow over a curved surface is thus formed in Eqn. B.50, by substituting similar components Eqn. B.45-B.48 into Eqn. B.39. BCs become; (1) $f = f' = 0$ at $\eta = 0$ on the surface, and (2) $f' = 2/(1 + 2\mathrm{A_p}\eta')$ for $\eta > 0$, away from the surface. A simplified version is obtained in Eqn. B.51, within close agreement of Eqn. B.50, for very small convex curvature, and BCs; (1) $f = f' = 0$ at $\eta = 0$ and (2) $f' \to 2 - 4\mathrm{A_p}\eta$ for $\eta > 0$.

$$f''' + ff'' + 2\mathrm{A_p}(ff' + \eta ff'' + 2\eta f'' + 2\mathrm{A_p}\eta^2 f''' + f'' + 2\mathrm{A_p}\eta f'' - 2\mathrm{A_p}f') = 0 \qquad \text{(B.50)}$$

$$f''' + ff'' + 2\mathrm{A_p}\eta f'^2 = 0 \qquad \text{(B.51)}$$

To solve the similar solution, function $f(\eta)$ is required. A Taylor-series solution is assumed per Eqn. B.52, where $\mathrm{C_i}$ are constants, with BCs, $\mathrm{C_0} = \mathrm{C_1} = 0$. Then by substituting Eqn. B.52, into B.39, a similar function $f(\eta)$ in Eqn. B.53 is formed. $\mathrm{F_0}$ is the flat solution ($\mathrm{K} = \mathrm{A} = 0$), or location of inflection from concave to convex. And $\mathrm{G_i}$ adjustment for curvature with $\mathrm{A}, \mathrm{C_2}$. High powers are very small, thus neglected, forming an approximate solution in Eqn. B.54. Further reduction to Eqn. B.55, is also acceptable for small curvature [7], alike ogive and parabola nose cones. Values for $\mathrm{C_2}$ as a function of proportionality A, and airspeed are found with Fig. B.5 [7], and $\mathrm{F_0}, \mathrm{G_1}, \mathrm{G_2}, \mathrm{G_3}$ are defined by Taylor-series in Eqn. B.56-B.59 [23].

$$f = \sum_{i=0}^{\infty} \frac{\mathrm{C}_i \eta_i}{i!} \qquad \text{(B.52)}$$

$$f = \sqrt[3]{\mathrm{C_2}}\mathrm{F_0}\left(\eta\sqrt[3]{\mathrm{C_2}}\right) - \mathrm{A_p}\mathrm{G_1}\left(\eta\sqrt[3]{\mathrm{C_2}}\right) + \frac{{\mathrm{A_p}}^2}{\sqrt[3]{\mathrm{C_2}}\mathrm{G_2}}\left(\eta\sqrt[3]{\mathrm{C_2}}\right) + \sum_{n=1}^{\infty}\frac{(-1)^n{\mathrm{A_p}}^n}{{\mathrm{C_2}}^{\frac{n-1}{3}}}\mathrm{G_n}\left(\eta\sqrt[3]{\mathrm{C_2}}\right) \quad \text{(B.53)}$$

$$f = \sqrt[3]{\mathrm{C_2}}\mathrm{F_0}\left(\eta\sqrt[3]{\mathrm{C_2}}\right) - \mathrm{A_p}\mathrm{G_1}\left(\eta\sqrt[3]{\mathrm{C_2}}\right) + \frac{{\mathrm{A_p}}^2}{\sqrt[3]{\mathrm{C_2}}}\mathrm{G_2}\left(\eta\sqrt[3]{\mathrm{C_2}}\right) - \frac{{\mathrm{A_p}}^3}{\sqrt[3]{{\mathrm{C_2}}^2}}\mathrm{G_3}\left(\eta\sqrt[3]{\mathrm{C_2}}\right) \quad \text{(B.54)}$$

$$f = \sqrt[3]{\mathrm{C_2}}\cdot\mathrm{F_0}\left(\eta\sqrt[3]{\mathrm{C_2}}\right) - \mathrm{A_p}\cdot\mathrm{G_1}\left(\eta\sqrt[3]{\mathrm{C_2}}\right) \quad \text{(B.55)}$$

$$\mathrm{F_0}\left(\eta\sqrt[3]{\mathrm{C_2}}\right) = \frac{\left(\eta\sqrt[3]{\mathrm{C_2}}\right)^2}{2!} - \frac{\left(\eta\sqrt[3]{\mathrm{C_2}}\right)^5}{5!} + \frac{11\left(\eta\sqrt[3]{\mathrm{C_2}}\right)^8}{8!} - \frac{375\left(\eta\sqrt[3]{\mathrm{C_2}}\right)^{11}}{11!} + \frac{27897\left(\eta\sqrt[3]{\mathrm{C_2}}\right)^{14}}{14!} - \frac{3817742\left(\eta\sqrt[3]{\mathrm{C_2}}\right)^{17}}{17!} + \ldots \quad \text{(B.56)}$$

$$\mathrm{G_1}\left(\eta\sqrt[3]{\mathrm{C_2}}\right) = \frac{2\left(\eta\sqrt[3]{\mathrm{C_2}}\right)^3}{3!} - \frac{10\left(\eta\sqrt[3]{\mathrm{C_2}}\right)^6}{6!} + \frac{324\left(\eta\sqrt[3]{\mathrm{C_2}}\right)^9}{9!} - \frac{22896\left(\eta\sqrt[3]{\mathrm{C_2}}\right)^{12}}{12!} + \frac{2854146\left(\eta\sqrt[3]{\mathrm{C_2}}\right)^{15}}{15!} - \frac{595343808\left(\eta\sqrt[3]{\mathrm{C_2}}\right)^{18}}{18!} + \ldots \quad \text{(B.57)}$$

$$\mathrm{G_2}\left(\eta\sqrt[3]{\mathrm{C_2}}\right) = \frac{12\left(\eta\sqrt[3]{\mathrm{C_2}}\right)^4}{4!} - \frac{128\left(\eta\sqrt[3]{\mathrm{C_2}}\right)^7}{7!} + \frac{8184\left(\eta\sqrt[3]{\mathrm{C_2}}\right)^{10}}{10!} - \ldots \quad \text{(B.58)}$$

$$\mathrm{G_3}\left(\eta\sqrt[3]{\mathrm{C_2}}\right) = \frac{96\left(\eta\sqrt[3]{\mathrm{C_2}}\right)^5}{5!} - \frac{1832\left(\eta\sqrt[3]{\mathrm{C_2}}\right)^8}{8!} + \frac{203784\left(\eta\sqrt[3]{\mathrm{C_2}}\right)^{12}}{12!} - \ldots \quad \text{(B.59)}$$

To determine δ, whilst satisfying BCs, two data sets are required, as an output of the similar curved flow solution derived above:

(1) Potential velocity profile $\mathrm{U_p}/\mathrm{U_{pw}} = e^{-\mathrm{K}y}$, with y in terms of η; $y = 2\eta\cdot[\mathrm{U_{pw}}/\nu x]^{-1/2}$

(2) Curved similar solution velocity profile $u/\mathrm{U_{pw}} = f'(\eta)/2$, determined by rearranging Eqn. B.45, and solving differential $f'(\eta)$ for η.

These curve sets are plotted together against η, and the point of intersection, represents convergence of the; curved surface BL similar solution (1), with the external flow velocity, modelled by potential flow (2). Effectively, when BL velocity equates to external velocity at the BL edge, as location of BL thickness $\delta \sim y$. Therefore, at the point of intersection, corresponding η, is used to determine δ in Eqn. B.60. The algorithm is in Appendix B.2.3. Fig. 4.14 is an intersection example of the curve similar, and potential velocity profiles, to identify δ. Table 4.4 has BL thicknesses, and Table B.2 similar function and derivative solutions for the ogive and parabola.

$$\delta = \frac{2\eta_\delta}{\sqrt{\mathrm{U_{pw}}/\nu x}} \quad \text{(B.60)}$$

Table B.2: HWA: Curved Surface Similarity Function

OGIVE					**PARABOLA**				
η	f	f'	f''	f'''	η	f	f'	f''	f'''
0.000	0.000	0.000	1.096	-0.002	0.000	0.000	0.000	1.082	-0.017
0.025	0.000	0.030	1.096	-0.003	0.025	0.000	0.029	1.081	-0.017
0.050	0.002	0.060	1.096	-0.004	0.050	0.002	0.058	1.081	-0.019
0.075	0.004	0.090	1.096	-0.006	0.075	0.004	0.088	1.080	-0.021
0.100	0.007	0.120	1.095	-0.009	0.100	0.006	0.117	1.080	-0.023
0.125	0.010	0.150	1.095	-0.012	0.125	0.010	0.146	1.079	-0.027
0.150	0.015	0.180	1.095	-0.017	0.150	0.014	0.175	1.078	-0.031
0.175	0.020	0.210	1.094	-0.022	0.175	0.019	0.204	1.077	-0.036
0.200	0.026	0.240	1.094	-0.028	0.200	0.025	0.234	1.076	-0.042
0.225	0.033	0.270	1.093	-0.035	0.225	0.032	0.263	1.075	-0.049
0.250	0.041	0.300	1.092	-0.043	0.250	0.039	0.292	1.074	-0.056
0.275	0.050	0.330	1.090	-0.052	0.275	0.048	0.321	1.072	-0.064
0.300	0.059	0.360	1.089	-0.061	0.300	0.057	0.350	1.070	-0.073
0.350	0.081	0.419	1.085	-0.082	0.350	0.077	0.407	1.066	-0.093
0.400	0.105	0.479	1.080	-0.106	0.400	0.101	0.465	1.060	-0.115
0.450	0.133	0.538	1.073	-0.132	0.450	0.128	0.522	1.053	-0.141
0.500	0.164	0.596	1.065	-0.162	0.500	0.157	0.579	1.045	-0.168
0.550	0.198	0.654	1.055	-0.193	0.550	0.190	0.635	1.035	-0.198
0.600	0.236	0.712	1.044	-0.227	0.600	0.226	0.691	1.023	-0.230
0.700	0.320	0.825	1.015	-0.298	0.700	0.307	0.800	0.995	-0.298
0.800	0.416	0.934	0.978	-0.374	0.800	0.399	0.906	0.959	-0.369
0.900	0.524	1.039	0.933	-0.449	0.900	0.503	1.007	0.915	-0.440
1.000	0.644	1.138	0.880	-0.519	1.000	0.617	1.104	0.864	-0.507
1.100	0.774	1.232	0.820	-0.581	1.100	0.741	1.194	0.806	-0.566
1.200	0.914	1.318	0.753	-0.630	1.200	0.875	1.278	0.742	-0.615
1.300	1.062	1.396	0.682	-0.664	1.300	1.017	1.354	0.673	-0.649
1.400	1.219	1.467	0.608	-0.683	1.400	1.168	1.423	0.602	-0.668
1.500	1.384	1.530	0.533	-0.687	1.500	1.325	1.484	0.529	-0.672
1.600	1.554	1.584	0.458	-0.685	1.600	1.489	1.538	0.457	-0.668
1.800	1.911	1.668	0.303	-0.764	1.800	1.831	1.621	0.311	-0.697
2.000	2.283	1.712	0.079	-1.491	2.000	2.188	1.670	0.128	-1.130
2.200	2.656	1.675	-0.54	-5.013	2.200	2.549	1.660	-0.30	-3.338
2.400	2.998	1.360	-2.81	-18.41	2.400	2.894	1.471	-1.75	-11.75
2.600	3.183	0.044	-10.8	-62.45	2.600	3.143	0.662	-6.70	-39.05
2.800	2.784	-4.60	-36.3	-192.3	2.800	3.040	-2.17	-22.3	-118.2
3.000	0.454	-19.3	-110.0	-542.3	3.000	1.784	-11.0	-67.0	-327.5

Table B.3: HWA: Proportionality Constant A_p $[10^{-3}]$

U_∞ (m/s)	10	15	20	25	30	35	40	45	50
Ogive Open Cavity	0.97	0.78	0.66	0.60	0.55	0.51	0.49	0.81	0.43
Ogive Closed Cavity	0.80	0.74	0.64	0.57	0.53	0.50	0.47	0.45	0.41
Parabola Open Cavity	5.04	3.81	3.24	2.94	2.64	2.47	2.32	2.22	2.11
Parabola Closed Cavity	4.65	3.65	3.15	2.78	2.55	2.38	2.22	2.14	2.00

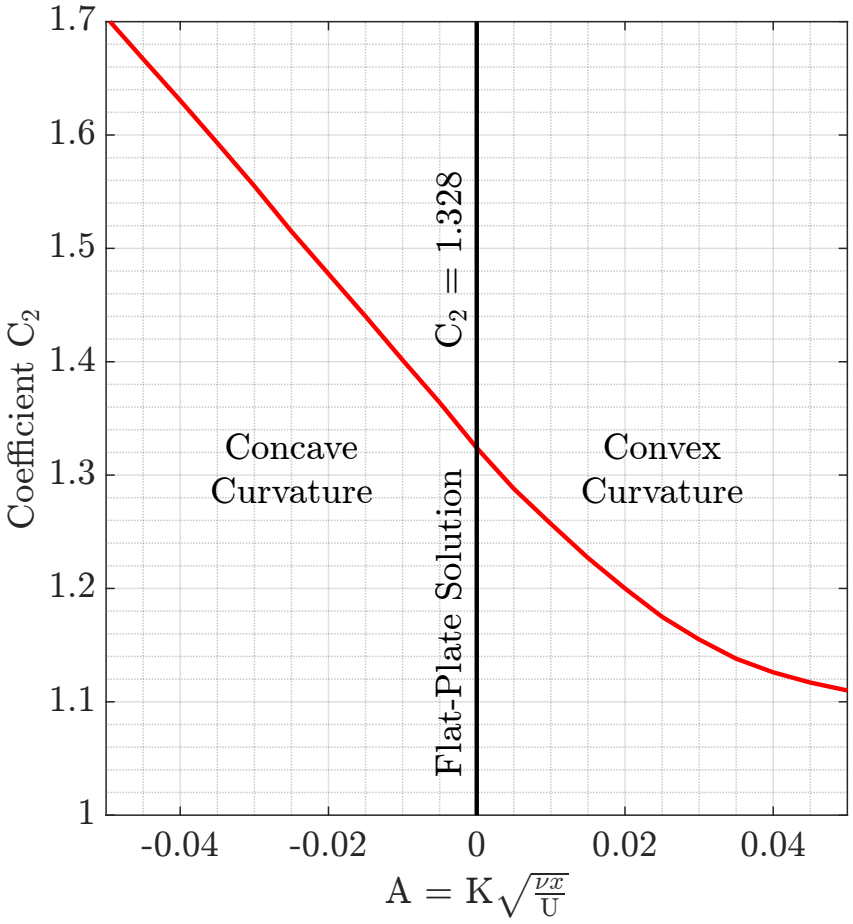

Figure B.5: Curvature Constant C_2 based on Proportionality Constant A_p [7]

Appendix C

Signal Analysis

C.1 Fourier Transform

$$y_{k+1} = \sum_{j=0}^{N-1} \omega^{ik} x_{j+1} \tag{C.1}$$

Fourier Transform (FT) is a mathematical means to resolve temporal signal x of N samples in the frequency domain, per Eqn. C.1: $\omega = e^{-2\pi i/n}$, with n complex roots, imaginary $i = \sqrt{-1}$, and indices j and k for $0 \rightarrow n-1$. FFT is fast discrete FT, attaining frequency spectrum in reduced time, by decomposing the signal into frequency components, and factorising discrete matrices into a product of sparse factors. FT characterises system frequency response, to identify dominant modes, which represent the response. In fluid dynamics, FT supports mathematical re-construction of a flow-field, to assess elements responsible for certain flow phenomena. In cavity flow, vorticity is the root cause of oscillation, acoustics and vibration. Therefore, extracting vortex mode structures from USP is precedential.

Sound pressure level (SPL) is used to assess the magnitude of oscillatory fluid phenomena, alike cavity flow. SPL is a measure of the pressure level of a sound with respect to human perception, representing average variation in atmospheric pressure caused by a sound wave, per the relationship; $\text{SPL} = 20\log_{10}\left(p/p_{\text{ref}}^2\right)$: p is the FT output amplitude, and $p_{\text{ref}} = 20\mu\text{Pa}$ is the reference value at SPL = 0dB, the minimum sound pressure a human can perceive.

C.2 Dynamic Mode Decomposition (DMD)

DMD was developed by Schmid & Sesterhenn[127–129] as a diagnostics tool, to reduce high-dimensional data into spatio-temporal coherant structures, and decompose complex flow-fields into a structural representation of spatial dimensionality. Likened to POD, DMD includes FT in time, for correlation of spatial modes with temporal frequency, for growth or decay rate. DMD extracts low-rank spatio-temporal features of a high-dimension system, for physical interpretation of spatial structures, and aligned temporal responses. DMD can estimate future-state, using dominant structures to create a dynamic model of the system process, providing capability via sampled data for control alike adaptive AI. DMD is limited best-fit, mapping nonlinear dynamics, to a least-square linear system, assuming 2D state space coordinates.

C.2.1 Theory and Architecture

A series of state-based snapshots $\mathbf{x}_k$, from a dynamic system at time t_k for $k = 1, 2, ...m$, are algorithmically regressed to a locally linear dynamic system; $\mathbf{x}_{k+1} = \mathbf{A}\mathbf{x}_k$. $\mathbf{A} = \exp(A\Delta t)$ is a discrete time-map, of continuous-time dynamics matrix A with $dx/dt = A\mathbf{x}$. The solution is given as eigenvalues λ_k, and vectors ϕ_k, of $\mathbf{A}$ in Eqn. 4.66. $\mathbf{b}$ are eigenvector IC coefficients $\mathbf{x_1}$, so $\mathbf{x_1} = \mathbf{\Phi b}$, extracted through a low-rank eigendecomposition of matrix $\mathbf{A}$, using least-square best-fit of $\mathbf{x}_k$, for $k = 1, 2, ...m$ of $\|\mathbf{X}_{k+1} - \mathbf{A}\mathbf{X}_k\|_2$, to minimise; $k = 1, 2, ...m - 1$. This is an approximation, holding for sample window $\mathbf{A}$. Future-state can be predicted, as dynamics were decomposed onto time-scales of prescribed λ_k. To reduce error, m snapshots are allocated to data matrix $\mathbf{X}, \mathbf{X}'$ in Eqn. 4.65. Using samples from a nonlinear dynamic system, decomposed to a optimal linear approximation where $\mathbf{X}' \approx \mathbf{A}\mathbf{X}$, with best-fit $\mathrm{A} = \mathrm{X}'\mathrm{X}^{\dagger}$; $\dagger$ is Moore-Penrose pseudo inverse, minimising error to $\|\mathbf{X}' - \mathbf{A}\mathbf{X}\|_F$, and $\|\cdot\|_F$ is Frobenius norm in Eqn. 4.67[130].

$$\mathbf{X} = \begin{bmatrix} . & . & & . \\ \mathbf{x}_1 & \mathbf{x}_2 & ... & \mathbf{x}_{m-1} \\ . & . & & . \end{bmatrix} \qquad \mathbf{X}' = \begin{bmatrix} . & . & & . \\ \mathbf{x}_2 & \mathbf{x}_3 & ... & \mathbf{x}_m \\ . & . & & . \end{bmatrix} \tag{C.2}$$

$$\mathbf{x}_k = \sum_{r}^{j=1} \phi_j \lambda_j^k b_j = \mathbf{\Phi \Lambda}^k \mathbf{b} \tag{C.3}$$

$$\|\mathbf{X}\|_F = \sqrt{\sum_{j=1}^{n} \sum_{k=1}^{m} X_{jk}^2} \tag{C.4}$$

C.2.2 Algorithm

The algorithm in Appendix F.3.3 was developed from Schmid[127–129] and Kutz[130] with reference to Seena & Sung's[69] for cavity flow, and Singh et al[71] for experimental cavity flow. The DMD process executed is summarised into five steps as follows;

(1) **Singular Value Decomposition** (SVD) $\mathbf{X} \approx \mathbf{U\Sigma V}^*$: `[U,S,V] = svd(X,'econ')`

- `'econ'` is economy size decomposition of $\mathbf{X}$, to remove rows/columns of zeros from $\mathbf{\Sigma}$, and columns in $\mathbf{U}, \mathbf{V}$ that multiply zeros in SVD.
- $\mathbf{U} \in \mathbb{C}^{n \times r}$ is the left singular vector or orthonormal POD modes of $\mathbf{X}$ for $\mathbf{U}^*\mathbf{U} = \mathbf{I}$.
- $\mathbf{\Sigma} \in \mathbb{C}^{r \times r}$ or `S` is the matrix of diagonal singular values.
- $\mathbf{V} \in \mathbb{C}^{m \times r}$ is right singular vectors of $\mathbf{X}$ for $\mathbf{V}^*\mathbf{V} = \mathbf{I}$, $*$ is conjugate transpose.
- r prescribes rank reduction of the $\mathbf{X}$ SVD approximation.

(2) **Rank-R Reduction**: SVD output matrices in $\mathbf{X} \approx \mathbf{U\Sigma V}^* \rightarrow$ `[U,S,V]` are truncated by rank-r, found by dividing diagonal values of $\mathbf{\Sigma} \sim$`S` by the diagonal value sum. Then taking a cumulative sum denoted σ; `sigma = cumsum(diag(S)/sum(diag(S)))`. Rank-r is the $\sigma \sim 0.99$ index when 99% of dynamic system energy is captured.

(3) **Dynamic Reduction**: discrete-time linear dynamic matrix $\mathbf{A}$, is reduced to POD subspace dynamic representation $\tilde{\mathbf{A}}$, with pseudo-inverse of $\mathbf{X}$ from SVD, and $r \times r$ projection of matrix $\mathbf{A}$ to POD modes in Eqn. 4.68. $\tilde{\mathbf{A}}$ is the low-dimensional linear model in POD coordinates: $\tilde{\mathbf{x}}_{\mathbf{k+1}} = \tilde{\mathbf{A}}\tilde{\mathbf{x}}_{\mathbf{k}}$, to be reconstructed back to high-dimensional state; $\mathbf{x_k} = \mathbf{U}\tilde{\mathbf{x}}_{\mathbf{k}}$.

$$\mathbf{A} = \mathbf{X}'\mathbf{V\Sigma}^{-1}\mathbf{U}^* \qquad \rightarrow \qquad \tilde{\mathbf{A}} = \mathbf{U}^*\mathbf{A}\mathbf{U} = \mathbf{U}^*\mathbf{X}'\mathbf{V\Sigma}^{-1} \tag{C.5}$$

(4) **Eigendecomposition**: $\tilde{A} \rightarrow \tilde{\mathbf{A}}\mathbf{W} = \mathbf{W}\mathbf{\Lambda}$ with `[W,D] = eig(Atilde)`, to compute eigenvector $\mathbf{W}$ columns, and eigenvalue λ_k diagonal matrix $\mathbf{\Lambda}$ = `D`.

(5) **Dynamic Reconstruction** of $\mathbf{A}$ from eigendecomposition output of eigenvalues $\mathbf{\Lambda}$ as `lambda = diag(D)`, and eigenvector columns of $\mathbf{\Phi} = \mathbf{X'V\Sigma^{-1}W}$; as `phi = X2*Vr/Sr*W`; `X2` is $\mathbf{X'}$. An approximate solution of the future state is thus given by Eqn. C.6.

$$\mathbf{x}(t) \approx \sum_{k=1}^{r} \phi_k \exp(\omega_k t) b_k = \mathbf{\Phi} \exp(\mathbf{\Omega} t)\mathbf{b} \tag{C.6}$$

- $\mathbf{\Phi}$ = matrix of DMD modes in eigenvector ϕ_k columns, the size of state $\mathbf{x}$.
- $\mathbf{\Omega}$ = diagonal matrix of discrete-time eigenvalues λ_k.
- $\omega_k = \log(\lambda_k)/\Delta t$ is continuous-time eigenvalues, or frequency when divided by 2π.
- $\mathbf{b} = \mathbf{\Phi}^{\dagger}\mathbf{x_1}$, initial amplitude mode coefficient vector b_k, as `b = mldivide(phi,X)`.

C.2.3 Reduction and Graphing

There are two consequences when using DMD to process experimental results, as follows:

(1) **High Spatial Resolution with Risk of Flow Interference**: The model was designed for DMD, with pressure taps densely distributed in space, surface flush to sustain flow behaviour. Less is captured compared to PIV or CFD, which produces high spatial and temporal resolution with no flow interference. Nonetheless, cavity flow system dynamics are strong enough to be recognised by DMD, and assessed for mode behaviour.

(2) **Complex Conjugates**: experimental data produces complex conjugates[127], as the spectrum is symmetric to temporal frequencies[127], incurring eigenvalue and vector output, either non-oscillatory and real, or complex conjugates of a mode oscillating about the real axis. As cavity flow is oscillatory, the DMD modes are mostly complex conjugates.

Complex conjugate combination is executed, by checking if adjacent eigenvectors and values share absolute value, and removing the secondary if equal, Fig. 4.20 provides an example. Schmid[127], Kutz[130] and Krake[131] combined conjugates from experimental data. Singh et al[71] produced a similar eigencircle distribution of only positive real and imaginary modes, after combining complex conjugates from open cavity flow, supporting the present reduction.

Dominant modes ϕ have the largest eigenvector norm in space, with corresponding eigenvalues closest to unity in an eigencircle, i.e., Mode 1 in Fig. 4.20, and the norm plot Fig. 4.21. As DMD assumes 2D space, the algorithm was executed on each cavity wall, to create eigencircle and norm data, represented by graphs in Fig. 4.20 and 4.21. Fig. 4.22 is an example for L/D = L/W = 3 at U_∞ = 50m/s, with the conic nose U/S. In these plots, Mode 1-6 are in order of dominance, not frequency, and the respective frequency order of each defines its mode. In most cases, the 2nd or 3rd mode in the cavity spectra holds dominance, aligned to plot peaks.

Mode shapes are reconstructed from $\mathbf{\Phi}$ in space, to identify key flow structures, corresponding to extreme oscillatory cavity dynamics. Notably, those of the fuselage cases, where BLs are much thinner, increasing magnitude response. Mode shapes are graphed in a similar way to

$C_{p,rms}$, plotting the value of ϕ_k at respective spatial coordinates, with a contour plot. Fig. C.1 is an example for the conic nose cavity with L/D = L/W = 1 at U_∞ = 50m/s.

Due to the large swathe of data from this experimental campaign, and the capacity of what DMD can provide, i.e. several modes, thus mode shapes per case. DMD was primarily used to identify the frequency of spatially dominant modes 1-4 in the cavity, as presented in Appendix D.2. Then used to compute Strouhal number of the flow. Correlative peak SPL from FFT at the determined frequency, was aligned to each mode frequencies.

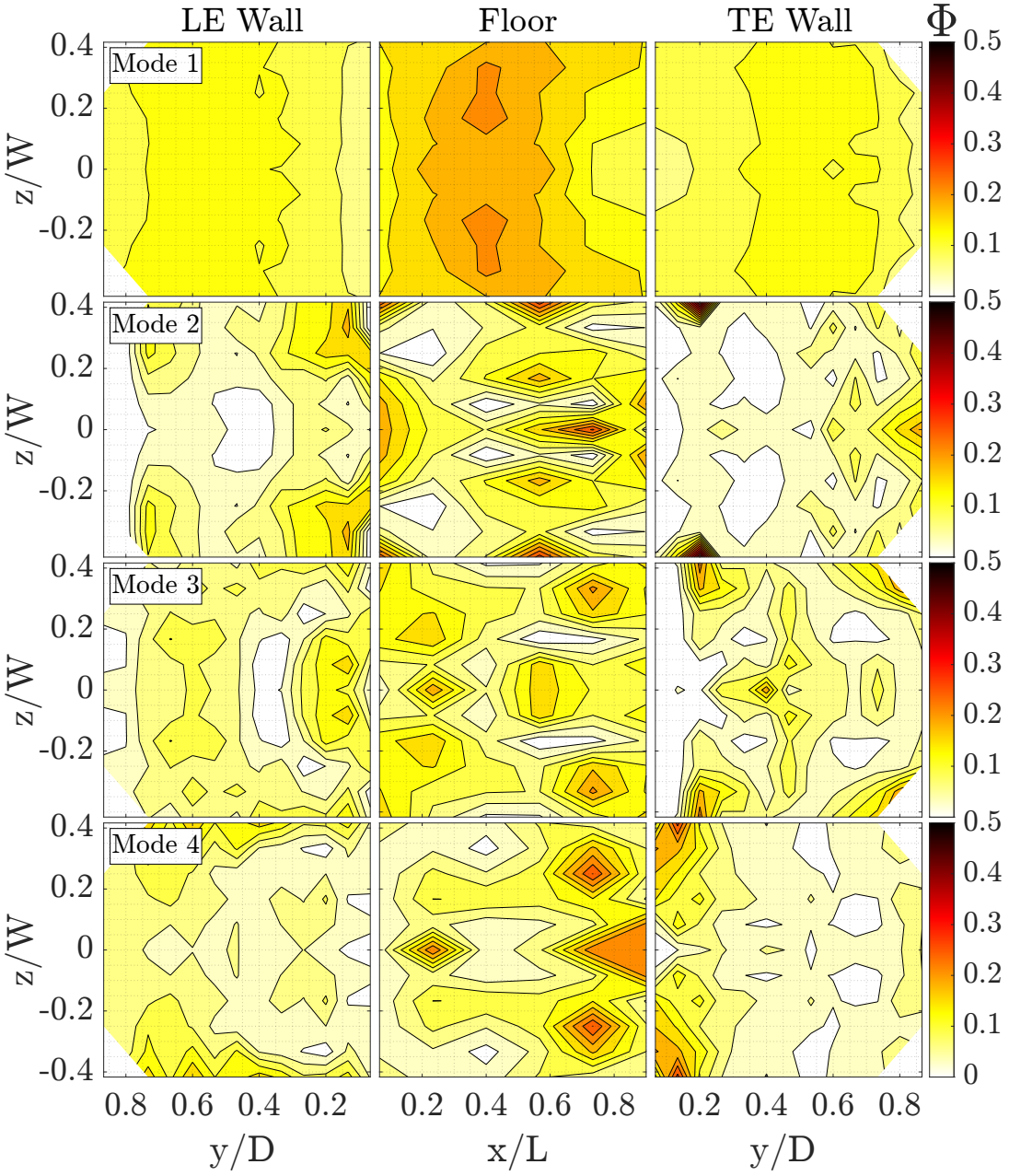

Figure C.1: USP: Modes of C5: L/D = L/W = 1, Conic U/S, U_∞ = 50m/s

Appendix D

Additional Supporting Data

D.1 Surface Pressure Data

Due to the large set of pressure data generated for each case, primary data is presented in the main text, with secondary given as additional support, in interest of the reader.

D.1.1 Effect of Internal Cavity Geometry: Length and Width

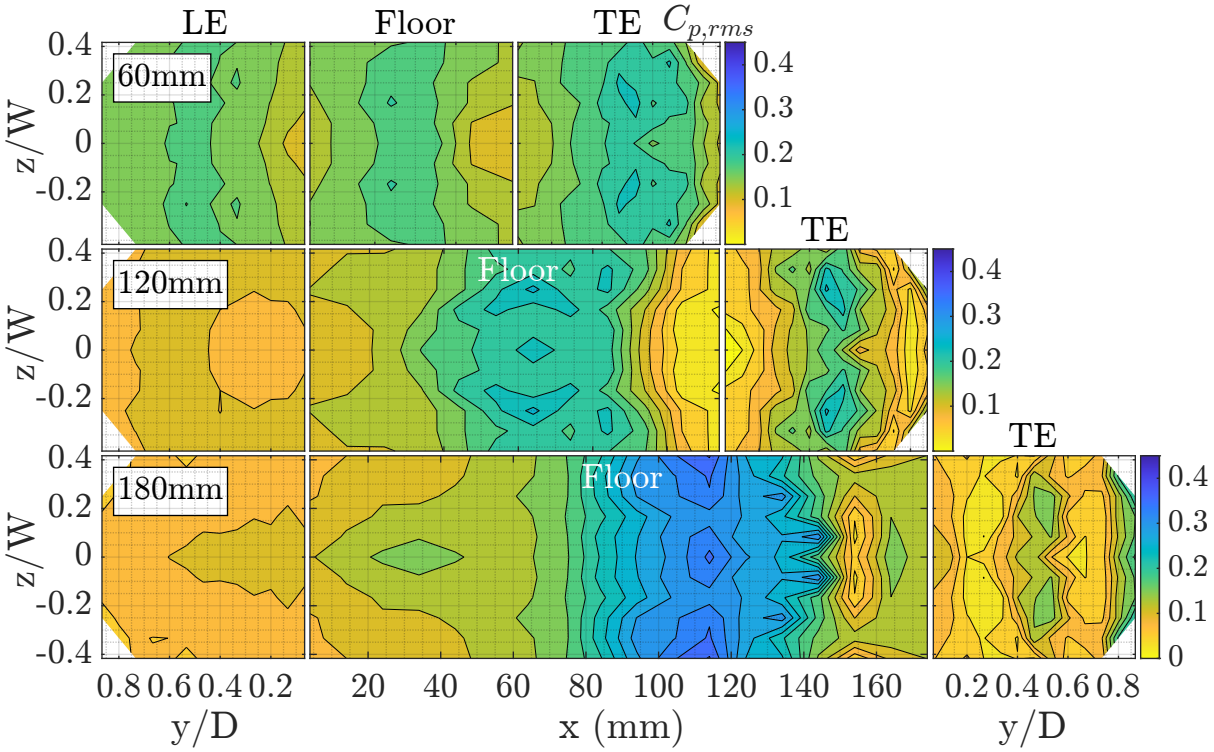

Figure D.1: USP: ΔL for C13, C15, C17: Parabola U/S, W = 60mm, Re_∞/m = 3.1×10^6

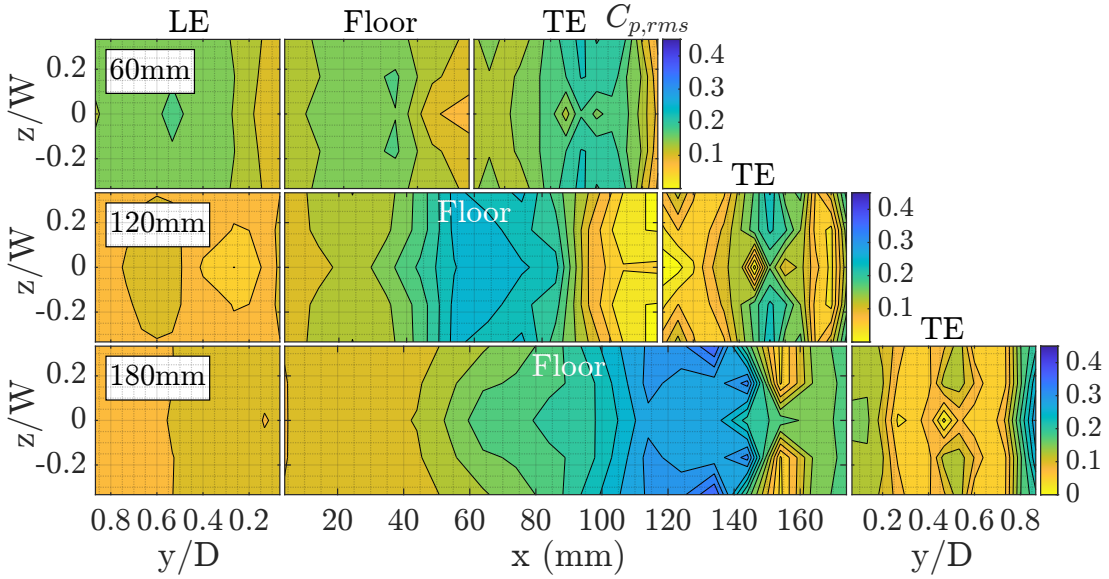

Figure D.2: USP: ΔL for C14, C16, C18: Parabola U/S, W = 30mm, Re_∞/m = 3.1×10^6

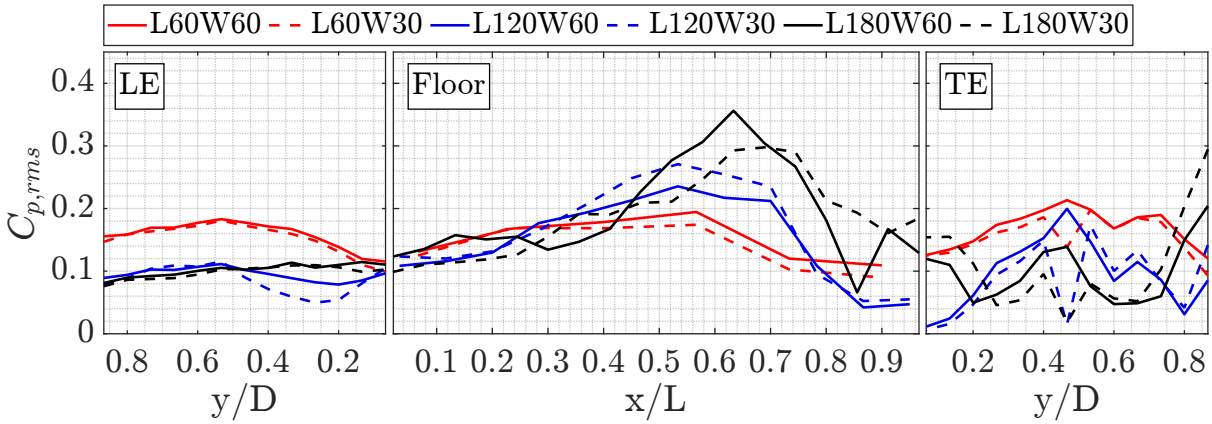

Figure D.3: USP: ΔL and ΔW: Parabola U/S at Re_∞/m = 3.1×10^6

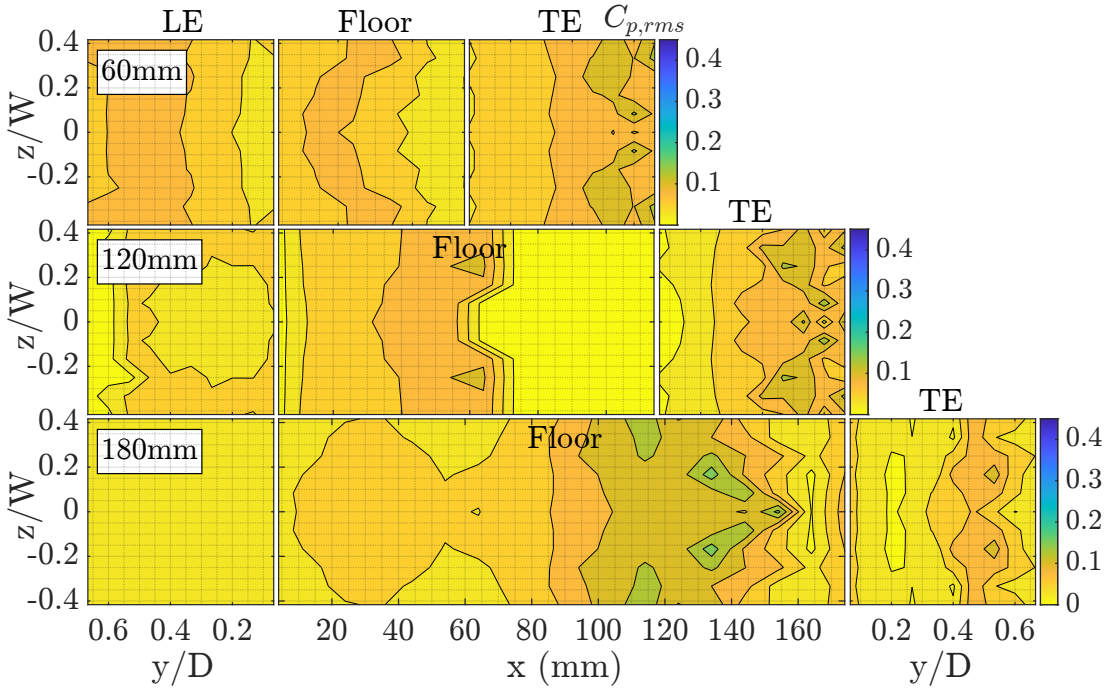

Figure D.4: USP: ΔL for C19, C21, C23: Flat-Plate U/S, W = 60mm, Re_∞/m = 3.1×10^6

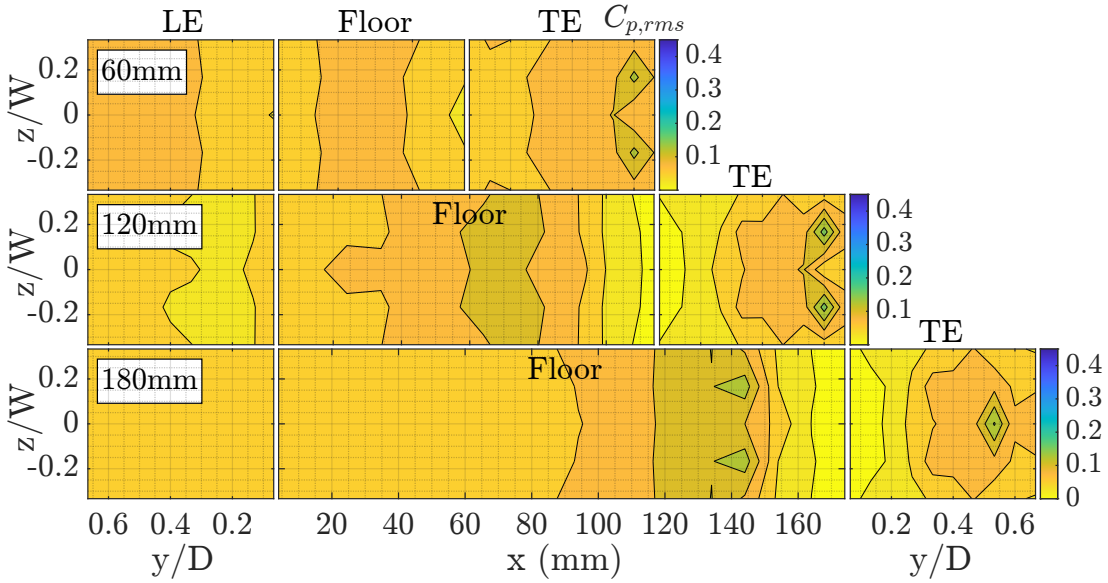

Figure D.5: USP: ΔL for C20, C22, C24: Flat-Plate U/S, W = 30mm, $Re_\infty/m = 3.1\times10^6$

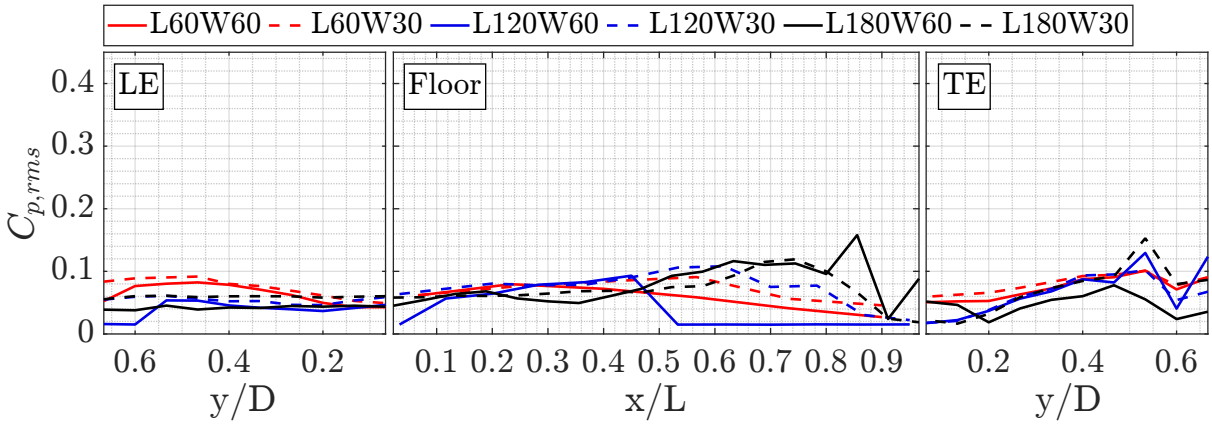

Figure D.6: USP: ΔL and ΔW: Flat-Plate U/S at $Re_\infty/m = 3.1\times10^6$

D.1.2 Effect of Free-Stream Reynolds Number Re_∞/m

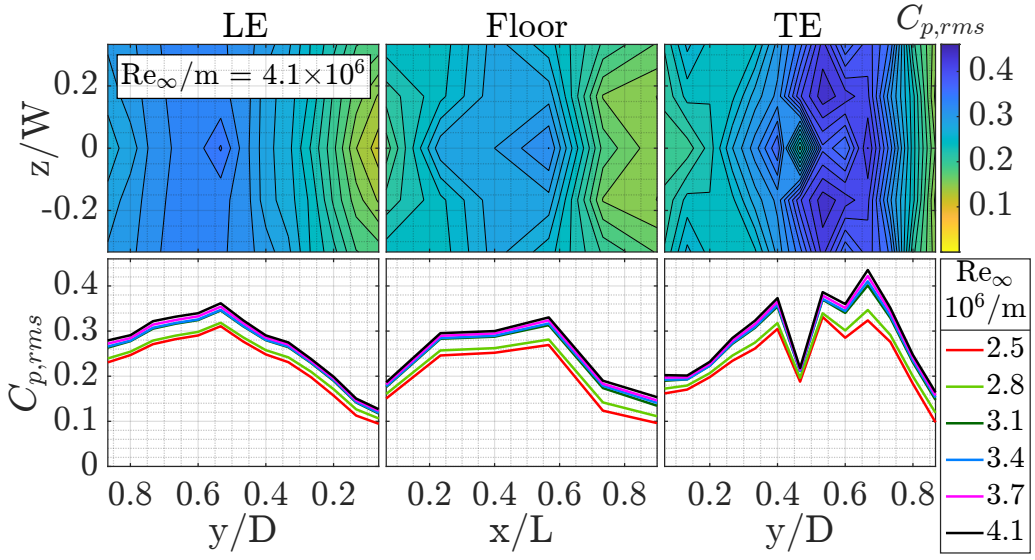

Figure D.7: USP: ΔRe_∞/m for C2: L/D = 1, L/W = 2, Conic U/S

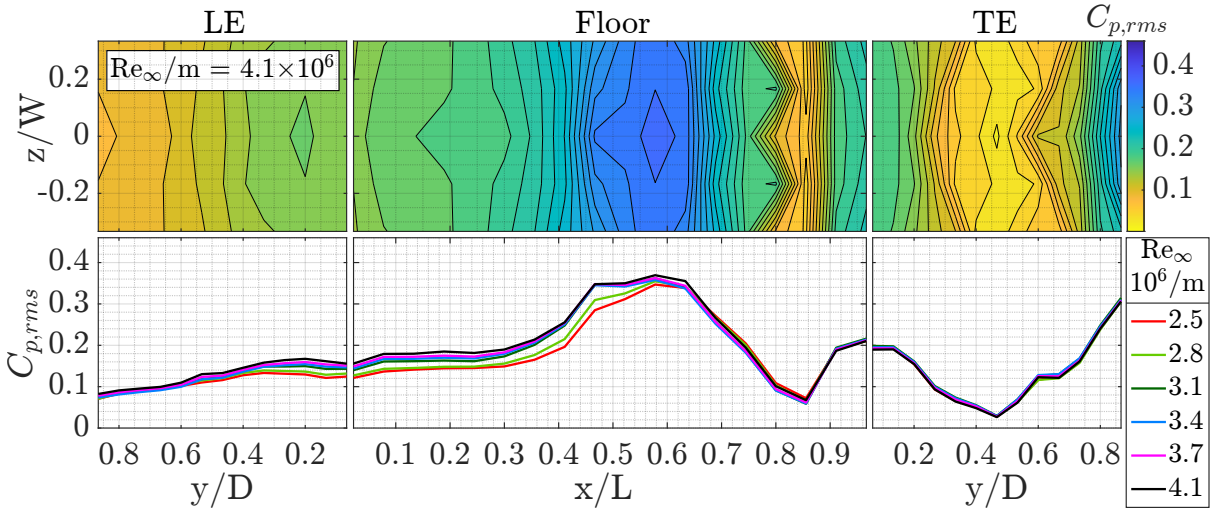

Figure D.8: USP: $\Delta \mathrm{Re}_\infty$/m for C6: L/D = 3, L/W = 6, Conic U/S

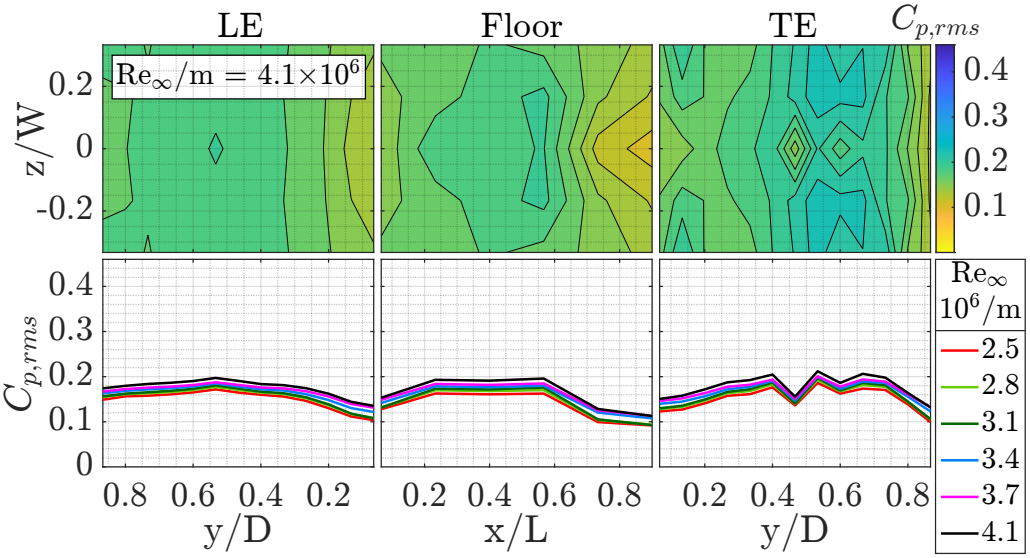

Figure D.9: USP: $\Delta \mathrm{Re}_\infty$/m for C8: L/D = 1, L/W = 2, Ogive U/S

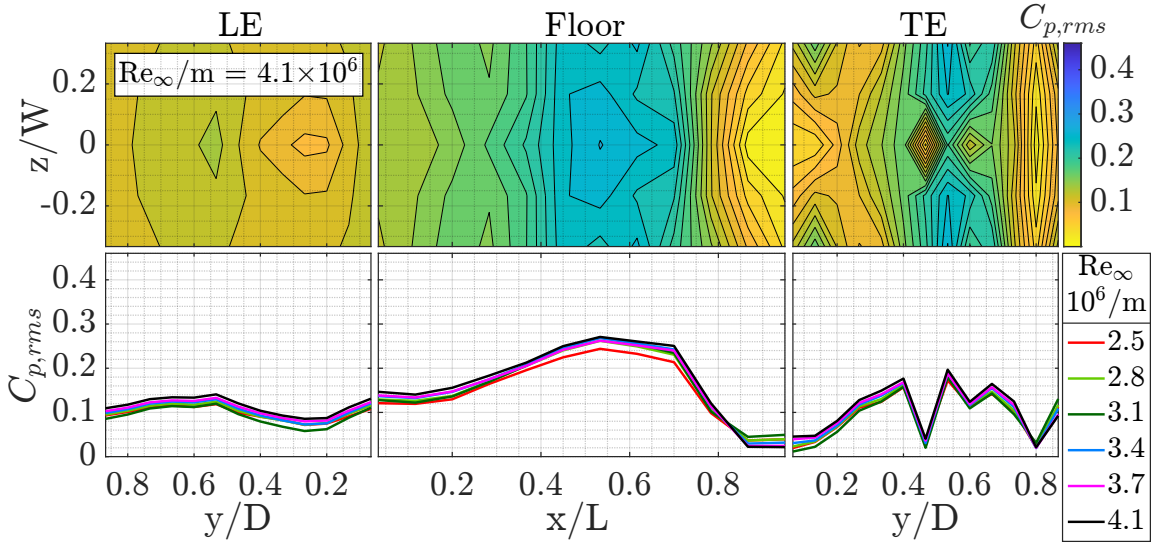

Figure D.10: USP: $\Delta \mathrm{Re}_\infty$/m for C10: L/D = 2, L/W = 4, Ogive U/S

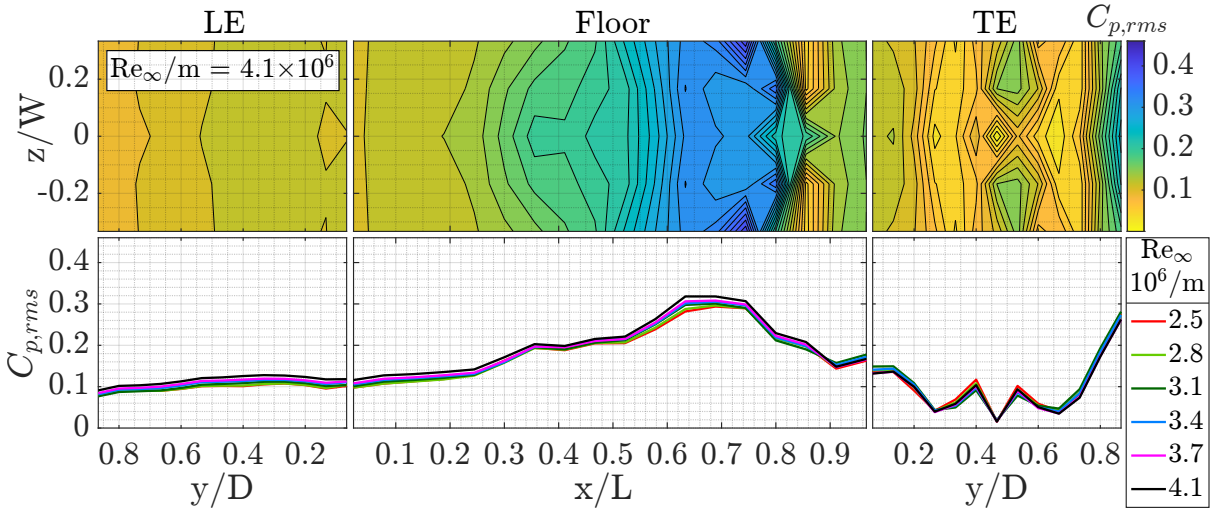

Figure D.11: USP: $\Delta\mathrm{Re}_\infty/\mathrm{m}$ for C12: L/D = 3, L/W = 6, Ogive U/S

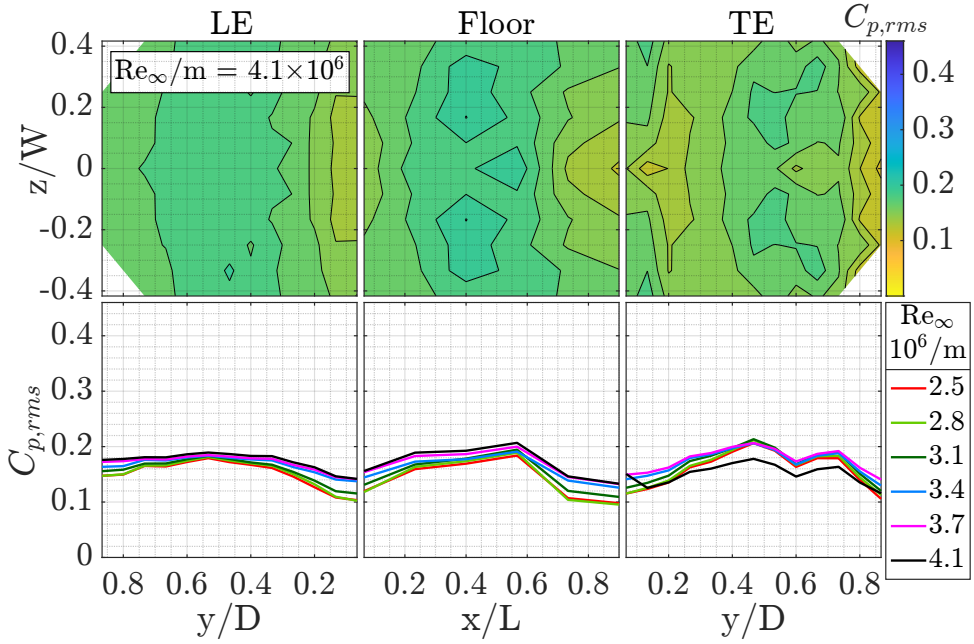

Figure D.12: USP: $\Delta\mathrm{Re}_\infty/\mathrm{m}$ for C13: L/D = 1, L/W = 1, Parabola U/S

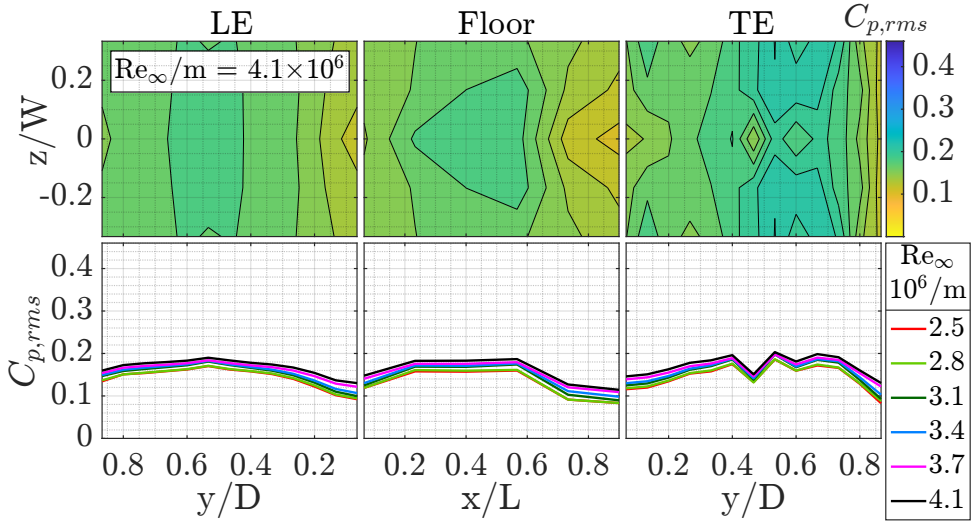

Figure D.13: USP: $\Delta\mathrm{Re}_\infty/\mathrm{m}$ for C14: L/D = 1, L/W = 2, Parabola U/S

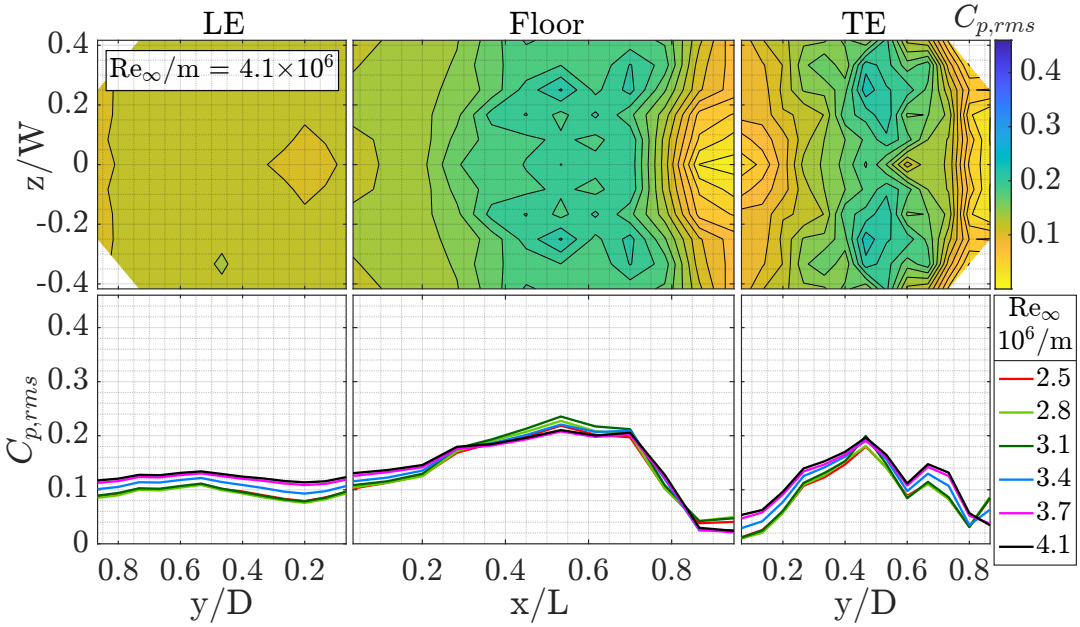

Figure D.14: USP: $\Delta\mathrm{Re}_\infty$/m for C15: L/D = 2, L/W = 2, Parabola U/S

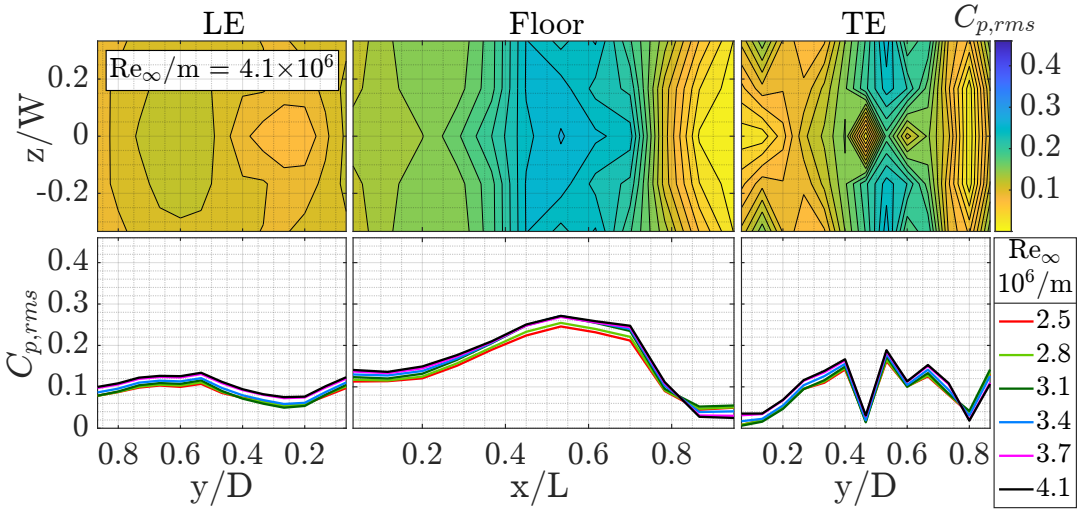

Figure D.15: USP: $\Delta\mathrm{Re}_\infty$/m for C16: L/D = 2, L/W = 4, Parabola U/S

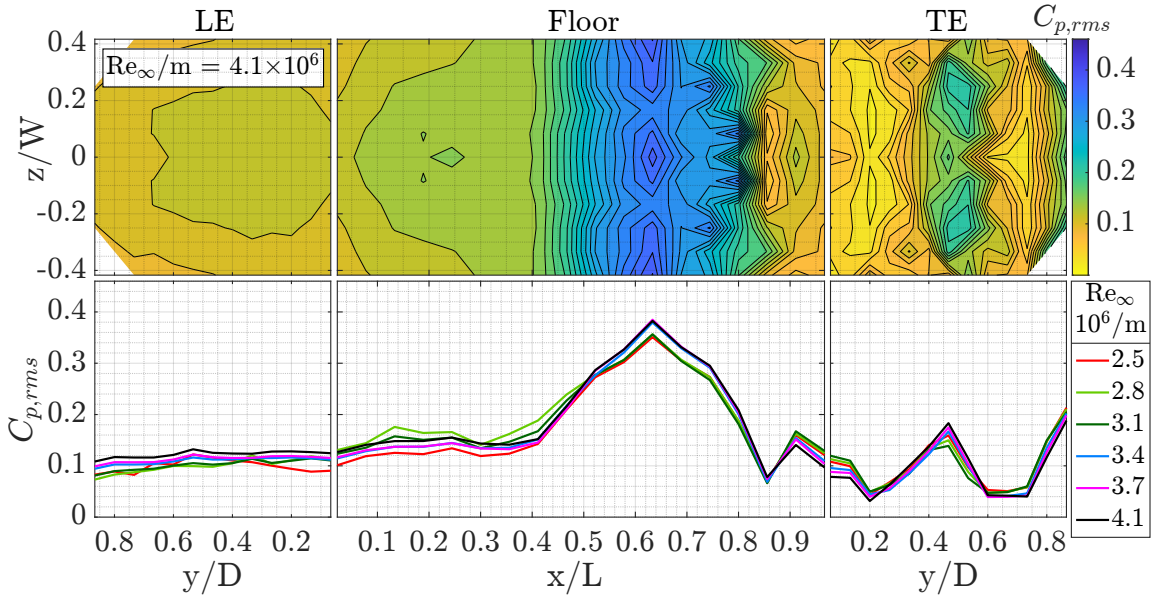

Figure D.16: USP: $\Delta\mathrm{Re}_\infty$/m for C17: L/D = L/W = 3, Parabola U/S

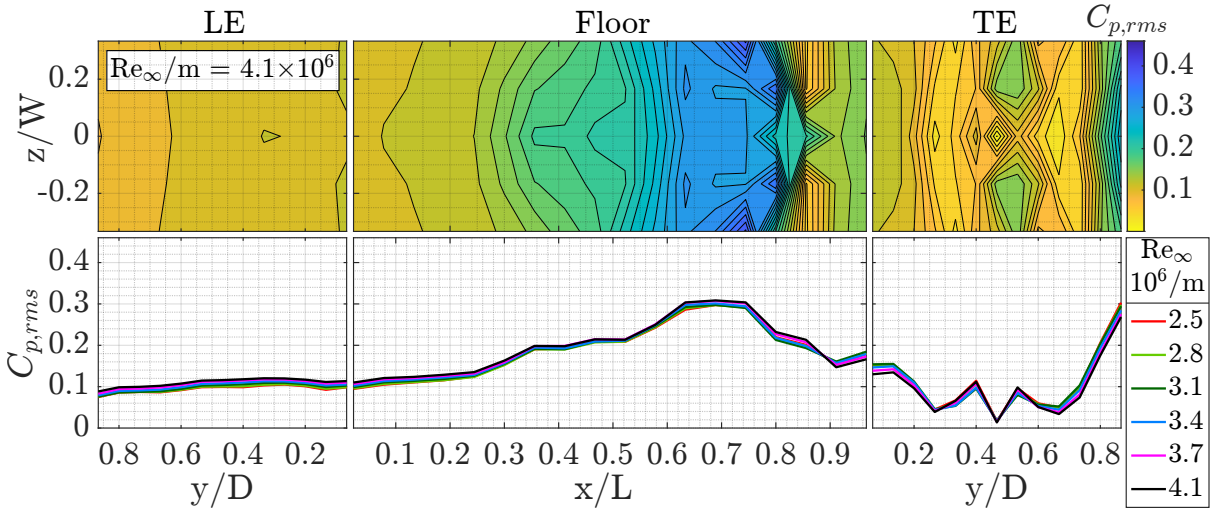

Figure D.17: USP: $\Delta\mathrm{Re}_\infty$/m for C18: L/D = 3, L/W = 6, Parabola U/S

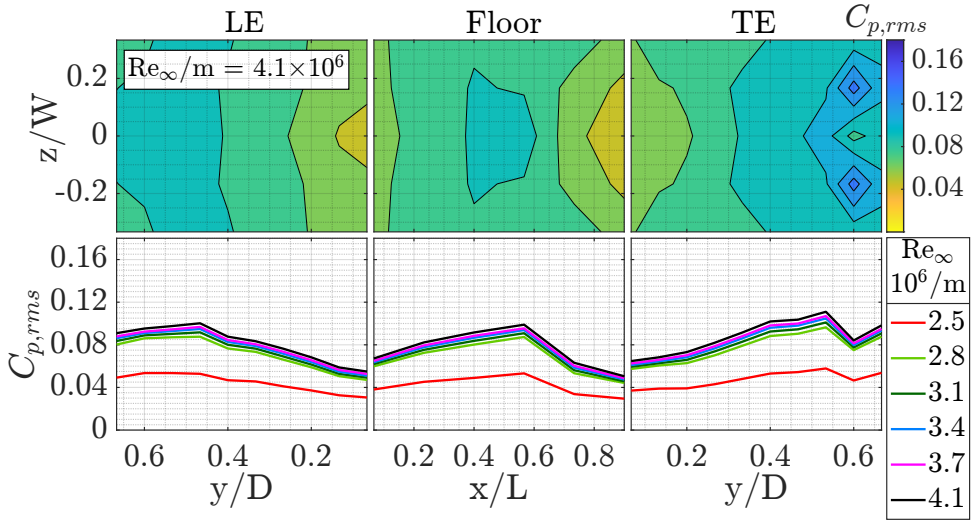

Figure D.18: USP: $\Delta\mathrm{Re}_\infty$/m for C20: L/D = 1, L/W = 2, Flat U/S

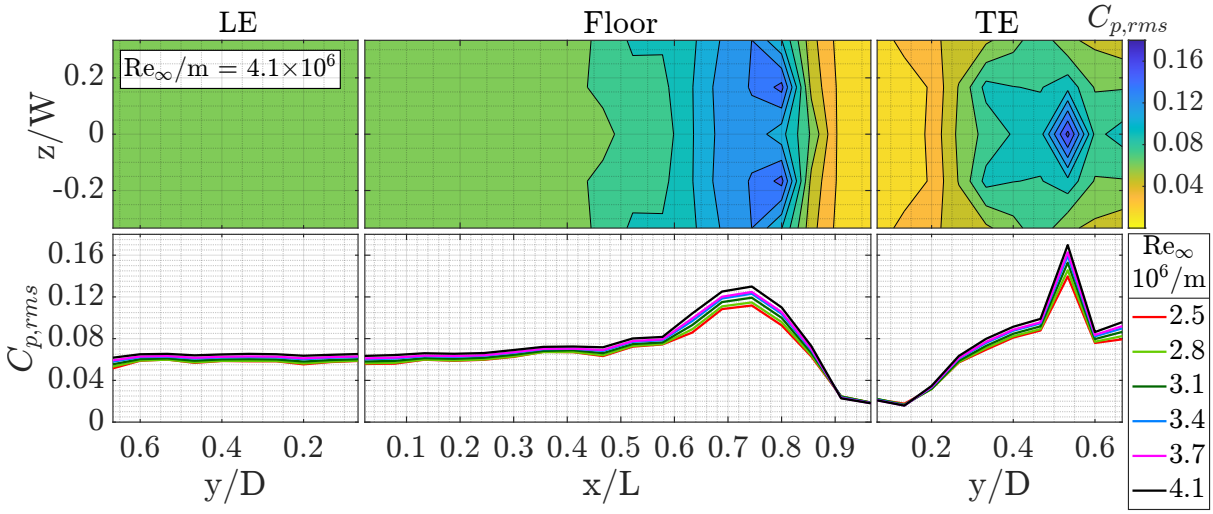

Figure D.19: USP: $\Delta\mathrm{Re}_\infty$/m for C24: L/D = 3, L/W = 6, Flat U/S

D.2 Surface Pressure Spectral Data

Tables D.1-D.24 present dominant mode f (Hz) from DMD, and corresponding SPL (dB) from FFT, of USP data for each cavity case, and U_∞ (m/s) per Section 4.5.2. There was deviation in space for mode dominance, however, mode 1-3 frequencies tend to remain only switching dominance in space, also with U_∞. There were slight deviations of 1-5Hz in space, which is considered measurement uncertainty, from the tube distortion effect.

Table D.1: USP: Modes of C1: L/D = 1, L/W = 1, Conic U/S

U_∞	Mode 1		Mode 2		Mode 3		Mode 4	
(m/s)	f (Hz)	SPL (dB)	f (Hz)	SPL (dB)	f (Hz)	SPL (dB)	f (Hz)	SPL (dB)
10	22	167	50	175	99	148	199	154
15	25	175	51	177	199	152	-	-
20	31	178	50	175	199	147	-	-
25	34	180	53	184	84	164	199	149
30	38	186	56	197	199	161	-	-
35	39	190	57	198	199	167	-	-
40	44	191	62	199	202	170	-	-
45	51	192	73	197	101	211	199	186
50	50	193	81	202	-	-	-	-
55	50	197	89	205	-	-	-	-
60	93	206	-	-	-	-	-	-
65	33	208	207	182	-	-	-	-

Table D.2: USP: Modes of C2: L/D = 1, L/W = 2, Conic U/S

U_∞	Mode 1		Mode 2		Mode 3		Mode 4	
(m/s)	f (Hz)	SPL (dB)	f (Hz)	SPL (dB)	f (Hz)	SPL (dB)	f (Hz)	SPL (dB)
10	18	167	50	181	100	165	199	152
15	26	172	50	178	100	169	199	147
20	34	170	50	177	100	162	199	145
25	31	175	50	173	100	162	199	157
30	38	168	50	182	100	165	199	150
35	50	198	100	171	100	168	199	150
40	50	178	65	183	100	171	199	152
45	21	181	50	191	73	203	199	153
50	50	191	81	184	162	168	199	154
55	18	190	50	184	89	205	199	155
60	18	197	72	184	96	193	199	160
65	100	194	123	177	165	171	199	162

Table D.3: USP: Modes of C3: L/D = 2, L/W = 2, Conic U/S

U_∞	Mode 1		Mode 2		Mode 3		Mode 4	
(m/s)	f (Hz)	SPL (dB)	f (Hz)	SPL (dB)	f (Hz)	SPL (dB)	f (Hz)	SPL (dB)
10	18	170	50	180	199	145	-	-
15	26	174	50	177	199	139	-	-
20	26	180	50	184	100	160	199	145
25	33	195	50	197	100	214	-	-
30	31	200	50	201	100	188	-	-
35	50	203	57	207	100	190	-	-
40	50	205	80	200	-	-	-	-
45	23	210	50	212	73	209	-	-
50	25	210	50	193	163	190	-	-
55	35	220	88	215	-	-	-	-
60	96	205	206	187	-	-	-	-
65	100	210	208	190	-	-	-	-

Table D.4: USP: Modes of C4: L/D = 2, L/W = 4, Conic U/S

U_∞	Mode 1		Mode 2		Mode 3		Mode 4	
(m/s)	f (Hz)	SPL (dB)	f (Hz)	SPL (dB)	f (Hz)	SPL (dB)	f (Hz)	SPL (dB)
10	18	171	50	175	100	150	199	151
15	28	180	50	169	100	151	199	150
20	34	176	50	171	100	152	199	152
25	50	180	84	189	100	160	199	152
30	50	198	100	165	100	150	199	154
35	50	196	115	165	199	176	-	-
40	50	201	65	186	199	150	-	-
45	21	177	50	185	73	201	199	154
50	50	190	80	182	161	162	178	160
55	37	209	50	186	88	213	177	164
60	50	180	72	175	96	202	-	-
65	50	187	104	197	183	208	-	-

Table D.5: USP: Modes of C5: L/D = 3, L/W = 3, Conic U/S

U_∞	Mode 1		Mode 2		Mode 3		Mode 4	
(m/s)	f (Hz)	SPL (dB)	f (Hz)	SPL (dB)	f (Hz)	SPL (dB)	f (Hz)	SPL (dB)
10	28	180	51	198	90	185	150	160
15	29	195	51	200	197	150	-	-
20	30	200	89	203	152	152	197	144
25	24	203	43	207	89	160	199	160
30	24	205	53	211	89	155	199	144
35	24	207	52	212	90	159	200	172
40	30	202	50	212	100	201	-	-

45	31	205	62	211	89	207	100	206
50	23	212	67	210	102	215	-	-
55	34	223	50	226	80	217	-	-
60	34	228	50	226	176	204	-	-
65	50	227	100	223	-	-	-	-

Table D.6: USP: Modes of C6: L/D = 3, L/W = 6, Conic U/S

U_∞	Mode 1		Mode 2		Mode 3		Mode 4	
(m/s)	f (Hz)	SPL (dB)	f (Hz)	SPL (dB)	f (Hz)	SPL (dB)	f (Hz)	SPL (dB)
10	18	157	50	172	100	148	199	148
15	19	149	26	179	50	169	100	150
20	30	165	50	177	69	158	100	154
25	43	175	50	181	100	150	199	153
30	25	164	50	181	100	167	199	150
35	29	171	50	175	58	190	199	148
40	22	184	50	178	65	186	-	-
45	28	185	50	184	73	194	-	-
50	37	184	50	189	81	180	-	-
55	28	188	50	190	89	208	199	163
60	50	188	96	197	199	173	-	-
65	50	187	91	188	104	193	208	179

Table D.7: USP: Modes of C7: L/D = 1, L/W = 1, Ogive U/S

U_∞	Mode 1		Mode 2		Mode 3		Mode 4	
(m/s)	f (Hz)	SPL (dB)	f (Hz)	SPL (dB)	f (Hz)	SPL (dB)	f (Hz)	SPL (dB)
10	19	168	50	174	100	146	199	148
15	26	169	50	173	100	150	199	151
20	34	176	50	172	100	155	199	146
25	50	170	84	171	100	156	199	145
30	50	167	100	171	199	155	-	-
35	50	172	57	191	115	162	199	154
40	50	175	65	190	84	172	116	165
45	50	181	73	195	199	150	-	-
50	50	188	81	191	97	177	162	165
55	34	184	50	183	166	163	-	-
60	50	195	96	201	116	178	-	-
65	100	220	124	199	209	189	-	-

Table D.8: USP: Modes of C8: L/D = 1, L/W = 2, Ogive U/S

U_∞	Mode 1		Mode 2		Mode 3		Mode 4	
(m/s)	f (Hz)	SPL (dB)	f (Hz)	SPL (dB)	f (Hz)	SPL (dB)	f (Hz)	SPL (dB)
10	19	164	50	180	100	166	199	153
15	26	177	50	170	100	164	199	152
20	34	170	50	172	69	157	100	170
25	42	173	50	156	84	165	100	156
30	18	158	50	178	100	167	199	145
35	50	179	57	192	100	179	199	157
40	50	172	65	193	100	167	-	-
45	50	182	73	197	100	170	-	-
50	50	189	81	189	100	173	-	-
55	50	185	88	206	176	167	-	-
60	50	192	96	201	-	-	-	-
65	100	197	208	188	-	-	-	-

Table D.9: USP: Modes of C9: L/D = 2, L/W = 2, Ogive U/S

U_∞	Mode 1		Mode 2		Mode 3		Mode 4	
(m/s)	f (Hz)	SPL (dB)	f (Hz)	SPL (dB)	f (Hz)	SPL (dB)	f (Hz)	SPL (dB)
10	19	154	50	179	100	134	199	141
15	26	172	50	178	100	148	199	144
20	34	174	50	179	100	160	199	142
25	42	176	50	181	100	168	199	147
30	50	186	100	165	199	143	-	-
35	50	182	67	183	199	155	-	-
40	34	181	50	199	65	188	199	153
45	50	184	73	200	92	183	199	153
50	50	191	84	186	-	-	-	-
55	50	187	88	206	-	-	-	-
60	37	188	96	201	193	169	-	-
65	53	191	104	192	208	172	-	-

Table D.10: USP: Modes of C10: L/D = 2, L/W = 4, Ogive U/S

U_∞	Mode 1		Mode 2		Mode 3		Mode 4	
(m/s)	f (Hz)	SPL (dB)	f (Hz)	SPL (dB)	f (Hz)	SPL (dB)	f (Hz)	SPL (dB)
10	19	176	50	179	199	149	-	-
15	26	179	50	179	199	151	-	-
20	34	171	50	169	69	155	199	149
25	42	176	50	177	84	164	199	149
30	50	186	100	187	199	152	-	-
35	57	184	115	167	199	154	-	-
40	32	180	50	180	65	188	199	150

45	50	193	73	185	199	157	-	-
50	34	187	50	187	81	192	162	174
55	39	191	63	185	89	206	-	-
60	28	203	50	193	73	190	96	203
65	100	191	208	187	-	-	-	-

Table D.11: USP: Modes of C11: L/D = 3, L/W = 3, Ogive U/S

U_∞	Mode 1		Mode 2		Mode 3		Mode 4	
(m/s)	f (Hz)	SPL (dB)	f (Hz)	SPL (dB)	f (Hz)	SPL (dB)	f (Hz)	SPL (dB)
10	25	172	50	174	84	157	199	139
15	29	178	59	173	97	162	137	152
20	35	186	55	186	97	190	138	157
25	37	199	72	198	88	192	120	177
30	47	200	153	200	197	193	-	-
35	28	205	50	211	73	215	154	191
40	22	206	42	215	66	222	89	200
45	23	209	36	213	68	224	134	195217
50	26	211	42	220	100	224	150	216
55	27	220	53	228	76	231	97	223
60	53	222	62	230	96	227	114	226
65	16	222	48	231	100	199	121	192

Table D.12: USP: Modes of C12: L/D = 3, L/W = 6, Ogive U/S

U_∞	Mode 1		Mode 2		Mode 3		Mode 4	
(m/s)	f (Hz)	SPL (dB)	f (Hz)	SPL (dB)	f (Hz)	SPL (dB)	f (Hz)	SPL (dB)
10	19	166	50	182	100	158	199	147
15	25	180	50	172	96	163	199	145
20	50	168	68	155	100	150	199	142
25	42	171	50	173	83	165	199	137
30	50	176	100	167	150	153	199	145
35	50	176	58	191	115	160	172	147
40	50	176	65	186	130	160	199	150
45	50	185	73	194	92	176	182	159
50	50	190	80	183	125	173	182	165
55	89	205	101	182	157	171	182	167
60	74	188	96	202	122	178	192	168
65	39	189	104	200	182	184	207	180

Table D.13: USP: Modes of C13: L/D = 1, L/W = 1, Parabola U/S

U_∞	Mode 1		Mode 2		Mode 3		Mode 4	
(m/s)	f (Hz)	SPL (dB)	f (Hz)	SPL (dB)	f (Hz)	SPL (dB)	f (Hz)	SPL (dB)
10	20	171	50	173	100	148	199	149
15	26	167	50	169	53	158	199	140
20	34	178	50	170	69	158	199	143
25	42	172	50	173	84	168	199	150
30	50	179	100	177	150	160	199	149
35	44	175	58	197	117	172	199	151
40	50	176	67	191	132	165	199	162
45	18	184	73	197	199	155	-	-
50	31	185	50	188	81	193	161	171
55	50	185	90	208	100	177	-	-
60	50	186	98	201	193	172	-	-
65	100	209	104	198	209	185	-	-

Table D.14: USP: Modes of C14: L/D = 1, L/W = 2, Parabola U/S

U_∞	Mode 1		Mode 2		Mode 3		Mode 4	
(m/s)	f (Hz)	SPL (dB)	f (Hz)	SPL (dB)	f (Hz)	SPL (dB)	f (Hz)	SPL (dB)
10	20	156	50	179	100	165	199	150
15	34	171	50	173	100	163	199	151
20	34	168	50	171	100	152	199	150
25	42	173	50	177	83	171	199	151
30	50	186	100	174	199	153	-	-
35	50	177	57	190	91	174	199	156
40	18	177	50	177	66	192	199	147
45	18	181	50	177	73	195	199	154
50	28	188	50	190	81	191	241	137
55	50	185	88	207	-	-	-	-
60	50	183	72	181	96	203	192	166
65	56	193	83	195	104	201	208	186

Table D.15: USP: Modes of C15: L/D = 2, L/W = 2, Parabola U/S

U_∞	Mode 1		Mode 2		Mode 3		Mode 4	
(m/s)	f (Hz)	SPL (dB)	f (Hz)	SPL (dB)	f (Hz)	SPL (dB)	f (Hz)	SPL (dB)
10	20	169	50	177	152	137	199	148
15	26	172	50	175	100	150	199	150
20	26	163	50	178	199	150	-	-
25	42	181	50	184	84	169	199	146
30	50	187	199	152	-	-	-	-
35	50	191	57	186	199	150	-	-
40	35	184	50	186	66	189	199	151

45	50	188	73	195	-	-	-	-
50	50	209	81	208	155	176	-	-
55	33	195	50	189	63	207	89	207
60	63	202	96	203	-	-	-	-
65	27	208	64	209	100	194	208	175

Table D.16: USP: Modes of C16: L/D = 2, L/W = 4, Parabola U/S

U_∞	Mode 1		Mode 2		Mode 3		Mode 4	
(m/s)	f (Hz)	SPL (dB)	f (Hz)	SPL (dB)	f (Hz)	SPL (dB)	f (Hz)	SPL (dB)
10	20	157	50	177	100	156	199	150
15	26	172	50	171	100	148	199	151
20	34	167	50	169	69	157	100	158
25	42	170	50	172	83	164	100	156
30	50	167	55	164	100	162	199	151
35	58	190	100	163	116	170	199	153
40	50	170	65	197	130	162	199	146
45	28	166	50	180	73	203	199	154
50	20	175	50	186	80	186	160	163
55	33	171	50	186	89	204	167	158
60	50	204	73	182	96	200	133	168
65	13	191	50	181	104	196	209	188

Table D.17: USP: Modes of C17: L/D = 3, L/W = 3, Parabola U/S

U_∞	Mode 1		Mode 2		Mode 3		Mode 4	
(m/s)	f (Hz)	SPL (dB)	f (Hz)	SPL (dB)	f (Hz)	SPL (dB)	f (Hz)	SPL (dB)
10	25	174	50	178	100	161	199	152
15	26	182	101	179	199	149	-	-
20	27	185	50	190	92	162	199	144
25	28	198	50	192	69	188	152	150
30	29	199	51	206	86	189	101	171
35	33	199	52	206	90	190	-	-
40	38	201	60	207	125	184	153	177
45	37	203	52	211	73	207	100	189
50	38	204	73	213	86	205	121	198
55	33	213	47	211	70	208	89	202
60	25	216	42	213	62	212	96	210
65	23	214	50	211	72	206	86	206

Table D.18: USP: Modes of C18: L/D = 3, L/W = 6, Parabola U/S

U_∞	Mode 1		Mode 2		Mode 3		Mode 4	
(m/s)	f (Hz)	SPL (dB)	f (Hz)	SPL (dB)	f (Hz)	SPL (dB)	f (Hz)	SPL (dB)
10	20	162	50	177	53	142	199	142
15	27	175	50	173	199	143	-	-
20	34	162	50	170	68	151	102	150
25	40	180	50	181	83	161	166	138
30	17	173	50	175	100	162	148	149
35	50	175	57	186	93	158	199	145
40	16	181	50	175	65	187	199	147
45	26	183	50	184	73	196	92	168
50	50	187	81	182	122	160	162	161
55	27	189	50	187	89	204	118	168
60	50	184	73	185	96	197	122	168
65	85	181	105	196	168	164	210	180

Table D.19: USP: Modes of C19: L/D = 1, L/W = 1, Flat U/S

U_∞	Mode 1		Mode 2		Mode 3		Mode 4	
(m/s)	f (Hz)	SPL (dB)	f (Hz)	SPL (dB)	f (Hz)	SPL (dB)	f (Hz)	SPL (dB)
10	20	166	50	156	100	132	152	120
15	26	172	50	166	62	141	103	131
20	30	167	50	163	102	154	150	133
25	32	165	67	163	100	153	150	135
30	38	176	50	158	100	148	150	139
35	53	171	72	160	100	150	150	150
40	31	163	54	164	75	155	100	130
45	22	167	50	164	74	160	150	-
50	24	172	67	170	100	140	150	126
55	16	176	50	173	90	200	-	-
60	16	177	89	170	105	191	-	-
65	25	172	73	167	97	187	-	-

Table D.20: USP: Modes of C20: L/D = 1, L/W = 2, Flat U/S

U_∞	Mode 1		Mode 2		Mode 3		Mode 4	
(m/s)	f (Hz)	SPL (dB)	f (Hz)	SPL (dB)	f (Hz)	SPL (dB)	f (Hz)	SPL (dB)
10	16	168	50	168	199	116	-	-
15	26	163	50	174	199	118	-	-
20	34	187	50	163	69	154	100	164
25	42	176	50	173	84	164	128	154
30	29	155	50	185	100	166	-	-
35	50	164	58	204	-	-	-	-
40	18	169	66	171	84	155	125	155

45	18	172	50	170	73	195	88	169
50	18	172	50	180	71	187	92	173
55	19	177	90	201	-	-	-	-
60	24	180	59	173	97	201	-	-
65	19	176	105	201	186	166	210	169

Table D.21: USP: Modes of C21: L/D = 2, L/W = 2, Flat U/S

U_∞	Mode 1		Mode 2		Mode 3		Mode 4	
(m/s)	f (Hz)	SPL (dB)	f (Hz)	SPL (dB)	f (Hz)	SPL (dB)	f (Hz)	SPL (dB)
10	24	142	52	160	100	140	199	125
15	25	148	53	178	100	143	198	124
20	26	149	51	158	69	152	100	130
25	28	163	58	182	100	169	152	141
30	28	170	53	169	72	156	152	128
35	29	175	56	190	71	158	152	137
40	33	179	69	182	103	154	152	138
45	30	189	80	193	152	158	199	130
50	44	181	81	186	152	162	199	141
55	39	193	90	203	-	-	-	-
60	20	191	37	203	97	189	112	177
65	22	194	55	204	105	193	-	-

Table D.22: USP: Modes of C22: L/D = 2, L/W = 4, Flat U/S

U_∞	Mode 1		Mode 2		Mode 3		Mode 4	
(m/s)	f (Hz)	SPL (dB)	f (Hz)	SPL (dB)	f (Hz)	SPL (dB)	f (Hz)	SPL (dB)
10	16	165	50	168	100	133	199	120
15	26	163	50	177	100	142	152	130
20	23	152	34	187	50	161	100	143
25	28	154	50	177	85	160	100	147
30	23	158	50	168	100	157	-	-
35	50	170	58	187	-	-	-	-
40	23	182	50	166	66	190	132	155
45	55	171	74	195	112	166	221	139
50	21	181	29	187	50	175	82	180
55	31	188	90	207	-	-	-	-
60	32	199	97	195	-	-	-	-
65	23	180	105	198	209	163	-	-

Table D.23: USP: Modes of C23: L/D = 3, L/W = 3, Flat U/S

U_∞	Mode 1		Mode 2		Mode 3		Mode 4	
(m/s)	f (Hz)	SPL (dB)	f (Hz)	SPL (dB)	f (Hz)	SPL (dB)	f (Hz)	SPL (dB)
10	26	146	50	140	102	158	199	126
15	27	149	50	157	101	160	199	125
20	20	159	44	158	100	165	190	120
25	24	158	43	170	51	158	193	121
30	25	155	54	177	100	162	198	119
35	26	171	52	185	60	160	198	120
40	27	155	58	180	100	163	199	125
45	28	170	58	195	100	165	-	-
50	29	172	57	196	83	154	104	141
55	26	184	50	203	89	155	202	129
60	21	186	50	202	97	167	-	-
65	16	180	50	193	104	165	208	140

Table D.24: USP: Modes of C24: L/D = 3, L/W = 6, Flat U/S

U_∞	Mode 1		Mode 2		Mode 3		Mode 4	
(m/s)	f (Hz)	SPL (dB)	f (Hz)	SPL (dB)	f (Hz)	SPL (dB)	f (Hz)	SPL (dB)
10	16	152	35	133	50	164	100	145
15	24	140	55	164	100	147	199	127
20	34	156	50	175	73	158	100	143
25	18	149	43	179	50	155	100	152
30	31	149	51	160	100	156	199	122
35	33	157	58	199	100	150	115	146
40	30	159	50	173	66	177	89	156
45	21	163	50	166	73	194	85	161
50	50	165	82	187	163	151	188	151
55	21	177	41	170	50	175	93	207
60	26	171	50	173	97	199	168	159
65	29	173	105	203	134	169	210	174

D.3 Hot-Wire Spectral Data

Presented in Tables D.25-D.32 are frequency (kHz) and SPL (dB), for mode 1-4 of each HWA case, and select U_∞ (m/s) and velocity profile points, highlighting important data features, for assessment of HWA signals. Selection of these vertical points is discussed in Section 5.3.

Table D.25: HWA: Modes of C5: Cavity Open, Conic U/S

Velocity Point		Mode 1		Mode 2		Mode 3		Mode 4	
U_∞	Y (mm)	f (kHz)	SPL	f (kHz)	SPL	f (kHz)	SPL	f (kHz)	SPL
20	1.2	4.05	108	9.58	90	-	-	-	-
20	1.5	4.03	107	9.59	90	-	-	-	-
	3.2	3.96	104	9.6	88	12.96	79	15.28	77
	32.3	3.75	97	9.68	85	12.96	78	15.6	75
30	1.2	3.03	116	9.93	99	-	-	-	-
	1.5	3	116	9.93	98	-	-	-	-
	3.2	2.95	112	9.95	93	12.96	85	-	-
	32.3	2.8	100	7.5	77	9.99	88	12.96	81
40	3.2	6.58	131	13.6	137	-	-	-	-
	32.3	1.94	104	6.57	145	12.6	133	13.03	141
50	1.2	7.45	114	12.87	111	-	-	-	-
	1.5	7.46	114	12.83	111	-	-	-	-
	3.2	6.6	112	7.22	111	7.5	109	12.76	114
	32.3	6.57	113	7.18	111	7.5	105	10.72	93

Table D.26: HWA: Modes of C11: Cavity Open, Ogive U/S

Velocity Point		Mode 1		Mode 2		Mode 3		Mode 4	
U_∞	Y (mm)	f (kHz)	SPL	f (kHz)	SPL	f (kHz)	SPL	f (kHz)	SPL
20	1.2	4.27	106	9.5	89	-	-	-	-
	1.5	4.24	105	9.52	88	-	-	-	-
	3.2	4.19	101	9.54	87	14.88	77	-	-
	32.3	4.03	97	9.59	85	15.16	76	-	-
30	1.2	9.78	102	-	-	-	-	-	-
	1.5	9.79	104	-	-	-	-	-	-
	3.2	9.8	99	-	-	-	-	-	-
	32.3	3.2	100	9.86	88	12.98	71	-	-
40	1.2	3.05	153	3.47	149	12.97	122	-	-
	1.5	3.05	153	3.47	145	12.97	122	-	-
	3.2	3.05	140	3.46	137	12.97	117	-	-
	32.3	0.3	100	2.2	83	6.85	101	12.97	116
50	1.2	6.97	124	12.97	125	-	-	-	-
	1.5	6.86	124	12.97	125	-	-	-	-
	3.2	6.85	127	12.97	127	-	-	-	-
	32.3	1.9	104	6.85	106	12.97	117	-	-

Table D.27: HWA: Modes of C17: Cavity Open, Parabola U/S

Velocity Point		Mode 1		Mode 2		Mode 3		Mode 4	
U_∞	Y (mm)	f (kHz)	SPL	f (kHz)	SPL	f (kHz)	SPL	f (kHz)	SPL
20	1.2	6.58	99	8.7	90	-	-	-	-
	1.5	6.57	99	8.7	90	-	-	-	-
	3.2	6.51	99	8.77	87	12.94	86	-	-
	32.3	0.3	106	6.41	96	8.8	85	21.95	85
30	1.2	6.18	113	8.87	106	-	-	-	-
	1.5	6.16	114	8.88	107	-	-	-	-
	3.2	6.11	106	8.89	97	12.94	93	-	-
	32.3	5.99	100	6.9	83	8.93	89	12.94	89
40	1.2	6.41	125	-	-	-	-	-	-
	1.5	6.4	126	-	-	-	-	-	-
	3.2	5.61	113	-	-	-	-	-	-
	32.3	2.75	88	5.55	103	6.18	109	6.38	96
50	1.2	8.61	124	-	-	-	-	-	-
	1.5	8.54	124	-	-	-	-	-	-
	3.2	8.4	120	-	-	-	-	-	-
	32.3	6.97	100	8.1	104	8.2	94	8.37	81

Table D.28: HWA: Modes of C23: Cavity Open, Flat U/S

Velocity Point		Mode 1		Mode 2	
U_∞	Y (mm)	f (kHz)	SPL	f (kHz)	SPL
20	1.2	10.42	95	-	-
	1.5	10.42	96	-	-
	3.2	10.43	97	-	-
	32.3	10.48	88	13.18	82
30	32.3	10.77	100	11.53	101
40	32.3	10.65	116	10.95	116
50	3.2	6.4	136	-	-
	32.3	10.65	132	-	-

Table D.29: HWA: Modes of C25: Cavity Closed, Conic U/S

Velocity Point		Mode 1		Mode 2		Mode 3		Mode 4	
U_∞	Y (mm)	f (kHz)	SPL	f (kHz)	SPL	f (kHz)	SPL	f (kHz)	SPL
20	1.2	10.46	91	-	-	-	-	-	-
	1.5	10.46	91	13.23	86	-	-	-	-
	3.2	10.47	90	13.23	85	-	-	-	-
	32.3	1.44	98	10.46	87	13.23	82	-	-
30	1.2	10.67	108	10.75	110	-	-	-	-
	1.5	10.63	106	10.79	109	-	-	-	-
	3.2	10.47	98	10.89	100	-	-	-	-

30	32.3	1.25	81	2.09	101	10.23	91	11.4	84
40	1.2	9.73	132	-	-	-	-	-	-
	1.5	9.75	132	-	-	-	-	-	-
	3.2	9.85	127	-	-	-	-	-	-
	32.3	0.7	104	6.4	91	10.3	93	11.17	95
50	1.2	8.95	118	-	-	-	-	-	-
	1.5	8.93	118	-	-	-	-	-	-
	3.2	7.09	110	9.07	112	11.04	110	-	-
	32.3	0.34	107	6.44	93	9.7	95	11.16	95

Table D.30: HWA: Modes of C26: Cavity Closed, Ogive U/S

Velocity Point		Mode 1		Mode 2		Mode 3		Mode 4	
U_∞	Y (mm)	f (kHz)	SPL	f (kHz)	SPL	f (kHz)	SPL	f (kHz)	SPL
20	1.2	10.78	88	11.67	82	-	-	-	-
	1.5	10.79	88	11.64	82	-	-	-	-
	3.2	10.8	87	11.6	80	-	-	-	-
	32.3	0.46	98	10.8	86	11.68	78	-	-
30	1.2	9.59	103	11.9	105	-	-	-	-
	1.5	9.6	103	11.94	107	-	-	-	-
	3.2	3.9	115	9.63	100	12	102	-	-
	32.3	3.65	101	6.19	84	9.7	91	12.08	85
40	1.2	10.89	122	-	-	-	-	-	-
	1.5	10.91	122	-	-	-	-	-	-
	3.2	10.93	119	-	-	-	-	-	-
	32.3	2.59	103	6.4	92	10.07	93	11.04	91
50	1.2	7.12	112	9.65	117	11.91	112	-	-
	1.5	7.09	111	9.65	117	11.9	111	-	-
	3.2	7.08	106	9.65	110	-	-	-	-
	32.3	1.06	105	7.09	98	9.89	99	10.58	95

Table D.31: HWA: Modes of C27: Cavity Closed, Parabola U/S

Velocity Point		Mode 1		Mode 2		Mode 3		Mode 4	
U_∞	Y (mm)	f (kHz)	SPL	f (kHz)	SPL	f (kHz)	SPL	f (kHz)	SPL
20	1.2	10.84	80	10.95	87	-	-	-	-
	1.5	10.81	81	10.96	88	-	-	-	-
	3.2	10.74	80	10.97	87	-	-	-	-
	32.3	0.16	103	0.33	92	10.69	77	10.98	85
30	32.3	1.45	101	6.26	79	11.41	90	11.5	79
40	1.2	2.14	126	2.7	126	6.77	112	11.12	113
	1.5	2.15	125	2.78	125	6.54	111	11.14	113
	3.2	2.21	120	2.78	120	6.51	107	11.14	106
	32.3	2.39	104	2.78	97	6.35	96	11.73	94

50	1.2	3.77	118	6.76	111	7.51	110	9.55	117
	1.5	3.81	117	6.76	110	7.51	109	9.56	116
	3.2	3.97	115	6.76	107	7.51	105	9.6	110
	32.3	4.35	105	6.74	99	7.5	97	9.99	103

Table D.32: HWA: Modes of C28: Cavity Closed, Flat U/S

Velocity Point		Mode 1		Mode 2		Mode 3	
U_∞	Y (mm)	f	SPL	f	SPL	f	SPL
20	1.5	10.48	98.3	-	-	-	-
	3.2	10.5	95.7	-	-	-	-
	32.3	10.54	86	12.88	80.2	-	-
30	3.2	10.91	114	-	-	-	-
	32.3	12.04	96.9	12.22	94.4	-	-
40	32.3	5.89	115	10.95	116	11.06	114.8
50	32.3	9.89	124.8	-	-	-	-

Appendix E

Viscid Physical Cavity Model

This study observed a significant change in cavity response due to decreasing BL δ, and increasing $dp/dx < 0$, as a large increase in internal cavity surface pressure, shifting dominant frequency, and mode structure by proxy, with cavity geometry. An update to Rossiter's [2] model was thus proposed, composing dimensionless frequency from a viscid physical model, considering Plumblee et al [3], East [8] and Block [6] for incompressible flow, as follows.

E.1 Dimensionless Frequency

First, we consider the number of periodic components, or modes m. In cavity flow, three distinct factors coalesce; m_f and m_v, empirically phased by γ_v, as defined by Rossiter [2]. m_f is feedback from the cavity TE, m_v is vorticity from the cavity LE, and $\gamma_v = 0.25$ for best fit [2,6,8]. To give each cavity mode per;

$$m - \gamma_v = (m_f + m_v) - \gamma_v \tag{E.1}$$

Secondly, contoured $C_{p,rms}$ and its spectra, indicate large pressure oscillations, dependant on internal cavity geometry and U/S δ. Past research, aligns this behaviour to a standing wave for $\mathrm{L/D} \leq 1$ [3,8], and a primary recirculation mechanism [15,43] for $1 < \mathrm{L/D} < 5$. Both fed by periodic shedding of vorticity from the cavity LE, and feedback from the TE [2]. A standing wave is more dependant on the latter, as a function of cavity depth [8], represented by mode 1.

Thirdly, periodic component frequencies based on Strouhal number (St) for cavity flow, are proportional to U_∞, and inversely to cavity length. However, St decreases with increasing Re_∞ for incompressible $\mathrm{M}_\infty < 3$, due to: (1) increasing U_∞ or cavity length, with constant viscosity ν_∞, or, (2) decreasing ν_∞ at constant U_∞, and cavity length. Therefore, a relationship between viscosity, and U_∞ with cavity geometry, is required for incompressible flow. As viscosity is predominant over compressibility, and inertia is weak compared to higher speed flow, where M_∞ is prevalent. A correlative relationships to Strouhal is suggested of:

$$\mathrm{St} = \frac{f\mathrm{L}}{\mathrm{U}_\infty} \propto f\left(\mathrm{U}_\infty \sim \mathrm{Re}_\infty, \mathrm{L}, \mathrm{D}, \delta, \delta^*, \frac{dp}{dx}\right)$$

Based on Prandtl BL formulation in Appendix B, effective viscosity with respect to Re_∞, is reasonably represented by BL metrics of; disturbance δ, and mass displacement δ^* thickness. Leading to key wave equations to construct cavity dimensionless frequency, as follows.

Fourthly, the BL U/S thus viscid profile entering the cavity, defines flow separation at the cavity LE, which forms a SL over the cavity mouth. Separation occurs from the BL into the cavity, due to $dp/dx > 0$, which decelerates the flow, prompting curvature thus shed vorticity, proportional to effective viscid disturbance length δ/L, depth δ/D, and displaced mass depth δ^*/D, to relate U/S viscosity to cavity geometry. SL propagation is thus a function of gross cavity pressure oscillation, driven by U/S viscosity, resulting LE shed vorticity, and amplified by TE feedback. The resulting cycle drives mass momentum in and out of the cavity [97]. Therefore, it is reasonable to assume, vorticity $\propto \delta^*$, phase difference $\gamma_v\lambda_v$ to feedback, and propagation in time; $\kappa \mathrm{U}_\infty \Delta t$ through δ/L. While feedback $\propto$ distance travelled over the cavity, by a ratio cavity length to δ^*/D, travelling U/S in time by $\mathrm{a_c}\Delta t$, through δ/L. $\kappa = 0.57$ is the empirical constant ratio of U_∞, vortices travel over the cavity [2] in the SL, and $\mathrm{a_c}$ is cavity speed of sound.

Fifthly, to determine $\mathrm{a_c}$, we consider its relationship to a_∞. Rossiter [2] assumed $\mathrm{a_c} = \mathrm{a}_\infty$ for subsonic flow. However, for incompressible flow, separation characteristics change due to stronger viscosity. Effectively, the approaching flow already holds displaced mass δ^*, further displaced through $dp/dx > 0$, creating a differential between FS and cavity pressure $\mathrm{a_c} < \mathrm{a}_\infty$, with respect to δ/L. This model uses Rossiter's derivation, accounting viscid flow to form Eqn. E.4, which creates an incompressible relation alike East's Eqn. E.2 [8], and Block's Eqn. E.3 [6].

Sixthly, dimensionless dp/dx U/S, is represented by $\bar{p}_x$ is Eqn. E.5, implemented as an exponential exponent, to represent decay or growth of favourable or adverse dp/dx U/S respectively, with respect to adverse $dp/dx > 0$ into the cavity, impacting feedback U/S. For a flat-plate U/S with $dp/dx = 0$; $\mathrm{e}^{\bar{p}_x} \to 1$, as induced $dp/dx > 0$ at the cavity LE, is unaltered by U/S dp/dx.

$$\frac{\mathrm{a}_\infty}{\mathrm{a_c}} = 1 + \mathrm{A_e}\left(\frac{\mathrm{L}}{\mathrm{D}}\right)^{\mathrm{B_e}} \qquad \text{(E.2)} \qquad\qquad \frac{\mathrm{a}_\infty}{\mathrm{a_c}} = 1 + \frac{0.514}{\mathrm{L/D}} \qquad \text{(E.3)}$$

$$\frac{\mathrm{a}_\infty}{\mathrm{a_c}} = \left(1 + \frac{\delta}{\mathrm{L}}\right) \qquad \text{(E.4)} \qquad\qquad \bar{p}_x = \frac{dp}{dx}\frac{1}{\rho \mathrm{U}_\infty^2}\frac{\mathrm{L}}{\delta^*/\mathrm{D}} \qquad \text{(E.5)}$$

Lastly, considering periodic shed vorticity from the cavity LE alike edge-tones [144], and feedback waves reflected off the TE [2], produce a sequence of periodic pressure oscillations per Eqn. E.1. It is reasonable to assume, they are related in frequency. Let us suppose, flow separation at the cavity LE initialises vorticity, such that, transition from the BL to SL drives frequency. Therefore, SL propagation must be a function of BL δ, and cavity length, for effective SL wavelength; δ/L, which feeds interaction with the TE, where its reflected U/S at $\mathrm{a_c}$, or progresses D/S, dependant on SL cycle. Such that, vortices travel over the cavity at $\kappa \mathrm{U}_\infty$ in Δt, and feedback waves travel U/S at $\mathrm{a_c}$ in Δt, by δ/L for a viscous wavelength frequency relationship:

$$\frac{f\mathrm{L}}{\delta} = \frac{\kappa \mathrm{U}_\infty}{\lambda_v} = \frac{\mathrm{a_c}}{\lambda_f} \qquad \text{(E.6)}$$

Coalescing these factors, a viscid physical model arises, to derive dimensionless cavity frequency, as a function of vorticity shed by displaced mass δ^*, $\bar{p}_x$ in Eqn. E.7, and feedback over cavity length by $\bar{p}_x$, over effective mass depth δ^*/D in Eqn. E.8. Fig. 7.1 provides the schematic.

$$m_v\lambda_v = \delta^*\mathrm{e}^{\bar{p}_x} + \gamma_v\lambda_v + \kappa \mathrm{U}_\infty \frac{\delta}{\mathrm{L}}\Delta t \qquad \text{(E.7)} \qquad\qquad m_f\lambda_f = \frac{\mathrm{L}\mathrm{e}^{\bar{p}_x}}{\delta^*/\mathrm{D}} - \mathrm{a_c}\frac{\delta}{\mathrm{L}}\Delta t \qquad \text{(E.8)}$$

Re-arranging Eqn. E.7 for Δt, it is eliminated by substitution into Eqn. E.8, coalescing feedback and vorticity modes:

$$m_f \lambda_f = \frac{\mathrm{Le}^{\bar{p}_x}}{\delta^*/\mathrm{D}} - \frac{\mathrm{a_c}}{\kappa \mathrm{U}_\infty} \left(m_v \lambda_v - \delta^* \mathrm{e}^{\bar{p}_x} - \gamma_v \lambda_v \right) \tag{E.9}$$

Re-arranging Eqn. E.9 to group modes and phase to the LHS, and other variables to the RHS:

$$\kappa \frac{\mathrm{U}_\infty}{\mathrm{a_c}} m_f \lambda_f + \lambda_v \left(m_v - \gamma_v \right) = \kappa \frac{\mathrm{U}_\infty}{\mathrm{a_c}} \frac{\mathrm{Le}^{\bar{p}_x}}{\delta^*/\mathrm{D}} + \delta^* \mathrm{e}^{\bar{p}_x} \tag{E.10}$$

Substitute Eqn. E.6, rearranged for λ_v, and λ_f into Eqn. E.10, and reduce:

$$\kappa \frac{\mathrm{U}_\infty}{f} \frac{\delta}{\mathrm{L}} \left(m_f + m_v - \gamma_v \right) = \kappa \frac{\mathrm{U}_\infty}{\mathrm{a_c}} \frac{\mathrm{Le}^{\bar{p}_x}}{\delta^*/\mathrm{D}} + \delta^* \mathrm{e}^{\bar{p}_x} \tag{E.11}$$

Substitute relationships for $\mathrm{a}_\infty/\mathrm{a_c}$ in Eqn. E.4, and $\mathrm{M}_\infty = \mathrm{U}_\infty/\mathrm{a}_\infty$ into expanded Eqn. E.11:

$$\begin{gathered} \kappa \frac{\mathrm{U}_\infty}{f} \frac{\delta}{\mathrm{L}} \left(m_f + m_v - \gamma_v \right) = \kappa \mathrm{Le}^{\bar{p}_x} \left(\frac{\mathrm{U}_\infty}{\mathrm{a}_\infty} \frac{\mathrm{a}_\infty}{\mathrm{a_c}} \frac{\mathrm{D}}{\delta^*} + \frac{\delta^*}{\kappa \mathrm{L}} \right) \\ \downarrow \\ \frac{\mathrm{U}_\infty}{f} \frac{\delta}{\mathrm{L}} \left(m_f + m_v - \gamma_v \right) = \mathrm{Le}^{\bar{p}_x} \left(\frac{\mathrm{M}_\infty}{\delta^*/\mathrm{D}} \left(1 + \frac{\delta}{\mathrm{L}} \right) + \frac{\delta^*}{\kappa \mathrm{L}} \right) \end{gathered} \tag{E.12}$$

Re-arrange Eqn. E.12 to solve for $\mathrm{St} = f\mathrm{L}/\mathrm{U}_\infty$ below, to give dimensionless frequency of the viscid physical model in Eqn. E.13 per Fig. 7.1:

$$\begin{gathered} \frac{\delta}{\mathrm{L}} \left(m_f + m_v - \gamma_v \right) = \frac{f\mathrm{L}}{\mathrm{U}_\infty} \mathrm{e}^{\bar{p}_x} \left(\frac{\mathrm{M}_\infty}{\delta^*/\mathrm{D}} \left(1 + \frac{\delta}{\mathrm{L}} \right) + \frac{\delta^*}{\kappa \mathrm{L}} \right) \\ \downarrow \\ \frac{f\mathrm{L}}{\mathrm{U}_\infty} = \frac{\delta}{\mathrm{Le}^{\bar{p}_x}} \left(m_f + m_v - \gamma_v \right) \left[\frac{\mathrm{M}_\infty}{\delta^*/\mathrm{D}} \left(1 + \frac{\delta}{\mathrm{L}} \right) + \frac{\delta^*}{\kappa \mathrm{L}} \right]^{-1} \\ \downarrow \\ \mathrm{St_{HS}} = \frac{f\mathrm{L}}{\mathrm{U}_\infty} = \frac{\delta}{\mathrm{e}^{\bar{p}_x}} \left(m - \gamma_v \right) \left[\frac{\mathrm{M}_\infty}{\delta^*/\mathrm{D}} \left(\mathrm{L} + \delta \right) + \frac{\delta^*}{\kappa} \right]^{-1} \end{gathered} \tag{E.13}$$

E.2 Dimensionless Pressure Amplification

The model derived and presented in Section 7.2 follows Plumblee et al's [3] radiation impedance theory, to predict pressure at a point in the cavity, based on pressure at the mouth, source location and magnitude. The tables following compare numerical to experimentally attained SPL, with error ε (%), and mean ε_m (%) across mode and U_∞ for each U/S case with internal cavity L/D = L/W = 3, and select cases where BL data was attained with the cavity open.

Table E.1: Experiment vs. Numerical Amplitude: Conic Nose U/S C1: L/D = L/W = 1

U_∞	Mode 1 SPL		ε	Mode 2 SPL		ε	Mode 3 SPL		ε	Mode 4 SPL		ε	ε_m
m/s	Exp	Num	%	Exp	Num	%	Exp	Num	%	Exp	Num	%	%
10	167	166	0.6	175	179	2.6	148	145	2.0	154	149	3.2	2.1
15	175	167	4.5	177	177	0.2	152	151	1.0	-	-	-	1.9
20	178	169	5.1	179	176	1.7	147	149	1.4	-	-	-	2.7

25	180	170	5.5	184	186	1.1	164	150	7.9	149	153	2.0	4.2
30	186	171	8.0	197	187	5.0	161	157	2.5	-	-	-	5.2
35	190	172	9.5	198	186	6.0	167	159	4.8	-	-	-	6.7
40	191	173	9.4	199	187	6.0	170	161	5.3	-	-	-	6.9
45	192	174	9.4	199	188	5.5	211	199	5.6	176	161	8.5	7.1
50	193	175	9.3	202	189	6.4	212	199	6.1	178	163	8.4	7.5
	ε_m (%)		6.8	ε_m (%)		3.8	ε_m (%)		4.1	ε_m (%)		5.5	5

Table E.2: Experiment vs. Numerical Amplitude: Conic Nose U/S C5: L/D = L/W = 3

U_∞	Mode 1 SPL		ε	Mode 2 SPL		ε	Mode 3 SPL		ε	Mode 4 SPL		ε	ε_m
m/s	Exp	Num	%	Exp	Num	%	Exp	Num	%	Exp	Num	%	%
10	180	190	5.6	198	208	5.3	185	175	5.4	160	166	3.8	5.1
15	195	196	0.6	200	205	2.4	150	150	0.1	-	-	-	1.1
20	200	193	3.5	203	198	2.5	152	145	4.6	144	140	2.8	3.4
25	203	195	3.9	207	202	2.4	160	150	6.2	160	152	5.0	4.4
30	205	197	3.9	211	207	1.9	155	149	3.9	152	144	5.3	3.8
35	207	197	4.8	212	205	3.3	159	154	3.1	152	145	4.6	4.0
40	202	192	5.0	212	201	5.2	160	151	5.0	132	138	4.6	4.0
45	205	198	3.4	211	197	6.6	214	201	6.1	-	-	-	5.4
50	212	205	3.3	210	201	4.3	215	219	1.9	-	-	-	3.2
	ε_m (%)		3.8	ε_m (%)		3.8	ε_m (%)		4.0	ε_m (%)		4.4	3.9

Table E.3: Experiment vs. Numerical Amplitude: Ogive Nose U/S C11: L/D = L/W = 3

U_∞	Mode 1 SPL		ε	Mode 2 SPL		ε	Mode 3 SPL		ε	Mode 4 SPL		ε	ε_m
m/s	Exp	Num	%	Exp	Num	%	Exp	Num	%	Exp	Num	%	%
10	172	182	5.8	174	180	3.5	157	157	0.3	139	139	0.4	2.5
15	178	179	0.8	173	179	3.5	162	162	0.1	152	148	2.9	1.8
20	186	193	3.8	186	178	4.3	190	179	5.8	157	161	2.6	4.1
25	199	191	4.0	198	200	1.0	192	185	3.7	177	178	0.2	2.3
30	200	195	2.5	202	199	1.5	193	187	3.1	-	-	-	2.4
35	205	196	4.4	211	202	4.3	215	207	4.2	191	181	5.2	4.5
40	206	194	5.8	215	204	5.1	222	224	0.9	200	191	4.5	4.1
45	209	201	3.8	213	200	6.1	224	219	2.2	195	183	6.1	4.6
50	211	202	4.3	220	218	0.9	230	225	2.2	209	198	5.3	3.2
	ε_m (%)		3.9	ε_m (%)		3.4	ε_m (%)		2.5	ε_m (%)		3.4	3.3

Table E.4: Experiment vs. Numerical Amplitude: Parabola Nose U/S C17: L/D = L/W = 3

U_∞	Mode 1 SPL		ε	Mode 2 SPL		ε	Mode 3 SPL		ε	Mode 4 SPL		ε	ε_m
m/s	Exp	Num	%	Exp	Num	%	Exp	Num	%	Exp	Num	%	%
10	174	183	5.2	178	180	1.1	161	162	0.5	152	143	5.9	3.2
15	182	180	2.8	179	174	2.8	149	143	4.0	-	-	-	3.2

20	185	191	3.2	190	199	4.7	162	151	6.8	144	140	2.8	4.4
25	198	192	3.0	192	200	4.2	188	184	2.1	150	144	4.0	3.3
30	199	200	0.5	206	202	1.9	189	184	2.7	171	162	5.3	2.6
35	199	189	5.0	206	198	3.9	190	184	3.2	-	-	-	4.0
40	201	190	5.5	207	203	1.9	184	182	1.1	177	180	1.7	2.6
45	203	197	3.0	211	201	4.7	207	196	5.3	189	180	4.8	4.5
50	204	192	5.8	213	202	5.1	205	193	5.8	198	197	0.5	4.3
	ε_m (%)		3.8	ε_m (%)		3.4	ε_m (%)		3.5	ε_m (%)		3.6	3.6

Table E.5: Experiment vs. Numerical Amplitude: Flat-plate U/S C19: L/D = L/W = 1

U_∞	Mode 1 SPL		ε	Mode 2 SPL		ε	Mode 3 SPL		ε	Mode 4 SPL		ε	ε_m
m/s	Exp	Num	%	Exp	Num	%	Exp	Num	%	Exp	Num	%	%
10	166	168	1.2	156	160	2.6	132	126	4.5	120	124	3.3	2.9
15	172	169	1.7	166	160	3.6	141	143	1.4	131	128	2.3	2.3
20	167	169	1.2	163	160	1.8	154	148	3.9	133	128	3.8	2.7
25	165	164	0.6	163	162	0.6	153	146	4.6	135	131	3.0	2.2
30	176	171	2.8	158	162	2.5	148	152	2.7	139	146	5.0	3.3
35	171	171	0.4	160	164	2.5	150	149	0.6	150	154	2.7	1.6
40	163	170	4.3	164	166	1.2	155	150	3.2	130	120	7.7	4.1
45	167	168	0.6	164	155	5.5	160	155	3.1	139	136	2.2	3.6
50	176	171	2.8	170	164	3.5	140	146	4.3	126	128	1.6	3.1
	ε_m (%)		1.7	ε_m (%)		2.6	ε_m (%)		3.1	ε_m (%)		2.9	2.7

Table E.6: Experiment vs. Numerical Amplitude: Flat-plate U/S C21: L/D = L/W = 2

U_∞	Mode 1 SPL		ε	Mode 2 SPL		ε	Mode 3 SPL		ε	Mode 4 SPL		ε	ε_m
m/s	Exp	Num	%	Exp	Num	%	Exp	Num	%	Exp	Num	%	%
10	142	143	0.7	160	153	4.4	140	136	2.9	125	131	4.8	3.2
15	148	144	2.7	178	170	4.7	143	147	2.8	124	126	1.2	2.8
20	149	149	0.3	158	158	0.1	152	148	2.6	130	126	3.1	1.5
25	163	155	4.9	182	173	4.8	169	166	1.7	141	141	0.2	2.9
30	170	162	4.9	169	172	1.9	156	154	1.2	128	127	1.0	2.3
35	175	164	6.4	185	176	4.9	158	151	4.4	137	142	3.3	4.8
40	179	167	6.7	182	176	3.3	154	148	3.7	138	142	2.9	4.2
45	184	169	8.1	193	193	0.1	158	166	5.1	131	138	5.3	4.7
50	181	167	7.7	196	193	1.9	162	166	2.7	141	137	2.7	3.8
	ε_m (%)		4.7	ε_m (%)		2.9	ε_m (%)		3.0	ε_m (%)		2.7	3.5

Table E.7: Experiment vs. Numerical Amplitude: Flat-plate U/S C23: L/D = L/W = 3

U_∞	Mode 1 SPL		ε	Mode 2 SPL		ε	Mode 3 SPL		ε	Mode 4 SPL		ε	ε_m
m/s	Exp	Num	%	Exp	Num	%	Exp	Num	%	Exp	Num	%	%
10	146	150	2.7	170	175	4.7	158	163	3.1	126	128	1.6	3.0

15	149	158	6.0	157	150	4.7	160	166	3.8	125	131	4.8	4.8
20	159	153	3.8	152	158	3.9	165	168	1.8	120	130	8.3	4.4
25	158	163	3.1	170	175	2.9	158	148	6.3	121	131	8.3	5.1
30	155	165	6.5	177	174	1.7	162	168	3.7	119	118	0.8	3.2
35	171	166	3.9	185	176	4.8	160	156	2.5	120	117	2.5	3.4
40	155	158	1.9	180	174	3.3	163	168	4.9	125	132	5.6	3.9
45	170	161	5.3	195	192	1.5	165	167	1.2	126	131	4.0	3.0
50	172	162	5.8	196	193	1.5	154	145	5.8	141	138	2.1	3.8
	ε_m (%)		4.3	ε_m (%)		3.2	ε_m (%)		3.7	ε_m (%)		4.2	3.9

E.3 Strouhal Number

Due to the large set of data generated for each case, primary data is presented in the main text, with secondary given as additional support, in the interest of the reader.

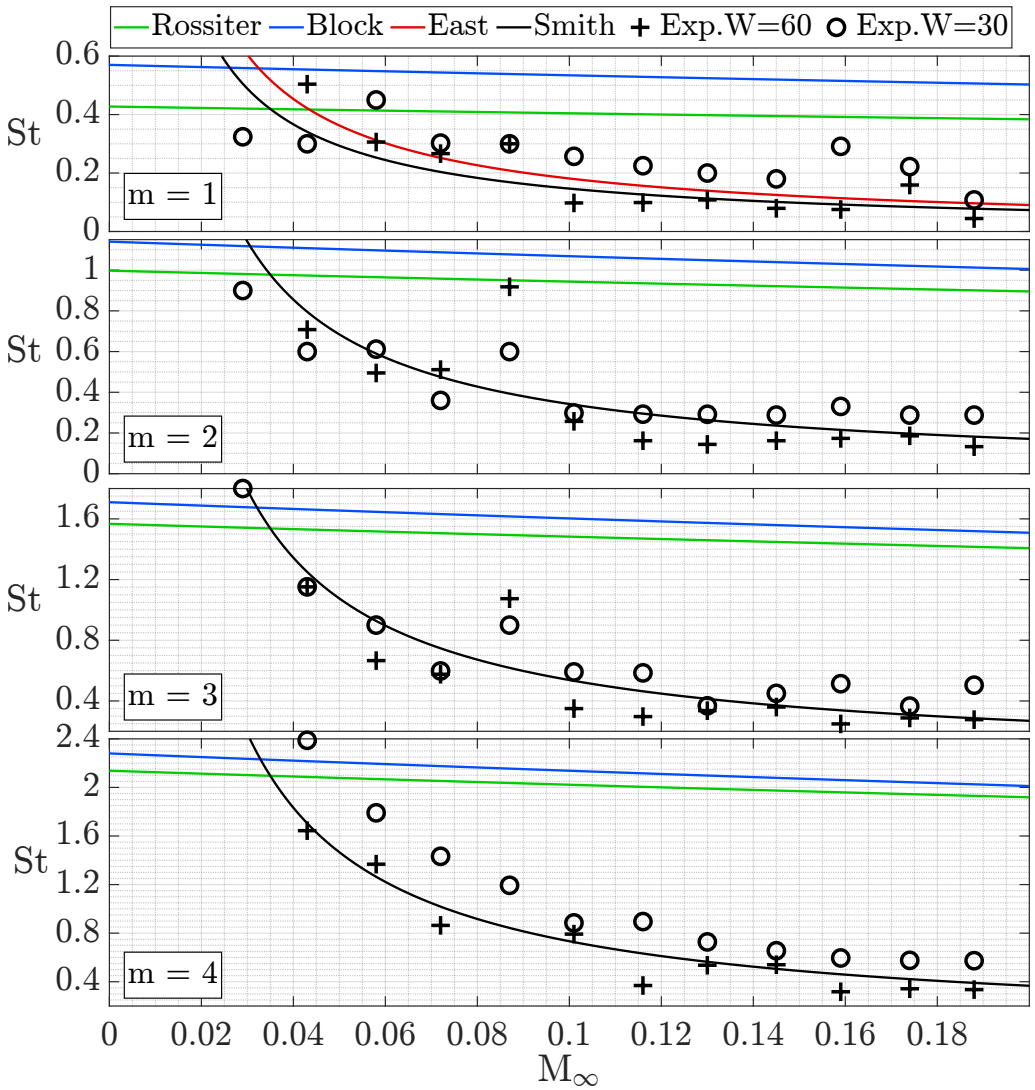

Figure E.1: Strouhal Number: Ogive Nose U/S

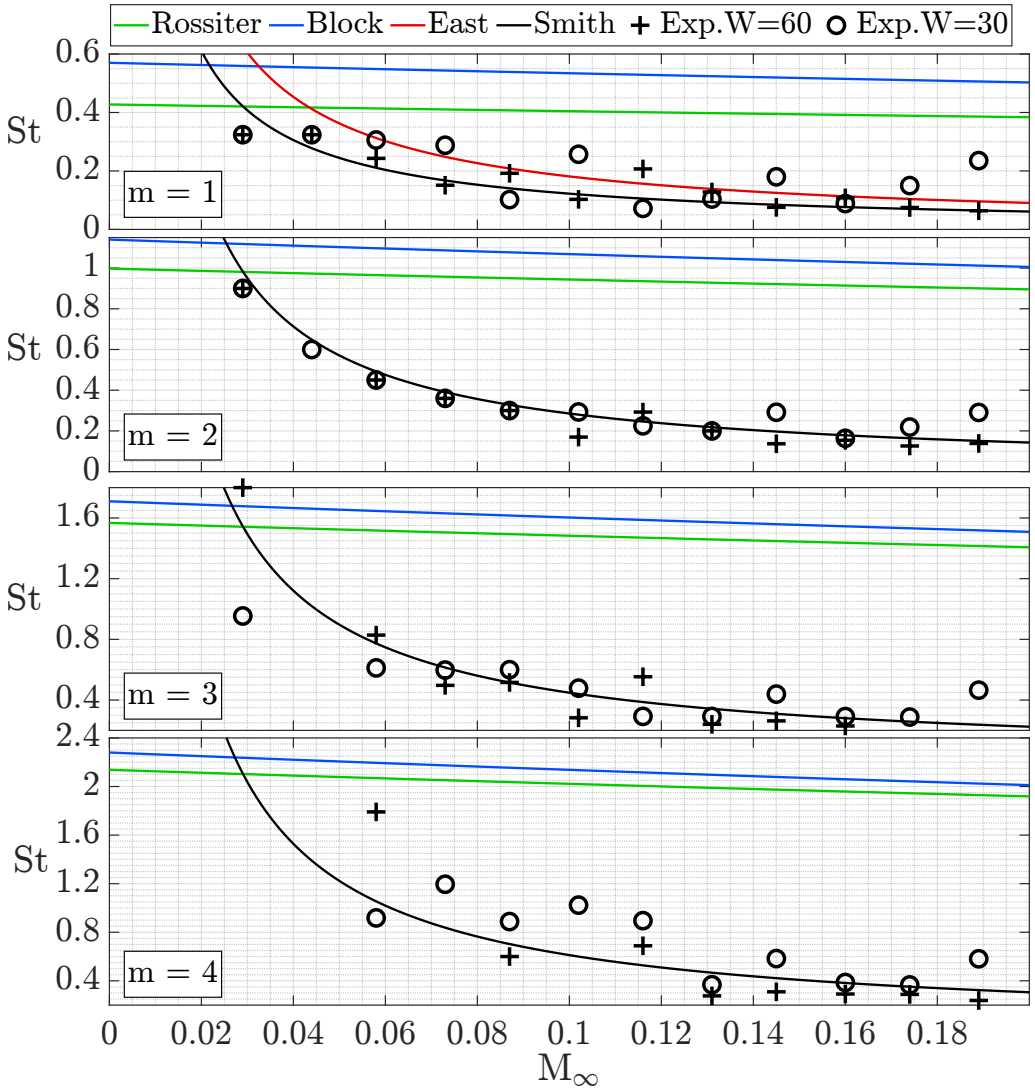

Figure E.2: Strouhal Number: Parabola Nose U/S

Appendix F

Algorithms

F.1 Pressure Data Processing

F.1.1 Unsteady Surface Pressure Reduction

```
% AIRSPEED (m/s), GEOMETRY (mm): nose (N), length (L), depth (D), width (W)
U = 10:5:65; N = ["NC","NO","NP","NF"]; L  = [60,60,120,120,180,180];
D = 60;      W = [60,30,60,30,60,30];   LD = string(L/D); LW = string(L./W);
load("Ps");  load("port"); load("loc");
for n = 1:4
    for j = 1:6
        p   = importdata(strcat("LD",LD(j),"_LW",LW(j),"_",N(n),".mat"));
        rho = zeros(length(p),width(p{1})-1); t = p{1}(6:end-4,1);
        for k = 1:length(p)
            rho(k,:) = p{k}(5,2:end); % density (kg/m3)
        end
        for i = 1:12
            for m = 1:length(rho)
                P{c,i}(:,m)  = tubedist(p{i}(6:end-4,m+1),rho(i,m),...
                               Ps{c}(i,m),port(c,m),loc(c,m));
                CP{c,i}(:,m) = P{c,i}(:,m)./(0.5*rho(i,m)*U(i)^2);
            end
            MEAN{c}(i,:) = CP{c,i}(end-3,:);
        end
        for i = 1:12
            for o = 1:length(rho)
                sum   = 0;
                for k = 1:length(t)
                    sum = sum + (CP{c,i}(k,o))^2;
                end
                RMS{c}(i,o) = sqrt((1/length(t))*sum); % RMS
            end
```

```
        end
    end
end
```

F.1.2 Tube Distortion Code

```
% SET-UP: Transducer (3), Port (2), Plastic Tube (3), Tap (1), Model (0)
% INPUT: P3 =  MPS pressure (Pa), OUTPUT: P0 = corrected pressure (Pa)
function P0 = tubedist(Pi,rho,Ps,port,loc)
    % TRANSDUCER VOLUME (m3): differs per scanivalve port
    pts = [1:4:61;2:4:62;3:4:63;4:4:64]; [ro,co] = size(pts); O = 0;
    for r = 1:ro
        for c = 1:co
            if r == 1 && port == pts(r,c)
                Vv = [0,0,0.000919]*1.6387064*1e-5;
            elseif r == 2 && port == pts(r,c)
                Vv = [0,0,0.000611]*1.6387064*1e-5;
            elseif r == 3 && port == pts(r,c)
                Vv = [0,0,0.000457]*1.6387064*1e-5;
            elseif r == 4 && port == pts(r,c)
                Vv = [0,0,0.000765]*1.6387064*1e-5;
            end
        end
    end
    L  = [12,750,9.398]/1000;       % tube length          (m)
    R  = [0.4,0.4,0.3048]/1000;     % tube internal radius (m)
    Vt = pi*(R.^2).*L;              % tube volume          (m3)
    f  = 500;                       % MPS scan frequency   (Hz)
    [Pr,mu,a,gam,k] = air(Ps,rho); % AMBIENT CONDITIONS
    for j = 1:3
        % BESSEL FUNCTION 1ST KIND: shear wave number, 0th & 2nd order
        alpha = sqrt(-1)*sqrt(sqrt(-1))*R(j)*sqrt((rho*f)/mu);
        J0(j) = besselj(0,alpha); J2(j) = besselj(2,alpha);
        n(j)   = 1/(1 + ((gam-1)/gam)*... % Polytropic Constant (-)
                 (besselj(2,alpha*sqrt(Pr))/besselj(0,alpha*sqrt(Pr))));
        phi(j) = (f/a)*sqrt(J0(j)/J2(j))*sqrt(gam/n(j));
    end
    %% COMPLEX PRESSURE RATIOS
    for j = 1:length(Pi)
        P2P3 = cosh(phi(3)*L(3))+n(3)*(Vv(3)/Vt(3))*(1/k)*phi(3)*...
               L(3)*sinh(phi(3)*L(3));
        P1P2 = cosh(phi(2)*L(2))+n(2)*(Vv(2)/Vt(2))*(1/k)*phi(2)*...
               L(2)*sinh(phi(2)*L(2))+(Vt(3)/Vt(2))*(phi(3)/phi(2))*...
               (L(2)/L(3))*(J0(2)/J0(3))*(J2(3)/J2(2))*(sinh(phi(2)*L(2))/...
```

```
            sinh(phi(3)*L(3)))*(cosh(phi(3)*L(3))-(1/P2P3));
        P0P1 = cosh(phi(1)*L(1))+n(1)*(Vv(1)/Vt(1))*(1/k)*phi(1)*...
            L(1)*sinh(phi(1)*L(1))+(Vt(2)/Vt(1))*(phi(2)/phi(1))*...
            (L(1)/L(2))*(J0(1)/J0(2))*(J2(2)/J2(1))*(sinh(phi(1)*L(1))/...
            sinh(phi(2)*L(2)))*(cosh(phi(2)*L(2))-(1/P1P2));
        P0P3 = abs(P2P3*P1P2*P0P1);  P0(j) = Pi(j)*P0P3;
    end
end
```

F.1.3 Atmospheric Conditions

```
function [Pr,mu,a,g,k]  = air(P,rho)
    R   = 287.05; g   = 1.401;      % gas constant, heat ratio (J/kg.K,-)
    k   = 1.4;    M   = 28.9647;    % polytropic, molar mass   (-,g/mol)
    T0  = 273.15; T   = P/(rho*R); % temperature              (K)
    Sk  = 202.2;  Smu = 111.8       % sutherland constants     (K)
    kt0 = 2.4e-2; mu0 = 1.72*e-5;  % thermal conduc/viscosity (W/m.K)
    a   = sqrt(g*P/rho);            % speed of sound           (m/s)
    % Specific Heat at Constant Pressure (-): Daubert & Danner Correlation
    A = 28958; B = 9390; C = 3012; D = 7580; E = 1484;
    cp = (A + B*((C/T)/sinh(C/T))^2 + D*((E/T)/cosh(E/T))^2)/M;
    kt = kt0*(T/T0)^(3/2)*((T0+Sk)/(T+Sk));   % thermal conductivity (W/m.K),
    mu = mu0*(T/T0)^(3/2)*((T0+Smu)/(T+Smu))  % dynamic viscosity    (kg/m.s)
    Pr = cp*mu/kt;                            % prandtl number       (-)
end
```

F.2 Hot-Wire Data Processing

F.2.1 Hot-Wire Acquisition

```
%% CREATE ANALOG INPUT (HOTWIRE & PID) DAQ SESSION
if ~exist('InputDAQ', 'var')
    InputDAQ = daq('ni');
    addinput(InputDAQ,'cDAQ1Mod1','ai0','Voltage'); % HW TEMP
    addinput(InputDAQ,'cDAQ1Mod1','ai1','Voltage'); % HW E1
    InputDAQ.Channels(1).Name = "Temp"; InputDAQ.Channels(2).Name = "HW_E1";
end
InputDAQ.Rate = 2^15; SampRate = InputDAQ.Rate; Duration = 60;
%% DECLARE EXPERIMENTAL PARAMETERS: location, airspeed
pt = 30; Y = logspace(0,log10(270),pt); Ytrans = Y(end)-Y;
U  = zeros(pt,1); T = zeros(pt,1); Uinf = 45;
% LOOP: aquire data for each y-axis increment on traverse.
SaveFolder = fullfile('../Caroline_BL',num2str(Uinf)); mkdir(SaveFolder);
for i = 1:length(Y)
```

```
    start(InputDAQ,"NumScans",round(Duration*InputDAQ.Rate)); t = tic;
    hwaitbar = waitbar(0,['Collecting Data Wait ',int2str(Duration),' s']);
    while InputDAQ.Running
        waitbar(toc(t)/Duration); pause(1); % WAITBAR
    end
    close(hwaitbar);
    uiwait(msgbox(['Data at ',num2str(round(Ytrans(i),2)),' mm']));
    data  = read(InputDAQ, "all"); Point = [data.Temp,data.HW_E1];
    fname = [num2str(i),'_',num2str(Uinf),'ms_Y',num2str(Y(i),'%2.0f'),...
             '_', datestr(now,'YYYYmmDD_HHMM'),'.mat'];
    fullfname = fullfile(SaveFolder,fname); save(fullfname,"Point");
end
```

F.2.2 Hot-Wire Reduction

```
load matrix;  load Y;   Ui = 10:5:50;
SR   = 2^15;  t   = 60; N = SR*t;  % data sample rate/time/number
EAD  = 10;    bit = 16;            % A/D input range (volts)/res(bits)
A    = 1.396; B   = 0.895;         % power law coefficient
dT   = 1;     dP  = 0.01;          % temperature/pressure variation
dUdE = 46.5;                       % slope sensitivity factor
CASE = char('C_c','O_c','P_c','F_c','C_n','O_n','P_n','F_n');
for c = length(cases)
    for k = length(Ui)
        for j = 1:length(matrix)
            if matrix(j,1) == c && matrix(j,2) == Ui(k)
               T0  = matrix(j,4)-273;
               Cpr = matrix(j,11:15); Cpo = matrix(j,16:20);
           end
        end
        for i = 1:length(Y)
            %% LOAD DATA:
            file = dir(['DATA\',CASE(c,:),'\',num2str(Ui(k)),'ms\',...
                        num2str(i),'_',num2str(Ui(k)),'ms_Y*.mat']);
            load(fullfile(file.folder, file.name));
            temp = Point(:,1); Tw = mean(Point(:,1)); E = Point(:,2);
            Upr  = Cpr(1)+Cpr(2).*E+Cpr(3).*E.^2+Cpr(4).*E.^3+Cpr(5).*E.^4;
            Upo  = Cpo(1)+Cpo(2).*E+Cpo(3).*E.^2+Cpo(4).*E.^3+Cpo(5).*E.^4;
            U(:,i) = (Upr(:,1) + Upo(:,1))/2; % CALIBRATION
            Um{c}(k,i) = mean(U(:,i));        % mean velocity (m/s)
            rms = 0; sig = 0; Ss = 0; Ks = 0;
            for j = 1:N
                rms = rms + (U(j,i)-Um{c}(k,i))^2;
                si  = si  + (((U(j,i)-Um{c}(k,i))^2)/(N-1));
```

```
            end
            Urms{c}(k,i) = sqrt((1/(N-1))*rms);      % root mean square
            TI{c}(k,i)   = Urms{c}(k,i)/Um{c}(k,i); % turbulence intensity
            sig{c}(k,i)  = sqrt(si);                 % time variance
            for j = 1:N
                Ss = Ss+(((U(j,i)-Um{c}(k,i))^3)/(N*sig{c}(k,i)^3)); % skew
                Ks = Ks+(((U(j,i)-Um{c}(k,i))^4)/(N*sig{c}(k,i)^4)); % kurtosis
            end
            Skew{c}(k,i) = Ss; Kurt{c}(k,i) = Ks;
            [acf{k,c}(:,i),lag{k,c}(:,i)] = autocorr(U(:,i)); % correlation
            its{c}(k,i) = trapz(lag{k,c}(:,i),acf{k,c}(:,i)); % int time scale

            % ISO UNCERTAINTY
            Uca = 0.01/100;                                    % calibrator
            Uli = (std(Upo)-std(Upr))/100;                     % linearise
            Ure = (1/sqrt(3))*(1/Um{c}(k,i))*(EAD/(2^bit))*dUdE; % A/D res
            Upo = (1/sqrt(3))*(1-cos(deg2rad(1)));             % probe pos
            Ute = (1/sqrt(3))*(1/Um{c}(k,i))*(dT/(TO-Tw))...
                   *sqrt(((A/B)*(1/sqrt(Um{c}(k,i)))) + 1);    % sensor temp
            Ude = dT/273;                                      % air density
            Upr = (1/sqrt(3))*dP;                              % pressure
            Uhu = (1/sqrt(3))*(1/Um{c}(k,i))*dP*Um{c}(k,i)*dP;  % humidity
                    dP*Um{c}(k,i)*dP;
            Ut{c}(k,i) = 2*sqrt((Uca+Uli+Ure+Upo+Ute+Ude+Upr+Uhu)^2);
        end
    end
end
```

F.2.3 Flat-Plate Boundary Layer Characteristics

```
for j = 1:2                                          % LOOP: CASE
    for k = 1:length(Ui)                             % LOOP: AIRSPEED
        u = U_M{c(j)}(k,1:le); U = U_M{c(j)}(k,le);  % velocity data
        Y = logspace(0,log10(270),30);               % y-axis positions
        uU{j,k} = u./U;                              % velocity profile
        for i = 1:le                                 % LOOP: vertical location
            if uU{j,k}(i) >= 0.99                    % BL thickness
                d(j,k) = Y(i-1) + (0.99 - uU{j,k}(i-1))*((Y(i)-Y(i-1))/...
                         (uU{j,k}(i)-uU{j,k}(i-1))); break;
            end
        end
        ds(j,k) = abs(trapz(Y,(1-uU{j,k}(:))));              % displacement
        ta(j,k) = abs(trapz(Y,uU{j,k}(:).*(1-uU{j,k}(:)))); % momentum
        tw(j,k) = 0.332*sqrt((rho(j,k)*mu(j,k)*U^3)/(1.2192+0.54));  % shear
```

```
        dsb(j,k) = 1.72*(d(j,k)/5.3); tab(j,k) = 0.664*(d(j,k)/5.3); % blasius
        ds7(j,k) = d(j,k)/8;          ta7(j,k) = (7/72)*d(j,k);      % 1/7 law
    end
end
```

F.2.4 Falkner-Skan Similar Solution

F.2.4.1 Numerical Runge Kutta Solution

```
function [eta,f,fd,fdd,fddd,error] = FalknerSkanRungeKutta(m,B)
    % SIMILAR VARIABLE ETA and FUNCTION: initial BCs, guess 2nd derivative
    dE   = 0.01; mEta  = 10; eta = 0:dE:mEta;   N   = (mEta)/dE;
    f(N) = 0;    fd(N) = 0;  fdd0 = 0:0.0001:2; fdd = zeros(length(fdd0));
    % RUNGE KUTTA FOURTH ORDER: LOOP 1: calculate f'(eta) for f"(0) IC
    % predictions, N = infinity (large enough to reduce computation)
    for i = 1:length(fdd0)
            fdd(1) = fdd0(i);
            for k = 1:N
                x1 = fd(k);           y1 = fdd(k);                    % 1ST
                z1 = - m - ((m+1)/2)*f(k)*fdd(k) + m*fd(k)*fd(k);
                x2 = fd(k) + x1*dE/2; y2 = fdd(k) + y1*dE/2;          % 2ND
                z2 = - m - ((m+1)/2)*(f(k) + dE*x1/2)*(fdd(k)...
                     + dE*z1/2)+ m*(fd(k) + dE*y1/2)*(fd(k) + dE*y1/2);
                x3 = fd(k) + x2*dE/2; y3 = fdd(k) + y2*dE/2;          % 3RD
                z3 = - m - ((m+1)/2)*(f(k) + dE*x2/2)*(fdd(k)...
                     + dE*z2/2) + m*(fd(k)+dE*y2/2)*(fd(k)+dE*y2/2);
                x4 = fd(k) + x3*dE;   y4 = fdd(k) + y3*dE;            % 4TH
                z4 = - m - ((m+1)/2)*(f(k) + dE*x3)*(fdd(k)+ dE*z3)...
                     + m*(fd(k) + dE*y3)*(fd(k) + dE*y3);
                f(k+1)   = f(k)   + (dE/6)*(x1 + 2*x2 + 2*x3 + x4);
                fd(k+1)  = fd(k)  + (dE/6)*(y1 + 2*y2 + 2*y3 + y4);
                fdd(k+1) = fdd(k) + (dE/6)*(z1 + 2*z2 + 2*z3 + z4);
            end
            fdInf(i) = fd(N); delta(i) = abs(1-fdInf(i));
    end
    [error,in] = min(delta); fdd(1) = fdd0(in);  % best match, index f"(0)
    % LOOP 2: calculate f(eta), f'(eta) and f"(eta) from converged f"(0)
    for k = 1:N
        x1 = fd(k); y1 = fdd(k);                                      % 1ST
        z1 = - m - ((m+1)/2)*f(k)*fdd(k) + m*fd(k)*fd(k);
        x2 = fd(k) + x1*dE/2; y2 = fdd(k) + y1*dE/2;                  % 2ND
        z2 = - m - ((m+1)/2)*(f(k) + dE*x1/2)*(fdd(k) + dE*z1/2)...
             + m*(fd(k) + dE*y1/2)*(fd(k) + dE*y1/2);
        x3 = fd(k) + x2*dE/2; y3 = fdd(k) + y2*dE/2;                  % 3RD
        z3 = -m - ((m+1)/2)*(f(k) + dE*x2/2)*(fdd(k) + dE*z2/2)...
```

```
            + m*(fd(k) + dE*y2/2)*(fd(k) + dE*y2/2);
        x4 = fd(k) + x3*dE; y4 = fdd(k) + y3*dE;                    % 4TH
        z4 = - m - ((m+1)/2)*(f(k) + dE*x3)*(fdd(k) + dE*z3)...
            + m*(fd(k) + dE*y3)*(fd(k) + dE*y3);
        f(k+1)   = f(k)   + (dE/6)*(x1 + 2*x2 + 2*x3 + x4);
        fd(k+1)  = fd(k)  + (dE/6)*(y1 + 2*y2 + 2*y3 + y4);
        fdd(k+1) = fdd(k) + (dE/6)*(z1 + 2*z2 + 2*z3 + z4);
    end
    fdd = fdd(1:1001,1)'; fddd = zeros(1,length(fdd));
    for i = 1:length(eta)
        fddd(i) = -f(i)*fdd(i) - B*(1 - fd(i)^2);
    end
end
```

F.2.4.2 Wedge Boundary Layer Characteristics

```
load nu;            load rho;           load U_M;   rhp = 1.225;
B = deg2rad(45)/pi; X = (0:1:121)/1000; x = 0;      U   = 10:5:50;
m = B/(2-B);        Y = (50/121)*X;     L = X(end); cas = [5,1];
for i = 2:length(X)
    x = sqrt((X(i) - X(i-1))^2 + (Y(i) - Y(i-1))^2) + x;
end
xi = x/L; [eta,f,fd,fdd,fddd] = FalknerSkanRungeKutta(m,B);
for c = 1:2
    for u = 1:9
        C = U_M{cas(c)}(u,1); Ue = C*(xi^m);     % BL EDGE VELOCITY
        y = eta./sqrt((Ue*(m+1))/(2*nu(c,u)*x)); % y-axis
        for i = 1:length(eta)                    % VELOCITY PROFILE
            if fd(i) >= 0.999
                ed = eta(i); uU = fd(1:i); y = y(1:i); break;
            end
        end
        d(c,u)  = 1000*ed/sqrt((Ue*(1+m))/(2*nu(c,u)*x)); % BL thickness
        ds(c,u) = abs(trapz(y,1-uU))*1000;                % displacement
        ta(c,u) = abs(trapz(y,uU.*(1-uU)))*1000;          % momentum
        dp(c,u) = -rho(c,u)*m*(C^2)*(xi^(2*m-1));         % pressure gradient
        tw(c,u) = mu(c,u)*sqrt((m+1)/2)*...               % shear stress
                  sqrt((C^3)/(nu(c,u)*xi))*fdd(1);
    end
    dsb(c,:) = (1.72/5.3)*d(c,:); tab(c,:) = (0.664/5.3)*d(c,:);  % blasius
    ds7(c,:) = d(c,:)/8;          ta7(c,:) = (7/72)*d(c,:);       % 1/7 law
end
```

F.2.5 Murphy's Curved Surface Similar Solution

F.2.5.1 Curve Boundary Layer Characteristics

```
load nu; load rho; load p; load AC; U = 10:5:50; c = [2,3,6,7];
x = (0:1:145)/1000; y = (0:0.01:10)/1000; rhp = [1.215,1.192,1.215,1.192];
for i = 1:length(c)         % LOOP CASE
    for u = 1:length(U)     % LOOP VELOCITY
        Upw           = sqrt((2*p(i,u))/rhp(i));  % wall velocity
        [eta,uUp,A,K] = curve(i,nu(i,u),Upw,x,y); % velocity profile
        [uUc,fd]      = taylor(eta,A,AC);         % numerical solution
        for j = 1:length(y)  % velocity profile, BL thickness & dp/dx
            if uUc(j)/uUp(j) >= 1
                d(i,u) = y(j); eU = eta(1:j); uU = uUc(1:j); yU = y(1:j);
                dp(i,u) = -(rhp(i)*(Upw^2)*(fd(j)^2))/(4+4*A*eta(j)); break;
            end
        end
        ds(i,u) = abs(trapz(yU,1-uU)); ta(i,u) = abs(trapz(yU,uU.*(1-uU)));
        tw(i,u) = mu(i,u)*(Upw/4)*sqrt(Upw/nu(i,u)*xi)*C2;
    end
    dsb(i,:) = (1.72/5.3)*d(i,:); tab(i,:) = (0.664/5.3)*d(i,:); % blasius
    ds7(i,:) = d(i,:)/8;          ta7(i,:) = (7/72)*d(i,:);      % 1/7 law
end
```

F.2.5.2 Curvature Function

```
function [eta,uU,A,K] = curve(i,nu,Upw,X,y)
    syms x xie;             % CURVATURE GEOMETRY
    if i == 2 || i == 5     % ogive
        Y = 704.3*x^5-245.5*x^4+39.64*x^3-7.03*x^2+0.967*x-5e-6;
    elseif i == 3 || i == 6 % parabola
        Y = 4005.7*x^5-1796.5*x^4+312.5*x^3-28.2*x^2+1.56*x+1.2e-3;
    end
    dY = diff(Y); dYY = diff(dY);
    s = matlabFunction(sqrt(1 + dY.^2)); % ARC LENGTH
    for i = 2:length(X)
        xi(i) = xi(i-1) + integral(s,X(i-1),X(i));
    end
    % CURVATURE PARAMETER: K = abs(d2ydx2)/sqrt((1 + dydx^2)^3)
    K0 = abs(dYY)/((1+(dY^2))^(3/2));  A0 = K0/sqrt(Upw/(nu*xie));
    K1 = matlabFunction(K0);           A1 = matlabFunction(A0);
    K  = K1(X(end));                   A  = A1(X(end),xi(end));
    for i = 1:length(y)
        uU(i) = exp(-K*y(i)); eta(i) = (y(i)/2)*sqrt(Upw/(nu*xi(end)));
    end
end
```

F.2.5.3 Taylor-Series Numerical Solution

```
function [uUc,f1] = coeff(eta,A,AC)
    syms E;
    F0 = ((E^2)/factorial(2))-((E^5)/factorial(5))+....
         ((11*(E^8))/factorial(8))-((375*(E^11))/factorial(11))+...
         ((27897*(E^14))/factorial(14))-((3817742*(E^17))/factorial(17));
    G1 = ((2*(E^3))/factorial(3))-((10*(E^6))/factorial(6))+...
         ((324*(E^9))/factorial(9))-((22896*(E^12))/factorial(12))+...
         ((2854146*(E^15))/factorial(15))-((595343808*(E^18))/factorial(18));
    G2 = ((12*(E^4))/factorial(4))-((128*(E^7))/factorial(7))+...
         ((8184*(E^10))/factorial(10));
    G3 = ((96*(E^5))/factorial(5))-((1832*(E^8))/factorial(8))+...
         ((203748*(E^11))/factorial(11));
    C2 = interp1(AC(:,1),AC(:,2),A);
    f  = (C2^(1/3))*F0-A*G1+((A^2)/(C2^(1/3)))*G2-((A^3)/(2*(C2^(1/3))))*G3;
    fd = matlabFunction(diff(f)); f1 = zeros(1,length(eta));
    for i = 1:length(eta)
        f1(i) = fd((C2^(1/3))*eta(i));
    end
    uUc = f1/2;
end
```

F.2.6 Shear Stress

```
load U_M; load mu; load rho; nu = mu./rho; load Y; load Upw; load xi; load C2;
B = deg2rad(45)/pi; m = B/(2-B); [~,~,~,fdd,~] = FalknerSkanRungeKutta(m,B);
for c = 1:8
    for k = 1:9
        ui = U_M{c}(k,:);      yi = Y{c,k}/1000;  % velocity profile (x,y)
        C  = polyfit(yi,ui,8);                    % polyfit profile (x,y)
        syms y; u = C(1)*y^8 + C(2)*y^7 + C(3)*y^6 + C(4)*y^5 + ...
                    C(5)*y^4 + C(6)*y^3 + C(7)*y^2 + C(8)*y   + C(9);
        du = matlabFunction(diff(u)); dudy = du(yi(1));
        if c == 4 || c == 8     % BLASIUS SIMILAR SOLUTION
            twb(c,k) = 0.332*sqrt((rho(c,k)*mu(c,k)*U^3)/(1.22+0.54));
        elseif c == 1 || c == 5 % FALKNER-SKAN SIMILAR SOLUTION
            Ue       = U_M{c}(k,1)*(xi(c,k)^m);
            twf(c,k) = mu(c,k)*sqrt(((Ue^3)*(m+1))/(2*nu(c,k)*xi(c,k)))*fdd(1);
        else                    % MURPHY SIMILAR SOLUTION
            twc(c,k) = mu(c,k)*(Upw(c,k)/4)*sqrt(Upw(c,k)/nu(c,k)*xi(c,k))*C2(c,k);
        end
        tw{c,k} = dudy*mu{c,k}; % HWA: WALL SHEAR STRESS
    end
end
```

F.3 Modal Analysis

F.3.1 Unsteady Surface Pressure Fast-Fourier Transform

```
% SIGNAL DATA: no. samples, sample rate, max freq, single sided freq
load PO; load PP; load PF; P = [PC;PO;PP;PF];
N   = 5000;        n   = (N-1)/2;   sR  = 500;      fMax = sR/2;
df  = fMax/n;      f   = (-n:n)*df; pI  = (f >= 0); ff   = f(pI)';
amp = cell(24,12); psd = amp;       spl = amp;      c    = 1;
for n = 1:4           % LOOP U/S CASE
    for ld = 1:6      % LOOP L/D RATIO
        for k = 1:12  % LOOP VELOCITY
            CASE  = P{c,k};
            for i = 1:length(CASE(1,:)) % LOOP LOCATION
                [p,f] = pspectrum(CASE(2:end,i),sR,...
                        'FrequencyLimits',[0,fMax]);
                spl{c,k}(:,i) = 20*log10((p)/((2*10^-5)^2));
            end
        end
        c = c + 1;
    end
end
```

F.3.2 Hot-Wire Anemometry Fast-Fourier Transform

```
% SIGNAL DATA: no. samples, sample rate, max freq
N  = 1966407; n = (N-1)/2;   sR = 2^15;     fMax = sR/2;
df = fMax/n;  f = (-n:n)*df; pI = (f >= 0); ff   = f(pI)';
load matrix; Ui = 10:5:50; Y = logspace(0,log10(270),30);
CASE = char('C_c','O_c','P_c','F_c','C_n','O_n','P_n','F_n');
for c = 1:length(CASE)            % LOOP CASE
    for u = 1:9                   % LOOP VELOCITY
        for j = 1:length(matrix)
            if matrix(j,1) == c && matrix(j,2) == Ui(u)
               Cpr = matrix(j,11:15); Cpo = matrix(j,16:20);
           end
        end
        for i = 1:length(Y)       % LOOP VERTICAL LOCATION
            file = dir(['DATA\',CASE(c,:),'\',num2str(Ui(u)),'ms\',...
                  num2str(i),'_',num2str(Ui(u)),'ms_Y*.mat']);
            load(fullfile(file.folder, file.name)); E = Point(:,2);
            Upr = Cpr(1)+Cpr(2).*E+Cpr(3).*E.^2+Cpr(4).*E.^3+Cpr(5).*E.^4;
            Upo = Cpo(1)+Cpo(2).*E+Cpo(3).*E.^2+Cpo(4).*E.^3+Cpo(5).*E.^4;
            U   = (Upr + Upo)/2; % CALIBRATION
            [p,f] = pspectrum(U,sR,'FrequencyLimits',[0,fMax]); % FFT
```

```
            spl{c,u}(:,i) = 20*log10((p)/((2*10^-5)^2));        % SPL
        end
    end
end
```

F.3.3 Dynamic Mode Decomposition

```
P = [PC; PO; PP; PF]; dt = t(2)-t(1); c = 1; load('t');
for n = 1:4
    for j = 1:6
        for k = 1:12
            X1 = P{c,k}(:,1:end-1); X2 = P{c,k}(:,2:end); % data matrices
            [U,S,V] = svd(X1,'econ');                     % decomposition
            sig_sum = cumsum(diag(S)/sum(diag(S)));       % truncate by R
            for ss = 1:length(sig_sum)
                if round(sig_sum(ss),2) >= 0.95
                    r = ss; break
                end
            end
            Ur = U(:,1:r); Sr = S(1:r,1:r); Vr = V(:,1:r);
            atilde   = Ur'*X2*Vr/Sr;          % ranked dynamic matrix
            [W,D]    = eig(atilde);           % eigendecomposition/values
            phi{c,k} = X2*Vr/Sr*W;            % eigenvectors (dmd modes)
            lam{c,k} = diag(D);               % discrete-t eigenvalues
            ome{c,k} = log(lam{c,k})/dt;      % continous-t eigenvalues
            b{c,k}   = phi{c,k}\X1(:,1);      % amplitude
            t_dyn    = zeros(r,length(t));    % time dynamic
            for l = 1:length(t)
                t_dyn(:,l) = (b{c,k}.*exp(ome{c,k}*t(l)));
            end
            dmd{c,k} = phi{c,k}*t_dyn;
        end
        c = c + 1;
    end
end
[rows,cols] = size(phi);  % EXTRACT MODES AND FREQUENCIES
for r = 1:rows
    for c = 1:cols
        for i = 1:width(phi{r,c})
            nph{r,c}(i) = norm(phi{r,c}(:,i));
        end
        [mod{r,c},ind{r,c}] = maxk(nph{r,c},6); ii = length(ind{r,c});
        for i = 1:ii
            mph{r,c}(:,i) = phi{r,c}(:,ind{r,c}(i));
```

```
            mom{r,c}(:,i) = ome{r,c}(ind{r,c}(i));
        end
    end
end
```

F.4 Amplitude Prediction

F.4.1 Radiation Impedance Model

```
M = [0.03,0.04,0.06,0.07,0.09,0.1,0.12,0.13,0.14]; % Mach No.
L = [0.06,0.06,0.12,0.12,0.18,0.18]; D = 0.06;     % Length, Depth (m)
W = [0.06,0.03,0.06,0.03,0.06,0.03]; zeta = W./L;  % Width (m)
load T; load P0; load f; U = 10:5:50;   % temp, pressure, frequency, velocity
kap = 0.57; load d; load ds; load dpdx; % SL cons., BL & displacement thk.
for i = 1:24                                % LOOP GEOMETRY CASES (i)
    xd = L(i);     yd = 0; zd = 0;          % source coordinates (m)
    x  = 0.6*L(i); y  = D; z  = (1/3)*W(i); % field coordinates  (m)
    for m = 1:length(M)              % LOOP MACH CASES (m)
        rho = P0(i,m)/(287*T(i,m));  % air density                (kg/m3)
        a   = sqrt(1.4*287*T(i,m));  % FS speed of sound          (m/s)
        px  = exp(dpdx(i,m)*(1/(rho*U(m)))...
              *(L(i)*D/d(i,m)));           % normal pressure gradient
        ac  = a/(1 + (d(i,m)/L(i)));       % cavity speed of sound (m/s)
        V   = kap*U(m) + ac;               % superimposed velocity (m/s)
        for j = 1:length(f{i}(m,:))        % LOOP FREQUENCIES (j)
            if j == 1
                A = ac*D*D;           % SOURCE STRENGTH MODE 1    (m3/s)
            elseif j == 2
                A = V*L(i)*D;         % SOURCE STRENGTH MODE 2    (m3/s)
            elseif j == 3
                A = U(m)*L(i)*d(i,m); % SOURCE STRENGTH MODE 3    (m3/s)
            elseif j == 4
                A = U(m)*D*ds(i,m);   % SOURCE STRENGTH MODE 4    (m3/s)
            end
            ka = (2*pi*f*L(i))/(ac*d(i,m));       % feedback wave no.
            kab = ka*(L(i)/(ds(i,m)/D));          % normal feedback wave no.
            kv = (2*pi*f*L(i))/(kap*U(m)*d(i,m)); % vorticity wave no.
            kvb = kv*ds(i,m);                     % normal vorticity wave no.
            kb = kab + kvb;                       % superimposed normal wave no.
            [R,X] = RX(kb,zeta(i),M(m));          % radiation impedence
            [gm,xi,eta] = gm(kb,D,R,X,L(i));      % boundary function
            % ITERATIVE CHARACTERISTIC REPONSE FUNCTION
            for nx = 1:j
                phi  = cosh(pi*gm*y/D)*cos(pi*z/W(i))*cos(pi*nx*x/L(i));
```

```
                phid = cosh(pi*gm*yd/D)*cos(pi*zd/W(i))*cos(pi*nx*xd/L(i));
                ppi(nx) = ((gm*phi*phid)/((sinh(2*pi*gm)+2*pi*gm)))*...
                (1/((kb^2)-((pi*L(i))^2)*((nx/L(i))^2+(1/W(i))^2-(gm/D)^2)));
            end
            pp = ((sqrt(-1)*16*pi*rho(i,m)*V*kb*A)/(W(i)*D*px))*sum(ppi);
            spl{i}(m,j) = 20*log10(abs(pp)/20e-6); % SPL (dB)
        end
    end
end
```

F.4.2 Characteristic Radiation Coefficients

```
function [R,X] = RX(kbi,zi,Mi)
    syms t kb M B z;
    r1 = ((sec(t)*sin((kb/(B^2))*(sec(t)+M)))/((sec(t)+M)^2))+...
         ((sec(t)*sin((kb/(B^2))*(sec(t)-M)))/((sec(t)-M)^2));
    r2 = (sin(t)-(cos(t)/(B*z)))*...
          (((sin((kb/B)*z*sec(t)*(1+M*sin(t))))/((1+M*sin(t))^2))+...
           ((sin((kb/B)*z*sec(t)*(1-M*sin(t))))/((1-M*sin(t))^2)));
    r3 = ((2*B*sin(t)*cos(t))/(kb*z))*...
         (((cos((kb/B)*z*sec(t)*(1+M*sin(t))))/((1+M*sin(t))^3)) + ...
          ((cos((kb/B)*z*sec(t)*(1-M*sin(t))))/((1-M*sin(t))^3)));
    x1 = ((sec(t)*cos((kb/(B^2))*(sec(t)+M)))/((sec(t)+M)^2)) + ...
          ((sec(t)*cos((kb/(B^2))*(sec(t)-M)))/((sec(t)-M)^2));
    x2 = (sin(t)-(cos(t)/(B*z)))*...
         (((cos((kb/B)*z*sec(t)*(1+M*sin(t))))/((1+M*sin(t))^2)) + ...
          ((cos((kb/B)*z*sec(t)*(1-M*sin(t))))/((1-M*sin(t))^2)));
    x3 = ((2*B*sin(t)*cos(t))/(kb*z))*...
         (((sin((kb/B)*z*sec(t)*(1+M*sin(t))))/((1+M*sin(t))^3)) + ...
          ((sin((kb/B)*z*sec(t)*(1-M*sin(t))))/((1-M*sin(t))^3)));
    r1 = matlabFunction(int(r1,t)); r2 = matlabFunction(int(r2,t));
    r3 = matlabFunction(int(r3,t)); x1 = matlabFunction(int(x1,t));
    x2 = matlabFunction(int(x2,t)); x3 = matlabFunction(int(x3,t));
    kb = kbi; z = zi; M = Mi; B = sqrt(1-M^2);
    r1 = r1(B,M,kb,atan(B*z));   x1 = x1(B,M,kb,atan(B*z));
    r2 = r2(B,M,kb,acot(B*z),z); x2 = x2(B,M,kb,acot(B*z),z);
    r3 = r3(B,M,kb,acot(B*z),z); x3 = x3(B,M,kb,acot(B*z),z);
    r4 = (B/(kb*z))*...
         (((cos((kb/(B^2))*(sqrt(1+(B*z)^2)+M)))/((sqrt(1+(B*z)^2)+M)^2)) + ...
        ((cos((kb/(B^2))*(sqrt(1+(B*z)^2)-M)))/((sqrt(1+(B*z)^2)-M)^2)));
    x4 = (B/(kb*z))*...
         (((sin((kb/(B^2))*(sqrt(1+(B*z)^2)+M)))/((sqrt(1+(B*z)^2)+M)^2)) + ...
         ((sin((kb/(B^2))*(sqrt(1+(B*z)^2)-M)))/((sqrt(1+(B*z)^2)-M)^2)));
    r5 = (B/(kb*z))*(((cos((kb/(B^2))*(1+M)))/((1+M)^2)) + ...
```

```
                    ((cos((kb/(B^2))*(1-M)))/((1-M)^2)));
    x5 = (B/(kb*z))*(((sin((kb/(B^2))*(1+M)))/((1+M)^2)) + ...
                    ((sin((kb/(B^2))*(1-M)))/((1-M)^2)));
    r6 = (B/(kb*z))*((1/((1+M)^2))+(1/((1-M)^2)));
    x6 = (1/(B*z))*((1/(1+M))+(1/(1-M)));
    r7 = ((2*kb)/(B^3))*(atan((1-M)/B)+atan((1+M)/B));
    x7 = 2/(B^2);
    x8 = ((2*M)/(B^3))*(atan((1-M)/B)-atan((1+M)/B));
    R  = -((B^3)/(pi*kb))*(r1-r2-r3+r4-r5+r6-r7);     % RADIATION RESISTANCE
    X  =  ((B^3)/(pi*kb))*(-x1+x2-x3+x4-x5+x6+x7-x8); % RADIATION REACTANCE
end
```

F.4.3 Boundary Function g_m

```
function [gm,xi,eta] = gm(kb,D,R,X,L)
    for xi = 0:0.00000001:1
        ep = ((kb*D*R*coth(2*pi*xi))/(pi*L*(R^2 + X^2))) + ...
             sqrt(((kb*D*R*coth(2*pi*xi))/(pi*L*(R^2+X^2)))^2 + ...
             ((2*kb*D*X*xi*coth(2*pi*xi))/(pi*L*(R^2+X^2))) + ...
             (((((kb*D)/(pi*L))^2)/(R^2 + X^2))+(xi^2)));
        em = ((kb*D*R*coth(2*pi*xi))/(pi*L*(R^2+X^2))) - ...
             sqrt(((kb*D*R*coth(2*pi*xi))/(pi*L*(R^2+X^2)))^2 + ...
             ((2*kb*D*X*xi*coth(2*pi*xi))/(pi*L*(R^2+X^2))) + ...
             (((((kb*D)/(pi*L))^2)/(R^2+X^2)) + (xi^2)));
        Fp = cos(pi*ep)*((xi*sinh(pi*xi))-((kb*D*X)/...
                (pi*L*(R^2+X^2)))*cosh(pi*xi))-...
             sin(pi*ep)*((ep*cosh(pi*xi))-((kb*D*R)/...
                (pi*L*(R^2+X^2)))*sinh(pi*xi));
        Fm = cos(pi*em)*((xi*sinh(pi*xi))-((kb*D*X)/...
                (pi*L*(R^2+X^2)))*cosh(pi*xi))-...
             sin(pi*em)*((em*cosh(pi*xi))-((kb*D*R)/...
                (pi*L*(R^2+X^2)))*sinh(pi*xi));
        if abs(Fp) < 10e-8
            eta = ep; break;
        elseif abs(Fm) < 10e-8
            eta = em; break;
        end
    end
    gm = xi + eta*sqrt(-1);
end
```